Abstract

This thesis focuses on the valorization of furfural, a biomass-derived compound, via oxidation and hydrogenation reactions. Thus, for the mentioned transformations in the previous sentence, gold-modified LDH-based catalysts were prepared: MgAlZr-LDH for oxidation and NiAlZr-LDH for hydrogenation. Besides these studies, a photooxidation study of glucose was also performed over the Au/NiAlZr catalyst, where light activation resulted in the improvement of catalytic performance. Characterization by IR, XRD, BET, SAA, SEM, TEM, and UV-visible techniques is performed in this work. It allows a correlation between their structure and catalytic performance, which provides insight into their mechanisms in the studied reactions.

Resumen

Esta tesis se centra en la valorización del furfural, un derivado de la biomasa, mediante procesos de oxidación e hidrogenación. Se desarrollaron catalizadores basados en hidróxidos dobles laminares (LDH) modificados con oro: MgAlZr-LDH para la oxidación y NiAlZr-LDH para la hidrogenación. Además, se llevó a cabo un estudio sobre la fotooxidación de la glucosa utilizando el catalizador Au/NiAlZr, donde la activación por luz mejoró las prestaciones catalíticas. Los catalizadores fueron caracterizados mediante técnicas como IR, DRX, BET, SAA, SEM, TEM y UV-visible, lo que permitió correlacionar su estructura con sus rendimientos catalíticos y comprender mejor sus mecanismos de acción en las reacciones estudiadas.

ملخص

تركز هذه الأطروحة على تثمين الفورفورال، أحد مشتقات الكتلة الحيوية، من خلال عمليات الأكسدة والهدرجة. تم تطوير محفزات، تعتمد على هيدروكسيدات صفائحية مزدوجة (LDH) معدلة بالذهب، لهذه التحولات: MgAlZr-LDH للأكسدة وNiAlZr-LDH للهدرجة. ركزت دراسة إضافية على الأكسدة الضوئية للجلوكوز باستخدام محفز Au/NiAlZr، حيث أظهر التنشيط الضوئي أدا ″ء محسن″ا. وتم توصيف المحفزات باستخدام تقنيات مثل IR، وXRD، وBET، وSAA، وSEM، وTEM، والأشعة فوق البنفسجية المرئية، مما يسمح بربط بنيتها بأدائها التحفيزي، وتعميق فهم آليات عملها في التفاعلات التي تمت دراستها.

Dib Nihel

Thesis doctoral
2024

MODIFIED LDH-SUPPORTED AU CATALYSTS: SYNTHESIS, CHARACTERIZATION AND CATALYTIC PERFORMANCES IN FURFURAL LIQUID PHASE OXIDATION AND HYDROGENATION

MODIFIED LDH-SUPPORTED AU CATALYSTS: SYNTHESIS, CHARACTERIZATION AND CATALYTIC PERFORMANCES IN FURFURAL LIQUID PHASE OXIDATION AND HYDROGENATION

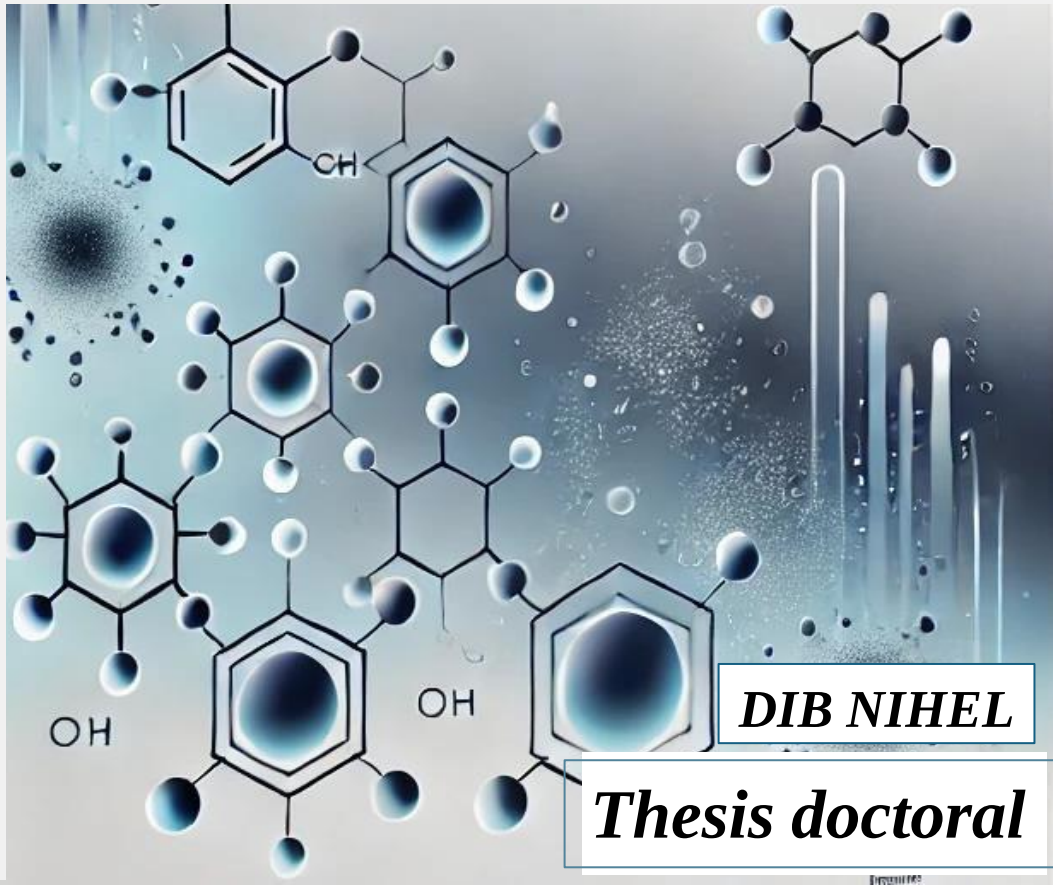

DIB NIHEL

Thesis doctoral

FACULTY OF SCIENCE – DEPARTMENT OF CHEMISTRY
UNIVERSITY OF TLEMCEN – ALGERIA
DEPARTMENT OF MATERIALS SCIENCE, METALLURGICAL ENGINEERING AND INORGANIC CHEMISTRY
UNIVERSITY OF CADIZ – SPAIN

To obtain the Doctorate degree in Nanoscience and Materials Technology

Presented by:

Ms. Nihel Dib

MODIFIED LDH-SUPPORTED AU CATALYSTS: SYNTHESIS, CHARACTERIZATION AND CATALYTIC PERFORMANCES IN FURFURAL LIQUID PHASE OXIDATION AND HYDROGENATION.

Pr. Miguel Angel CAUQUI LOPEZ	Professor	University of Cadiz	President
Pr. Redouane BACHIR	Professor	University of Tlemcen	Supervisor
Pr. Ginesa BLANCO MONTILLA	Professor	University of Cadiz	Co- supervisor
Pr. Sumeya BEDRANE	Professor	University of Tlemcen	Examiner
Dr. Marta STUCCHI	Professor	University of Milan	Examiner
Pr. Zoheir ARRAR	Professor	University of Tlemcen	Examiner

Dedication

To my dear parents

No words, however eloquent, can fully express my gratitude and appreciation for you. You have instilled in me a sense of responsibility, optimism, and self-confidence in the face of life's challenges. Your guidance has always led me toward success.

Your endless patience, understanding, and encouragement have been the indispensable support that has carried me through. I owe who I am today and who I will become tomorrow to you, and I will always do my best to be your pride and to never let you down. May God, the Almighty, grant your health, happiness, peace of mind, and protection from all harm.

To my sister Naila, my brother Mounir, and his wife Ghizlene, and my nephews,

Thank you for always being by my side, for your presence, your devoted love, and your kindness, which give flavor and meaning to my life. As a token of my sincere love and appreciation, I pray that God, the Almighty, grants you happiness and prosperity.

To my best friend, Guellil Wissem,

Your trust and encouragement were a beacon of light during my moments of despair. Thank you deeply for your invaluable support, for your big heart, and for all your qualities, which are too many to list. My life would not be as magical without you in it.

To Chaimae-Zoulikha Tabet Zatla, Zineb Bensaine, and Maroua Rakhma,

Your friendship is an honor and a source of pride for me. Thank you for brightening my life with precious moments of happiness. I sincerely hope that this work reflects my deepest love and appreciation for each of you.

Acknowledgments

First and foremost, I would like to thank the two universities that have made this co-tutelle possible: the **University of Tlemcen**, **Algeria**, and the **University of Cadiz**, **Spain**. This collaboration was indeed the main link for my thesis, in which proper exchange could take place between these two universities.

I would like to express my great acknowledgments to **Pr. Choukchou Braham Noureddine**, Director of the laboratory at the University of Tlemcen, for his warm welcome and assistance: his involvement and encouragement really made the difference in the good outcome of this work.

I am deeply grateful to my tutors, **Pr. Bachir Redouane** and **Pr. Ginesa Blanco Montilla**, for having guided me during this research, for the support received from them, and for the value of their advices. Without their knowledge, availability, and patience, this thesis would not have been possible.

I would like also to express my warm gratitude to my tutor **Pr. José Juan Calvino** for the continuous support given to me, the enlightening advices, and the goodness that has accompanied me during this period; only his indications allowed my job to go ahead. I would like to extend, with much appreciation, my thanks to **Pr. Sumeya Bedrane** for her support, encouragement, and valuable advice during this thesis. Her experience added much to my work.

I am very grateful to the members of the laboratories at both the University of Tlemcen and the University of Cadiz because of their welcoming attitude and friendly companionship that made our research experience so rewarding and pleasant. I would like to express my grateful acknowledgments to all the technicians in both institutions for their valuable help regarding the practical aspects of my work. Special mention must be made of **Ms. Fatima Mokri**, whose availability, efficiency, and perfect commitment have been relevant since the start of this work.

I would like to thank my friends **Wissem Guellil**, **Zineb Bensmaine**, and **Chaimae-Zoulikha Tabet Zatla**, who have been sharing this academic adventure with me. Their moral support, listening ear, and understanding kept me strong when the going gets really tough. We shared much more than studies, we shared moments of friendship that I will always cherish. I would also like to thank my friend, **Maroua Rakhma**, whose friendship and support mean so much to me, even outside my studies during this whole journey.

I would like, lastly, to express my most sincere thanks to my family, who have been my pillar throughout this adventure. To **my parents**, who taught me how hard one works and how much one must endure, and who were always there to support me during bad times. To my sister **Naila**, who always knew the right things to say to comfort and encourage me when I needed her. To my brother **Mounir** and my sister-in-law **Ghizlaine** for their help in surmounting several of my most painful setbacks. They have been constant motivation since their love, patience, and faith in me have not faltered. I am deeply indebted to them for their part in the partial success of this project and for what all they have done for me; I thank them with the profundity of my heart.

And finally, I want to remember the students with whom, for so many hours in the office and laboratory, I shared jokes, scientific discussions, and unforgettable moments during these years of hard work and long days. Their presence made this journey not only bearable but also enjoyable.

Table of figures

Table of figures

Table of figures

Table of schemes

List of tables

Abbreviations

- **FF**: Furfural
- **SA**.: Succinic Acid
- **FuA**: Furoic Acid
- **FmA**: Fumaric Acid
- **MA**: Maleic Acid
- **FA**: Furfuryl Alcohol
- **iPFE**: Isopropylfurfuryl Ether
- **LDH**: Layered Double Hydroxides
- **NPs**: Nanoparticles
- **UDP**: Urea Deposition-Precipitation
- **XRD**: X-ray Diffraction
- **FTIR**: Fourier Transform Infrared Spectroscopy
- **BET**: Brunauer, Emmett, and Teller
- **BJH**: Barrett, Joyner, and Halenda
- **TEM**: Transmission Electron Microscopy
- **HAADF**: High-Angle Annular Dark-Field
- **SEM**: Scanning Electron Microscopy
- **DRS UV-vis**: Diffuse Reflectance Spectroscopy in the ultraviolet-visible range
- **HPLC**: High-performance liquid chromatography
- **GC-MS**: Gas Chromatography-Mass Spectrometry
- **TOF**: Turnover Frequency
- **NMR**: Nuclear Magnetic Resonance
- **LSPR**: Localized Surface Plasmon Resonance
- **FFD**: Full Factorial Design

Important:

The nomenclature of **Layered Double Hydroxides (LDHs)**, as seen in formulas like **$MgAl_2Zr_{4.5}$** or **$NiAl_2Zr_{4.5}$**, reflects the ratios of metal cations in the structure. In these examples, the number "**2**" corresponds to the molar ratio of Mg to Al (**Mg/Al**), while "**4.5**" denotes the ratio of Mg to the combined total of Al and Zr (**Mg/(Al+Zr**)). This notation is consistently applied throughout this thesis.

Summary

Summary

General introduction

Due to the pressing global energy demands, coupled with stringent environmental regulations and the ongoing depletion of fossil fuel reservoirs, there has been a notable surge in interest across various scientific domains towards renewable energy resources. Recent endeavors have been concentrated on synthesizing specific chemicals from biomass as a viable and efficient strategy to substitute traditional fossil fuel sources. Lignocellulosic biomass has emerged as a promising low-cost feedstock due to its abundant and renewable nature on Earth. Over recent decades, biomass has garnered significant attention, with numerous studies highlighting its substantial potential as a renewable resource. Lignocellulosic biomass, primarily composed of cellulose, hemicellulose, and lignin, represents a complex organic matrix with a great industrial significance as a carbone source. Cellulose, a partially crystalline polymer, has found widespread applications across various industries, as a precursor for glucose, a crucial chemical intermediate utilized in the production of polyols and organic acids. However, lignin and hemicellulose, the other major constituents of lignocellulosic biomass, remain underutilized. Their current applications typically yield low added value or are predominantly focused on energy generation. Efforts to enhance the valorization of lignin and hemicellulose, unlocking their full potential for higher-value products, represent a significant avenue for research and development in biomass utilization. The utilization of lignocellulosic biomass as a cost-effective and renewable material is a huge challenge for various industries, encompassing energy, chemical intermediates, pharmaceuticals, and agri-food sectors. While processes for extracting platform molecules such as furfural from biomass exist [9, 10], the transformation of these molecules into higher-value products through economically viable processes remains a substantial challenge for scientific research.

The work carried out in this doctoral thesis is part of the research and development of new profitable industrial processes aimed on one hand to use of renewable raw materials in order to integrate a circular economy and to increasingly reduce carbon impacts for the production of energy and widely used chemicals on another hand.

This thesis focuses on three specific biomass valorization ways: furfural oxidation, furfural hydrogenation, and glucose photo-oxidation. These ways offer promising prospects for the selective conversion of biomass into high value-added chemicals.

The stated objective for this thesis is to prepare a series of heterogeneous catalysts based on low-content gold nanoparticles supported on Zr-modified linear double hydroxides (LDHs). The catalysts are used for biomass derived furfural valorisation reactions by oxidation and hydrogenation. They are also used for the photo-oxidation reaction of biomass derived glucose.

Although, the main objective of this thesis is to develop innovative catalysts and processes to improve the efficiency and selectivity of reactions, studies are also conducted to deepen the knowledge of the reaction mechanisms involved in these different biomass valorisation ways.

Depending on the targeted reaction, two families of LDHs have been synthesized, namely MgAl-LDHs and NiAl-LDHs.

This manuscript is organized into five chapters as follows:

Chapter I is dedicated to bibliographical reminders concerning biomass, furfural, glucose, LDHs and gold nanoparticles.

Chapter II is dedicated to the presentation of the different experimental methods and techniques used for the preparation of the different materials and catalysts, the characterizations and the catalytic tests.

In chapters III, IV and V are reported respectively the results of characterizations and catalytic tests of Au/MgAlZr catalysts in furfural oxidation, Au/NiAlZr in furfural hydrogenation and Au/NiAlZr in glucose photo-oxidation.

Finally, the main results and discussions are summarized in a conclusion-discussion.

Chapter I*. Bibliographic study*

One of the main objectives of this thesis is to develop cost-effective and efficient catalytic processes for the valorization of lignocellulosic biomass as a source of energy and raw materials for different chemical industries. Indeed, each year, more than 40 million tons of non-edible vegetable raw material, including wheat stalks, corn stover (encompassing stalks and leaves), wood chips from forestry, and by-products of wood industries are produced. A large part is often relegated to waste **[1]**.

The prospect of converting this woody plant waste into chemicals and/or "second generation" biofuels is very promising, as it offers environmentally sustainable alternative that doesn't compromise food resources for our planet. This endeavor aligns with the broader objective of harnessing untapped resources to fulfill our energy and organic raw material requirements while mitigating environmental impact and increasingly integrating a circular economy.

For this reason, we report in this chapter a bibliographic reminder concerning lignocellulosic biomass as well as a reminder of the state of the art for the transformation of furfural and the use of LDHs and gold nanoparticles as catalysts.

PART I. BIOMASS

I. Biomass: definitions, composition and sources

The term biomass broadly encompasses all living matter, defined as any organic matter available on a renewable basis. This includes dedicated energy crops and trees, residues from agricultural food and feed crops, aquatic plants, wood and wood residues, animal wastes, and various other waste materials **[2]**. Since the onset of the initial oil crisis, this concept has been extended to include organic plants and animal products used for energy or agronomic purposes. According to the classification established by Hoogwijk et al. **[3]**, biomass production can be categorized into eight distinct classes :

- Biomass generated from unused agricultural land, not designated for food or animal feed, is specifically cultivated as dedicated crops known as energy crops. These crops are intentionally grown to be used as a renewable energy source, distinct from those intended for food or feed purposes.
- Biomass generated through deforestation (forest maintenance) or clearing of agricultural land refers to the organic matter derived from the removal of trees or vegetation for various purposes such as land management or agricultural activities.
- Agricultural residues encompass a wide range of organic materials left over from various agricultural activities. This includes residues from cereal crops, vineyards, orchards, olive groves, fruits, vegetables, and agribusiness operations.
- Forestry residues comprise organic material derived from forestry activities and wood processing operations. These residues include leftover materials such as branches, bark, and sawdust generated during logging, timber processing, and other forestry-related activities.
- Agricultural residues from livestock farming refer to organic waste materials produced as byproducts of animal husbandry. These residues include manure, slurry, litter, droppings, and other waste products generated from the raising and housing of livestock animals.
- Organic waste from households encompasses a variety of biodegradable materials discarded by individuals or families. This includes paper, cardboard, green waste (such as grass clippings and garden trimmings), food scraps, and other organic materials generated from daily household activities.
- Biomass directly utilized for non-food and non-energy purposes, such as wood used in paper production, refers to organic material employed in applications unrelated to food consumption or energy generation. In this context, wood is utilized as a raw material in the paper-making industry, serving as a primary component for manufacturing various paper products.
- Organic waste from ordinary industrial sources encompasses various biodegradable materials commonly found in industrial waste streams. This includes items such as paper, cardboard, wood, and putrescible waste (biodegradable waste that can decompose rapidly and may emit foul odors as it rots).

Some distinguish between "dry biomass," which includes various wood wastes and agricultural residues (woody wastes) often referred to as "wood-energy," and "wet biomass," comprised of wastes of agricultural origin (such as manures, slurries), agri-food waste, or urban waste (like green waste, sewage sludges, fermentable fraction of household waste), which can be converted into energy or used as fertilizer or soil amendment. Within the scope of our study, we are particularly focused on "dry biomass," which we will also term as "lignocellulosic" biomass **[**4**]**.

Figure I-1: Some examples of lignocellulosic biomass sources

In 2021, the global harvested area for major crops amounted to approximately 221 million hectares for wheat, 206 million hectares for maize, 165 million hectares for rice, 49 million hectares for barley, and 41 million hectares for sorghum **[5]**. Alternatively, projections suggest that by 2050, the annual worldwide production of postharvest residues from cereal crops could range between 2.004 and 2.116 gigatons **[6]**. Disparities in cultivated area, crop varieties, and yields exhibit substantial variations across countries, primarily influenced by factors such as climatic conditions, specific soil attributes, and diverse agricultural practices. Among these crops, cereals emerge as paramount due to their extensive cultivated area and substantial production.

I.1. Lignocellulosic biomass compounds

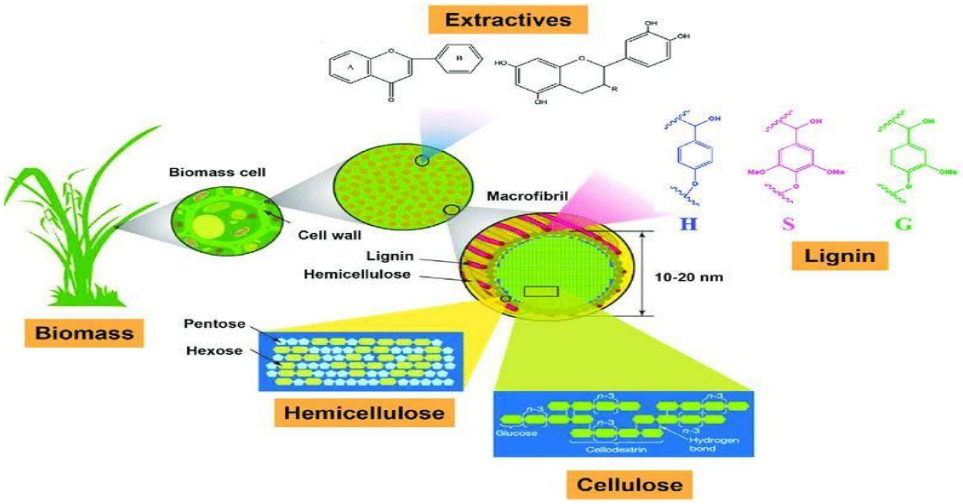

Figure I-2: The major components of biomass.

The major components of biomass are:

I.1.1. Cellulose

Cellulose serves as a fundamental component of the structural membrane in plant cells. Classified as a sugar, it is constitute of a glucose polymer with the chemical formula $(C_6H_{10}O_5)_n$, where n typically falls within the range of 200 to 3000 (**Figure I-3**). Despite its well-established chemical structure, the crystalline and fibrous arrangements of cellulose remain partially elucidated. In its natural state, cellulose exhibits fibrous characteristics and has partial crystallinity. It is frequently found in association with hemicelluloses. This combined structure is referred to as holocellulose **[7]**.

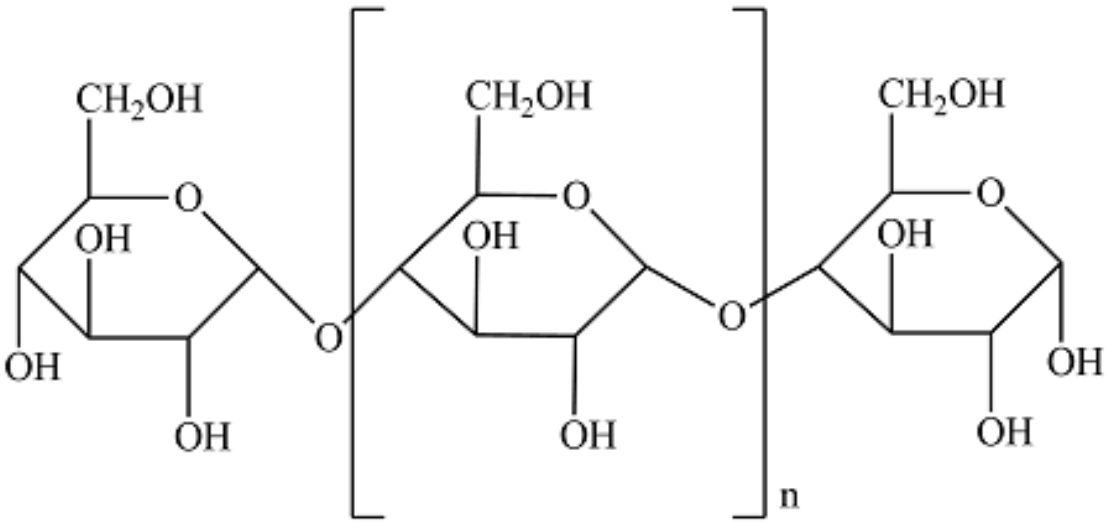

Figure I-3: Structural formula of cellulose.

I.1.2. Hemicellulose

Hemicellulose refers to a group of water-soluble polysaccharides extractable from plant cell walls through acidic solutions. This class of polymers is highly diverse, characterized by various

monomers and branching structures, which makes it challenging to precisely define. In its natural state, hemicellulose typically exhibits a degree of polymerization ranging between 200 and 300, and its structure varies depending on the plant species. **Figure I-4** illustrates the most prevalent monosaccharide units found in different hemicellulose families. In wood cell walls, the most common hemicelluloses belong to the xylan, mannan, and galactan families, composed of linear backbones primarily consisting of xylose, mannose, and galactose, respectively.

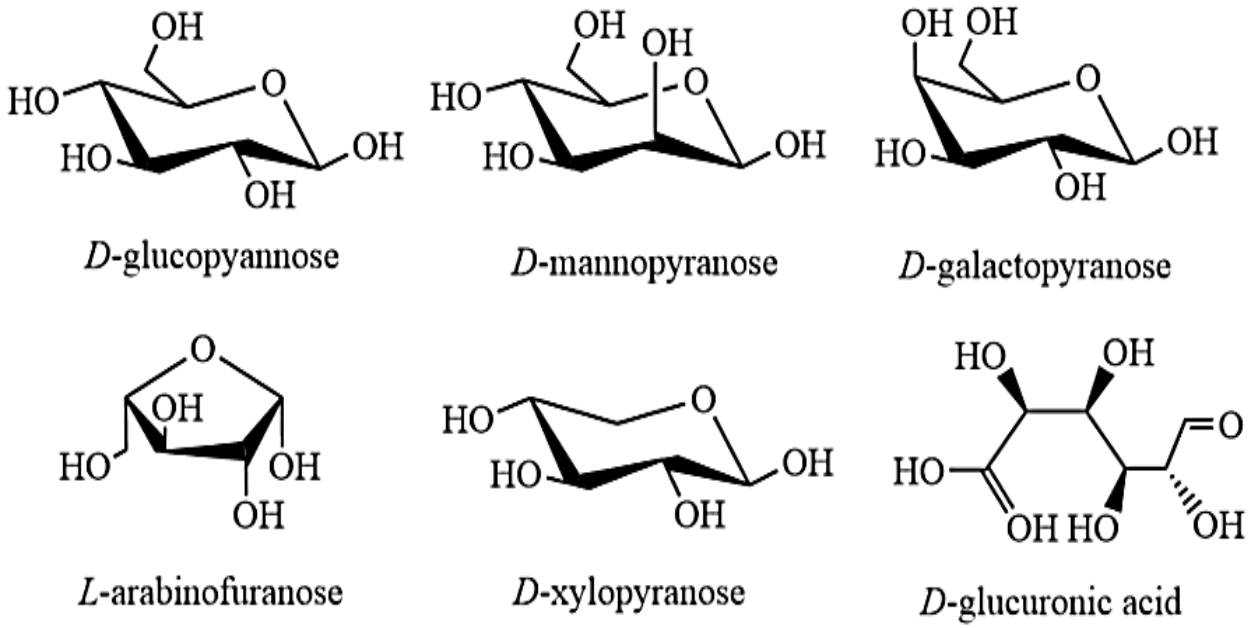

Figure I-4: Monomer sugars found in hemicellulose [8].

I.1.3. Lignin

Lignin is a group of compounds classified as phenolic compounds. Its structure is typically influenced by various factors such as the type of biomass and its age. Due to the difficulty of isolating native lignin from wood without inducing degradation, its precise chemical structure and molecular weight remain elusive. However, approximate molecular weights have been identified, averaging between 5,000 to 10,000 g/mol for hardwoods (predominantly hardwoods) and approximately 20,000 g/mol for softwoods (mainly softwoods). **Figure I-5** illustrates the fundamental unit of lignin.

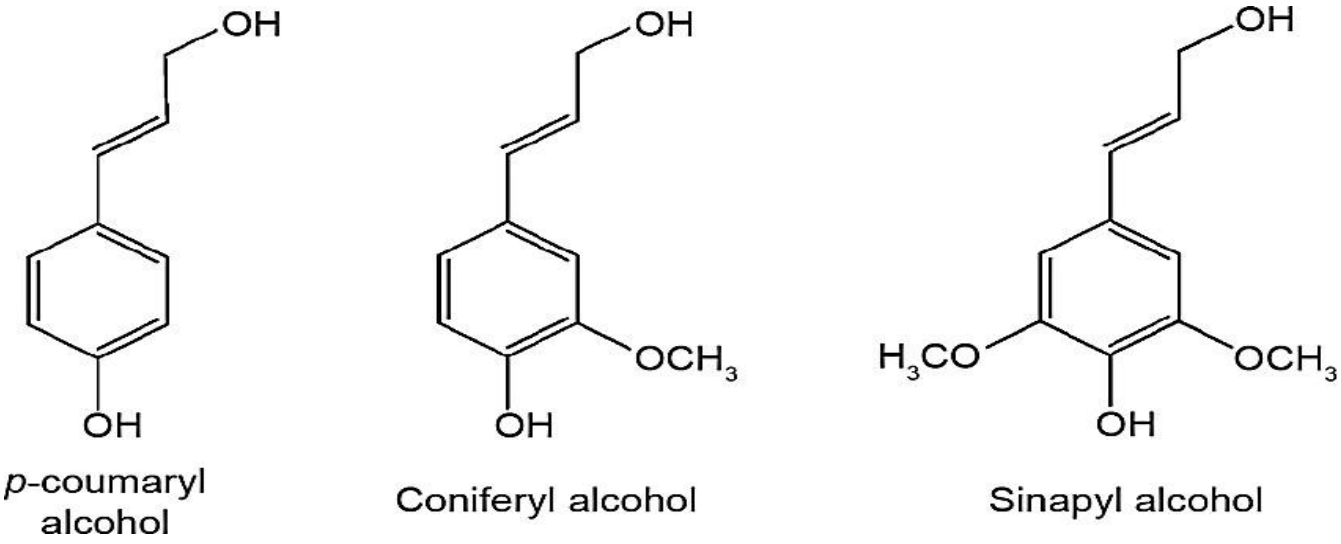

Figure I-5: Basic structural unit of lignin [9].

PART II. Furfural

I. Furfural

Furfural is a key platform molecule produced in significant quantities from lignocellulosic biomass, particularly through the dehydration of xylose obtained from the acid hydrolysis of hemicellulose. Its primary application lies in serving as a selective extraction solvent in the production of lubricating oils. Additionally, furfural acts as a precursor to furfuryl alcohol, which is further utilized in the synthesis of synthetic resins **[10]**.

I.1. Physicochemical properties of furfural

Furfural is a heterocyclic aldehyde belonging to the furan family. Its chemical formula, ($C_5H_4O_2$), was established at the start of the twentieth century by the Scottish chemist John Stenhouse, who successfully produced it from corncobs and oat bran through hydrodistillation in a sulfuric acid medium **[11]** . Table I-1 provides a summary of the physicochemical properties of furfural.

Table I-1: The physicochemicalproperties of furfural.

physicochemical properties	Basic information
N° CAS	98-01-1
IUPACname	Furan-2-carbaldehyde
Structural formula	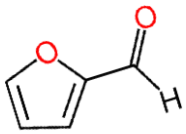
Brute formula	$C_5H_4O_2$
Appearance	Colorless to yellow liquid, with characteristic odor
Molar mass	96,08 g mol-1 (C 62,5 %, H 4,2 %, O 33,3 %)
Boiling temperature	162 °C
Solubility at 20°C	In water 83 g L^{-1}, completely soluble in solvents organic
Density at 20°C	1,159 g mL^{-1}

Furfural has two significant functional groups: an aldehyde group (CHO) and a conjugated system (C=C-C=C). Due to these functional groups, furfural exhibits versatility in numerous applications. The aldehyde group of furfural can undergo various types of reactions, including acetylation, acylation, aldol and Knoevenagel condensation, reduction to alcohols, reductive amination to amines, decarboxylation, oxidation to carboxylic acids, and Grignard reactions. Additionally, the

furan ring system (C=C-C=C) in furfural is amenable to alkylation, hydrogenation, oxidation, halogenation, open ring reactions, and nitration.**[12, 13]**

I.2. Furfural production sources and methods

Furfural is globally produced from the by-products of agro-industries such as corn cobs, wheat straw, and bagasse, which are rich in pentosans (polypentoses like xylans and arabinans). The proportion of these pentosans varies depending on the source of the biomass. For instance, the amount of in pentosans sugarcane bagasse range from 26% to 28%. These pentosans undergo hydrolysis into pentoses, which are subsequently dehydrated in an acidic medium to yield furfural (**Scheme I-1**).

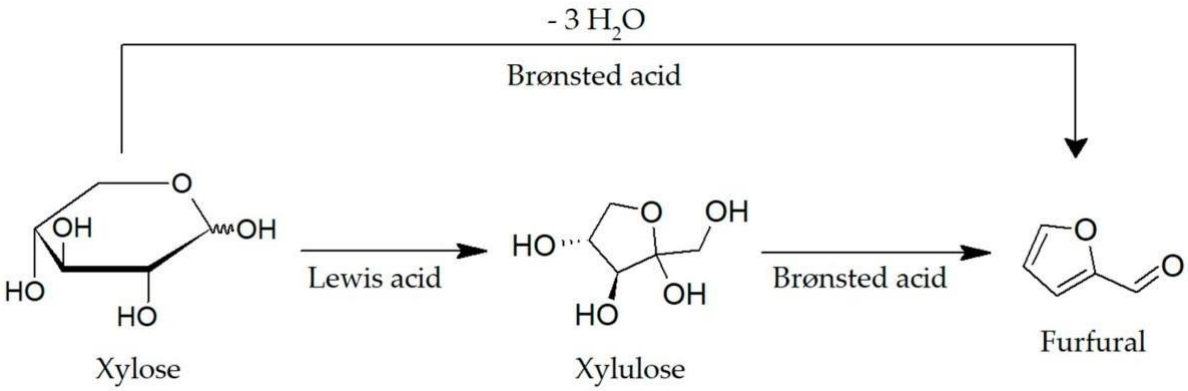

Scheme I-1: Furfural production from pentosans.

Scheme I-2 shows a mechanism of production of pentoses from a depolymerization process of pentosans by hydrolysis proposed by X. Déglise **[14]**. It suggests that the hydrolysis of pentosans begins with the protonation of the oxygen atom linking two pentose monomers. This protonation leads to the cleavage of the carbon-oxygen bond, resulting in the formation of a carbocation. Subsequently, the carbocation undergoes hydration to form a hydroxyl group, releasing a proton in the process. Repetition of these steps results in the depolymerization of pentosans into pentoses.

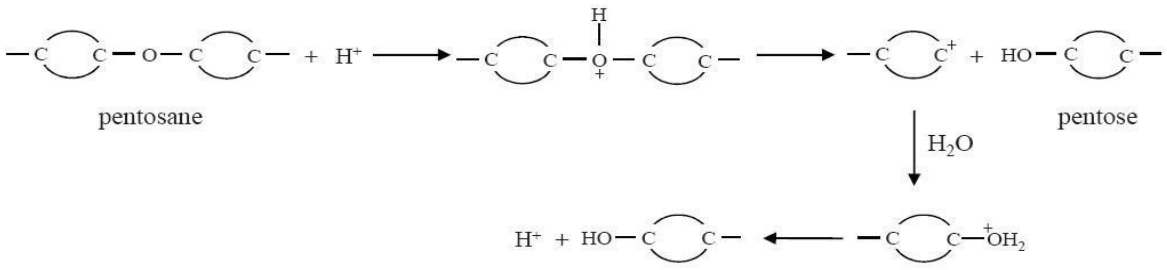

Scheme I-2: Mechanism of hydrolysis of pentosans into pentoses [14].

As it was reported by **B. Danon et al [15]** several mechanisms for the dehydration of pentoses to furfural can be considered. Theses mechanisms depend on the reaction conditions and the catalytic system employed. Two classes of potential mechanisms that vary depending on the initial form of the pentose have been identified:

- Dehydration of the acyclic (linear) form of the pentoses via intermediates formed either by enolization **[16]** or by β-elimination **[17]**;
- Dehydration of the cyclic (pyranic) form of the pentoses via protonation of the hydroxyl group at the C_2 position **[18]**.

Scheme I-3 represents different possible routes for the dehydration of xylose to furfural proposed in the literature.

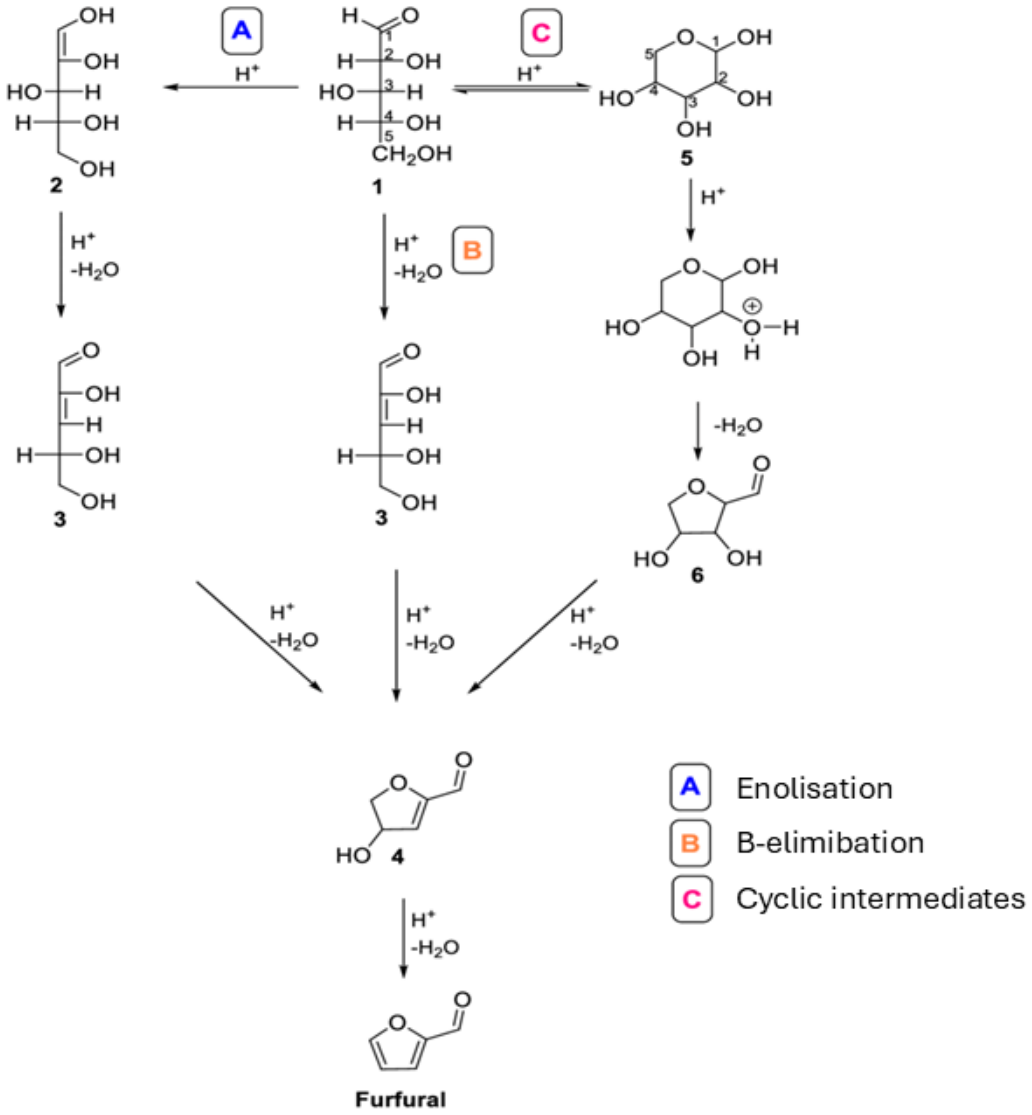

Scheme I-3: Possible mechanisms for the dehydration of xylose to furfural [16-18].

I.3. Furfural valorization

The large-scale production of furfural has significantly advanced the chemistry of furan derivatives. Furfural plays a crucial role as a petrochemical extractant in the manufacturing process of lubricating oils, which are derived from the residual components of atmospheric distillation of petroleum. Moreover, furfural serves as a key precursor to furfuryl alcohol. Almost 65% of global furfural transformation is currently directed towards furfuryl alcohol synthesis. Furfuryl alcohol is a versatile compound widely utilized in the synthesis of various chemical products, including furanic resins, solvents (such as MTHF and THF), and levulinic acid esters.

Over the last two decades, new applications for furfural have emerged, particularly in the production of biofuels (alkanes: C_8-C_{15}) through aldol condensation reactions coupled with catalytic hydrodeoxygenation. **Scheme I-4** provides a comprehensive illustration of the various chemical products that can be derived from furfural.

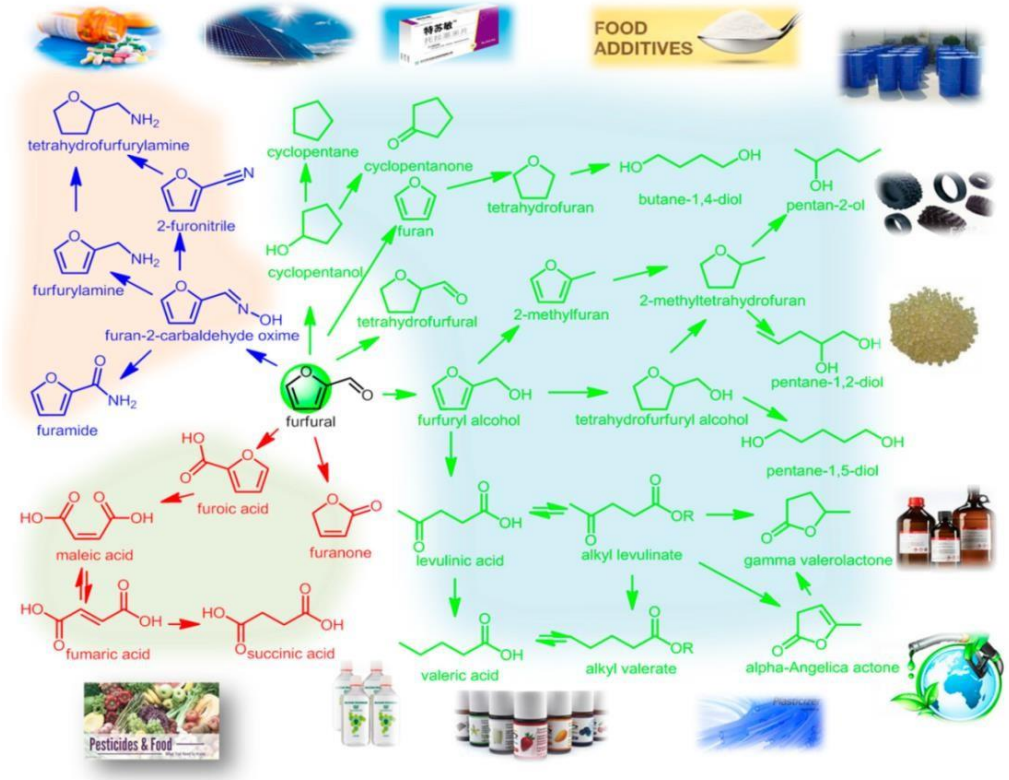

Scheme I-4: Downstream products of furfural, obtained by hydrogenation (in green), oxidation (in red), cyanation, and other processes (in blue) [19].

I.4. Development history

- Furfural, originally discovered as a byproduct of formic acid synthesis by **Johann Wolfgang Döbereiner** in 1821**[20]**, has since witnessed significant milestones in its understanding and development.

- in 1840, **John Stenhouse** discovered that furfural could be derived by distilling various crops (such as corn, oats, bran, and sawdust) **[21]** with aqueous sulfuric acid. Additionally, he suggested its molecular formula as ($C_5H_4O_2$).
- In 1845, **George Fownes** officially named this oil "furfural"**[22]**.
- The structure of furfural was deduced by **Karl Harris** in 1901.
- In 1922, the American Quaker Oats Company achieved the industrialization of furfural **[23]**. This milestone marked the beginning of furfural's application in the industrial field, primarily used in the decolorization of wood resins and refined lubricating oil.
- In the 1940s, furfural found widespread applications in the fields of synthetic rubber, medicine, and pesticides **[24]**.
- After the 1960s, with the development of furfural derivatives, particularly the extensive use of furan resin in the foundry industry, the furfural industry experienced significant growth and advancement**[25]**.
- In 2004, the US Department of Energy recognized furfural as a prominent bio-based chemical within the top 30 **[26]**. Furfural is acknowledged as a crucial organic chemical raw material, capable of producing various compounds such as maleic anhydride, oxalic acid, decanol, and tetrahydrofuran. Its applications extend to the synthesis of furfural resin, furan resin, rubber vulcanization accelerators, rubber anti-aging agents, and preservatives. Primarily utilized in sectors such as medicine, pesticides, veterinary drugs, and food, furfural plays a pivotal role in diverse industries **[27]**.

I.5. Why furfural?

Furfural is acknowledged as a platform molecule, featuring five carbons and a gross formula of $C_5H_4O_2$, with a molar mass of 96.08 g/mol. It is obtained through the dehydration of saccharides and is industrially produced, frequently sourced from agricultural residues. Its value in utilization stems from its availability without competing with the food chain, rendering it a sustainable and environmentally friendly option.

On a global scale, furfural is manufactured from agricultural residues rich in pentoses, such as corn cobs, oat hulls, bagasse, and other similar materials.**[28]** Furfural is primarily utilized as a raw material for the synthesis of various chemicals, including furfuryl alcohol, methyltetrahydrofuran, and furan. **[29]**. In recent years, several studies have focused on the valorization of furfural and its derivatives, particularly in the production of biofuels **[30, 31]**, as well as a new generation of bioproducts and bioplastics. For instance, furfural can be converted into dimethylfuran (DMF), a biofuel with high energy density, through selective catalytic hydrogenation. DMF has shown promising properties as a renewable alternative to fossil fuels. Moreover, furfural serves as a precursor

for the production of bioplastics, where it can be polymerized into furan-based resins or incorporated into biodegradable polymer matrices, offering an eco-friendly alternative to petroleum-derived plastics

I.6. Bibliography

I.6.1. Furfural oxidation

- **Lin et al. [32]**investigated the gas-phase oxidation of furfural under mild conditions (0.5 MPa O_2, 40°C) in a batch system. They utilized a gold nanoparticle catalyst (6.4 ± 2.5 nm), specifically Au (PVP)/Nb_2O_5, where Nb_2O_5 remained in its original crystal structure. Notably, Au (PVP)/Nb_2O_5 (calcined at 400°C) demonstrated a 43% furfural conversion rate with 100% selectivity towards furoic acid.

- **Xiang et al. [33]** investigated the oxidation reaction of furfural using $MgOH_2$ as a catalyst under specific conditions: 0.02 mol furfural, 0.1 mol H_2O_2, 0.375 mol H_2O, and 1 mmol $Mg(OH)_2$ at 70°C. Their findings indicated a 100% conversion of furfural with product distribution as follows: 2.6% 2-formyloxyfuran, 40.2% 2(5H)-furanone, 32.7% succinic acid, 2.5% furoic acid, 2.4% 2,3-furanone, and 19.5% other byproducts.

- **Alba-Rubio et al.[34]** in 2017 reported oxidation of furfural with H_2O_2 using Ti-Si. They have achieved a conversion of 90% and a selectivity of 70% towards maleic acid.

- **Guo et al.[35]** employed a biphasic system with phosphomolybdic acid as a catalyst for the oxidation of furfural to maleic acid. Their results showed a 50.4% conversion of furfural, a yield of 34.5%, and a selectivity of 68.6% towards maleic acid, utilizing oxygen as the oxidant.

- **Song et al.[36]** employed copper salts and phosphomolybdic acid in an aqueous solution as a catalyst for the oxidation of furfural using O_2 as the oxidant. The reaction was conducted at 98°C, resulting a 95.2% conversion of furfural, with a selectivity of 51.7% towards maleic acid.

- **Choudhary et al. [37]** studied the oxidation reaction of furfural with H_2O_2 using an Amberlyst-15 solid acid catalyst in aqueous media to form succinic acid. Amberlyst-15 catalyzed the reaction, achieving over 99% conversion, with selectivities of 74% for fumaric acid, 74% for maleic acid, less than 1% for furoic acid, and 11% for succinic acid.

- In 2021 **Yang et al.[38]** showed that the coexistence of Br^- and alkali sites could play a vital role in the oxidation of furfural, which could remarkably improve the yield of maleic acid at 90◦C for 3 h, a MA yield of 72.4% was obtained with KOH and KBr as a co-catalyst in aqueous phase.

I.6.2. Furfural hydrogenation (production of octane number boosters)

In the literature, numerous researchers have delved into the synthesis of octane number enhancers derived from furfural, a compound sourced from lignocellulosic biomass. Key products under investigation include alcoholic furfural, 2-methylfuran, and furan. This research aims to explore the potential of these derivatives in increasing the octane number of fuels, thereby contributing to the development of sustainable and efficient additives for gasoline. Furthermore, researchers have

investigated the hydrogenation reaction of furfural using LDHs as catalysts. This reaction can yield a range of products, including but not limited to alcoholic furfural, 2-methylfuran, and furan, among others.

- **Tarazanov et al. [39]** conducted the hydrogenation of furfural within a temperature range of 120°C to 250°C under a hydrogen pressure of 40 bars, employing catalysts composed of copper (68% Cu/ZnO) and nickel (20% Ni/Al_2O_3). The process achieved complete (100%) conversion of furfural with approximately 95% selectivity towards 2-methylfuran (2-MF) when using the copper-based catalyst. In contrast, the nickel-based catalyst resulted in a 99% conversion of furfural with exclusive (100%) selectivity for tetrahydrofurfuryl alcohol (THFA), and no 2-MF was observed in the product mixture.

- **Kojčinović et al. [40]** investigated the hydrogenation, hydrodeoxygenation, and etherification reactions of furfural using unsupported MoO_2 and MoO_3 catalysts in a three-phase batch reactor. The reactions were conducted at temperatures between 170°C and 230°C, hydrogen pressures ranging from 0 to 80 bars, catalyst loadings of 0 to 2% by weight, and reactant concentrations from 5% to 20% by weight. MoO_2 achieved a conversion of 54.5%, with selectivity's of 9.2% for isopropyl levulinate (IPL) and 9.4% for isopropyl furfural (iPFE), and a mass balance of 72.1%. In contrast, MoO_3 exhibited a lower conversion of 11.8%, with the highest yield being 6.3% for isopropyl furfural (iPFE), and yields for isopropyl levulinate (IPL), furfuryl alcohol (FA), and isopropyl methyl furan (diPMF) all below 1%. This indicates that MoO_2 was significantly more effective in achieving higher conversion and selectivity for octane-boosting additives compared to MoO_3.

- In 2018, Ren et al. **[41]** conducted the hydrodeoxygenation of furfural using copper-based catalysts at temperatures ranging from 140°C to 220°C. The study found that at 140°C, the conversion was 79.2% with furfuryl alcohol (FA) as the main product (97.4%) and 2-methylfuran (2-MF) at 1.01%. As the temperature increased to 160°C, conversion rose to 84.7%, with FFA at 90.7% and 2-MF at 5.62%. At 180°C, the conversion reached 100%, with FFA at 20.3% and 2-MF at 73.4%. At higher temperatures (200°C, 210°C, and 220°C), the conversion remained at 100%, but selectivity shifted significantly towards 2-MF, with FA decreasing to 0.6% at 200°C, 1.1% at 210°C, and 0.3% at 220°C, and 2-MF increasing to 90.8%, 90.4%, and 88.4%, respectively.

- In 2017, **Wang et al.[42]** conducted the hydrogenation of furfural in isopropanol at 210°C using a 10% Ni-10%Cu/Al_2O_3 bimetallic catalyst, achieving a high conversion of 91% of furfural with 2-methylfuran as the highest yield at 75.6 mol%.

- In 2018, Prakruthi et al. **[43]** investigated the hydrogenation reaction of furfural using the LDH-based Cu/D-Cu-Al catalyst at a temperature of 220°C under 6 bars of hydrogen pressure. The study found that copper species impregnated on dealuminated Cu-Al oxide exhibited enhanced activity in converting furfural (FF) to furfuryl alcohol (FA). Hydrogen uptake and FF conversion increased

proportionately as the copper loading varied from 5 to 15 wt%, with the maximum yield of 87 mol% FA observed with the 15 wt% Cu-loaded sample. The percent occupancy of copper active species in the pores was calculated based on the decrease in pore volume, and a factor called pore occupancy hydrogenation efficiency was introduced to explain the conversion ability of the copper-loaded mixed oxides. In contrast, mixed oxides derived from Cu-Al layered double hydroxides (LDH) without dealumination showed only moderate conversion.

- In 2020, **Meng et al. [44]** conducted the hydrogenation of furfural at 200°C under 3 MPa of hydrogen pressure, employing NiZnAl-layered double hydroxides (LDHs) as catalysts. A series of NiZn alloy catalysts supported on mesoporous metal oxides (MMO) were synthesized through precise in situ reduction of LDH precursors with different Ni/Zn ratios (3/1, 1/1, and 1/3). The resulting Ni_1Zn_3-MMO catalyst showed significantly enhanced catalytic performance for the hydrodeoxygenation reaction of furfural, achieving a 95% yield of 2-methylfuran.
- In 2021, **Liu et al.[45]** utilized NiMo-LDHs as catalysts for the hydrodeoxygenation (HDO) of furfural in isopropanol at 240°C under 0.1 MPa hydrogen pressure. The primary product obtained was 2-methylfuran (2-MF) with a conversion rate of 37%.
- Additionally, other researchers have explored alternative catalysts. In 2017, **Thompson et al.[46]**conducted the hydrogenation of furfural at 150°C under 1 bar of hydrogen, employing three catalysts: 3% Pd/Al_2O_3, 5% Re/Al_2O_3, and the bimetallic catalyst Pd-Re/Al_2O_3. The selectivities of alcoholic furfural (FAL) were found to be 70–80% compared to bimetallic catalysts, but only 40% compared to 3% Pd/Al_2O_3. The main products obtained included FAL, furan, and 2-methylfuran (2-MF).
- In 2017, **Pino et al.[47]** employed Pd-Fe/SiO_2 and Pd-Fe/Al_2O_3 catalysts for the hydrogenation of furfural under 4 bars of H_2 for 1 hour at 250°C. Both catalysts achieved an 80% conversion. The gas-phase reaction mainly yielded 2-methylfuran with 40% selectivity over the bimetallic Pd-Fe/SiO_2 catalyst, while the decarbonylation reaction dominated over the Pd-Fe/Al_2O_3 catalyst, resulting in furan as the main product with 40% selectivity. Pd/Al_2O_3. The main products obtained included FA, furan, and 2-methylfuran (2-MF).
- In the same year, **Gong et al.[48]** investigated furfural hydrogenation using a metallic nickel catalyst supported by doped activated carbon (Ni/NAC) in 2-propanol at 140°C under 1 bar of hydrogen. They obtained furfuryl alcohol (FOL) and tetrahydrofurfuryl alcohol (THFOL) as products with an almost 100% furfural conversion.
- Additionally, in 2017, **Wang et al.[42]** conducted the hydrogenation of furfural in isopropanol at 210°C with a 10% Ni-Cu/Al_2O_3 bimetallic catalyst, achieving a highly efficient conversion of furfural to 2-methylfuran (91%).
- In 2020, **Meng et al. [41]** conducted the hydrogenation of furfural at 200°C under 3 MPa of hydrogen pressure, employing NiZnAl-layered double hydroxides (LDHs) as catalysts. A

series of NiZn alloy catalysts supported on mesoporous metal oxides (MMO) were synthesized through precise in situ reduction of LDH precursors with different Ni/Zn ratios (3/1, 1/1, and 1/3). The resulting Ni_1Zn_3-MMO catalyst showed significantly enhanced catalytic performance for the hydrodeoxygenation reaction of furfural, achieving a 95% yield of 2-methylfuran.

Table I-2: Catalytic Activity and Selectivity in Furfurals' Hydrogenation and Oxidation Processes.

Reference	Temperature (°C)	Pressure	Catalyst	Conversion (%)	Selectivity (%)	Main Product
Lin et al. [32]	40	0.5 MPa O_2	Au (PVP)/Nb_2O_5	43%	100%	Furoic acid
Xiang et al. [33]	70	-	$Mg(OH)_2$	100%	32.7%	Succinic acid
Alba-Rubio et al. [34]	-	H_2O_2	Ti-Si	90%	70%	Maleic acid
Guo et al. [35]	-	O_2	Phosphomolybdic acid	50.4%	68.6%	Maleic acid
Song et al. [36]	98	O_2	Copper salts + phosphomolybdic acid	95.2%	51.7%	Maleic acid
Choudhary et al. [37]	-	H_2O_2	Amberlyst-15	-	-	Succinic acid
Yang et al. [38]	90	3 h	KOH + KBr	-	72.4%	Maleic acid
Tarazanov et al. [39]	120-250	40	Cu/ZnO + Ni/Al_2O_3	100%	95% Cu: 2-MF, 100% Ni: THFA	2-MF (Cu), THFA (Ni)
Kojčinović et al. [40]	170-230	0-80	MoO_2 + MoO_3	54.5% (MoO_2), 11.8% (MoO_3)	9.2% IPL, 9.4% IFE (MoO_2)	IFE, IPL
Ren et al. [41]	140-220	-	Cu-based catalysts	100%	88.4% - 90.8%	2-MF (high temp.), FFA (low temp.)
Wang et al. [42]	210	-	10% Ni-Cu/Al_2O_3	91%	-	2-MF
Prakruthi et al. [43]	220	6	Cu/D-Cu-Al LDH	87 mol% FAL	-	FAL
Meng et al. [44]	200	3 MPa	NiZnAl LDH	95%	-	2-MF
Liu et al. [45]	240	0.1 MPa	NiMo LDH	37%	-	2-MF
Thompson et al. [46]	150	1	Pd/Al_2O_3 + Re/Al_2O_3	-	70-80%	FAL, furan, 2-MF
Pino et al. [47]	250	4	Pd-Fe/SiO_2 + Pd-Fe/Al_2O_3	-	-	2-MF, furan
Gong et al.	140	1	Ni/NAC	100%	-	FOL,

[48]	THFOL

I.6.3. Conclusion

The summary table provides an overview of catalytic performances for the hydrogenation and oxidation of furfural, highlighting the use of various catalysts and experimental conditions.

For furfural oxidation, the results demonstrate that catalysts such as phosphomolybdic acid, Ti-Si systems, and $Mg(OH)_2$ achieve notable conversions and selectivities. For instance, phosphomolybdic acid combined with oxygen achieved a conversion of 50.4% with a selectivity of 68.6% toward maleic acid, while Ti-Si systems with hydrogen peroxide reached a 90% conversion and 70% selectivity toward maleic acid. On the other hand, $Mg(OH)_2$ stands out with a 100% conversion of furfural but exhibited lower selectivity (32.7%) for succinic acid, with other by-products in the reaction mixture. Furthermore, copper salts combined with phosphomolybdic acid showed high conversion (95.2%) but moderate selectivity (51.7%) toward maleic acid under similar oxidation conditions.

For furfural hydrogenation, catalysts based on Layered Double Hydroxides (LDHs), such as NiZnAl LDH and Cu/D-Cu-Al LDH, have demonstrated outstanding performances. NiZnAl LDH achieved a 95% conversion to 2-methylfuran (2-MF), while Cu/D-Cu-Al LDH facilitated a high yield of furfuryl alcohol (FAL). Similarly, Ni-Cu/Al_2O_3, with 10% Ni and Cu, exhibited a high conversion rate of 91% to 2-MF. Copper-based systems, such as Cu/ZnO combined with Ni/Al_2O_3, showed full conversion (100%), yielding 2-MF and tetrahydrofurfuryl alcohol (THFA) as the main products, depending on the metal used. NiMo LDH and Pd-based catalysts, such as Pd/Al_2O_3 combined with Re/Al_2O_3, also displayed versatility, offering selective production of furfural derivatives, including furfuryl alcohol and 2-MF.

The data indicate that LDHs and Cu-based catalysts are particularly effective in both hydrogenation and oxidation reactions, offering high yields and targeted selectivity under various conditions. For oxidation reactions, the choice of oxidants such as O_2 or H_2O_2, combined with the appropriate catalyst, significantly influences the product distribution. In hydrogenation reactions, the performance of LDHs underscores their versatility, making them promising candidates for sustainable furfural valorization processes.

.

PART III. Glucose

I. Glucose

Glucose, also known as D-glucose, is a simple sugar and the most important monosaccharide in human metabolism. It belongs to the group of hexoses, which are six-carbon sugars, and has the molecular formula $C_6H_{12}O_6$ (**Figure I-6**). Structurally, glucose exists in two forms: the open-chain (acyclic) form and the cyclic form. In the cyclic form, glucose can exist as either α-glucose or β-glucose, depending on the orientation of the hydroxyl group attached to the first carbon atom (anomeric carbon).

I.1. Structure and Properties

Structurally, glucose exists in two forms: the open-chain (acyclic) form and the cyclic form. In the cyclic form, glucose can exist as either α-glucose or β-glucose, depending on the orientation of the hydroxyl group attached to the first carbon atom (anomeric carbon). In aqueous solutions, glucose predominantly exists in its cyclic form, where the molecule forms a six-membered ring, called a pyranose ring. This cyclic structure is more stable than the open-chain form and accounts for about 99% of glucose in solution. The open-chain form, which contains an aldehyde group, is present only in trace amounts but is crucial for the reactivity of glucose, particularly in reducing sugar reactions.

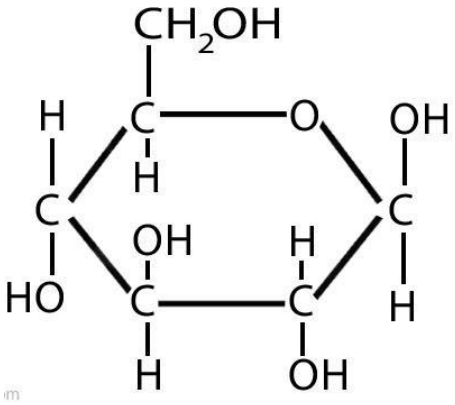

Figure I-6 : Glucose structure.

I.2. Industrial Applications

Beyond its biological importance, glucose has significant industrial applications. It is a fundamental building block in the food and beverage industry, particularly in the production of sweeteners like high-fructose corn syrup (HFCS). Glucose is also used as a fermentable sugar in the production of ethanol, which is employed in alcoholic beverages and as a biofuel.

In the pharmaceutical industry, glucose serves as an excipient in drug formulations, providing stability, and serving as a bulking agent. It is also utilized in intravenous solutions as a quick source of energy for patients.

Additionally, glucose plays a role in various biochemical research applications, where it is used as a standard in assays to measure enzyme activities and as a carbon source in cell culture media. Its role in the Maillard reaction, a chemical reaction between amino acids and reducing sugars that gives browned food its flavor, is another critical application in the food industry.

I.3. Photocatalytic Conversion of Glucose

The photocatalytic conversion of glucose represents an emerging area of interest within the field of green chemistry and renewable energy. Photocatalysis refers to the acceleration of a photoreaction in the presence of a catalyst, typically involving the absorption of light to drive chemical transformations. In the context of glucose, photocatalysis offers a sustainable approach to converting this abundant and renewable resource into valuable chemicals and energy.

The mechanism of photocatalysis involves the absorption of photons by the photocatalyst, which generates electron-hole pairs. The photons excite electrons in the catalyst's conduction band, creating free electrons (e^-) and leaving behind holes (h^+) in the valence band. These excited electrons and holes are highly reactive and participate in redox reactions. In the case of glucose oxidation, the electrons reduce molecular oxygen (O_2) to form reactive oxygen species (ROS) such as superoxide anion (O_2^-), while the holes oxidize glucose, leading to the formation of products like gluconic acid and hydrogen gas. This process is driven by light energy, making it a clean and sustainable method for chemical transformations.

One of the main attractions of glucose photocatalysis lies in its potential for the production of hydrogen, a clean fuel with high energy density. In this process, glucose can be oxidized in the presence of a photocatalyst under light irradiation, leading to the generation of hydrogen gas. This approach is particularly promising as it leverages the renewable nature of glucose, which can be derived from biomass, including agricultural waste and cellulose, making it an eco-friendly alternative to fossil fuel-based hydrogen production.

Titanium dioxide (TiO_2) is one of the most commonly used photocatalysts for glucose conversion due to its high stability, non-toxicity, and strong oxidizing power under ultraviolet (UV) light. However, recent research, including our work, has focused on developing novel photocatalysts that can operate under visible light, which constitutes the majority of sunlight.

In our study, we are particularly interested in exploring the photocatalytic conversion of glucose using layered double hydroxides (LDHs) as photocatalysts under sunlight. LDHs are known for their tunable composition, high surface area, and the ability to intercalate various anions, making them promising candidates for photocatalysis.

Hybrid photocatalysts are systems that combine multiple materials, typically a semiconductor and metal nanoparticles, to take advantage of the complementary properties of each. These materials offer enhanced photocatalytic activity by broadening the light absorption spectrum, improving electron-hole separation, and increasing overall efficiency. For example, when LDHs are combined with metal nanoparticles such as gold or silver, they become more efficient under both UV and visible light, which is especially important for processes like glucose oxidation or hydrogen production. The metal particles help to capture electrons and reduce recombination, thus enhancing the photocatalytic performance.

The use of LDHs under sunlight offers several advantages, including the potential to harness a broader spectrum of solar radiation compared to traditional photocatalysts like TiO_2. This can lead to improved efficiency and selectivity in the photocatalytic process, allowing for the effective conversion of glucose into hydrogen or other valuable chemicals under environmentally friendly conditions. Furthermore, hybrid photocatalysts, which combine materials like semiconductors with metal nanoparticles, have the potential to further enhance the absorption of light and the separation of electron-hole pairs, improving the efficiency of the reaction.

Beyond hydrogen production, the photocatalytic transformation of glucose can lead to the formation of various value-added chemicals, including organic acids (such as gluconic acid) and alcohols. These products have wide-ranging applications in the food, pharmaceutical, and chemical industries. For instance, gluconic acid, which can be produced through the photocatalytic oxidation of glucose, is used in food additives, pharmaceuticals, and as a chelating agent.

Moreover, the mild reaction conditions typically associated with photocatalysis such as ambient temperature and pressure make it an attractive alternative to conventional chemical processes, which often require harsh conditions and generate significant waste. This aligns with the principles of green chemistry, which aim to minimize the environmental impact of chemical production.

The ongoing research into glucose photocatalysis, including our work with LDHs and sunlight, is exploring ways to enhance the process's efficiency, selectivity, and scalability. For instance, the development of hybrid photocatalysts, which combine multiple materials or functionalities, holds potential for optimizing the reaction pathways and improving the overall yield of desired products.

In conclusion, the photocatalytic conversion of glucose not only offers a pathway to sustainable energy production but also opens new avenues for the generation of valuable chemicals from renewable resources. Our focus on utilizing LDHs as photocatalysts under sunlight further contributes to the advancement of this promising field, with the potential to make significant impacts on both energy production and chemical synthesis.

PART IV. Layered Doubles Hydroxides LDHs

The significance of Lamellar Double Hydroxides (LDHs) stems from their unique two-dimensional structure and anionic exchange capacity, offering opportunities for accessing a wide range of intercalation compounds. This can be achieved by modifying the chemical composition of the hydroxide sheet or through chemical alterations in the structural interlamellar domain. The growing interest in LDHs is driven by their anionic exchange properties, magnetic and electrochemical characteristics, usefulness in heterogeneous catalysis and pharmaceutical applications. As a result, ongoing research efforts are focused on structural characterization, developing novel compounds, and implementing new preparation methods. These methods aim to facilitate the intercalation of various anions, both organic and inorganic, as well as the trapping or immobilization of different species. This approach imbues these hybrid materials with unique reactivity, making them versatile in diverse applications.

I. Layered doubles hydroxides LDHs

The term LDH, or lamellar double hydroxide, refers to synthetic or natural double-layered materials, also known as anionic clays due to the charge carried by the layers. These materials consist of two types of metallic cations (divalent and trivalent) within the layers, while the interlayer space contains anions and water molecules.

Figure I-7 presents a schematic representation of a layered double hydroxide.

These clays are quite rare in nature. One notable example is hydrotalcite, a white powder like talc, with a chemical composition of $Mg_6Al_2(OH)_{16}CO_3{\cdot}4H_2O$. Hydrotalcite was first discovered in Switzerland in 1842 **[49]**, and it typically occurs in the form of platelets or lamellar aggregates **[50]**. While the stoichiometry and chemical formula of hydrotalcite were recognized as early as 1915, it wasn't until the 1960s that the precise structure of lamellar double hydroxides was accurately described **[51]**.

Anionic clays have garnered significant attention due to their appealing properties as anionic exchangers and catalyst precursors. **[49]**.

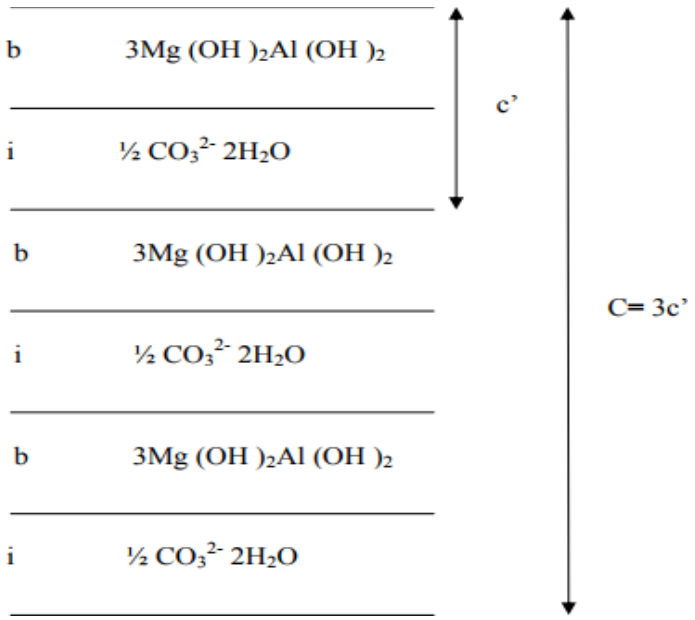

Figure I-7: Schematic representation of Hydrotalcite i: inter layer space b: leaflet.

I.1. Historical

Double lamellar hydroxides, also known as anionic clays due to the charge carried by the layers, denote mineral compounds composed of Mg, Al, and CO_3, commonly existing in the form of lamellar aggregates or platelets, often referred to as hydrotalcite. The challenging identification of this mineral in the field is attributed to its striking physical resemblance to talc. Besides hydrotalcite, another hydroxycarbonate comprising magnesium and iron was discovered and named pyroaurite due to its visual resemblance to gold post heat treatment. Subsequently, it was recognized that this mineral shares an isostructural nature with hydrotalcite and other minerals containing diverse elements. All these compounds exhibit similar characteristics owing to their double lamellar structure.

The first precise formula of hydrotalcite, $[Mg_6Al_2(OH)_{16}]CO_3{\cdot}4H_2O]$, along with other isomorphic compounds, was introduced by E. Manasse. He was the pioneer in acknowledging the significance of carbonate ions in this structural type. Consequently, he persisted for several years with the notion that these compounds were merely mixed hydroxides **[49]**.

Additionally, Aminoff and Broome **[52]** identified the presence of two polytypes of hydrotalcite using X-ray diffraction analyses. The first polytype exhibits rhombohedral symmetry (3R), while the second polytype displays hexagonal symmetry (2H). The latter was later named manasseite in honor of its discoverer, E. Manasse.

The recognition of similarities between various minerals and their compositions remained elusive until the publication of the Frondel article **[53]**. The confusion and uncertainties stemmed from

a shortage of adequate crystallographic data, further complicated by the relatively intricate and unconventional compositions of these materials.

Furthermore, the works of **Manasse** and **Aminoff** and **Broome** received relatively little attention. It wasn't until the 1930s and 1940s that **Feitknecht [54]** made noteworthy contributions, being recognized for the first controlled syntheses of double lamellar hydroxides. These syntheses involved the controlled precipitation of solutions of metal salts in a basic medium.

I.2. Structure of LDH

The structure of lamellar double hydroxides (LDHs) can be described as a stack of sheets composed of Mg $(OH)_2$ units, wherein each unit contains an octahedral Mg^{2+} cation surrounded by OH^- hydroxyl groups. These octahedral units are interconnected by their edges, forming infinite layers, with O-H bonds oriented perpendicular to the plane of the layers **[55]**. In LDH phases, trivalent M^{3+} cations substitute a portion of the divalent M^{2+} cations within the layers, leading to the formation of positively charged layers. This excess positive charge is balanced by anions and water molecules situated in the interlayer space, ensuring overall electroneutrality, **Figure I-8** shows a schematic representation of a layered double hydroxide (LDH) phase.

The general formula of lamellar double hydroxides is:

$[M^{2+}_{1-y} M^{3+}_{y} (OH)_2]^{y+} [X^{n-}]_{y/n}.m [H_2O]$

With:

• M^{2+} and M^{3+}: represent the divalent and trivalent cations that occupy the octahedral sites, respectively.

- X^{n-}: represents the intercalated compensation equation of valence n.
- m: the number of water molecule
- Y : the fraction of the cation ($^{3+}$) in the structure that is defined as $Y= M^{3+}/M^{2+} +M^{3+}$ **[56]**.

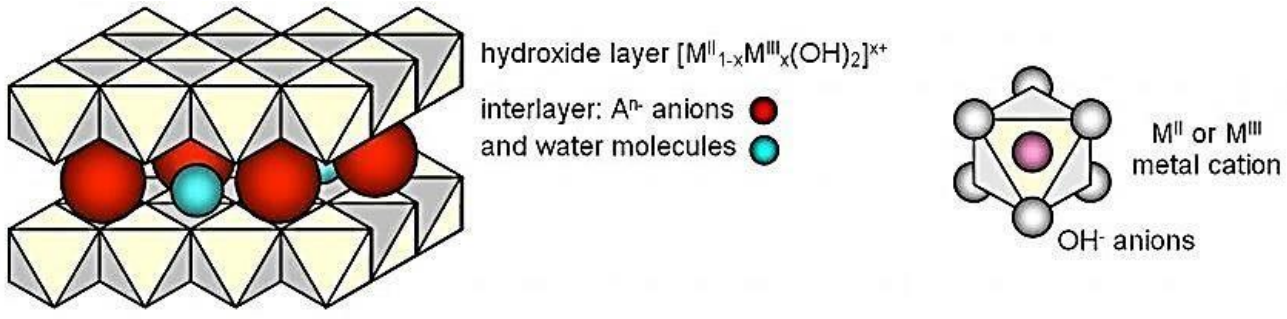

Figure I-8: Schematic representation of an LDH phase.

For natural compounds, the ratio M^{2+} / M^{3+} is generally close to 3, and x = $[M^{3+}]$ / ($[M^{3+}]$ + $[M^{2+}]$), trivalent metal content, of the order of 0.25. In synthetic materials, the relative proportions of di and trivalent cations may vary and x generally takes values between 0.20 and 0.33 **[57, 58]**.

This formulation shows the structure of the double lamellar hydroxide phases, consisting of two distinct parts: the sheet $[M^{2}{}_{1-x}\ M^{3}{}_{x}\ (OH)_2]^{x+}$ and the interlayer $[X_m{}^{-x} / m\ .nH_2O]^{x-}$, and shows clearly that it is possible to synthesize a large number of compounds with different stoichiometries, or even with more than two metals and two different anions, **Figure I-9** shows the general structure of a LDH.

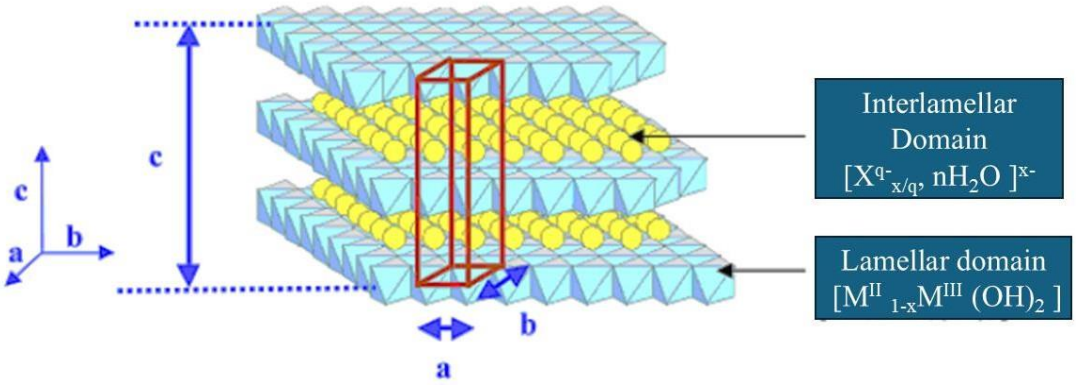

Figure I-9: General structure of LDH, with a: Metal-Metal distance, b: Metal-Oxygen distance, c: 3 times the distance between sheets.

I.2.1. M^{2+} and M^{3+} Nature

All divalent and trivalent metal cations capable of fitting within the octahedral sites of the compact structure formed by the hydroxyl groups in the brucitic layer have the potential to form Layered Double Hydroxides (LDHs). However, there exists a constraint on the ionic radius of these cations. The Be^{2+} cation is considered too small for octahedral coordination, whereas the Ca^{2+}, Ba^{2+}, and Cd^{2+} ions are too large to occupy the octahedral sites. Additionally, these larger cations tend to favor higher coordination numbers. In practical terms, these metals tend to adopt different structural arrangements, such as the hydrocalumite type, where a water molecule is incorporated into the coordination sphere to stabilize the metal cation in a specific coordination state. This phenomenon has been extensively documented, particularly in the case of calcium **[59-61]**.

In a recent advancement, a compound characterized by a matrix based on [Ca-Al] and possessing a structure similar to hydrotalcite was successfully synthesized.

This accomplishment was achieved by stabilizing the compound with aromatic sulfonate anions.**[62]**

The structure of hydrocalumite and hydrotalcite-type materials has been demonstrated by the work of **Rousselot et al. [63]**, following X-ray diffraction studies on $Ca_2M^{3+}(OH)_6Cl.2H_2O$ matrices by working on different trivalent cations M^{3+} : Al^{3+}, Ga^{3+}, Fe^{3+} and Sc^{3+}. On the other hand, the local order around Fe^{3+} cations in a matrix based on $Ca_2Fe\ (OH)_6(CrO_4^{2-})_{0.5}.nH_2O$ has been studied by spectroscopy and X-ray absorption **[64]**.

On the one hand, we found the combination of a monovalent and a trivalent, $[LiAl_2\ (OH)_6]OH.2H_2O$, whose synthesis is reported by **Serena et al. [65]** by hydrothermal route at 130 °C, and **Poeppelmeir et al. [66]**, at room temperature.

On the other hand, **Tayloret al. [67]** report two compounds resulting from the combination of a divalent and a tetravalent, Co-Si and Co-Ti, but since then no work has confirmed the possibility of preparing such phases. **Intissar et al.** have reported the association of a divalent cation, Co^{2+}, a trivalent Al^{3+} and a tetravalent Sn^{4+} by conventional coprecipitation**[68]** as well as that of trivalent Fe^{3+} cations in a matrix of type [Co_2AL-C1] **[69]** . The incorporation of tetravalent cations as Ti^{4+} into a [Co-Al] type matrix was also studied using diffraction and X-ray absorption **[70]**. In all cases, it was found that the tetravalent cation (Ti, Sn or Zr) was not present as a substitution in the leaflet but rather on the surface of LDH platelets in the form of amorphous oxide. These phase segregations could even be directly demonstrated by a coupled TEM-EDX analysis **[71]**.

I.2.2. The interface space

In the interfacial space delimited by the stacks of hydroxylated sheets, there are water molecules and anions **[49]**, and sometimes even alkaline cations.

The first single-crystal X-ray diffraction studies **[56, 72]**, and powder diffraction **[73]** , also NMR **[74]** show that the species occupying this space are arranged in a rather messy way. With regard to the nature of the anion which will be used to compensate for the positive charge of the brucitic layers, there is practically no restriction, provided that pure crystallized phases are obtained. Indeed, it is generally found that the final crystallinity state of a LDH phase strongly depends on the type of anion in the interfering space.

Here are some examples of anions intercalated in the LDHs phases **[75]**:

- Simple anions: CO_2^-, OH^-, F^-, Cl^-, Br^-, I^-, NO^{3-} ...**[76]** and complexes: $(NiCl_4)^{2-}$, $(CoCl_4)^{2-}$, $(IrCl_6)^{2-}$ ... **[75]**
- Cyanocomplexes: $[Fe(CN)_6]^{4-}$, $[Fe(CN)_6]^{3-}$, $[Co(CN)_6]^{4-}$, $[Mo(CN)_8]^{4-}$ ...**[75]**.
- Oxometallates molybdates, polyxometallates, oxocomplexes **[75]**.
- Organic anions: benzoates, tetraphthalates, carboxylates, tartrates, malonates, laurates **[77]**.
- Polymers: polyacrylates, polyethylene glycol, poly (styrene) sulfonates, polyaniline, poly (vinyl) alcohol **[75]**.

Figure I-10 represents different types of arrangements of alkyl chains in the interlayer space of layered double hydroxides (LDHs). In general, the thickness of the interlayer space is governed by factors such as the number, size, and orientation of the anions, as well as their interactions with the hydroxyl groups of the layers. For anions with n-alkyl chains, the interlayer distance typically varies linearly with the number of carbons in the chain. Various arrangements of n-alkyl chains are feasible, including monolayer and bilayer arrangements.

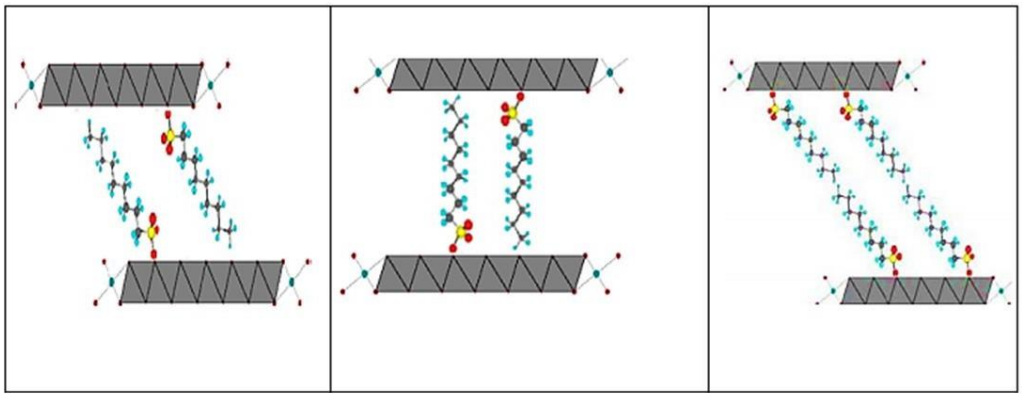

Figure I-10: Different types of arrangement of alkyl chains in the inter-sheet space of Double-Layered-Hydroxydes.

I.3. Preparation of HDLs

Different methods of preparation have been reported for LDH synthesis, including **[78]**:

I.3.1. Co-precipitation method:

This is the simplest and most commonly used method, popularized by the advancements introduced by **Miyata et al.** (1975) **[79]**. It enables the synthesis of lamellar double hydroxides with a wide range of cations and anions in the layers and interlayer spaces. Co-precipitation should be conducted at a pH value close to that at which the most soluble hydroxide is precipitated.

Figure I-11 shows the method for montage preparation co-precipitation. The pH-variable process entails adding a mixture of M^{2+}/M^{3+} salt solutions to an alkaline solution containing the desired anion with stirring. This results in a continuous alteration of the solution's pH during precipitation. A second alkaline solution is gradually added to sustain the desired pH value **[80-83]**.

However, certain LDH phases cannot be obtained through co-precipitation due to the complexation of the anions by the metals present in the solution. In such cases, the preparation is carried out using alternative methods, such as the anion exchange reaction.

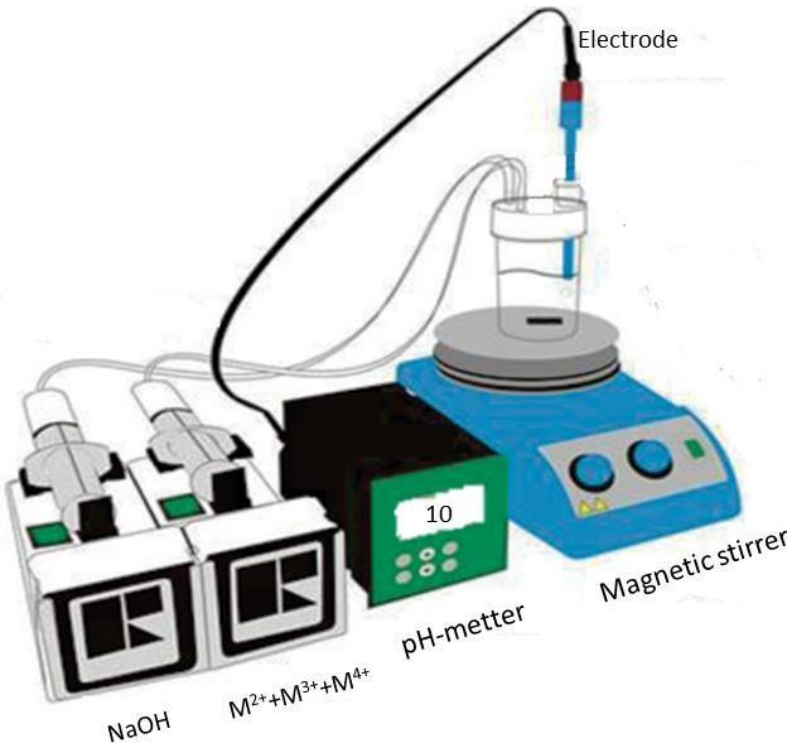

Figure I-11: Co-precipitation method.

I.3.2. Anion exchange method:

To conduct an anion exchange, the precursor LDH material, usually containing chloride or nitrate ions, is suspended in a solution containing the desired anion for insertion. The pH is adjusted, and the mixture is stirred in a free CO_2 environment, as carbonate anions have a preference for intercalation and can be challenging to exchange. It's important to note that exchanges occur more readily in phases containing intercalated nitrate anions compared to materials with carbonate anions or chlorides, due to the higher affinity of NO_3^- ions over Cl^- ions **[84]**, **Figure I-12** represents a schematic representation of anion exchange in layered double hydroxides (LDHs).

This affinity decreases as follows:

$CO_3^{2-} >> Cl^- > NO_3^-$ **[85]**

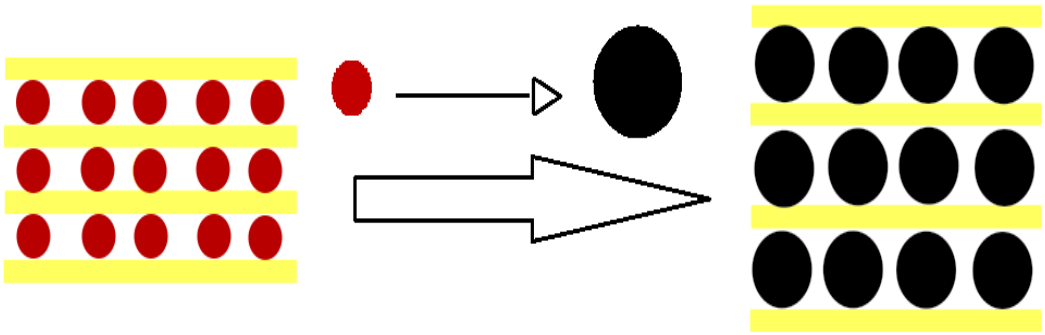

Figure I-12: Schematic representation of anion exchange in Lamellar-Double-Hydroxides.

I.3.3. Reconstruction:

In general, following calcination at temperatures around 450°C and the formation of mixed oxides, it has been demonstrated that double lamellar hydroxides possess the unique property of regenerating simply by re-dispersing in an aqueous solution. This phenomenon, known as the "memory effect" of lamellar double hydroxides **[86, 87]**, relies on the volatile nature of the initial anionic species present in the interlayer space. These species decompose completely without forming stable compositions with the metals present. The most suitable precursor phase for this regeneration is the one containing carbonate anions, although reconstruction is also feasible from phases intercalated with nitrate or organic anions. This regeneration occurs at room temperature and can even occur through simple exposure to air, facilitating CO_2 adsorption and ambient humidity **[88]**.

I.3.4. Salt-oxide method:

This method was initiated with the work of **Boehm et al.[89]** by the synthesis of [ZnCr-Cl]; the same compound was prepared by **Lal et al.[90]** which progressively added chromium chloride in the adequate proportion to the aqueous suspension of zinc oxide maintained with mechanical stirring. The balance equation of the reaction is then written as follows:

$$M_2O + xM_3X_{3/m} + (n+1)\,H_2O \longrightarrow [M_2^{1-x}\,M_3^{x}\,(OH)_2X_{x/m}^{m-}]\,nH_2O + xM_2\,X_{2/m}^{m-}$$

This method is also used for the preparation of LDH materials with different combinations of divalent and trivalent metals giving rise to well-crystallized products **[90]**.

I.3.5. Urea method:

Constantino et al.[91] reported a new approach to synthesize LDH phases by thermal decomposition of urea. Urea serves as a precipitating agent for homogeneous metal solutions, hydroxides or salts that are insoluble in the presence of anions. Acting as a weak Bronsted base (with a pKb of 13.8) and highly soluble in water, urea hydrolysis can be regulated by reaction temperature **[92, 93]**, resulting in the formation of cyanate ammonium. Typically, this process produces cyanate carbonate **[93]** .

$$CO(NH_2)_2 \longrightarrow NH_4\,CON$$

$$NH_4CON + H_2O \longrightarrow (NH_4)_2\,CO_3$$

The overall reaction that occurs is as follows:

$$CO(NH_2)_2 + 2H_2O \longrightarrow (NH_4)_2\,CO_3$$

The hydrolysis of ammonium to ammonia and carbonates to hydrogenated carbonates modifies the pH to 9, which corresponds to the precipitation of a large number of metals.

The hydrolysis of ammonium to ammonia and carbonates to hydrogenated carbonates alters the pH to 9, facilitating the precipitation of numerous metals. Optimal conditions for synthesizing LDH with high crystalline quality in a relatively short timeframe using this method involve dissolving solid urea in a 0.5 M solution of selected metal chlorides to achieve a molar ratio of urea to metal ions of 3.3. Compounds prepared according to this procedure exhibit uniform sizes and platelet primary particles with distinct hexagonal shapes, offering significant potential for nanotechnology applications. LDHs provide two-dimensional nanometric spaces suitable for developing functional materials **[91]**.

The pairs of metals synthesized using urea method are: (Mg-Al); (Zn-Al); (Ni-Al) **[93]**.

I.3.6. Ground Sol–Gel method:

Segal et al. (1984) **[94]** defined this method as the production of inorganic oxides, either from colloidal dispersions or from metal alkoxides. A broad definition of sol-gel processes encompasses a colloidal material synthesis pathway involving sol and/or gel intermediates. This approach was initially employed by **Lopez et al.** (1996) **[95]** for the synthesis of the Mg-Al phase. The synthesis of the LDH Mg/M^{3+} phase (M = Al, Ga, In) involves dissolving magnesium ethoxide and the acetylacetonate of the trivalent metal in an alcohol/acid mixture (35% in an aqueous solution). Subsequently, a solution containing acetone and M^{3+}acetylacetonate is added, and the pH is adjusted using an ammonia solution. The mixture is stirred until a gel is formed, which is then isolated by filtration, washed, and dried **[96]**. Recently, some LDHs have been prepared via sol-gel processes using slow metal alkoxide hydrolysis.

I.3.7. Hydrothermal treatment method:

Hydrothermal synthesis and post-synthesis hydrothermal treatment are distinguished as follows:

I.3.7.1. Hydrothermal synthesis method

This process, as described by **Paush et al.** (1986) **[58]**, is relatively complex and necessitates substantial equipment. It involves the synthesis of a hydrotalcite phase through the treatment of a mixed suspension of magnesium and aluminum oxides at 100°C under a carbon dioxide atmosphere at 100 MPa. The authors reported the formation of the LDH phase [Mg_R-Al-CO_3] in compositional domains where the degree of substitution, denoted as R, ranged from 1.3 to 3.

I.3.7.2. Hydrothermal recrystallization method

The objective is to further process the hydrothermal products obtained from the direct or indirect methods described above to enhance crystallinity. Typically, the re-suspended material is heated to approximately 100-150°C in a sealed vessel under autogenous pressure.

I.4. Applications

Lamellar double hydroxides, both in their pristine state and following thermal decomposition, constitute a class of materials distinguished by unique chemical and physicochemical characteristics. These properties encompass a wide range of compositions, facile synthesis methods, cost-effectiveness, low toxicity, and a high specific surface area. Such attributes underscore their potential for many applications across various fields. The increasing attention toward these materials is motivated by their layered structures and the flexibility in accommodating different combinations of cations and anions. This adaptability is exemplified in numerous patents across industrial, medical, and environmental sectors, reflecting the growing interest and exploration of their utility **[81, 97, 98]**.

The most important and reported applications are:

I.4.1. Catalyst precursors

The hydrotalcite-type phases can be transformed via heat treatment and reduction into homogeneous mixed oxides characterized by a small crystalline size, typically on the scale of a few micrometers. This property imparts a high specific surface area to the resulting materials, offering advantages in catalysis, particularly where interfacial reactions play a significant role. Additionally, these materials serve as excellent supports, facilitating the dispersion of oxide phases and minimizing segregation phenomena, thereby enhancing catalytic performance. They are widely employed as catalysts in various reactions **[88]**, including the synthesis of alcohols.

The specific surface areas achieved typically range from 100 to 200 m^2/g, attributed to the presence of inter-crystalline mesopores. A notable advancement in catalysis over the past decade has been the development of basic catalysis in fine chemistry, with lamellar double hydroxides serving as precursors of basic oxides**[99, 100]**. This has spurred numerous studies, including their utilization as catalysts in various organic reactions such as polymerization and aldol condensation **[101]** .

The imperative of environmental preservation has steered current research toward solid catalysts. Among these, Mg-Al type phases have been extensively investigated in reactions such as aldol condensation, esterification, and isomerization of double bonds. Additionally, lamellar double hydroxides containing transition metal cations or noble metals (Pd, Ru, Rh, Pt, Ir) are being considered as precursors of multifunctional hydrogenation catalysts [102]. Moreover, numerous studies have explored the use of lamellar double hydroxides as supports or catalysts for the degradation of chemical pollutants **[103]**, **Figure I-13** represents the different areas of application of layered double hydroxides (LDHs).

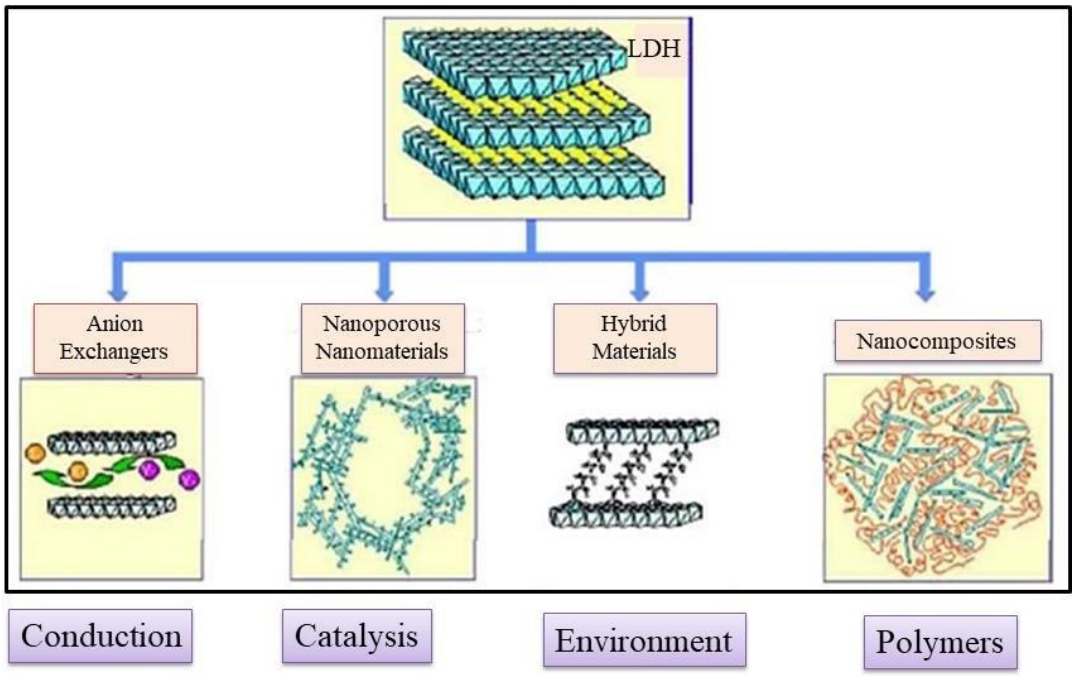

Figure I-13: The different areas of application of LDHs.

The emergence of basic catalysis in fine chemistry represents a recent advancement in catalysis, with lamellar double hydroxides serving as precursors for basic oxides and fueling numerous research endeavors **[99, 100]**. These materials have been extensively explored for their catalytic roles in various organic reactions, including polymerization and aldol condensation, showcasing their versatility and potential impact in catalysis **[101, 102]**.

I.4.2. Environmental applications

Lamellar double hydroxides have the ability to trap negatively charged species by surface adsorption and / or anion exchange by the virtue of their high specific surface area and the flexibility of their interfacial space **[104, 105]**. This ability to trap anions finds its application in the field of the depollution of soils or waters. In the same way, the products resulting from their calcination are also capable of trapping organic or inorganic anions by means of ion exchange and reconstruction reactions **[106, 107]**. The effectiveness of these compounds in the treatment of water polluted by nitrates, phosphates or chromates anions has already been demonstrated **[108, 109]** as well as the trapping of toxic molecules such as those used as pesticides in agriculture (MCPA82 etc))**[110]** and similarly for the sorption of Ni on the mineral pyrophillite **[111]**. **Seida et al.**(2000) demonstrate the efficiency of iron-rich lamellar double hydroxides for the removal of humic substance **[112]**.

Layered Double Hydroxides (LDHs) are valued for their surface properties and anionic exchange capabilities, making them indispensable in environmental applications, particularly in remediation efforts aimed at polluted water and soil. LDHs play a vital role in immobilizing various

inorganic contaminants found in water and soil, including oxyanions like arsenites, chromates, as well as halogenated elements such as bromides, chlorides, and fluorides. Furthermore, LDHs are used in removing and sequestering organic pollutants, with applications ranging from membranes used in separating pyrene from methanol to addressing issues related to polycyclic aromatic hydrocarbons.

I.4.3. Medical applications

Hydrotalcite-type Layered Double Hydroxides (LDHs), specifically [Mg-Al-CO_3], are utilized to regulate the effects of hydrochloric acid and pepsin in the stomach. This application extends to the treatment of gastric ulcers, where LDHs serve as effective agents for managing acidity-related gastrointestinal conditions. **[53]**. Indeed, hydrotalcites function as antacids by adjusting the gastric pH to an optimal range of 3 to 6 upon oral ingestion, as reported by A. Playle **[113]**. Furthermore, their alkaline properties make them effective as anti-pepsin agents and intestinal phosphate absorbents.

The [Mg-Al-Fe] phase demonstrates high efficacy in preventing and treating diseases related to iron deficiency. **[82, 114].**

I.4.4. Biochemical applications

Certain lamellar double hydroxides have demonstrated success in transporting biochemical molecules like DNA or ATP to targeted cells. Upon reaching the targeted cell, these molecules can be released simply by dissolving the lamellar double hydroxide phase **[115]**. In order to enable them to acquire stability with respect to light and heat, vitamins A, C and E are intercalated in Zn-Al-based double-layered hydroxides **[115]** by the co-precipitation method **[116]**.

I.4.5. Applications for the immobilization of enzymes

Lamellar double hydroxides demonstrate considerable promise as matrices for enzyme immobilization **[117-119]**. Their suitability for this application stems from their unique properties, including low isoelectric points and predominantly negative surface charges.

Figure I-14 illustrates several processes documented in the literature for the fabrication of Enz-LDH nanohybrids based on LDH matrices, enzymes, and their corresponding applications **[120]**. The fundamental principle involves immobilizing a significant quantity of enzyme while preserving its structural integrity and activity, thereby facilitating substrate diffusion to the enzyme. The versatile acid-base properties, dictated by the M^{2+}/M^{3+} pair, enable the selection of an immobilization matrix tailored to the enzyme's optimal activity pH. These diverse immobilization methods can be summarized as follows:

1- Adsorption: Biomolecules are adsorbed onto the surface of double-layered hydroxide platelets, such as ZnAl-Cl, MgAl-Cl, or LDH-dodecylsulfate and dodecylsulphonate types. Colloidal particles of LDH, such as MgAl-lactate or NiAl-NO_3, enhance biomolecule adsorption. Stabilization

of the bio membrane can be achieved through additional chemical cross-linking of the biomolecules. Composites of LDH with materials like chitosan or polyacrylic acid-co-acrylamide have also been utilized as matrices for enzyme immobilization.

2- Reconstruction Methods: Reconstruction methods involve reconstructing from delaminated or calcined double lamellar hydroxide phases.

3- Chemical Grafting: Chemical grafting involves interposing a double lamellar hydroxide with glutamate.

4- Confinement: Biomolecules are confined during the material preparation process, which can occur through coprecipitation or electro generation.

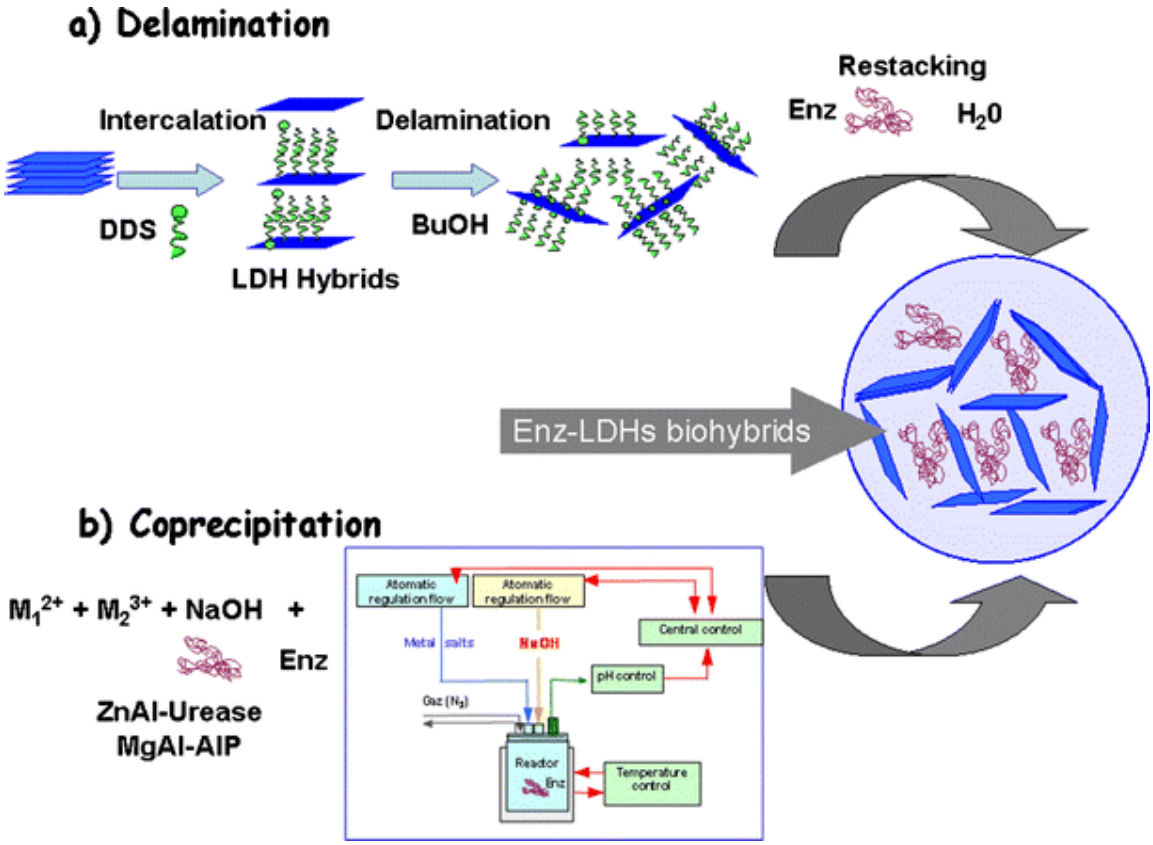

Figure I-14: Method of immobilization of enzymes in lamellar double hydroxides.

I.4.6. Other applications

Double layered hydroxides are being extensively studied for various applications. In the case of cationic clays, which serve as pillar materials **[121, 122]**, they act as microporous catalyst precursors for specific reactions. Lamellar double hydroxides are also investigated as anchoring materials for anionic clays **[87, 123]**..

In agricultural films, patents have been filed for resin mixtures incorporating 12 to 30% by weight of double-layered hydroxides. These clays help prevent film deterioration while maintaining

transparency. Moreover, introducing polymers into the porosity of concrete, as demonstrated with Macro Defect Free Cement (MDFC), enhances its workability **[124]**.

Aluminous cement composites, such as $CaO\text{-}Al_2O_3$, combined with polyvinyl alcohol acetate; exhibit significantly improved flexural strength compared to ordinary cement. However, the modulus of rupture remains fragile. The interfacial zone, composed of crystallites of aluminous hydrates mixed intimately with the polymer, exhibits a nanocomposite character **[125, 126]**.

Hawthorne et al. 1974 **[127]** have succeeded in improving the mechanical properties by the polymerization of a vinyl monomer on the surface of a mineral.

Kato et al. 1979 **[128]** reported the thermal properties of nylon-6 nanocomposite obtained from aminocaproic acid and montmorillonite.

A few years later, Toyota researchers use the same polymer but dispersed in the same inorganic network, the mechanical properties are greatly improved **[129, 130]**.

Recent research on the utilization of lamellar double hydroxides (LDHs) as nanofillers has shown promising results. For instance, incorporating only 5% by weight of organomodified LDH in polyimide (PI) nanocomposites leads to a remarkable 43% increase in ultimate strength, along with an elevation in the glass transition temperature. These LDH-polymer nanocomposites are sought after for their enhanced gas and fire barrier properties. Additionally, a patent highlights the fire resistance of nanocomposite materials comprising halogen-free thermoplastic polymers blended with double layered hydroxide materials.

Furthermore, biopolymers have been successfully incorporated between LDH lamellar, significantly impacting the textural properties of the resulting hybrid compound.

- **Leroux et al**. 2004 **[131]**demonstrated that incorporating alginate into the LDH matrix [Zn_2-Al] alters its original texture, imparting a tubular morphology. Alginate, a linear copolymer composed alternately of gluconate and mannuronate, finds extensive applications in food packaging and the pharmaceutical industry.

- In 2016, **Manikandan et al.** conducted a study on the selective vapor phase hydrogenation reaction of furfural. They employed a nickel hydrotalcite catalyst prepared via the coprecipitation method, followed by calcination to obtain mixed oxides **[132]**. Under optimal conditions specifically, a 2 hour reaction at 500°C under H_2, they achieved a furfural conversion rate of 98% with 95% selectivity to furfuryl alcohol. The results underscored the catalyst's high efficiency, attributed to the synergistic surface interaction between the metallic Ni and the basic Mg (Al) O sites.

- In 2017, **Li et al. [133]** investigated the selective hydrogenation reaction of 5-hydroxymethylfurfural (HMF) to produce high-quality liquid fuel 2,5-dimethylfuran (DMF), employing Ru-CoFe catalysts derived from calcination of double lamellar hydroxides. Under the experimental conditions of 180°C for 6 hours, they achieved a remarkable selectivity of 98.2% for DMF with complete conversion of HMF. The study demonstrated that the cooperative action of Ru

and CoFe facilitated the hydrogenation process of HMF to DMF. However, it was observed that the catalyst exhibited a loss of activity after 3 cycles of successive reactions.

- In their study, **Zhou et al.[134]** aimed to investigate the hydrogenation reaction of furfural in the aqueous phase using a series of oxides derived from hydrotalcite (Cu + Mg) / Al with a constant Cu / Mg ratio of 3, while varying the Cu / Mg ratio from 0.07 to 0.30. These oxides were prepared through the co-precipitation method followed by calcination. Remarkably, they achieved a furfural conversion of up to 98.5% for a Cu / Mg ratio of 0.2, under reaction conditions of 140°C and 4 MPa hydrogen pressure for 10 hours, with a selectivity of 94.8% to cyclopentanol. The catalytic activity showed a progressive improvement with the increase in Cu content in the hydrotalcite.
- **Taylor et al. [135]** investigated the hydrogenation of furfural to furfuryl alcohol and tetrahydrofurfuryl alcohol in the gas phase. The reactions were conducted at temperatures ranging from 155°C to 175°C, under 1 atm H_2 pressure, and with an H_2/furfural ratio of 25. The researchers found that lamellar films of double hydroxides, specifically Ni-Co-Al and Ni-Mg-Al, exhibited high activity under these conditions. Several catalyst ratios were tested, with the best results obtained using 0.7Ni1.1Co-Al, which achieved a 91% conversion and a 75.6% selectivity towards furfuryl alcohol, and 1.1Ni-0.8CoAl, which showed a 25% conversion with 78.6% selectivity towards furfuryl alcohol**.**
- **Kai et al. [136]** employed Cu-Fe based Layered Double Hydroxides (LDH) as catalysts for the hydrogenation reaction of furfural to levulinic acid. They achieved a conversion rate of 87% with levulinic acid selectivity of 83.6%.
- In their investigation, **Hora et al.** (2013) **[137]**, explored the liquid-phase aldol condensation reaction of furfural and acetone. They utilized Mg-Al hydrotalcite solid catalysts and mixed oxides of Mg-Al, varying the molar ratios from 2 to 4 (Mg/Al). The activity was tested at different reaction temperatures (20-100°C). The best results were obtained with the calcined catalyst having an Mg/Al ratio of 3 at 100 ° C, a furfural conversion >95% and a selectivity to C_8 and C_{13}>90% and as regards the by-products the selectivity did not exceed 5% in any experiment.
- **In 2015, Li et al. [138]** investigated the oxidation reaction of benzene. They employed a series of LDH Al-Co as precursors. The study revealed that the activity of the mixed oxide of Co-Al increased with the Co/Al molar ratio. The highest activity was observed for the ratio Co/Al = 5. However, a further increase in the molar ratio to 6 resulted in a significant decrease in activity due to the alteration in the surface state of the mixed oxide. Moreover, a 50 hour long-term stability test demonstrated that the optimized Co-Al mixed oxide exhibited stability for the total oxidation of benzene.
- **Diaz-Couce et al.[139]** synthesized Mo (II) complexes $[MoX_2(CO)_3(BDC)]$ (X = I, Br; H_2BDC = 2,2-bipyridine-5,5-dicarboxylic acid) and immobilized them by intercalation into two double lamellar hydroxides (LDHs), one containing synthesized Zn/Al and the other commercial Mg/Al. They investigated the catalytic activity of these complexes in the oxidation of olefins using

tert-butyl hydroperoxide (TBHP) as the oxidant and compared it to the activity of related complexes $[MoX_2(CO)_3(bpy)]$ (bpy = 2,2-bipyridine). Substrates including cis-cyclooctene, styrene, 1-octene, trans-hex-3-ol-1, and limonene were tested. The results showed that globaly all catalysts exhibited high selectivity for the epoxide of each substrate (greater than 90%, except for styrene), with varying levels of conversion.

- **Sobhana et al. [140]**explored the photocatalytic degradation of Orange II (OII) using MgZnAl-Cl LDHs modified with Au-Pd nanoparticles prepared via a co-precipitation process. The LDHs were used as supports for immobilizing bimetallic gold-palladium (Au-Pd) nanoparticles through a colloidal sol-immobilization process. While the LDH alone exhibited some photocatalytic activity, adsorption was the dominant process, with 36% adsorption and 22% degradation of OII. The addition of Au-Pd nanoparticles significantly enhanced photocatalytic performance, increasing degradation to 35% after 50 minutes, compared to 22% for pristine LDH. After 50 minutes of irradiation**,** a 65% conversion was achieved with Au-Pd@MgZnAl-LDH, compared to 58% for the unmodified LDH. This improvement suggests that Au-Pd acts as a **co-catalyst**, boosting the efficiency of OII degradation.

- **Jirátová et al. [141]** investigated the oxidation of ethanol using mixed oxide catalysts derived from lamellar double hydroxides (LDHs) containing various combinations of transition metal cations, including Cu, Co, Ni, Mn, and Al. The study showed that Mn containing ternary mixed oxides, particularly Cu-Ni-Mn, exhibited the highest catalytic activity, achieving 90% conversion of organic compounds to CO_2 and H_2O at 154°C. Other Mn containing oxides, such as Cu-Co-Mn and Co-Ni-Mn, reached the same 90% conversion but at higher temperatures of 173°C and 181°C, respectively. In contrast, Al containing ternary oxides required significantly higher temperatures, ranging from 194°C to 220°C, to achieve similar conversion. Additionally, acetaldehyde was identified as the main by-product in the oxidation process. Mn containing catalysts produced more acetaldehyde than Al-containing ones, with Cu-Ni-Mn and Co-Ni-Mn exhibiting the lowest acetaldehyde disappearance temperatures, indicating better efficiency in minimizing the by-product. This highlights the superior performance of Mn based catalysts, especially in terms of activity at lower temperatures.

- **Zhang et al.[142]** synthesized Ni-Al LDHs by a hydrothermal method using Au colloid nanoparticles as nuclei for the growth of Au / Ni-Al LDH the conductivity was improved as the Au/Ni-Al LDH-modified glassy carbon (GCE) electrode, compared to the GCE modified with Ni-Al LDHs. Ascorbic acid was used as a model molecule to study the electroanalytical properties of GCE modified by Au/Ni-Al LDHs. The results showed that a highly sensitive detection was obtained.

- **Sipos et al. [143]** synthesized CaFe and CaAl lamellar double hydroxides (LDHs) and their intercalated varieties using chemical methods. They also prepared and characterized metal ion composites such as Mn (II), Cu (II), Fe (III), or Ni (II) LDHs. These materials were then applied in

various reactions including epoxidation/oxidation of olefins with or without additional functionality, Baeyer-Villiger oxidation, aldol-condensation dimerization, or coupling reactions of the Ullmann type. The activities, selectivities, and recycling capacities of the catalysts were investigated. In the Baeyer-Villiger oxidation reaction of cyclohexanone in the liquid phase, Ca (II) Sn (IV) LDHs were used as catalysts. The optimal reaction conditions were determined as 70°C, benzonitrile as the solvent, and a reaction time of 24 hours. Under these conditions, a conversion of 14% could be achieved with 100% molar selectivity. In the dimerization condensation reaction of benzaldehyde and acetone, LDH CaFe catalysts were employed. These catalysts exhibited activity and selectivity for dimerization. The conversion rates varied, with a low of 6% and a high of 94% under ambient temperature conditions. Initially, the activity of intercalated materials was low, with only 0.5% conversion observed on DL-pipecolinate-CaFe LDH and 3% on L-prolinate-CaFe LDH at 298K in 24 hours. However, the selectivity for dimerization was high, reaching 95 mol% on DL-pipecolinate-CaFe LDH and 85 mol% on L-prolinate-CaFe LDH.

- **Zheng et al**. **[144]** successfully synthesized nano/micro-structured Zn-Mg-Al double-layer hydroxides (LDHs) using a one-step urea method. The results indicated that ZnMgAl LDHs exhibited high crystallinity with a large surface area, which is advantageous for adsorption. The optimal pH value for the adsorption of methyl orange on ZnMgAl-LDH was found to be 3.0.

After reviewing literature on various catalysts beyond LDHs, this research opted for the combination of gold nanoparticles (Au) with LDHs, forming Au/LDHs. This decision was made to leverage the unique and complementary properties offered by this catalytic combination. Gold nanoparticles are known for their high catalytic activity, selectivity in various reactions, and effectiveness under mild conditions. By integrating these characteristics with the lamellar structure of LDHs, Au/LDHs offer promising synergistic potential for the oxidation and hydrogenation of furfural. This approach aims to capitalize on the increased stability, enhanced catalytic activity, and improved selectivity that Au/LDHs provide compared to other catalytic systems.

- In essence, the strategic choice of Au/LDHs is based on their ability to combine the respective advantages of gold and LDHs, thereby offering a potentially more efficient hybrid catalytic system to address the objectives of this study on furfural oxidation and hydrogenation.

PART V. Gold nanoparticles

I. Introduction

The exploration of nanomaterials constitutes a dynamic field in research and an expanding economic sector, showcasing numerous potential applications in fields such as biology, medicine, chemistry, electronics, and cosmetics **[145, 146]**. The catalysis facilitated by gold nanoparticles holds significant importance both in fundamental principles and practical applications. Several factors elucidate this interest, with a primary focus on the catalytic activity of gold intricately tied to the nanometric scale of the particles.

Gold, traditionally regarded as an inert and nonreactive metal, possesses remarkable catalytic activity. This is evident when gold is present in the form of soluble complexes like gold (I) or gold (III), as well as in the configuration of highly dispersed nanocrystals. The exploration of gold's catalytic properties opens many ways for further research and applications in various fields **[147]**.

The nanometer-sized gold particles on supports can act as catalysts for simple organic reactions, including oxidation and hydrogenation, even at or below room temperature. In this report, we highlight that gold nanoparticles (AuNPs) exhibit catalytic activity in furfural hydrogenation or oxidation reactions. The AuNP catalyzed oxidation proceeded smoothly at room temperature with a loading of 0.25 wt% AuNP. Similarly, the hydrogenation of furfural proceeded effectively under the influence of AuNPs **[147]**.

Catalysts based on gold display particularly noteworthy properties, distinctly observable only at the nanoparticle level, and diminishing as the size increases towards the micrometer scale. Another contributing factor to the fascination with gold catalysis stems from the longstanding misconception that gold lacked any catalytic activity. Consequently, grasping this catalytic activity, refining reaction mechanisms, and unveiling novel mechanisms for reactions catalyzed by gold represent an emerging frontier in the field of heterogeneous catalysis. Indeed, a third crucial aspect underscoring the significance of nanoparticle research is that, when prepared as colloids or supported particles, they act as a linkers between homogeneous and heterogeneous catalysis **[148, 149]**. Until now, these two disciplines have progressed somewhat autonomously, but gold nanoparticles have the potential to serve as a nexus for these two fields.

The growing interest in gold nanoparticles as catalysts is evident in the exponential increase in publications addressing this topic **[150-153]**.

The catalysis of organic reactions by gold catalysts has historically received limited attention, primarily due to the misconception that gold is expensive and inert. However, the successful utilization of supported gold catalysts for pollution abatement has challenged this perception, leading to a surge of interest in gold catalysis for organic synthesis. Both supported Au catalysts and homogeneous gold (III) catalysts have proven effectivness in oxidation processes utilizing one of the most attractive oxidants, O_2/air. These processes proceed at satisfactory rates even at room temperature, exhibit selectivity, and avoid rapid catalyst decomposition **[151]**.

The catalytic performances of gold nanoparticles are contingent upon their compositions and morphologies. Presently, scientists are dedicating increased efforts to organize gold nanostructures onto various supports to enhance their catalytic properties **[154-156]**. Numerous studies have indicated that highly dispersed gold nanoparticles deposited on diverse supports can demonstrate exceptionally robust activities for a range of reactions at low temperatures **[157-159]**. Various parameters, including gold particle size, support properties, and preparation procedures, seem to play a pivotal role in the highly catalytic activity exhibited by supported gold catalysts.

LDHs (Layered Double Hydroxides) have gained widespread use as effective supports for various reactions owing to their tunable surface properties **[160]**. Recently, there has been a growing interest in LDH supported basic gold nanoparticles within the scientific community, particularly for numerous applications in a range of organic reactions **[161-163]**. Previous studies have highlighted that heterogeneous gold nanoparticle catalysts supported on LDH exhibit distinct performances, different from other commonly used gold catalysts like Au/TiO_2 and Au/Al_2O_3. This distinction arises from synergistic effects between gold nanoparticles and robust LDH basic sites **[164-166]**. These findings have motivated the exploration of LDH supported gold nanoparticles as novel catalysts for furfural oxidation and hydrogenation reactions. To the best of our knowledge, the potential of LDH supported gold nanoparticles as active materials for oxidation and hydrogenation reactions of biomass-derived furfural has been relatively underexplored.

II. Conclusion

The main purpose of this thesis is to synthesize lamellar double hydroxides (LDHs) with compositions of M-Al (where M can be either Mg or Ni) and subsequently modify them with Zr. The next step involves depositing gold nanoparticles onto these modified LDHs using the urea deposition-precipitation (UDP) method. The synthesized materials will undergo thorough characterization using various physico-chemical techniques. Finally, the catalytic capabilities of these materials will be assessed in liquid phase reactions, particularly focusing on the oxidation and hydrogenation of furfural. This research aims to develop a more efficient hybrid catalytic system by leveraging the unique properties of gold nanoparticles and LDHs, with the potential for significant advancements in bio-derived products conversion processes.

References:

[1] K. Sanderson, Nature, 474 (2011) S12.

[2] B. Kamm, P.R. Gruber and M. Kamm, Biorefineries-industrial processes and products, Wiley-VCH Weinheim, 2006.

[3] M. Hoogwijk, A. Faaij, R. Van Den Broek, G. Berndes, D. Gielen and W. Turkenburg, Biomass and bioenergy, 25 (2003) 119.

[4] C. Couhert, Pyrolyse flash à haute température de la biomasse ligno-cellulosique et de ses composés: production de gaz de synthèse, École Nationale Supérieure des Mines de Paris, 2007.

[5] A. Shamshitov, G. Kadžienė and S. Supronienė, Plants, 13 (2024) 766.

[6] K. Hakala, M. Kontturi and K. Pahkala, Agricultural and Food Science, 18 (2009) 347.

[7] M. Janmohammadi, Z. Nazemi, A.O.M. Salehi, A. Seyfoori, J.V. John, M.S. Nourbakhsh and M. Akbari, Bioactive Materials, 20 (2023) 137.

[8] J.-F. Sun, Q.-Q. Xu, J.-L. Qi, D. Zhou, H.-Y. Zhu and J.-Z. Yin, ACS sustainable chemistry & engineering, 8 (2020) 14630.

[9] S. Achinas, V. Achinas and G.J.W. Euverink, Engineering, 3 (2017) 299.

[10] F.W. Lichtenthaler, Accounts of chemical research, 35 (2002) 728.

[11] W. De Jong and G. Marcotullio, International journal of chemical reactor engineering, 8 (2010).

[12] A.F. de Lacerda Filho, J.J.F. Palacin, R.J. de Almeida Rigueira, A. Ribeiro and E. de Castro Melo, Renewable and sustainable energy reviews, 39 (2014) 1208.

[13] K. Yan and A. Chen, Energy, 58 (2013) 357.

[14] X. Déglise, Revue forestière française, 34 (1982) 249.

[15] B. Danon, G. Marcotullio and W. de Jong, Green Chemistry, 16 (2014) 39.

[16] T. Ahmad, L. Kenne, K. Olsson and O. Theander, Carbohydrate research, 276 (1995) 309.

[17] C.D. Hurd and L.L. Isenhour, Journal of the American chemical society, 54 (1932) 317.

[18] E.R. Garrett and B.H. Dvorchik, Journal of pharmaceutical sciences, 58 (1969) 813.

[19] Y. Wang, D. Zhao, D. Rodríguez-Padrón and C. Len, Catalysts, 9 (2019) 796.

[20] J. Döbereiner, Annalen der Pharmacie, 3 (1832) 141.

[21] J. Stenhouse, Philosophical Transactions of the Royal Society of London, (1850) 467.

[22] H. Hoydonckx, W. Van Rhijn, W. Van Rhijn, D. De Vos and P. Jacobs, Ullmann's encyclopedia of industrial chemistry, (2000).

[23] K.J. Yong, T.Y. Wu, C.B.T.L. Lee, Z.J. Lee, Q. Liu, J.M. Jahim, Q. Zhou and L. Zhang, Biomass and Bioenergy, 161 (2022) 106458.

[24] N.J. Mazumdar, R. Kataki and K. Pant, Catalysis for Clean Energy and Environmental Sustainability: Biomass Conversion and Green Chemistry-Volume 1, (2021) 705.

[25] R. Mariscal, P. Maireles-Torres, M. Ojeda, I. Sádaba and M.L. Granados, Energy & environmental science, 9 (2016) 1144.

[26] A.E. Eseyin and P.H. Steele, (2015).

[27] A. Jaswal, P.P. Singh and T. Mondal, Green Chemistry, 24 (2022) 510.

[28] K.J. Zeitsch, The chemistry and technology of furfural and its many by-products, Elsevier, 2000.

[29] R. Xing, W. Qi and G.W. Huber, Energy & Environmental Science, 4 (2011) 2193.

[30] R. Ramos, Z. Tišler, O. Kikhtyanin and D. Kubička, Catalysis Science & Technology, 6 (2016) 1829.

[31] L. Faba, E. Díaz, A. Vega and S. Ordónez, Catalysis today, 269 (2016) 132.

[32] M. Lin, C. Mochizuki, T. Ishida, Y. Zhang, M. Haruta and T. Murayama, Catalysis today, 410 (2023) 143.

[33] X. Xiang, B. Zhang, G. Ding, J. Cui, H. Zheng and Y. Zhu, Catalysis Communications, 86 (2016) 41.

[34] A. Alba-Rubio, J.L.G. Fierro, L. León-Reina, R. Mariscal, J. Dumesic and M.L. Granados, Applied Catalysis B: Environmental, 202 (2017) 269.

[35] H. Guo and G. Yin, The Journal of Physical Chemistry C, 115 (2011) 17516.

[36] S. Shi, H. Guo and G. Yin, Catalysis Communications, 12 (2011) 731.

[37] H. Choudhary, S. Nishimura and K. Ebitani, Applied Catalysis A: General, 458 (2013) 55.

[38] T. Yang, W. Li and A.T. Ogunbiyi, Molecular Catalysis, 504 (2021) 111488.

[39] S. Tarazanov, K. Grigoreva, A. Shipitcyna, O. Repina, M. Ershov, S. Kuznetsova and P. Nikulshin, Fuel, 271 (2020) 117594.

[40] A. Kojčinović, Ž. Kovačič, M. Huš, B. Likozar and M. Grilc, Applied Surface Science, 543 (2021) 148836.

[41] G. Ren, G. Wang, H. Mei, Y. Xu and L. Huang, Chemical Physics Letters, 703 (2018) 1.

[42] Z. Fu, Z. Wang, W. Lin, W. Song and S. Li, Applied Catalysis A: General, 547 (2017) 248.

[43] H. Prakruthi, B. Chandrashekara, J. Prakash and Y. Bhat, Journal of industrial and engineering chemistry, 62 (2018) 96.

[44] X. Meng, L. Wang, L. Chen, M. Xu, N. Liu, J. Zhang, Y. Yang and M. Wei, Journal of Catalysis, 392 (2020) 69.

[45] W. Liu, Y. Yang, L. Chen, E. Xu, J. Xu, S. Hong, X. Zhang and M. Wei, Applied Catalysis B: Environmental, 282 (2021) 119569.

[46] S.T. Thompson and H.H. Lamb, Journal of Catalysis, 350 (2017) 111.

[47] N. Pino, S. Sitthisa, Q. Tan, T. Souza, D. López and D.E. Resasco, Journal of Catalysis, 350 (2017) 30.

[48] W. Gong, C. Chen, H. Zhang, Y. Zhang, Y. Zhang, G. Wang and H. Zhao, Molecular Catalysis, 429 (2017) 51.

[49] F. Cavani, F. Trifirò and A. Vaccari, Catalysis today, 11 (1991) 173.

[50] V. Rives and M.A. Ulibarri, Coordination Chemistry Reviews, 181 (1999) 61.

[51] Z. Xu and H. Zeng, The Journal of Physical Chemistry B, 105 (2001) 1743.

[52] A.G.F. Aminoff, Oönskade, oförväntade och negativa konsekvenser av innovationer-en litteraturanalys (Available on Internet), Hanken School of Economics, 2010.

[53] R. Mostarih, Elaboration de phases hydroxydes doubles lamellaires intercalant des anions sulfates: étude de leur évolution structurale, thermique et hygrométrique, Université Blaise Pascal-Clermont-Ferrand II, 2006.

[54] W. Feitknecht and M. Gerber, Helvetica Chimica Acta, 25 (1942) 106.

[55] M. Titulaer, H. Talsma, J. Jansen and J. Geus, Clay Minerals, 31 (1996) 263.

[56] H. Taylor, Mineralogical Magazine, 39 (1973) 377.

[57] J.H. Choy, S.Y. Kwak, J.S. Park, Y.J. Jeong and J. Portier, Journal of the American Chemical Society, 121 (1999) 1399.

[58] N. Drici, Hydroxydes doubles lamellaires, synthèse, caractérisation et propriétés, Université Sorbonne Paris Cité, 2015.

[59] R. Allmann, Chimia, 24 (1970) 99.

[60] R. Segni, Caractérisation structurale, propriétés d'échange et stabilité de matériaux de type hydrocalumite [Ca2M (OH) 6]+[Xn 1/n. xH2O]-avec M= Al, Fe, et Sc et X= SO4, CrO4, V2O7 et SiO3, Université Blaise Pascal-Clermont-Ferrand II, 2005.

[61] A. Terzis, S. Filippakis, H.-J. Kuzel and H. Burzlaff, Zeitschrift für Kristallographie-Crystalline Materials, 181 (1987) 29.

[62] A. Illaik, Synthèse et caractérisation de nanocomposites polymères/hydroxydes doubles lamellaires (HDL), Université Blaise Pascal-Clermont-Ferrand II, 2008.

[63] I. Rousselot, C. Taviot-Guého, F. Leroux, P. Léone, P. Palvadeau and J.-P. Besse, Journal of Solid State Chemistry, 167 (2002) 137.

[64] R. Segni, N. Allali, L. Vieille, C. Taviot-Guého and F. Leroux, Journal of Physics and Chemistry of Solids, 67 (2006) 1043.

[65] C.J. Serna, J.L. Rendon and J.E. Iglesias, Clays and Clay Minerals, 30 (1982) 180.

[66] K. Poeppelmeier and S. Hwu, Inorganic Chemistry, 26 (1987) 3297.

[67] R. Taylor, Clay Minerals, 19 (1984) 591.

[68] M. Intissar, J.-C. Jumas, J.-P. Besse and F. Leroux, Chemistry of materials, 15 (2003) 4625.

[69] M. Intissar, R. Segni, C. Payen, J.-P. Besse and F. Leroux, Journal of Solid State Chemistry, 167 (2002) 508.

[70] M. Intissar, S. Holler, F. Malherbe, J.-P. Besse and F. Leroux, Journal of Physics and Chemistry of Solids, 65 (2004) 453.

[71] M. Intissar, F. Malherbe, V. Prévot and F. Leroux, Journal of colloid and interface science, 299 (2006) 747.

[72] R. Allmann, Acta Crystallographica Section B: Structural Crystallography and Crystal Chemistry, 24 (1968) 972.

[73] A. De Roy, Synthèse et caractérisation de composés de type hydrotalcite: mesure de la conductivité ionique, 1990.

[74] A. Van der Pol, B. Mojet, E. Van de Ven and E. De Boer, The Journal of Physical Chemistry, 98 (1994) 4050.

[75] V. Rives and M.a.A. Ulibarri, Coordination Chemistry Reviews, 181 (1999) 61.

[76] C.J. Serna, J. White and S. Hem, Clays and Clay Minerals, 25 (1977) 384.

[77] C. Li, G. Wang, D.G. Evans and X. Duan, Journal of Solid State Chemistry, 177 (2004) 4569.

[78] S. Carlino, Solid State Ionics, 98 (1997) 73.

[79] S. Miyata, Clays and Clay Minerals, 23 (1975) 369.

[80] M. Gastuche, G. Brown and M. Mortland, Clay Miner, 7 (1967) e92.

[81] W.T. Reichle, Solid State Ionics, 22 (1986) 135.

[82] S. Miyata, Clays and Clay Minerals, 25 (1977) 14.

[83] S. Miyata and T. Hirose, Clays Clay Miner, 26 (1978) 441.

[84] Y. Nakagawa, J. Mater. Chem. A, 2 (2014) 6688.

[85] D.L. Bish, Bull. Mineral, 103 (1980) 5.

[86] K.-H. Goh, T.-T. Lim and Z. Dong, Water Research, 42 (2008) 1343.

[87] T. Kwon, G.A. Tsigdinos and T.J. Pinnavaia, Journal of the American Chemical Society, 110 (1988) 3653.

[88] M. Bellotto, B. Rebours, O. Clause, J. Lynch, D. Bazin and E. Elkaïm, The Journal of Physical Chemistry, 100 (1996) 8527.

[89] H.P. Boehm, J. Steinle and C. Vieweger, Angewandte Chemie International Edition in English, 16 (1977) 265.

[90] M. Lal and A.T. Howe, Journal of Solid State Chemistry, 39 (1981) 368.

[91] J.X. He, K. Kobayashi, M. Takahashi, G. Villemure and A. Yamagishi, Thin Solid Films, 397 (2001) 255.

[92] K.H. Goh, T.T. Lim and Z. Dong, Water Research, 42 (2008) 1343.

[93] V. Rives, Layered double hydroxides: present and future, Nova Publishers, 2001.

[94] D. Segal, Journal of Non-Crystalline Solids, 63 (1984) 183.

[95] T. Lopez, P. Bosch, E. Ramos, R. Gomez, O. Novaro, D. Acosta and F. Figueras, Langmuir, 12 (1996) 189.

[96] M. Othman, Z. Helwani and W. Fernando, Applied Organometallic Chemistry, 23 (2009) 335.

[97] P.V. Kamath, G.H.A. Therese and J. Gopalakrishnan, Journal of Solid State Chemistry, 128 (1997) 38.

[98] M.A. Aramendía, Y. Avilés, V. Borau, J.M. Luque, J.M. Marinas, J.R. Ruiz and F.J. Urbano, Journal of Materials Chemistry, 9 (1999) 1603.

[99] W. Reichle, S. Kang and D. Everhardt, Journal of Catalysis, 101 (1986) 352.

[100] K.A. Carrado, A. Kostapapas and S.L. Suib, Solid State Ionics, 26 (1988) 77.

[101] C. Busetto, G. Del Piero, G. Manara, F. Trifiro and A. Vaccari, Journal of Catalysis, 85 (1984) 260.

[102] M. Ulibarri, J. Fernandez, F. Labajos and V. Rives, Chemistry of materials, 3 (1991) 626.

[103] S. Kannan and C. Swamy, Catalysis Today, 53 (1999) 725.

[104] S.P. Newman and W. Jones, Journal of Solid State Chemistry, 148 (1999) 26.

[105] T. Toraishi, S. Nagasaki and S. Tanaka, Applied Clay Science, 22 (2002) 17.

[106] R.L. Goswamee, P. Sengupta, K.G. Bhattacharyya and D.K. Dutta, Applied Clay Science, 13 (1998) 21.

[107] W. Kagunya, M. Chibwe and W. Jones, Molecular Crystals and Liquid Crystals Science and Technology. Section A. Molecular Crystals and Liquid Crystals, 244 (1994) 155.

[108] B. Houri, A. Legrouri, A. Barroug, C. Forano and J.-P. Besse, Collection of Czechoslovak chemical communications, 63 (1998) 732.

[109] L.M. Parker, N.B. Milestone and R.H. Newman, Industrial & engineering chemistry research, 34 (1995) 1196.

[110] J. Inacio, C. Taviot-Gueho, C. Forano and J. Besse, Applied Clay Science, 18 (2001) 255.

[111] R.G. Ford, A.C. Scheinost, K.G. Scheckel and D.L. Sparks, Environmental science & technology, 33 (1999) 3140.

[112] Y. Seida and Y. Nakano, Water Research, 34 (2000) 1487.

[113] A. Playle, S. Gunning and A. Llewellyn, Pharmaceutica Acta Helvetiae, 49 (1973) 298.

[114] U. Deschler, P. Kleinschmit and P. Panster, Angewandte Chemie International Edition, 25 (1986) 236.

[115] S.-Y. Kwak, Y.-J. Jeong, J.-S. Park and J.-H. Choy, Solid State Ionics, 151 (2002) 229.

[116] J.-H. Choy, S.-J. Choi, J.-M. Oh and T. Park, Applied Clay Science, 36 (2007) 122.

[117] L. Ren, J. He, D. Evans, X. Duan and R. Ma, Journal of Molecular Catalysis B: Enzymatic, 16 (2001) 65.

[118] J. He, M. Wei, B. Li, Y. Kang, D.G. Evans and X. Duan, Layered double hydroxides, Springer, 2006, p. 89.

[119] M.B.A. Rahman, M. Basri, M.Z. Hussein, M.N.H. Idris, R.N.Z.R.A. Rahman and A.B. Salleh, Catalysis Today, 93 (2004) 405.

[120] C. Forano, S. Vial and C. Mousty, Current Nanoscience, 2 (2006) 283.

[121] D. Tennakoon, W. Jones, J. Thomas, J. Ballantine and J. Purnell, Solid State Ionics, 24 (1987) 205.

[122] A. Moini and T.J. Pinnavaia, Solid State Ionics, 26 (1988) 119.

[123] M. Doeuff, T. Kwon and T.J. Pinnavaia, Synthetic Metals, 34 (1989) 609.

[124] J. Birchall, A. Howard and K. Kendall, Nature, 289 (1981) 388.

[125] O.O. Popoola, W.M. Kriven and J.F. Young, Journal of the American Ceramic Society, 74 (1991) 1928.

[126] S. Rodger, S. Brooks, W. Sinclair, G. Groves and D. Double, Journal of materials science, 20 (1985) 2853.

[127] D.-G. Hawthorne, J. Hodgkin, B. Loft and D. Solomon, Journal of Macromolecular Science—Chemistry, 8 (1974) 649.

[128] C. Kato, K. Kuroda and M. Misawa, Clays and Clay Minerals, 27 (1979) 129.

[129] G. Carja, R. Nakamura, T. Aida and H. Niiyama, Microporous and Mesoporous Materials, 47 (2001) 275.

[130] K. Yano, A. Usuki, A. Okada, T. Kurauchi and O. Kamigaito, Journal of Polymer Science Part A: Polymer Chemistry, 31 (1993) 2493.

[131] F. Leroux, J. Gachon and J.-P. Besse, Journal of Solid State Chemistry, 177 (2004) 245.

[132] M. Manikandan, A.K. Venugopal, K. Prabu, R.K. Jha and R. Thirumalaiswamy, Journal of Molecular Catalysis A: Chemical, 417 (2016) 153.

[133] Q. Li, P. Man, L. Yuan, P. Zhang, Y. Li and S. Ai, Molecular Catalysis, 431 (2017) 32.

[134] M. Zhou, Z. Zeng, H. Zhu, G. Xiao and R. Xiao, Journal of Energy Chemistry, 23 (2014) 91.

[135] T.P. Sulmonetti, S.H. Pang, M.T. Claure, S. Lee, D.A. Cullen, P.K. Agrawal and C.W. Jones, Applied Catalysis A: General, 517 (2016) 187.

[136] K. Yan and A. Chen, Fuel, 115 (2014) 101.

[137] L. Hora, V. Kelbichová, O. Kikhtyanin, O. Bortnovskiy and D. Kubička, Catalysis Today, 223 (2014) 138.

[138] D. Li, Y. Ding, X. Wei, Y. Xiao and L. Jiang, Applied Catalysis A: General, 507 (2015) 130.

[139] M. Diaz-Couce, J. Marreiros, M.J. Ferreira, P.D. Vaz, C.D. Nunes and M.J. Calhorda, Inorganica Chimica Acta, 455 (2017) 483.

[140] L. Sobhana, M. Sarakha, V. Prevot and P. Fardim, Applied Clay Science, 134 (2016) 120.

[141] K. Jirátová, F. Kovanda, J. Ludvíková, J. Balabánová and J. Klempa, Catalysis Today, 277 (2016) 61.

[142] X. Zhang, J. Bai and H.-M. Zhang, Applied Clay Science, 119, Part 2 (2016) 410.

[143] P. Sipos and I. Pálinkó, Catalysis Today, (2016).

[144] Y.-M. 10.1039/c7ta07795eZheng, N. Li and W.-D. Zhang, Colloids and Surfaces A: Physicochemical and Engineering Aspects, 415 (2012) 195.

[145] E. Gaffet, Comptes Rendus Physique, 12 (2011) 648.

[146] J.R. Peralta-Videa, L. Zhao, M.L. Lopez-Moreno, G. de la Rosa, J. Hong and J.L. Gardea-Torresdey, Journal of hazardous materials, 186 (2011) 1.

[147] W.K. Cho, J.K. Lee, S.M. Kang, Y.S. Chi, H.S. Lee and I.S. Choi, Chemistry–A European Journal, 13 (2007) 6351.

[148] A. Corma and H. Garcia, Chemical Society Reviews, 37 (2008) 2096.

[149] A. Corma, Catalysis Reviews, 46 (2004) 369.

[150] A. Arcadi and S.D. Giuseppe, Current Organic Chemistry, 8 (2004) 795.

[151] A.S.K. Hashmi and G.J. Hutchings, Angewandte Chemie International Edition, 45 (2006) 7896.

[152] C. Obradors and A.M. Echavarren, Chemical Communications, 50 (2014) 16.

[153] D.T. Thompson, Nano Today, 2 (2007) 40.

[154] D. Widmann and R.J. Behm, Accounts of chemical research, 47 (2014) 740.

[155] J.B. Priebe, M. Karnahl, H. Junge, M. Beller, D. Hollmann and A. Brückner, Angewandte Chemie International Edition, 52 (2013) 11420.

[156] P. Rodriguez, D. Plana, D.J. Fermin and M.T. Koper, Journal of Catalysis, 311 (2014) 182.

[157] C.Y. Ma, Z. Mu, J.J. Li, Y.G. Jin, J. Cheng, G.Q. Lu, Z.P. Hao and S.Z. Qiao, Journal of the American Chemical Society, 132 (2010) 2608.

[158] B. Godin, F. Ghysel, R. Agneessens, T. Schmit, S. Gofflot, S. Lamaudière, G. Sinnaeve, J.-P. Goffart, P.A. Gerin and D. Stilmant, BASE, (2010).

[159] C.-J. Jia, Y. Liu, H. Bongard and F. Schüth, Journal of the American Chemical Society, 132 (2010) 1520.

[160] G. Fan, F. Li, D.G. Evans and X. Duan, Chemical Society Reviews, 43 (2014) 7040.

[161] T. Mitsudome, Y. Mikami, M. Matoba, T. Mizugaki, K. Jitsukawa and K. Kaneda, Angewandte Chemie International Edition, 51 (2012) 136.

[162] T. Mitsudome, A. Noujima, Y. Mikami, T. Mizugaki, K. Jitsukawa and K. Kaneda, Angewandte Chemie, 122 (2010) 5677.

[163] J. Wang, X. Lang, B. Zhaorigetu, M. Jia, J. Wang, X. Guo and J. Zhao, ChemCatChem, 6 (2014) 1737.

[164] P. Liu, Y. Guan, R.A. van Santen, C. Li and E.J. Hensen, Chemical Communications, 47 (2011) 11540.

[165] F. Zhang, X. Zhao, C. Feng, B. Li, T. Chen, W. Lu, X. Lei and S. Xu, ACS Catalysis, 1 (2011) 232.

[166] W. Haiss, N.T. Thanh, J. Aveyard and D.G. Fernig, Analytical chemistry, 79 (2007) 4215.

Chapter II. Experimental section

I. Introduction

This chapter details the different methods of preparation of the materials studied as well as the different physicochemical and spectroscopic analysis techniques used for their characterization. It also presents the different protocols and operating modes used for the three catalytic tests, namely the oxidation of furfural, the assisted oxidation of glucose and the hydrogenation of furfural. The lamellar double hydroxides (LDH) used in this work are based on magnesium, aluminium and nickel metals that have been modified by Zr and also associated with gold nanoparticles. The characterization and analysis methods used in this work and detailed in this chapter are IR, XRD, BET, Raman, AAS, UV-Visible, SEM, TEM, HPLC and GC-MS.

II. Lamellar Double Hydroxides (LDH) synthesis by co-precipitation

II.1. Principal of synthesis

The technique of co-precipitation at a constant pH stands as a frequently used method for synthesizing alloys through the combination of multiple metals. This method allows to make uniform phases. Furthermore, the ability to produce solids makes co-precipitation a method of choice for the industrial production of alkaline catalysts. The structures of the resulting compounds in this preparation process are closely linked to the pH employed.

The initial development of LDH phases relied on **Miyata**'s pioneering work using the constant pH co-precipitation method **[1]**. This well-established approach, widely adopted for LDH-type materials, involves a stepwise addition of an aqueous solution containing metal salts to an initial medium of distilled water. The pH is meticulously controlled at a constant value by drop-wise addition of a basic solution. The pH used typically depends on the metals involved, with the complexation pH range for most metals being between 9 and 12. Customizing the pH values is essential for each specific system and metals ratio to ensure complete co-precipitation of metal cations and achieve the highest uniformity in the resulting material. Gradual reagent addition is often preferred to promote the crystallization of phases. After the reagent addition step, the precipitate is collected through several cycles of centrifugation and washing, followed by air-drying either at room temperature or at 80°C for 24 hour in a convection oven.

In laboratory settings, dedicated synthesis stations equipped with integrated interfaces, as illustrated in **Figure II-1**, have been purposefully engineered. These stations employ peristaltic pumps to facilitate exact regulation of multiple parameters, such as the rate of salt infusion, pH, temperature, and other variables. This rigorous parameter control is of paramount importance for attaining consistent and replicable synthesis results.

II.2. Experimental protocol

II.2.1. Synthesis of $MgAl_2$-LDH

$MgAl_2$-LDH synthesis was inspired by the work reported by G. Berrahou et al. **[2]**. First, a solution of magnesium nitrates and aluminum salts with a molar ratio of Mg/Al = 2

Was prepared by dissolving 0.2 mol of $Mg(NO_3)_3.9H_2O$ and 0.2 mol of $Al(NO_3)_2.6H_2O$ in 100 mL of distilled water (this solution is called MgAl salts).

Subsequently, 100 mL of a solution of Na_2CO_3 (0.05 mol) was placed in a flask at a temperature of 20-22°C. To this solution were added 100 mL of the MgAl salts solution as well as 100 mL of a sodium hydroxide solution (2M) drop wise and at the same time. This operation is ensured by a flow pump. The final pH of the mixture must have a value of 10 ± 0.05. Finally, the precipitate was recovered by centrifugation and the solid obtained was washed several times with distilled water until complete elimination of the excess nitrates and then finally dried at 80°C over 24 hours.

II.2.1.1 Modification of $MgAl_2$-LDH by Zr

The MgAl-LDH was modified by Zr in two ways either by in-situ modification by adding Zr during the synthesis of the LDH or by post-synthesis modification by adding Zr by impregnation onto the previously prepared LDH. Materials prepared according to the first way are designated by $MgAl_2Zr_{4.5}$-LDH and those prepared according to the second way are designated by $Zr_{4.5}$-$MgAl_2$-LDH.

II.2.1.1.1 Synthesis of $MgAl_2Zr_{4.5}$-LDH

These materials were prepared according to the same procedure described for the synthesis of $MgAl_2$-LDH. The Zr was added to the solution containing the metallic salts of Mg and Al.

The salts solution was obtained by dissolving 3.38g $Mg(NO_3)_3.9H_2O$, 2.03g $Al(NO_3)_2.6H_2O$ and 0.28g $ZrO(NO_3)_2.9H_2O$ in 100 mL of distilled water.

The solution thus prepared has a ratio of Mg/Al=2 and Al/Zr=4.5.

II.2.1.1.2 Synthesis of $Zr_{4.5}$-$MgAl_2$-LDH

Zr was added to $MgAl_2$-LDH by impregnation in excess water. 1g of $MgAl_2$-LDH was introduced in a beaker with 100 mL of distilled water. A solution of 0,28g of zirconium precursor $ZrO(NO_3)_2.9H_2O$ was added and the mixture was stirred for 24 hours. After filtration, the solid was washed and dried at 80°C over 24 hours.

For a comprehensive overview of the experimental conditions, the details of the experiment are represented in **Table II-1.**

Table II-1: Conditions used in the method experiment of Co-Precipitation.

	Materials used	Synthesis conditions
MgAl	- Aluminum nitrates: $Al(NO_3)_2.6H_2O$ - Magnesium nitrates: $Mg(NO_3)_3.9H_2O$ - Sodium hydroxide: NaOH - Sodium carbonate: Na_2CO_3	$MgAl_2$ - The pH of the solution between 9.95 and 10.05 at 25°C. - The flow rate=0.8ml/min - Centrifugation 3500 rpm for 10 minutes. - Drying at 80°C for 24 h followed by grinding.
MgAlZr	- Aluminum nitrates: $Al(NO_3)_2.6H_2O$ - Magnesium nitrates: $Mg(NO_3)_3.9H_2O$ - Zirconium nitrate $ZrO(NO_3)_29H_2O$ - Sodium hydroxide: NaOH - Sodium carbonate: Na_2CO_3	$MgAl_2Zr_{4.5}$ (Al/Zr=4.5) - The pH of the solution between 9.95 and 10.05 at 25°C. - The flow rate=0.8ml/min - Centrifugation 3500 rpm for 10 minutes. - Drying at 80°C for 24 h followed by grinding.
NiAl	- Aluminum nitrates: $Al(NO_3)2.6H_2O$ - Nickel nitrates: $Ni(NO_3)_3.6H2O$ - Sodium hydroxide: NaOH - Sodium carbonate: Na_2CO_3	$NiAl_2$ - The pH of the solution between 9.95 and 10.05 at 25°C. - The flow rate=0.8ml/min - Centrifugation 3500 rpm for 10 minutes. - Drying at 80°C for 24 h followed by grinding.
NiAlZr	- Aluminum nitrates: $Al(NO_3)_2.6H_2O$ - Nickel nitrates: $Ni(NO_3)_3.6H_2O$ - Zirconium nitrate $ZrO(NO_3)_29H_2O$ - Sodium hydroxide: NaOH - Sodium carbonate: Na_2CO_3	$NiAl_2Zr_{4.5}$ (Al/Zr=4.5) - The pH of the solution between 9.95 and 10.05 at 25°C. - The flow rate=0.8ml/min - Centrifugation 3500 rpm for 10 minutes. - Drying at 80°C for 24 h followed by grinding.

Figure II-1: The Equipment used for the LDH preparation.

II.2.2. Preparation of Au/LDH

Several Au/LDH catalysts with different LDHs as supports and different Au amount were synthesized through the urea deposition-precipitation (UDP) method within a 500 mL three-necked flask. To safeguard against any potential light-induced interactions, the flask was diligently shielded with aluminium foil and immersed in a water bath throughout the preparation process.

As model the preparation of 1g of catalyst with a gold weight percentage of 0.25%, the procedure detailed as follows was used **[2]**:

- 0.9975 g of the support material was placed into a three-necked flask containing 300 mL of distilled water while stirring, and the temperature was gradually raised to 80°C.
- Once the temperature reached a stable 80°C, 0.5 mL of a solution of $HAuCl_4 \cdot 3H_2O$ with a concentration of 10^{-2} M was added to the mixture then 0.0748 g of solid urea were introduced into the flask.
- After 16 hours, the solid was recovered through filtration, washed carefully with distilled water (typically four to five times) and finally dried at 80°C for 24 hours.
- In this procedure, the Au/urea ratio was approximately 1:75, based on the amounts of gold and urea used. The substrate/metal ratio was calculated to be approximately 1012:1, considering the mass of the support material ($MgAl_2$-LDH) and the amount of gold added.

II.3. Characterization and analyse techniques

II.3.1. Attenuated Total Reflectance Infrared Spectroscopy (FTIR-ATR)

II.3.1.1 Definition

FTIR-ATR is a surface analysis technique used to identify functional groups in materials by measuring infrared absorption. In this work, it was employed to investigate the chemical functionalities on the surface of the catalysts, with minimal sample preparation.

II.3.1.2 Principe

FTIR-ATR analysis provides information on the vibrational modes of chemical bonds, particularly those associated with surface functional groups. In our study, we focused on the mid-infrared region (4000–400 cm^{-1}) to detect characteristic bands such as –OH, C=O, and C–O groups, which help to evaluate surface modifications during the synthesis process.

II.3.1.3 Measurement conditions

Measurements were conducted at the laboratory of Catalysis and Synthesis in Organic Chemistry (LCSCO), University Abou Bekr Belkaid Tlemcen Algeria on a Fourier-transform infrared spectrometer, specifically the Agilent Technologies Cary 640 IRTF series.

The prepared samples were placed into the appropriate sample holders. A baseline correction was performed by scanning a blank KBr sample to account for background interference. The sample was then inserted into the spectrometer, and a scan was conducted to obtain the infrared spectrum. The resulting spectrum was analyzed to identify peaks corresponding to functional groups or molecular

bonds.

A diffuse reflection mode using an attenuated total reflection accessory (ATR) was used. The spectra were captured within the range of 4000 to 400 cm^{-1}

II.3.2. X-ray Diffraction (XRD)

II.3.2.1 Definition

X-ray diffraction (XRD) is used to characterise the crystalline structure of materials. It provides information on crystallinity, average crystallite size, and the identification of crystalline phases present in the catalysts.

II.3.2.2 Principle

XRD analysis relies on the diffraction of X-rays by the regularly arranged atoms in a crystal lattice. In this work, Bragg's law was applied to determine the structural properties of the materials, and the Scherrer equation was used to estimate the average crystallite size based on peak broadening.

Measurements were performed at room temperature over a 2θ range of 10° to 80°, with a step size of 0.04° and an acquisition time of 2 seconds per step. The instrumental broadening was corrected using LaB_6 as a reference material.

II.3.2.3 Measurement conditions

Sample preparation involves finely grinding the material to create a fine powder that can be deposited onto a sample holder. The sample holder, aided by a magnet, is positioned at the centre of the diffractometer chamber. It is capable of rotating around a vertical axis to enhance diffraction opportunities. Additionally, adjustments to the analysis conditions, such as altering the range of the incident X-ray angle, step size, and acquisition time, can be made to optimize the quality of the diffractograms **[9]**.

Measurements were conducted at the laboratory of Catalysis and Synthesis in Organic Chemistry (LCSCO), University Abou Bekr Belkaid Tlemcen Algeria on a using a Rigaku Miniflex 600 diffractometer equipped with a copper anode (with a wavelength of $\lambda K\alpha 1$ = 1.54060 Å). The diffractometer scanned the 2θ range from 2 to 80 degrees at room temperature, employing a step size of 0.01 degrees and an acquisition time of 2 minutes.

II.3.3. Measurement of specific surfaces and pore volumes (BET)

II.3.3.1 Definition

The textural properties of the catalysts were investigated through nitrogen adsorption-desorption at 77.4 K. The specific surface areas (m^2/g) were calculated using the Brunauer–Emmett–Teller (BET) method based on the analysis of adsorption and desorption isotherms **[7]**.

For mesoporous materials, pore volume (cm^3/g) and average pore diameter (Å) were estimated using the Barrett–Joyner–Halenda (BJH) method **[9]**, while for microporous materials, the t-plot or αs-plot methods were applied to determine the micropore volume and surface area **[12]**.

II.3.3.2 Principe

The BET theory assumes multilayer adsorption and is applied in the relative pressure range of 0.05–0.30, where a linear relationship is observed **[7]**. From the slope and intercept of this line, the monolayer volume (Vm) and BET constant (C) were determined, allowing the calculation of the specific surface area.

The pore size distribution and total pore volume were determined from the desorption branch using the BJH method, which is based on the Kelvin equation and assumes cylindrical pores open at one end **[8-9]**.

According to the International Union of Pure and Applied Chemistry (IUPAC), six types of isotherms and four types of hysteresis loops can be observed, offering detailed information on pore structure and surface properties **[5-6, 10]**. **Figure II-3** illustrates this classification.

All samples were degassed under vacuum prior to analysis to ensure removal of adsorbed contaminants **[14]**.

In accordance with the BET model, materials can be categorized based on their textural characteristics, primarily relying on six fundamental types of isotherms, **Figure II-3** represents IUPAC classification of the type of isotherms **[10].**

- Isotherms **type I**: are typical in most microporous solids. They exhibit significant increases in the volume of adsorbed N_2 at low pressures, attributed to the strong attraction of the narrow pores to the adsorbate isotherm.
- Isotherms **type II**: Characteristic of macroporous materials (≥50 nm), without pores or with very low specific surface areas. They show a linear increase of adsorbed gas volume versus relative gas pressure.
- Isotherms **type III**: are typically observed in samples characterized by low porosity and a limited affinity between the adsorbent and adsorbate.
- Isotherms **type IV**: are a hallmark of materials with porosity falling within the range of 2 to 50 nanometers, known as mesopores. They exhibit hysteresis phenomena, which entail different pressure equilibrium conditions between the adsorption and desorption branches.
- Isotherms **type V**: are displayed by materials that indicate a weak interaction between the adsorbent and adsorbate, coupled with mesoporosity.
- Isotherms **type VI**: are exceedingly rare and are characterized by step-like patterns in materials. They only manifest in solids with an exceptionally uniform, non-porous surface.

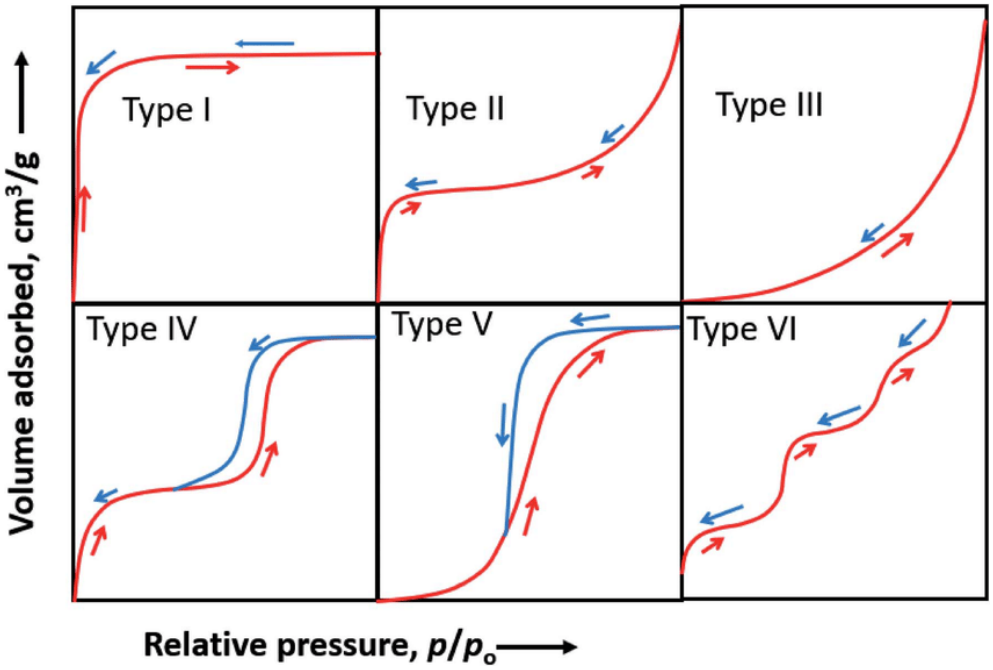

Figure II-3: IUPAC classification of the type of isotherms [10].

II.3.3.3 Measurement conditions

Measurements were conducted at the laboratory of Catalysis and Synthesis in Organic Chemistry (LCSCO), University Abou Bekr Belkaid Tlemcen Algeria on a Micromeritics 3flex apparatus.

For the measurement process, a known quantity of the sample is initially placed into a measuring cell. Subsequently, the sample undergoes a degassing procedure for 12 hours at 200°C, accomplished by using a flow of helium and nitrogen at a pressure approximately around 100 mTorr. Following the degassing phase, the sample is re-weighed to determine the extent of mass loss. The cell is then introduced into the measurement chamber and subsequently immersed in a bath of liquid nitrogen. The desorption step is recorded after the cell is heated back to room temperature.

II.3.4. Raman spectroscopy

II.3.4.1 Definition

The interaction between radiation and matter gives rise to numerous different physical phenomena including: reflection, transmission, absorption, and (elastic or inelastic) scattering, among others. Raman spectroscopy exploits the phenomenon of inelastic light scattering at low intensity. This interaction leads to a material's polarizability, resulting in deformation of the electron cloud (variation in polarizability).

Raman spectroscopy is a non-destructive analytical technique that requires very small quantities of material and no specific preparation. Spectra can be obtained from any state of matter: gas, liquid, or solid (amorphous or crystalline). However, it is essential for materials to be stable

concerning laser-induced heating. Additionally, there is the phenomenon of photoluminescence, which can interfere with the analysis, i.e., intense light emission from the material that can mask the weak Raman effect. To address this, the choice of wavelength is a crucial factor in increasing Raman detection by moving away from the spectral range of photoluminescence **[11]**.

II.3.4.2 Principle

During the interaction of a monochromatic light beam with matter, a photon transitions to a virtual state (short-lived excitation). Upon de-excitation, three conceivable phenomena can occur:

- Rayleigh scattering (elastic): if the photon's de-excitation matches its excitation frequency.
- Raman Stokes scattering (inelastic): if the photon's de-excitation is lower than its excitation.
- Raman Anti-Stokes scattering: if the photon's de-excitation is higher than its excitation.

Figure II-4 illustrates the various energy transitions during Raman and Rayleigh scattering. The virtual intermediate state does not have a physical meaning; the Raman process involves two photons during the same step. Only the initial and final electronic states are real. In cases where a real electronic level is close in energy to the virtual intermediate level, the process becomes resonant, leading to a high probability of transition and, hence, intense *Raman* signal.

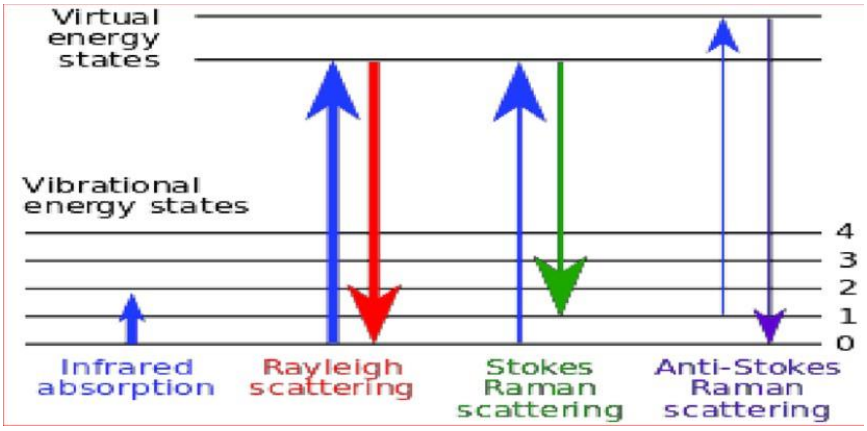

Figure II-4: Energy level diagram showing Rayleigh and Raman scattering.

II.3.4.3 Measurement conditions

The Raman analyses were conducted at the laboratory of Catalysis and Synthesis in Organic Chemistry (LCSCO), University Aboubekr Belkaid Tlemcen Algeria using a HORIBA Scientific spectrophotometer, specifically the Labram HR Evolution model, equipped with a laser wavelength of 633 nm, a grating of 1800 lines per millimeter, and acquisition and accumulation times of 30 s and 60 s, respectively. The obtained spectra were processed using the LabSpec 6 software.

II.3.5. Atomic absorption spectroscopy (AAS)

II.3.5.1 Defintion

Atomic absorption spectroscopy (AAS) is a technique employed in analytical chemistry to precisely determine the concentration of metallic elements within various samples. It involves measuring the absorption of light at specific wavelengths by the atoms of the elements of interest. This method is widely used across different industries such as environmental science, pharmaceuticals, and metallurgy because of its accuracy and reliability in elemental analysis.

II.3.5.2 Principle

Atomic Absorption Spectroscopy (AAS) is based on the principle that each element absorbs light at a unique wavelength due to the specific energy levels of electrons in its atoms. When atoms transition from their ground state to an excited state, they absorb energy in the form of photons at these resonant wavelengths.

The process occurs when incident radiation from a light source matches the energy required to promote an electron to an excited state. As atoms in the sample pass through the light beam, they absorb photons at the resonant wavelength, causing a reduction in the transmitted light intensity. This reduction, known as absorbance, is directly proportional to the concentration of the element in the sample, as described by Beer-Lambert's law **[12]:**

$$A = \log\left(\frac{I}{I_0}\right) KLC$$

Where:

I: intensity of the radiation after passing through the thermal source.

I0: intensity of the incident radiation.

k: absorption coefficient, a characteristic constant for absorbing species.

L: length of the light path.

C: concentration of absorbing atoms in the flame.

During the atomic absorption process, the energy supplied to the atom originates from a light source known as a hollow cathode lamp. This lamp emits radiation consisting of characteristic lines of the element under analysis, each with a specific wavelength. The light beam then falls onto the flame where the 'target' atom is located. The hollow cathode lamp contains an anode and a cathode in the form of a cylindrical cavity containing the element for which the emission spectrum is desired.

An electrical potential is applied between the anode and the cathode, aiming to ionize the filling gas present in the lamp. The ionized gas provides the essential energy for the evaporation of

metal atoms. These ions collide with the metal atoms, causing them to enter excited states.

They then return to their ground states, releasing the desired light radiation.

The basic experimental setup used in atomic absorption (**Figure II-5**) consists of four main parts: a source, a hollow cathode lamp, a burner and nebulizer, a monochromator, and a detector connected to an amplifier and an acquisition device.

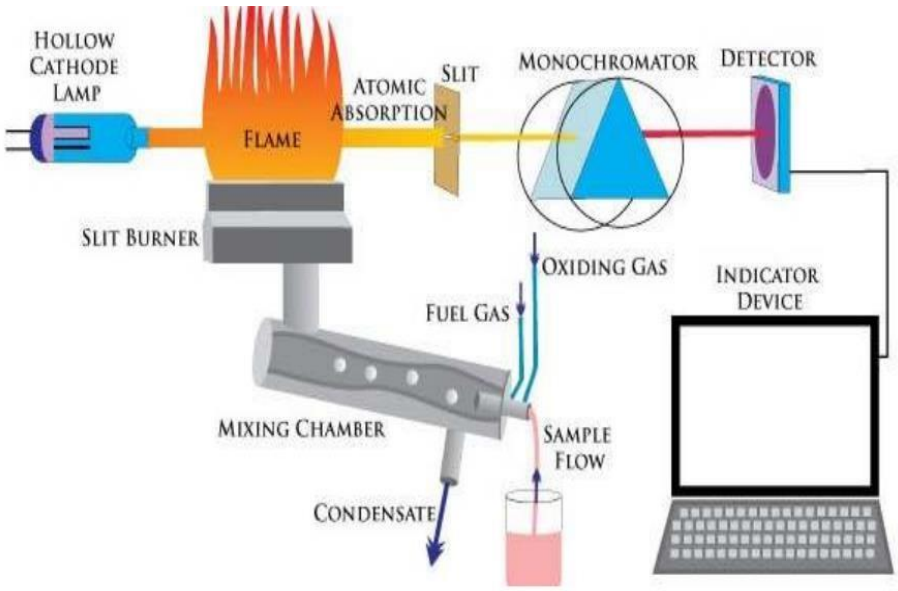

Figure II-5: Diagram of a flame atomic absorption spectrophotometer.

In AAS, most samples are in aqueous solution and are introduced into the atomizer via a nebulizer. The nebulizer generates an aerosol by creating a high-pressure gas flow that disperses the liquid sample into fine droplets. These droplets are then introduced into the atomizer, where they are vaporized and atomized in the flame.

There are two main types of flames used in atomic absorption:

- **Air/acetylene flame**: The most common, with a temperature of approximately 2500°C, suitable for analyzing a wide range of elements.
- **N_2O/acetylene flame**: Used for elements that form refractory oxides, which are less efficiently atomized in the air/acetylene flame **[13]**.

II.3.5.3 Measurement conditions

The measurements of the elements contained in the samples were conducted at the laboratory of Catalysis and Synthesis in Organic Chemistry (LCSCO), University Aboubekr Belkaid Tlemcen Algeria using a Perkin Elmer Analyst 300 atomic absorption spectrophotometer, employing a hollow cathode lamp and a specific operating current for each element to be quantified. To determine the concentration of each element, standard solutions within the linear range of the element are prepared.

Finally, the metal deposition rate is calculated using the following relationship **[13]:**

$$Deposit\ rate = (\frac{\%\ theoric - \%\ real}{\%\ theoric}) * 100$$

To perform an analysis using atomic absorption spectroscopy (AAS), preliminary calibration is required to ensure accurate measurements. This calibration involves preparing standard solutions from a known and certified mother solution. These standard solutions should cover a range of concentrations relevant to the expected analysis, such as around 8 ppm of gold in this case. These standard solutions are then used to calibrate the instrument, thereby ensuring the accuracy of the results obtained from the samples being analyzed.

II.3.6. UV-Vis diffuse reflection spectroscopy

II.3.6.1 Principle

The UV-Vis spectroscopy technique in diffuse reflection relies on analyzing the light flux reflected by samples in powder form. Information about the nature of materials is obtained when the chromophore absorbs a portion of the light radiation in the appropriate spectral range before reflection. This analysis is conducted under conditions where incident light radiation strikes the sample surface,

which may be partially transmitted and/or reflected.

If the sample has a sufficiently thick surface, transmitted radiation is negligible, and only reflected radiation is observed. Thus, light reflection consists of two types: specular and diffuse. Specular reflection (RS) is characterized by an identical spectral composition between incident and reflected radiation with corresponding reflection angles, referred to as true specular reflection (RSV). However, diffuse reflection (RD) results from the more or less deep penetration of incident radiation into the material, reflecting in various directions. This diffusion arises from incomplete absorption of radiation by molecules present in the material or absorption at its surface, **Figure II-6** represent the description of the two types of reflection: specular (RS) and diffuse (RD) **[14].**

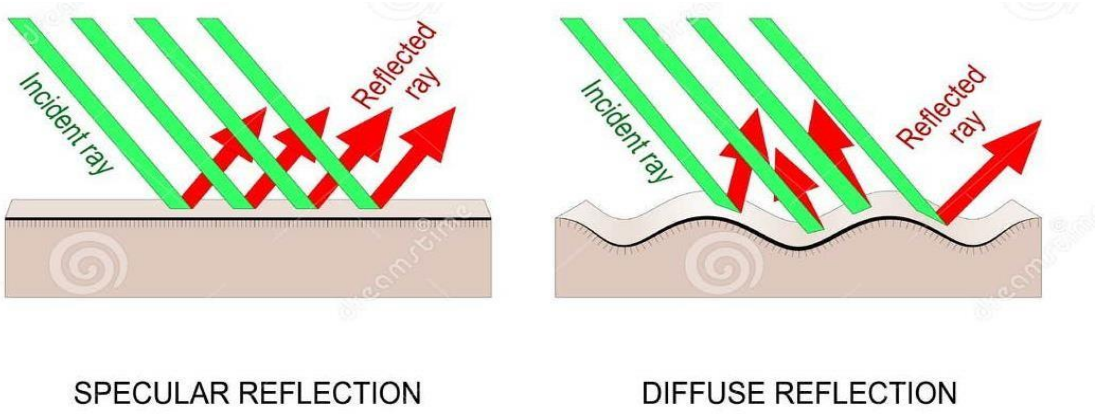

Figure II-6: Description of the two types of reflection: specular (RS) and diffuse (RD) [14]

Since specular reflection originates from the reflection of incident radiation at the material's surface, it does not provide insight into the material's absorbance power, unlike diffuse reflection. Ultimately, specular radiations are perceived as undesirable and are partially eliminated when implementing a selective optical setup. $BaSO_4$ was used as a reference materiel, which is a highly transmitting and slightly absorbing material. It reflects the transmitted light and helps increase the fraction of the intensity reaching the detector. The material's reflectance percentage is compared to that of a standard compound (white) over a wide range of wavelengths **[14]**.

Furthermore, this technique provides an estimation of the value of the bandgap (optical gap) in powders, within a spectral range from 200 to 800 nm. To calculate this value, Kubelka-Munk **[14]**

used a formula that relates the reflectance R to the absorbance A, which is as follows:

$$\propto = \frac{(1-R)^2}{2R}$$

Where: α: the absorption coefficient, and R the reflection coefficient.

II.3.6.2 Measurement conditions

The optical properties of the materials were analyzed at the laboratory of Catalysis and Synthesis in Organic Chemistry (LCSCO), University Aboubekr Belkaid Tlemcen Algeria by UV/Vis spectroscopy (200-800 nm) using a Perkin Elmer 800 UV-Vis spectrophotometer equipped with a diffuse reflectance accessory to capture the diffuse reflection of the reflected light with an integration time of 0.96 s, a scan speed of 60 nm/min, and a slit width of 2 nm. BaSO4 was used as the reference material.

II.3.6.3 Deconvolution

To determine the exact chemical composition of the samples from the experimental spectra, various software tools have been used for data processing. PeakFit is commonly used processing software for the separation and analysis of spectroscopy and chromatography peaks. It enables the detection, separation, and quantification of peaks obtained from each spectrum. Additionally, it can provide us with intensities, areas, centers, and widths of each peak. There is a variety of mathematical methods for spectral deconvolution, among which we have chosen the Gaussian method (**Figure II-7**).

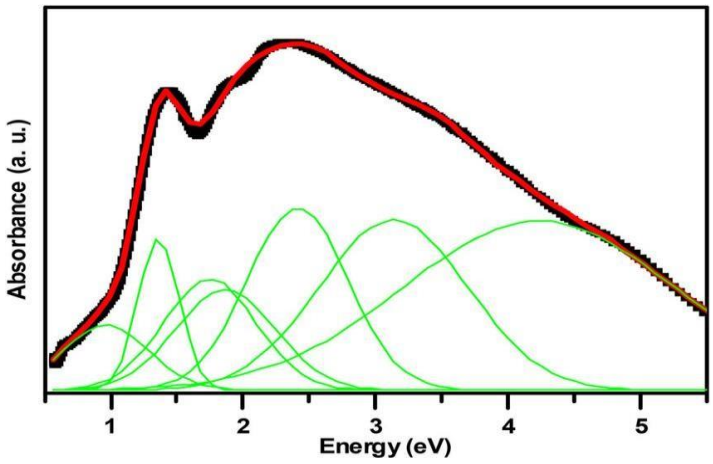

Figure II-7: Example of deconvolution spectrum of a sample [15].

II.3.7. Scanning Electron Microscopy (SEM) and Energy Dispersive Spectrometry

II.3.7.1 Principle

The FEG Nova NanoSEM 450 microscope is a high-resolution scanning electron microscope (SEM) that can measure and visualize features at the nanoscale. Typically, this microscope is capable of resolving structures down to about 1 nm, depending on the operating conditions and the nature of the sample. It is particularly well-suited for analyzing surface topography, morphology, and material composition of samples with nanometer-sized features, such as thin films, nanoparticles, and nanostructures.

The microscope's operation is based on the emission of electrons from a cathode and the detection of signals resulting from the interaction of these electrons with the sample. These electrons, when directed onto the sample's surface, penetrate deep into the material, influencing a volume known as the "interaction volume" or "interaction bulb." The size of this volume is influenced by the average atomic number of the sample and the energy of the incident electrons. Within this interaction volume, the electron beam loses its energy due to multiple collisions with the material's atoms, leading to the generation of various secondary effects. These effects include the emission of electrons and photons, electron absorption, induced currents, electrical potentials, localized temperature changes, and lattice vibrations, **Figure II-8** shows Schematic of electro

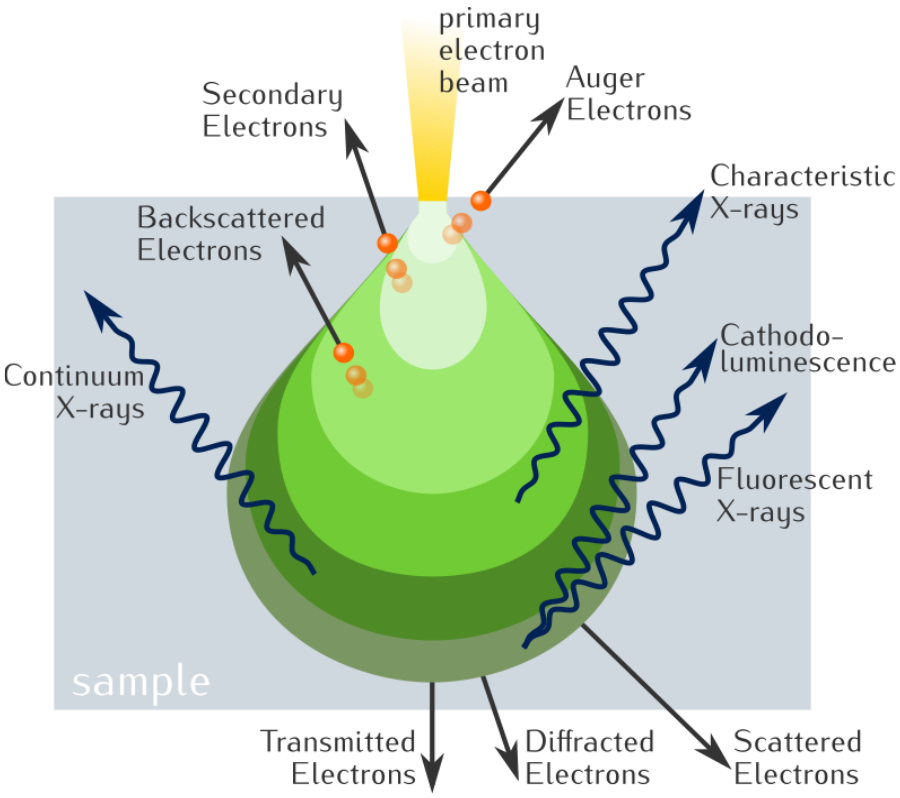

Figure II-8: Schematic of electron beam interaction.

The interaction between an electron beam and a sample generates various types of radiation. The accompanying diagram, **Figure II-8**, illustrates the different forms of radiation emitted during this interaction. These radiations are produced simultaneously, collectively facilitating both the observation and analysis of the sample under investigation.

II.3.7.2 The X-rays (or X photons)

The release of X-ray photons happens when an atom, ionized- due to the impact of an electron beam- returns to its ground state. This process entails an outer-layer electron of the atom filling the space left by an ejected inner-layer electron. The disparity in energy levels, between these two electron layers, causes the emission of X-ray photons. These photons possess distinct and characteristic energies specific to each element responsible for their generation.

These emitted photons are collected and sorted based on either their energies (Energy Dispersive Spectrometry - EDS) or their wavelengths (Wavelength Dispersive Spectrometry - WDS). This categorization yields valuable insights into the composition of the examined sample. X-ray photons have excellent penetrating capabilities and originate from an interaction volume of about one cubic micron. Energy Dispersive Spectrometry (EDX), as an analytical technique, enables both qualitative and quantitative analysis of the sample surface, facilitating the identification of mineral and metallic elements present.

II.3.7.3 Analysis condition

SEM analyses were performed at the Central Science and Technology Services of the University of Cádiz using a FEG Nova NanoSEM 450 microscope, operating at 30 kV.The SEM micrographs captured allowed us to study both the morphology and chemical composition of materials.

II.3.8. Transmission Electron Microscopy (TEM)

II.3.8.1 Principle

This technique allows direct observation of the catalysts at the nanoscale and provides information on the shape and distribution of the metal particles on the surface of the support. It is also possible to evaluate the size distribution of the metal particles and to assess their homogeneity or, if necessary, evaluating their heterogeneity. After measuring a large number of particles, histograms of the percentage distribution of particles of size di (i.e. ni or 100ni/Σ ni as a function of di) can be drawn. It is then possible to calculate the average diameter of the gold particles by the relation:

$$d_{moy} = \frac{\Sigma nidi}{\Sigma ni}$$

Where d is the mean particle diameter.

Transmission electron microscopy (TEM) was also used to obtain fine structural details on the powder samples of the substrates as well as the size of the gold deposited on them. This technique was also used to accurately average the particle size data of the gold. The preparation of electron transparent samples for (S) TEM inspection was performed using the Focused Ion Beam (FIB) technique. Only with this approach, we can characterize the actual structure of the catalytic coating in the honeycomb devices from composition maps and high-resolution images working in parallel and high-resolution images made in (S)TEM mode.

II.3.8.2 Analysis condition

In this study, a Talos F200X G2 TEM/STEM electron microscope was utilized for atomic-level characterization of samples. Operating at an accelerating voltage of 200 kV, it offers a point resolution of approximately 0.25 nm in High-Resolution TEM mode and 0.16 nm in High-Resolution STEM mode. The microscope features simultaneous detection with four STEM detectors, including High Angle Annular Dark Field (HAADF) detection for high-contrast imaging. It is also equipped with a Super-X EDS system featuring four windowless SDD detectors for enhanced elemental analysis, as well as a Gatan Continuum Electron Energy Loss Spectrometer for detailed spectroscopic studies. Specialized holders were employed for electron tomography and the investigation of air-sensitive samples.

II.4. Catalytic tests

The different materials prepared in the frame of this thesis were tested in aqueous phase furfural oxidation, furfural hydrogenation, and glucose oxidation reactions.

The aqueous phase furfural oxidation and furfural hydrogenation reaction were made at the laboratory of Catalysis and Synthesis in Organic Chemistry (LCSCO), University Abou Bekr Belkaid Tlemcen Algeria

The Glucose oxidation tests were made at Laboratory of Reactivity and Chemistry of Solids (LRCS), UMR CNRS 7314, University of Picardie Jules Verne, Energy Hub, 15 rue Baudelocque, FR-80000 Amiens, France in the frame of internship.

II.4.1. Furfural oxidation

The oxidation of furfural was carried out in a three-necked glass flask, the required quantities of previously distilled furfuraldehyde and H_2O_2 freshly prepared solution were charged in the reactor and heated to the target reaction temperature. A 0.08g of catalyst amount was added to the flask. At this time vigorous stirring of the reaction mixture was started and considered as the initial time of the reaction. Samples liquids were taken at different times and diluted with distilled water then filtered and analyzed by HPLC.

II.4.1.1 Analysis conditions

The furfural oxidation products were analyzed by HPLC- YL9100 with YL 9120 UV-visible detector and C18 column (250 mm × 4.6 mm, 5 μm, Fuli instruments). The products were analyzed at wavelength of 280 nm. Mobile phase was composed with 2% acetonitrile, 25% water, 73% H_2SO_4. The flow rate and column temperature were 1.0 mL min^{-1} and 30 °C, respectively.

The conversion of furfural was calculated using the following formula:

$$\text{Conversion (\%)} = \left(\frac{\text{Fur}_{int} - Fur_{fin}}{\text{Fur}_{int}}\right) \times 100$$

The selectivity of each product was calculated as follows:

$$\text{Selectivity (\%)} = \left(\frac{\text{n}_\text{i}}{n_T}\right) \times 100$$

Where Fur_{init} and Fur_{fin} indicate the initial and final mole number of furfural respectively, n_i and n_T indicate number of moles of product i and total number of moles of all products.

II.4.2. Furfural hydrogenation

Catalytic hydrogenation reactions of furfural were conducted in a 25 mL stainless steel autoclave equipped with an electromagnetic-driven stirrer and a PID temperature controller. For each test, catalyst (0.08 g), furfural (6 mmol), and solvent (99% isopropanol, 15 mL) were loaded into the autoclave.

The reactor was purged several times with nitrogen to eliminate air. Subsequently, the reactor was pressurized with H_2 to 1.0 MPa. The autoclave was heated to 180°C, while the reagents were vigorously stirred at a rate of 700 rpm. After 6 hours of reaction, the samples were filtered and analyzed by Bruker Scion GC-MS equipped with a DB-5 capillary column.

II.4.2.1 Analysis conditions

The GC analysis was conducted using a BRUKER Scion SQ instrument, operating under the following conditions:

- The injection conditions are :

Split : 1/5

PN2 : 7Psi

Tinj : 250°C

Tdet : 250°C

- The column used is a DB-5, capillary with methylphenyl siloxane as stationary phase (30m; 0.25mm). For mass spectrometry, the conditions are as follows:
  - Type of ionization: Electronic impact
  - Filament intensity: 70 eV
  - Type of mass analyzer: Quadrupole
  - Analysis mode : Scan TIC (from 20 to 600)

Furfural conversion and product selectivity were calculated using the following formulas:

$$\text{Conversion (\%)} = \left(\frac{\text{Fur}_{int} - Fur_{fin}}{\text{Fur}_{int}} \right) \times 100$$

The selectivity of each product is calculated as follows:

$$\text{Selectivity (\%)} = \left(\frac{\text{n}_\text{i}}{n_T} \right) \times 100$$

Where Fur_{init} and Fur_{fin} indicate the initial and final mole number of furfural respectively, n_i and n_T indicate number of moles of product i and total number of moles of all products.

II.4.3. Glucose oxidation

In the optimized procedure, 1.38 mmol of sugar and 55 mg of NaOH (1 equiv) were dissolved in 6 mL of water within a glass tube. The NaOH/glucose molar ratio is approximately 1:1. Subsequently, 25 mg of catalyst, consisting of $Au/NiAl_2Zr_{4.5}$-LDH and 200 µL of 30% aq. H_2O_2 were added to the solution. The reaction mixture was then stirred at room temperature under standardized illumination, which refers to the use of a calibrated light source to maintain constant irradiation conditions throughout the experiment. The light source used was the 94011A-ES solar simulator, which employs a 100 W ozone-free xenon lamp to produce a 1.5-inch x 1.5-inch (38 mm x 38 mm) collimated beam, closely simulating the sun's spectrum. The reaction was carried out for 90 minutes. After the reaction, the catalyst was separated by filtration through a nylon membrane (0.25 µm).

II.4.3.1 Analysis conditions

The resulting filtrate was freeze-dried, and the crude product was characterized by ^1H NMR in D_2O. The area of H_2 peak of synthesized gluconate (δ=4.14 ppm, d, J=3.7 Hz) was compared to the area of H_1 peaks of residual glucose ($H_1\alpha$: δ=5.24 ppm, d, J=3.7 Hz and $H_1\beta$: δ=4.65 ppm, d, J=7.9 Hz,) to calculate a conversion rate according to the formula:

$$\%\, Conv = \frac{\mathrm{A}\,(H_2\ \text{gluconate})}{\mathrm{A}\,(H_1\ \alpha\,\text{glucose}) + \mathrm{A}\,(H_1\beta\ \text{glucose}) + \mathrm{A}\,(H_2\ \text{gluconate})} \times 100$$

References:

[1] Z. Jiang, J. Wu, X. Liu, H. Yu, C. Jiao, J. Shen and Y. Pei, New Journal of Chemistry, 45 (2021) 14580.

[2] G. Berrahou-Harchaoui, R. Bachir, S. Bedrane, J.J. Calvino, J.C. Hernandez Garrido, , J. Porous Mater. 30 (2023) 55–64.

[3] N. Ameur, S. Bedrane, R. Bachir and A. Choukchou-Braham, Journal of Molecular Catalysis A: Chemical, 374 (2013) 1.

[4] B.C. Smith, Fundamentals of Fourier transform infrared spectroscopy, CRC press, 2011.

[5] M. Lee, X-Ray diffraction for materials research: from fundamentals to applications, CRC Press, 2017.

[6] T. Barakat, J.C. Rooke, E. Genty, R. Cousin, S. Siffert and B.-L. Su, Energy & Environmental Science, 6 (2013) 371.

[7] G. Leofanti, M. Padovan, G. Tozzola and B. Venturelli, Catalysis today, 41 (1998) 207.

[8] S. Brunauer, P.H. Emmett and E. Teller, Journal of the American chemical society, 60 (1938) 309.

[9] G. Sigmund, T. Hüffer, T. Hofmann and M. Kah, Science of the Total Environment, 580 (2017) 770.

[10] P. Mercera, J. Van Ommen, E. Doesburg, A. Burggraaf and J. Ross, Applied catalysis, 57 (1990) 127.

[11] M.H.A. RAHMAN, Sains Malaysiana, 49 (2020) 2261.

[12] R. Wolstenholme, Analytical Techniques in Forensic Science, (2021) 161.

[13] S. Ivanova, Universite Louis Pasteur, (2004).

[14] J.A. Broekaert, Analytical atomic spectrometry with flames and plasmas, John Wiley & Sons, 2006.

[15] R.W. Frei, Diffuse Reflectance Spectroscopy Environmental Problem Solving, CRC press, 2019.

[16] E. Abdel-Khalek, I. Ibrahim, T.M. Salama and A.M. Elseman, Ferroelectrics, 558 (2020) 150.

Chapter III.

Oxidation of furfural over Au/MgAlZr-LDH Catalysts characterizations and catalytic activity

I. Introduction

This chapter focuses on the oxidation of furfural, a crucial step in biomass valorisation. Furfural, derived from the hydrolysis of hemicellulose, represents a valuable raw material for the synthesis of high-value products. The oxidation of furfural offers pathways for the production of important intermediates such as succinic acid, which is used in various industrial sectors including pharmaceuticals, polymers, and agriculture.

For this, different catalytic systems based on modified LDH and Au nanoparticles and reaction conditions that promote efficient oxidation of furfural, with particular attention to improving selectivity and yield towards the desired products were explored.

The main goal is to assess the catalytic performance (activity and selectivity) of $MgAl_2$-LDH in the furfural oxidation reaction and to study the influence of Zr addition during and post-synthesis, as well as the impact of depositing Au nanoparticles on $MgAl_2$-LDH's catalytic performance.

MgAl-LDH materials were prepared according to the procedure reported in Chapter II, then modified with Zr either during the synthesis of the parent LDH or post-synthesis. These materials were used as supports for depositing 0.25 wt % Au by DPU (Deposition-Precipitation with Urea) method. All materials were characterised by FTIR spectroscopy, Raman spectroscopy, X-ray diffraction, scanning electron microscopy (SEM), and transmission electron microscopy (TEM), then tested in the reaction of aqueous-phase oxidation of furfural using H_2O_2 as the oxidant. The results obtained as well as their discussion are presented in the following paragraphs.

II. Physicochemical properties of LDH

II.1. Characterization by FTIR spectroscopy

The FTIR spectra corresponding to all samples are shown in **Figure III-1**.

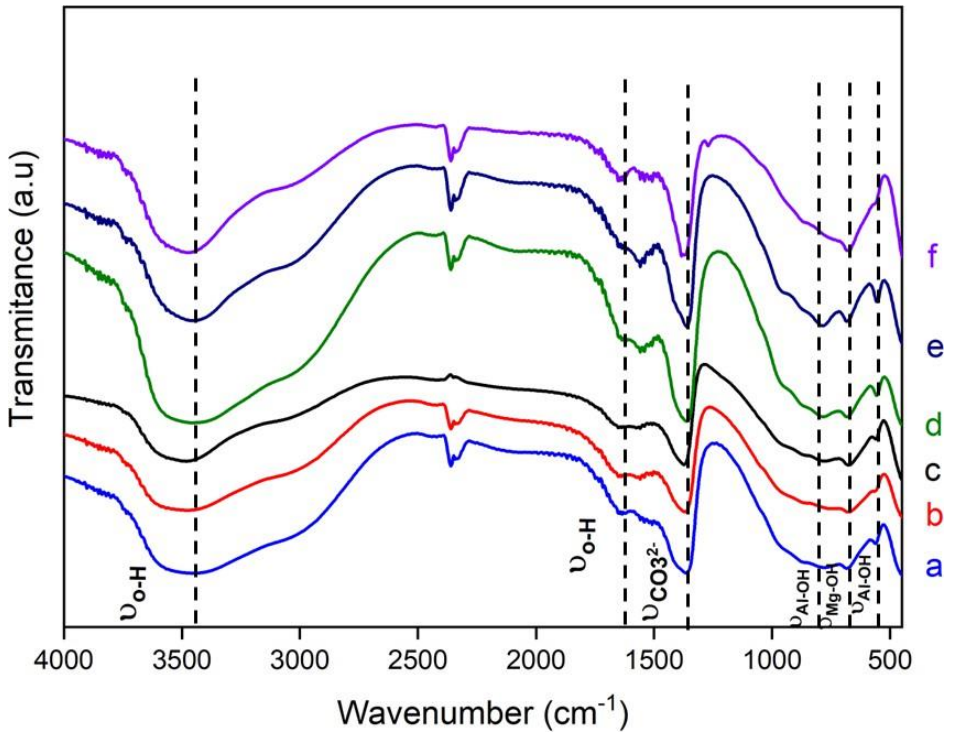

Figure III-1: FTIR spectra of $MgAl_2$-LDH (a), $MgAl_2Zr_{4.5}$-LDH (b), 0.25%Au/$MgAl_2Zr_{4.5}$-LDH (c), $Zr_{4.5}$-$MgAl_2$-LDH (d), 0.25%Au/$Zr_{4.5}$-$MgAl_2$ -LDH (e), 0.25%Au/$MgAl_2$-LDH (f).

All samples showed a broad intense band between 3500 and 3000 cm^{-1} due to the OH stretching mode of the layer's hydroxy groups and the interlayer's H_2O molecules **[1]**. Although the position of this band should be dependent on the nature of the cations layer, as its electronegativity will modify the electron density on the O-H bond (M-OH), the extreme broadness of this band, owing to hydrogen bonding, precludes any meaningful discussion **[2]**. The band at 2300–2350 cm^{-1} corresponds to CO_2 in the ambient air (**Figure III-1**) **[3]**.

The medium intensity absorption band around 1587 $cm^{-1}$is due to the deformation (νHOH bending) mode of interlayer's H_2O molecules **[4, 5]**. A sharp and intense band appears at 1360 cm^{-1} describing the interlayer's CO_3^{2-} ion stretching vibration **[6]**. Bands locatedat 963, 770 and 687 cm^{-1} are attributed to the ν1, ν2 and ν4 bands of CO_3^{2-}, respectively **[7]**. Bands observed below 1000 cm^{-1} are generally attributed to the vibration of M–O, M–O–M and O–M–O bonds in the brucite-like lattice **[8-14]**

Spectra of $Zr_{4.5}$-$MgAl_2$-LDH and $MgAl_2Zr_{4.5}$-LDH, (**Figure III-1b** and **c**) have similar profiles as the $MgAl_2$-LDH spectrum. However, bands below 1000 cm^{-1} attributed to M–O, M–O–M and O–M–O bonds are more intense for $Zr_{4.5}$-$MgAl_2$-LDH and $MgAl_2Zr_{4.5}$-LDH. This shows that the introduction of Zr into the $MgAl_2$-LDH material induces a modification of the polarity of the M-O-M bonds, the local atomic mass and intermolecular interactions **[15-19]**.

This result confirms that Zr brings structural and chemical modifications to $MgAl_2$-LDH. Finally, the FTIR spectra of the Au-containing materials revealed no modification compared to their LDH support counterparts. This is probably related to the low Au content but it could indicate that Au has not modified the crystalline structure of LDH as Zr has done but is only deposited on the surface of the LDH.

II.2. Characterization by Raman spectroscopy

In order to confirm the results obtained by FTIR, particularly the effect of Zr on the structure of LDH, characterizations in the absorption zone revealing M-O-M bonds below 1000 cm^{-1} were carried out by Raman spectroscopy. The Raman spectra grouped in **Figure III-2** confirm the findings made by FTIR characterization. Indeed, there is a band appearing at 1061 cm^{-1} typical of the C–O bond stretching of carbonate ion, which can be altered by H_2O molecules in the interlayer region of LDH. This band increase in the spectra corresponding to samples containing Zr can be attributed to multiple factors **[20, 21]**. Zirconium electronic and structural properties enhance scattering **[22]**. Its introduction in the LDH alters the molecular environment, affecting crystal structures and bonding configurations, consequently influencing scattering cross-sections **[23]**. Incorporation of Zr cations modifies vibrational modes, leading to shifts in frequencies **[24]**. Surface plasmon resonance effects induced by Zr may amplify local electromagnetic fields, boosting scattering **[25]**. Variations in sample preparation methods, including Zr containing compounds, impact signal intensity **[26]**.

The band situated at 555 cm^{-1} can be assigned to lattice vibrations of Mg–O–Al and Mg–O–Mg stretching in brucite-like layers.**[27, 28]**.

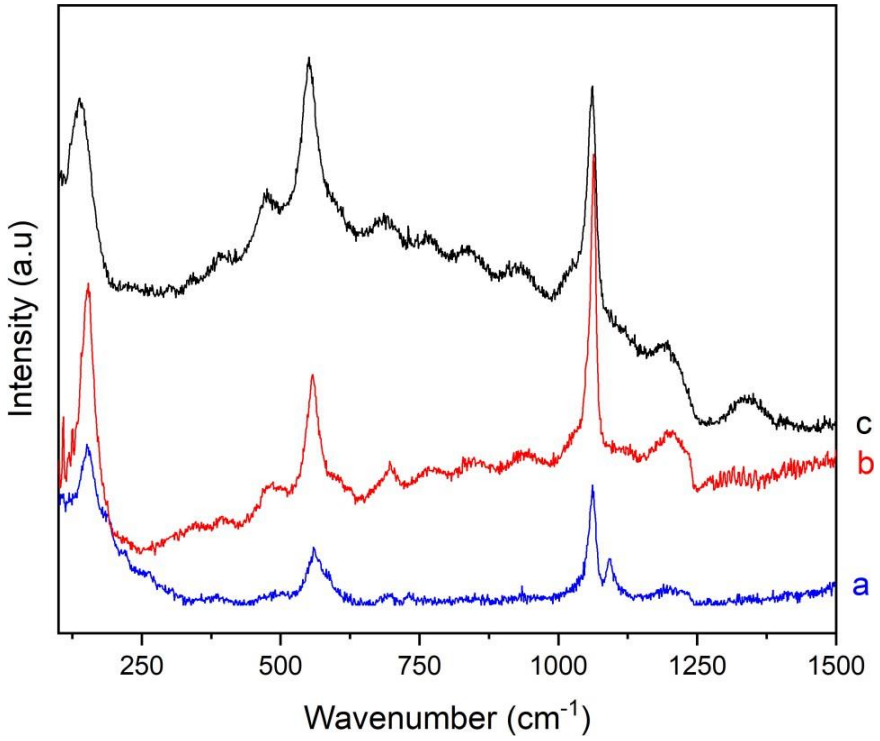

Figure III-2: Raman spectra of $MgAl_2$-LDH (a), $MgAl_2Zr_{4.5}$ -LDH (b), $Zr_{4.5}$-$MgAl_2$-LDH (c).

A new band appearing around 700 cm^{-1} is attributed to the presence of carbonate anions in different environments within the hydrotalcite structure **[29]**.

II.3. Characterization by X-ray Diffraction (XRD)

The X-ray diffraction patterns of the resultant products are illustrated in **Figure III-3**, juxtaposed with the LDH phases intercalated by carbonate ions. The observed phases manifest the characteristic 003 and 110 lines associated with the LDH structure, typified by a hexagonal R-3m lattice with rhombohedral symmetry.

The overall presentation embodies the typical traits of LDH (or hydrotalcite) type materials **[30]**. Notably, intense and symmetrical peaks are discernible at low values of 2θ, complemented by less intense and asymmetrical peaks at higher values of 2θ.

The first two reflections (003) and (006) exhibit relatively high intensity, consistent with previous observations. Their positions in 2θ directly yield the values of the interreticular (interfoliar) distances [$dhkl=d_{(003)} =2d_{(006)}$], consequently providing the parameter of the hexagonal mesh $c(Å)=3d_{(003)}$.

X-ray diffraction (XRD) analysis plays a paramount role in affirming and validating the structural attributes of the synthesized materials on individual substrates. Beyond mere validation, XRD characterization enables comprehensive exploration, affording the capability to determine the

average particle size present on each material. This meticulous analysis significantly augments our understanding of material composition and structure, there by enriching our comprehension of their properties **[31-33]**.

The (110) line, belonging to the (hk0) type, stands out as the sole observable line on the diffractogram. Its angular position allows for the visualization of the arrangement of metal cations within the brucitic sheets and facilitates the calculation of the lattice parameter $a(Å)=2d_{(110)}$, representing the cation–cation distance.

The visibility of the (110) line in the diffractograms depends on several factors, including the nature of the metal cations and their arrangement within the brucitic sheets, as well as the rate of substitution of the divalent metal by the trivalent metal.

Figure III-3 shows the XRD patterns of $MgAl_2$-LDH (a), $MgAl_2Zr_{4.5}$-LDH (b), $Zr_{4.5}$-$MgAl_2$-LDH (c), 0.25%Au/$MgAl_2$-LDH (d) 0.25%Au/$MgAl_2Zr_{4.5}$-LDH (e), 0.25%Au/$Zr_{4.5}$-$MgAl_2$-LDH (f) samples. All samples have sharp and intense peaks situated at 2Θ = 11.67°, 23.38°, 35.05°, 62.94° and 62.23°characteristic of the typical layered double hydroxide structure of MgAl-LDH and corresponding to (003), (006), (009), (110) and (113) planes respectively. Other broad peaks at 2Θ = 39.58° and 47.02° correspond to MgAl-LDH planes (015) and (018) respectively **[15]**. However, no gold characteristic peaks were observed which is mostly due to the very low gold content (0.25%) which might be under the technique detection limit **[34]**.

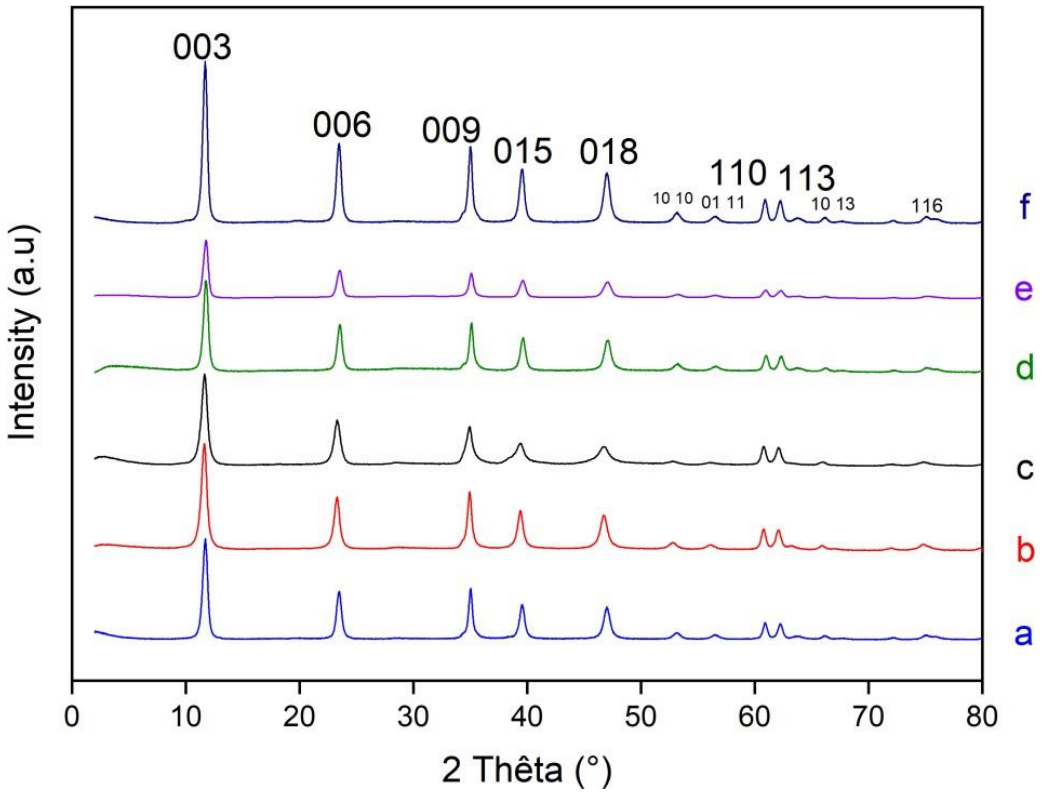

Figure III-3: XRD patterns of $MgAl_2$-LDH (a), $MgAl_2Zr_{4.5}$-LDH (b), $Zr_{4.5}$-$MgAl_2$-LDH (c), 0.25%Au/$MgAl_2$-LDH (d) 0.25%Au/$MgAl_2Zr_{4.5}$-LDH (e), 0.25%Au/$Zr_{4.5}$-$MgAl_2$-LDH (f).

The lattice parameters were calculated as $a = 2 \times {}_{(110)}$ and $c = 3 \times {}_{(003)}$ respectively (**Table III-1**). The (003) values correspond to the basal spacing of two consecutive brucite-like hydroxide layers in the hydrotalcites. Therefore, the interlayer free spacing could be calculated by subtracting the brucite sheet thickness (0.480 nm as reported by **N. Das et al.[35])** from the basal spacing $d_{(003)}$.Further analysis of the XRD patterns revealed some differences in the unit cell parameters among the three samples. Addition of Zr to $MgAl_2$-LDH leads to a slight variation of the "c" parameter with both synthesis techniques, while the "a" parameter remains constant. Indeed, the "c" parameter decreases with the one-pot preparation method and slightly increases with the impregnation method. This indicates that Zr was deposited in the LDH interlayer space in the $Zr_{4.5}$-$MgAl_2$-LDH sample. These results also may be explained by a Zr-induced distortion of the ordered layered structure when compared to MgAl hydrotalcite **[63]**.

Table III-1: Lattice parameters of materials.

Lattice parameters	d (110)	a (Å)	d (003)	c (Å)
$MgAl_2$-LDH	1.52	3.04	7.53	22.60
$MgAl_2Zr_{4.5}$-LDH	1.51	3.02	7.36	22.09
$Zr_{4.5}$-$MgAl_2$-LDH	1.51	3.03	7.49	22.70
0.25%Au/$MgAl_2$-LDH	1.52	3.04	7.54	22.62
0.25%Au/$MgAl_2Zr_{4.5}$-LDH	1.52	3.04	7.59	22.78
0.25%Au/$Zr_{4.5}$-$MgAl_2$-LDH	1.42	2.85	7.06	21.18

The addition of Au to $MgAl_2$-LDH and Zr-modified $MgAl_2$-LDHhas no influence on the crystallographic parameters. This suggests that Au was deposited on the surface of these supports. However, it is worth signalling the 0.25%Au/$Zr_{4.5}$-$MgAl_2$-LDH catalyst, where both "a" and "c" parameters decrease upon gold addition. These results suggest the presence of a strong interaction between Au, Zr, Mg and Al but they do not necessarily indicate the position of Au deposition since Zr can move by interaction with Au **[9]**. It was reported in the literature that the isomorphic replacement of Al^{3+} (ionic radius, 0.053nm) and/or Mg^{2+} (ionic radius, 0.065nm) by Zr^{4+} leads to an increase of the "a" parameter since Zr^{4+} (ionic radius, 0.072 nm) are bigger **[36]**. In our case, there was a decrease of both "a" and "c" parameters, which could be explained by the creation of vacancies in the LDH lattice upon addition of gold. As Au^{3+} (ionic radius, 0,085nm) are also bigger, the substitution of Al^{3+} and/or Mg^{2+} by $Au^{3+}$is ruled out as it would result in an increase of the lattice parameters.

II.4. Atomic Absorption Spectroscopy

Gold metal loadings for 0.25%Au/$MgAl_2$-LDH, 0.25Au/$MgAl_2Zr_{4.5}$-LDH and 0.25%Au/$Zr_{4.5}$-$MgAl_2$-LDH catalysts were measured by Atomic Absorption Spectroscopy (AAS) in order to check

the efficiency of the UDP method to deposit gold on $MgAl_2$-LDH, $MgAl_2Zr_{4.5}$-LDH and $Zr_{4.5}$-$MgAl_2$-LDH.

Results reported in **Table III-2** show good agreement between the theoretical and experimental gold loadings for most samples. However, in the case of the 0.25% Au/$MgAl_2Zr_{4.5}$-LDH catalyst, there is a discrepancy that can be explained by the presence of Zr, which could interfere with the incorporation or dispersion of gold in the layered double hydroxide matrix, possibly due to chemical interactions between these two elements.

Table III-2: Gold loadings as measured by atomic absorption spectroscopy (AAS).

Catalysts	Theoretical Au content (wt-%)	Experimental Au content (wt-%)
0.25%Au/$MgAl_2$-LDH	0.25	0.20 ± 0.02
0.25%Au/$MgAl_2Zr_{4.5}$-LDH	0.25	0.16 ± 0.02
0.25%Au/$Zr_{4.5}$-$MgAl_2$-LDH	0.25	0.24 ± 0.02

II.5. Characterization by adsorption-desorption of N_2

The textural attributes of Au/LDH type MgAl, modified by Zr, are evaluated through nitrogen adsorption-desorption isotherms, following the BET method detailed in Chapter II. This method is rooted in the analysis of porous materials and the determination of their specific surface area. The nitrogen adsorption and desorption isotherms of Au/LDH Type MgAl materials, modified by Zr, are depicted in **Figure III-4**.

Figure III-4a shows a N_2 adsorption–desorption isotherm representative of those of all samples. In fact, all isotherms are of type IV according to the IUPAC classification, and they all exhibit H3 type hysteresis loops, indicating the presence of mesopores in the form of slits in the samples **[37-39]**.

Figure III-4b shows the pores sizes distributions for all samples, showing strong heterogeneity in sizes, ranging from 2 to 50 nm.

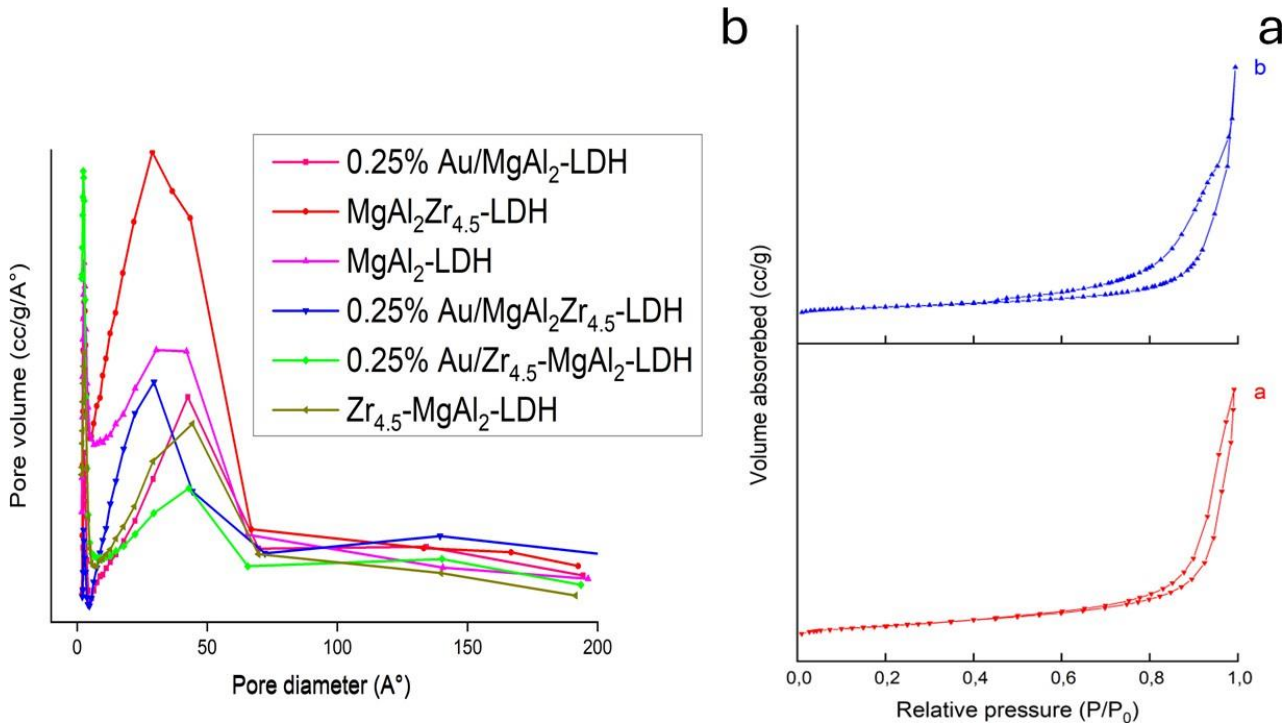

Figure III-4: N_2 adsorption–desorption isotherms $MgAl_2Zr_{4.5}$-LDH (a), 0.25%Au/$MgAl_2Zr_{4.5}$-LDH (b) and Figure III-15b: Pore size distribution of different materials.

It should be noted that the specific surface of $MgAl_2$-LDH which is 132m^2/g has substantially increased after addition of Zr by impregnation on $MgAl_2$-LDH whereas it decreases when Zr was introduced during the preparation of the LDH (**Table III-3**). This is in agreement with XRD results which indicate that in the first case Zr can occupy pillar positions between the LDH sheets.

The deposition of Au systematically induces a decrease in the specific surface area, which can be linked to an agglomeration of the LDH sheets during their basic treatment during the UPD method.

Table III-3: Porous structure characterization of different catalysts

Catalysts	S_{BET}(m^2/g)	V_p (cm^3/g) [1]	D_p (nm) [1]
$MgAl_2$-LDH	132	0.74	24
$MgAl_2Zr_{4.5}$-LDH	88	0.5	27
Zr-$MgAl_2$-LDH	158	1.05	27
0.25%Au/$MgAl_2$-LDH	55	0.61	41
0.25%Au/$MgAl_2Zr_{4.5}$-LDH	59	0.7	43
0.25%Au/$Zr_{4.5}$-$MgAl_2$-LDH	96	0.5	24

[1]Pore volume diameters determined from BJH method[3]

II.6. Characterization by UV-Visible diffuse reflection (UV-Vis/RD)

Diffuse reflectance DRUV-VIS spectroscopy was used to study the environment of metallic ions in the samples. **Figure III-5** shows the deconvoluted spectra of all materials and **Table III-4** summarizes the peaks centers of all deconvoluted spectra.The six spectra show characteristic bands of $MgAl_2$-LDH. These bands are slightly affected after addition of Zr and Au. In addition, a new band at 211-215 nm appears after addition of Zr. This is assigned to Zr^{4+} species **[40]**. Finally, the three materials containing Au (0.25%Au/$MgAl_2$-LDH, 0.25%Au/$MgAl_2Zr_{4.5}$-LDH and 0.25%Au/$Zr_{4.5}$-$MgAl_2$-LDH) exhibit bands at 522, 520 and 526 nm that are related to the gold plasmon resonance, characteristic of metallic nanoparticles. These results confirm on one hand, the introduction of Zr in the form of Zr^{4+}, and on the other hand, the deposition of Au^0 NPs.

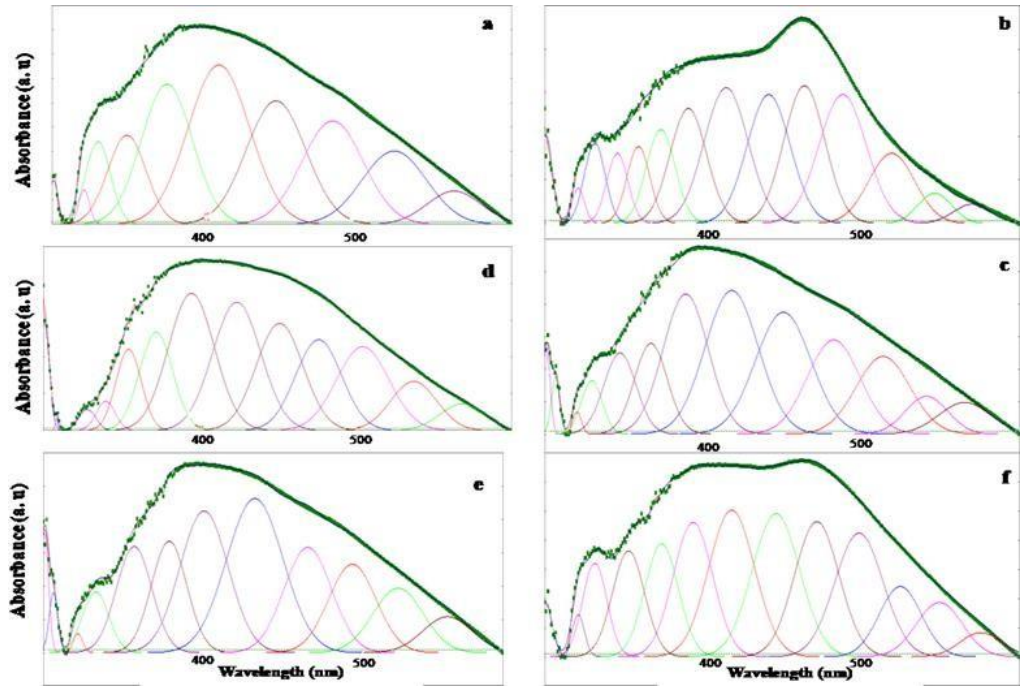

Figure III-5: DRS UV-vis spectra of $MgAl_2$-LDH (a), 0.25%Au/$MgAl_2$-LDH (b), $MgAl_2Zr_{4.5}$-LDH (c), 0.25%Au/$MgAl_2Zr_{4.5}$-LDH (d), $Zr_{4.5}$-$MgAl_2$-LDH (e), 0.25%Au/$Zr_{4.5}$-$MgAl_2$-LDH (f).

Table III-4: Peak centers of deconvoluted DRS-UV visible spectra.

	$MgAl_2$-LDH	$MgAl_2Zr_{4.5}$-LDH	Zr-$MgAl_2$-LDH	Au/ $MgAl_2$-LDH	Au/$MgAl_2Zr_{4.5}$-LDH	Au/Zr-$MgAl_2$-LDH
Peak center	202	201	200	200	200	203
	-	212	215	-	211	213
	248	243	250	252	241	246
	283	296	280	289	266	268
	339	342	357	346	341	357
	405	400	409	392	403	405
	475	474	479	454	464	464
	-	-	-	522	520	526
	-	-	-	-	-	-
	549	550	561	-	-	-
	-	-	-	590	575	586
	630	632	643	659	640	655
	710	715	722	722	712	726
	800	800	800	800	797	800

II.7. Characterization by Electron Microscopy

In order to visualize the surface and morphology of the materials prepared at a nanometre scale, particularly the shape of LDH and the sizes and distributions of Au particles, characterization by electron microscopy was undertaken. Thus, depending on the materials characterized and the information sought, three electron microscopy methods were used, in this case scanning electron microscopy (SEM), transmission electron microscopy (TEM) and High-Angle Annular Dark-Field Scanning Transmission Electron Microscopy (HAADF-STEM)

II.7.1. Characterization by Scanning Electron Microscopy (SEM)

The scanning electron microscopy (SEM) was performed on the MgAl-LDH and Zr-modified MgAl-LDH samples (**Figure III-6**). The corresponding SEM images show that the morphologies of LDH strongly depend on the composition of the matrices.

The formation of hydrotalcite by this preparative route has been confirmed by SEM (**Figure III-6**), where the “sand rose” characteristic morphology of hydrotalcite materials has been observed for all samples.

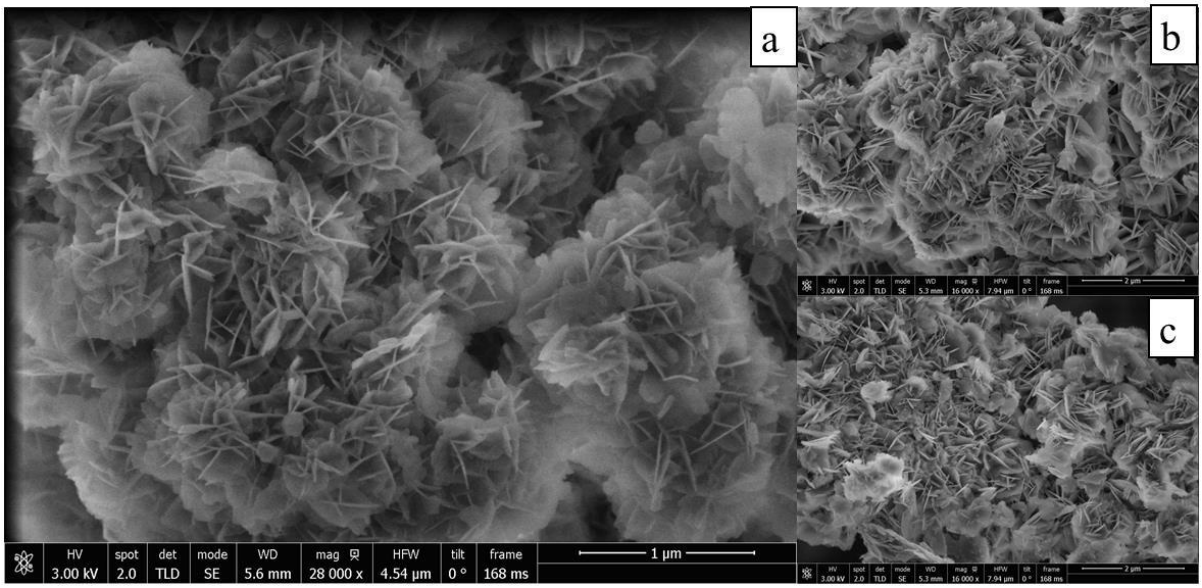

Figure III-6: SEM images of $MgAl_2$-LDH (a), $MgAl_2Zr_{4.5}$-LDH (b) and $Zr_{4.5}$-$MgAl_2$-LDH (c).

II.7.2. Characterization by Transmission Electron Microscopy (TEM) and High-Angle Annular Dark-Field Scanning Transmission Electron Microscopy (HAADF-STEM)

Electron microscopy, particularly in HAADF-STEM (High-Angular Annular Dark Field was used to collect information on the spatial distribution of elements and particle size.

In HAADF-STEM mode, images for each material, namely 0.25%Au/$MgAl_2$, 0.25%Au/$MgAl_2Zr_{4.5}$, and 0.25%Au/$Zr_{4.5}$-$MgAl_2$, with identical magnifications, were examined. These observations highlighted a uniform distribution of gold (Au) over the entire supports.

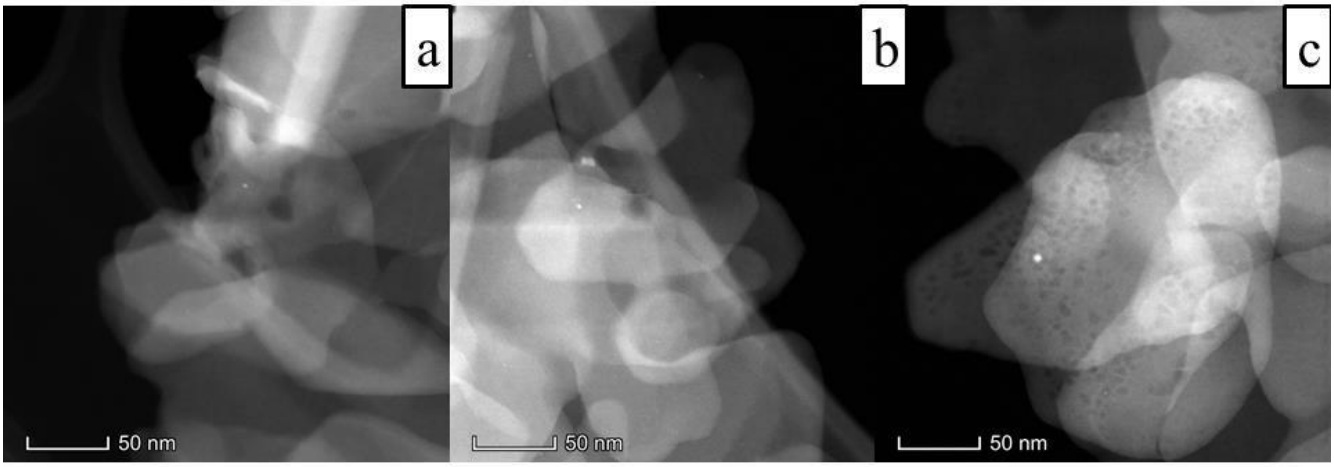

Figure III-7: HAADF-STEM images of 0.25% Au/$MgAl_2$-LDH (A) 0.25% Au/$MgAl_2Zr_{4.5}$-LDH (B) and 0.25% Au/$Zr_{4.5}$-$MgAl_2$-LDH.

Furthermore, a statistical analysis of the Au particle sizes was carried out. The results of this analysis are reported in **Figure III-7** as the gold nanoparticles size distribution.

It appears that the size of the Au nanoparticles ranges from 1 nm to 19 nm with an average size of 6.8 nm in $MgAl_2$-LDH. After addition of Zr by post-synthesis impregnation, the range of Au particle sizes is slightly shifted towards 3 nm to 19 nm with an average size of 8.2 nm in the $Zr_{4.5}$-$MgAl_2$-LDH material. However, the introduction of Zr during the synthesis of LDH drastically reduces the sizes of the Au particles. Thus, the sizes of the Au particles in the $MgAl_2Zr_{4.5}$-LDH material range from 0.5 nm to 5 nm with an average size of 1.2 nm. Note that almost 50% of the particles have sizes less than 1 nm and therefore sub-nanometre dimensions.

This reduction in particle size may be attributed to the interaction between the gold and zirconium during synthesis, which can promote a more uniform dispersion of Au nanoparticles and possibly hinder the growth of the gold particles. This can also explain the discrepancies observed in the Au loading as reported in **Table III-2**. While the theoretical Au content for all catalysts was set at 0.25 wt%, the experimental Au content was found to be lower than expected for the $MgAl_2Zr_{4.5}$-LDH catalyst (0.16 wt% compared to 0.20 wt% for 0.25%Au/$MgAl_2$-LDH and 0.24 wt% for 0.25%Au/$Zr_{4.5}$-$MgAl_2$-LDH). The presence of Zr could interfere with the incorporation or dispersion of gold in the LDH matrix, leading to a lower than expected gold content in the catalyst, which is consistent with the observed reduction in Au nanoparticle sizes.

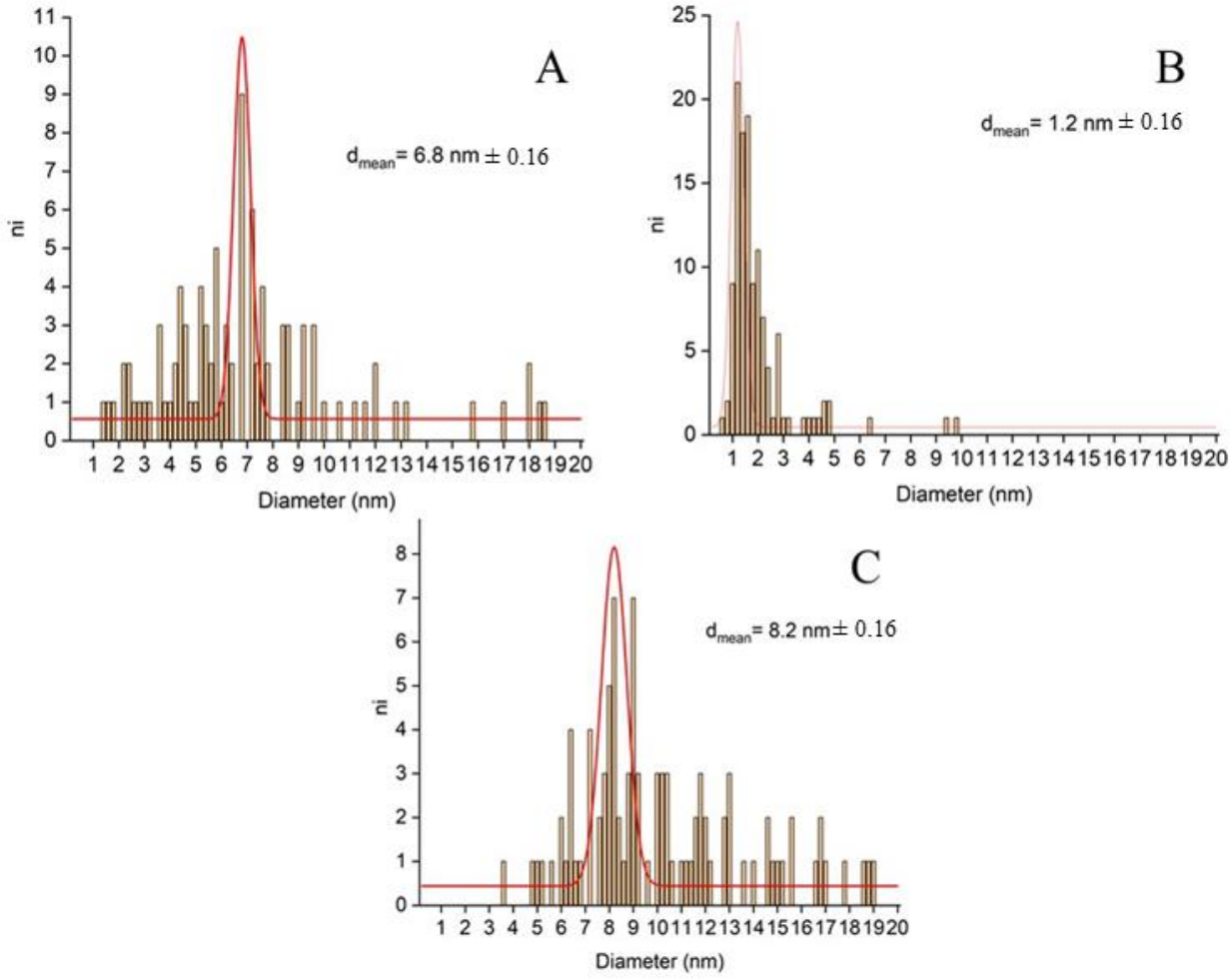

Figure III-8: Gold nanoparticles size distribution for 0.25%Au/ $MgAl_2$-LDH (A) 0.25%Au/ $MgAl_2Zr_{4.5}$-LDH (B) and 0.25%Au/ $Zr_{4.5}$-$MgAl_2$-LDH (C).

III. Catalytic tests

The catalytic performances of all materials in the furfural oxidation by H_2O_2 were tested as described in the Experimental section.

As a reminder, the products of the oxidation reaction of furfural by H_2O_2 and the operating conditions are shown in the **Scheme III-1**.

The oxidation of furfural was carried out using hydrogen peroxide (H_2O_2) as the oxidant, instead of oxygen (O_2), which is commonly used for this type of reaction. The choice of H_2O_2 was motivated by its increased selectivity, allowing better control over the reaction and minimization of unwanted side products. In addition, H_2O_2 is easier to handle and presents fewer risks compared to the use of pure oxygen.

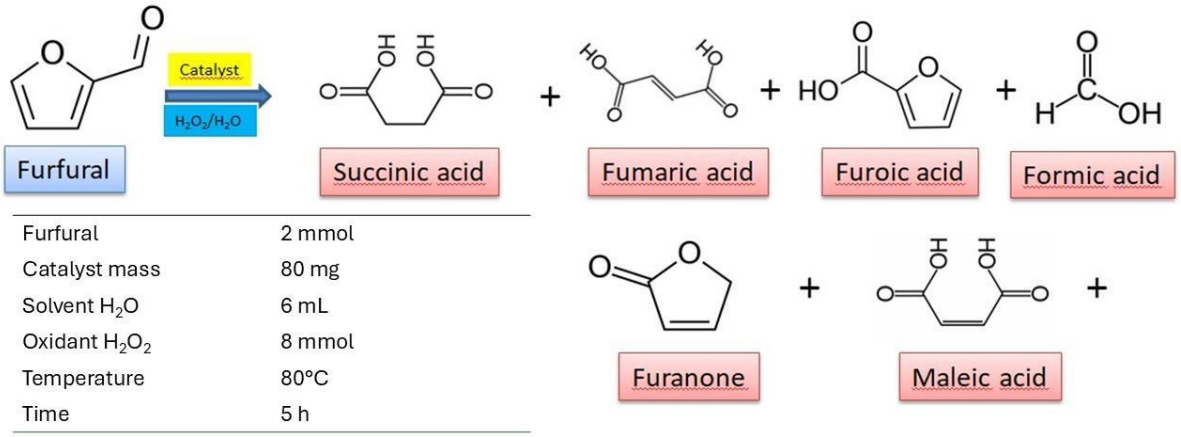

Furfural	2 mmol
Catalyst mass	80 mg
Solvent H_2O	6 mL
Oxidant H_2O_2	8 mmol
Temperature	80°C
Time	5 h

Scheme III-1: Distribution of Furfural oxidation reaction products and the operating conditions.

A blank test was registered by running the reaction without catalyst (**Figure III-9**). In this case, conversion reached 14% after 5h (**Table III-5**). Furoic acid (59% selectivity) and succinic acid (25% selectivity) are the main products. Smaller amounts of fumaric and maleic acids were detected as well (9 and 7% selectivity, respectively). This first result shows a very low chemical reactivity of furfural with H_2O_2, due to the oxidizing ability of H_2O_2 and the thermal effect.

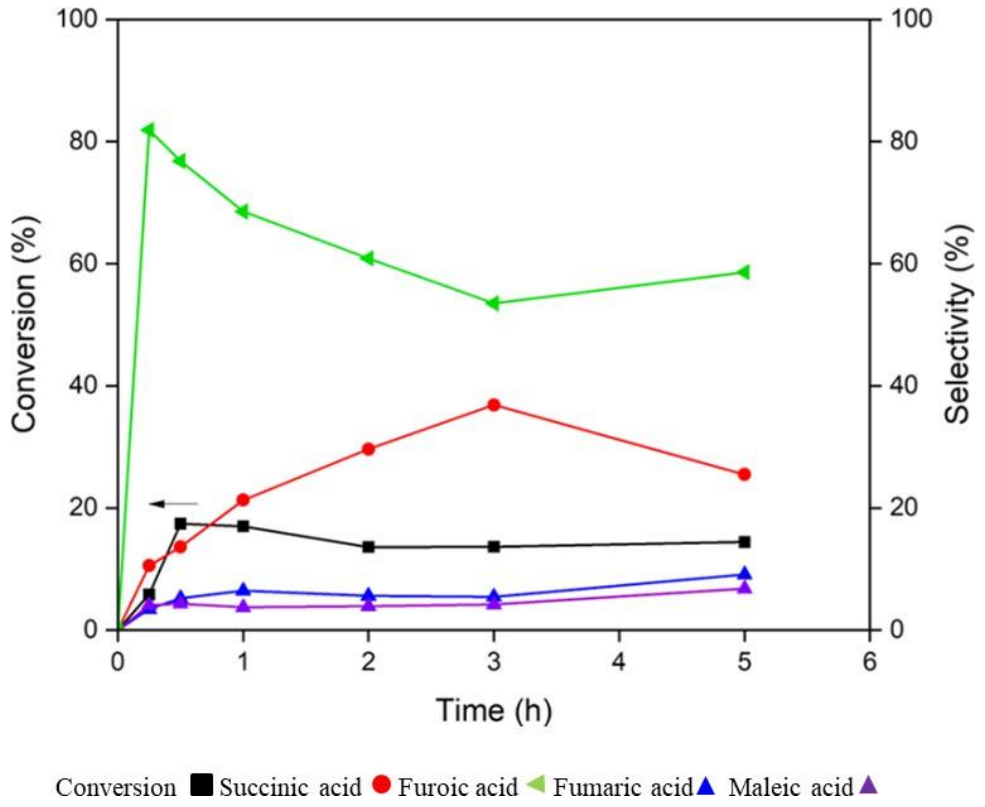

Figure III-9: Blank test: Conversion and product distribution for furfural oxidation without catalyst.

In **Figure III-10a** are reported the reaction results (furfural conversion and products distribution), with $MgAl_2$-LDH as catalyst. It shows a gradual increase of conversion over time, reaching up to 66% after 5 hours of reaction. Moreover, the selectivity which initially was directed towards furoic acid, changes over time and after 5 hours, succinic, furoic and fumaric acids were produced in equivalent quantities while maleic acid was not detected.

These results evidence the catalytic efficiency of $MgAl_2$-LDH improving the conversion from 14 to 66%. Moreover, the evolution of selectivity over time shows that the furoic acid is a primary product which is further transformed into succinic and fumaric acids.

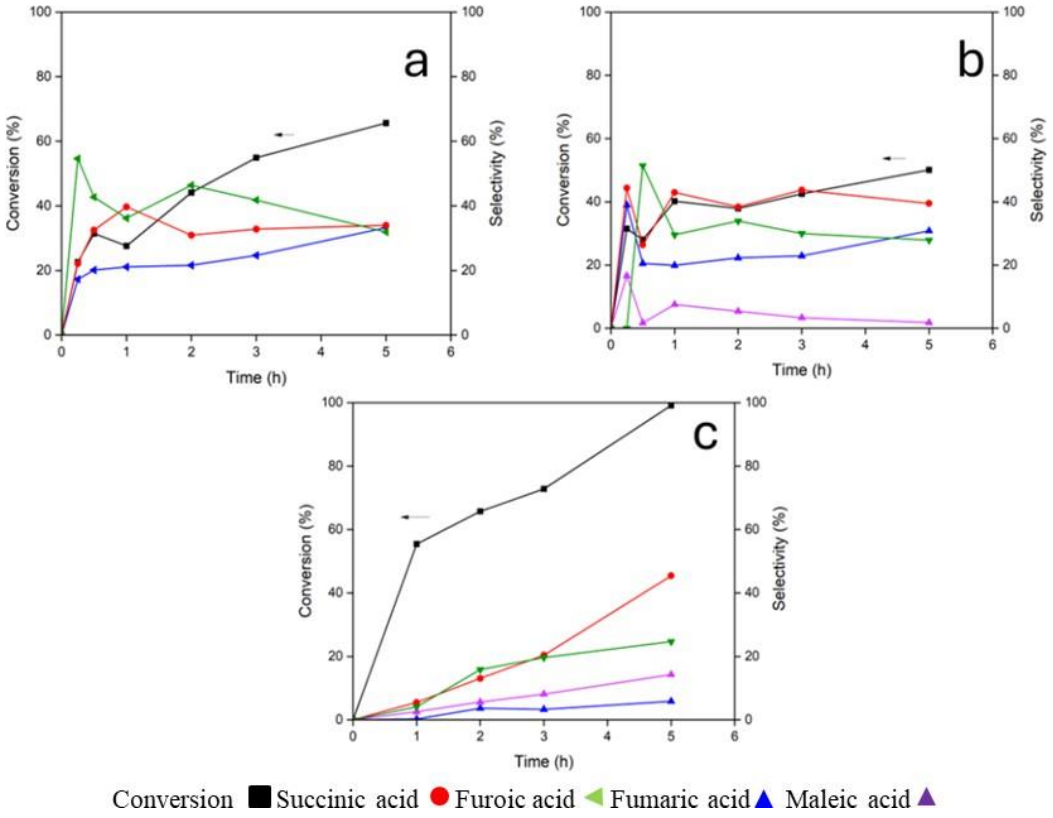

Figure III-10: Conversion and product distribution for furfural oxidation using $MgAl_2$-LDH (a), $MgAl_2Zr_{4.5}$-LDH (b) and $Zr_{4.5}$-$MgAl_2$-LDH (c)

III.1. Influence of Zr

Figure III-10b and **10c** show the effect of Zr on the activity and selectivity depending on the synthesis method. In one hand, **Figure III-10b** representing the results of the reaction with $MgAl_2Zr_{4.5}$-LDH as catalyst (one pot synthesis) shows that the introduction of Zr in $MgAl_2$-LDH during LDH synthesis does not bring any improving of the catalytic activity. Instead, the conversion drops from 66 to 50 %. Moreover, no particular effect on the furoic, succinic and fumaric acids selectivities is shown. (**Table III-5**).

In the other hand, Zr has an extremely beneficial effect on the activity $MgAl_2$-LDH when it is

added post-synthesis. In fact, the results reported on **Figure III-10c** show that with the $Zr_{4.5}$-$MgAl_2$-LDH catalyst, conversion reaches 99% with a selectivity of 45% towards succinic acid (**Table III-5**) after 5 hours.

This result suggests that the Zr introduced in post-synthesis would act as a metallic active site on the surface, thus increasing the number of active sites. However, this effect is not brought by Zr when it is introduced during the synthesis of LDH because it integrates the crystal structure of LDH as was shown by FTIR, Raman and XRD characterizations.

It is worth mentioning that when using Zr-containing catalysts, a small amount of maleic acid is generated, despite succinic acid being the main product. Maleic acid and succinic acid share a similar structure (**Scheme III-1**) differing only in the presence of a C=C double bond. The incorporation of Zr into layered double hydroxides (LDH) and the consequent production of maleic acid can be attributed to various factors. Firstly, Zr might catalyze secondary reactions such as the dehydration or isomerization of succinic acid into maleic acid. Additionally, the presence of Zr could result in the formation of specific reaction intermediates or by-products, including maleic acid, within the LDH during the reaction process.

III.2. Influence of gold nanoparticles

Figure III-11 presents conversions and product distributions of the three catalysts containing gold nanoparticles: Au/$MgAl_2$-LDH (a), Au/$MgAl_2Zr_{4.5}$-LDH (b), and Au/$Zr_{4.5}$-$MgAl_2$-LDH(c).

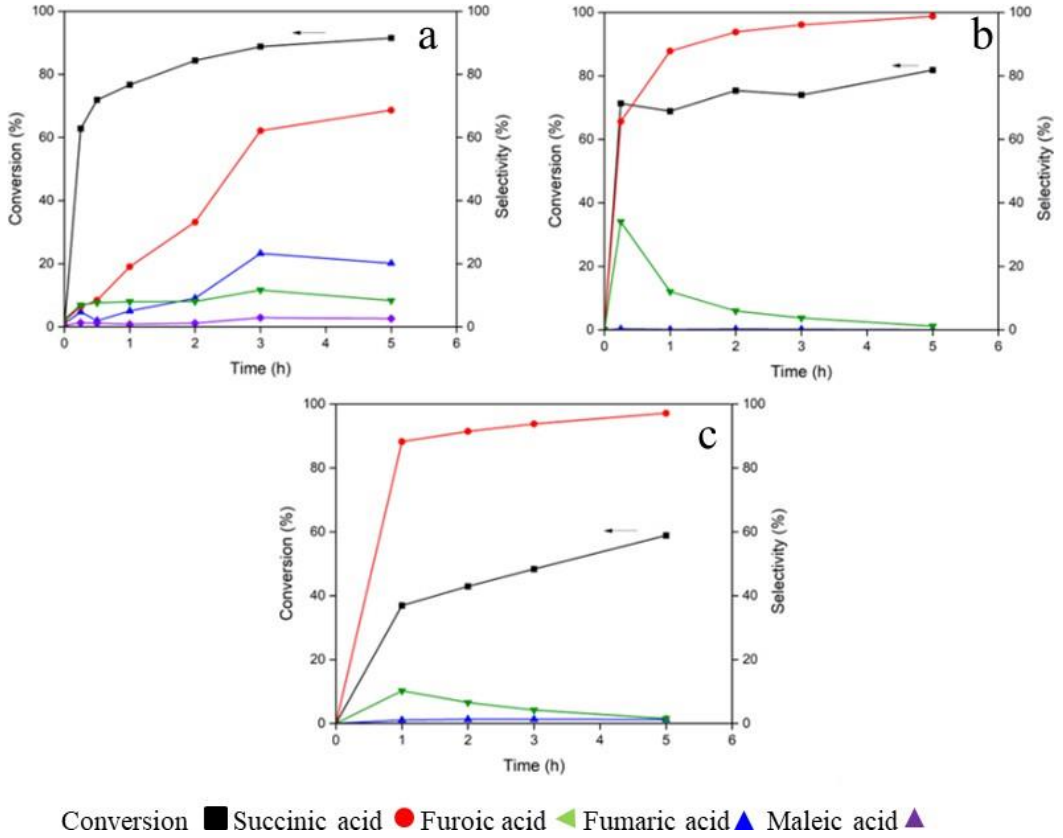

Figure III-11: Conversion and product distribution for furfural oxidation using 0.25%Au/$MgAl_2$-LDH (a), 0.25%Au/$MgAl_2Zr_{4.5}$-LDH (b) and 0.25%Au/$Zr_{4.5}$-$MgAl_2$-LDH (c).

In the case of Au/$MgAl_2$-LDH, the results clearly show the promoting effect of gold nanoparticles on activity and selectivity. Indeed, the conversion is very high from the beginning of the reaction and reaches 92% after 5 hours. In addition, the selectivity towards succinic acid is improved up to 70%. This beneficial effect of gold nanoparticles is also observed in the case of the Au/$MgAl_2Zr_{4.5}$-LDH catalyst, as evident in **Figure III-11b** and **Table III-5**, where the conversion exhibits remarkable stability throughout the evolution of the reaction, remaining consistently above 70% within the initial 15 minutes. In this case as well, the reaction is clearly oriented towards succinic acid with selectivity close to 70% right from the beginning and reaches 99% after 5 hours. Finally, with Au/$Zr_{4.5}$-$MgAl_2$-LDH (**Figure III-11c**, **Table III-5**) there is an unexpected decline in conversion when compared to the gold-free LDH (59 vs.99%).That might be related to the structural modification observed upon XRD characterization, where this sample was the only material with a decrease in the "a" and "c" parameters, result of the creation of structure vacancies in the LDH lattice. This catalyst also contains the biggest gold particles size (8.2nm) that may be less active than the smaller ones (1.2 nm in the case of Au/$Zr_{4.5}$-$MgAl_2$-LDH). Nevertheless, the effect of gold nanoparticles on selectivity is clearly shown. Indeed, within the first hour of reaction, the selectivity towards succinic acid is over 90% and reaches 97% at the end of the reaction.

The results reported in **Table III-5** clearly evidence a positive synergy between gold and zirconium, as a significant enhancement of the reaction selectivity towards succinic acid in observed with both Au-based Zr-doped catalysts (**Table III-5**, lines 6 and 7).

Table III-5: Furfural conversion and products selectivity after 5 hours of reaction.

	Conversion (%)	**Selectivity (%)**			
		SA	FuA	FmA	MA
Blank reaction	14	25	59	9	7
$MgAl_2$-LDH	66	34	33	32	0
$MgAl_2Zr_{4.5}$-LDH	50	39	28	30	2
$Zr_{4.5}$-$MgAl_2$-LDH	99	45	25	6	14
0.25%Au/$MgAl_2$-LDH	92	69	8	20	2
0.25%Au/$MgAl_2Zr_{4.5}$-LDH	**84**	**99**	**1**	**0**	**0**
0.25%Au/$Zr_{4.5}$-$MgAl_2$-LDH	59	97	2	1	0

SA: Succinic Acid, FuA: Furoic Acid, FmA: Fumaric Acid, MA: Maleic Acid.

Table III-6: Conversion of Furfural to Succinic Acid in the literature.

Catalyst	Oxidant used	Furfural conversion (%)	S.A Selectivity (%)	Reaction's temperature	Reference
Amberlyst-15	H_2O_2	≥99	74	80°C/24h	[41]
Nb_2O_5	H_2O_2	≥99	25	80°C/24h	
ZSM-5	H_2O_2	≥99	17	80°C/24h	
ZrO_2	H_2O_2	≥99	17	80°C/24h	
SO_4/ZrO_2	H_2O_2	97	10	80°C/24h	
Au/C	H_2O_2	98	25	110 °C/4h N_2 pressure = 1 bar	[42]
SO_3H-CD-Carbon	H_2O_2	99	80	60°C/1h	[43]
Amberlyst-35	H_2O_2	99	78	60°C/1h	
Cobalt-Porphyrin on CNT-NH_2	O_2	60	89	100°C/ 20h.	[44]
Amberlyst-15	O_2	93	/	100 °C, 20h.	[45]
Hydrotalcite-Supported Gold Nanoparticles	O_2	100	/	150°C/4h	[46]
0.25%Au/$MgAl_2Zr_{4.5}$-LDH	**H_2O_2**	**84**	**99**	**80°C/5h**	**Present work**

Table III-6 shows a comparative analysis of different catalysts reported in the literature for the conversion of furfural to succinic acid highlights the outstanding performances of the catalyst developed in the present work. With an 84% conversion, 0.25%Au/MgAl2Zr4.5-LDH is the only catalyst achieving a total selectivity towards succinic acid production. In comparison, the other catalysts with total conversion (≥99%), such as Amberlyst-15, Amberlyst-35 and SO3H-CD-Carbon, show lower selectivity, not exceeding 80%. From an industrial point of view, total selectivity means an important cost reduction as no separation steps will be required for the reaction products. This

suggests a promising advancement in catalyst development, with significant potential to enhance the production of succinic acid from furfural.

By incorporating these insights into Table III-6, a clearer understanding emerges regarding how reaction conditions impact the catalytic performance of each material. The table now compares conversion rates alongside critical experimental factors, such as oxidant amount, which influence the selectivity of each catalyst. This enhanced comparison highlights the strong correlation between conversion and selectivity, offering valuable insights into the advantages of the 0.25%Au/$MgAl_2Zr_{4.5}$-LDH catalyst in achieving both high conversion and excellent selectivity for succinic acid. Such a detailed comparison emphasizes the catalyst's potential for industrial applications, where high selectivity is key to reducing downstream separation costs and improving overall process efficiency.

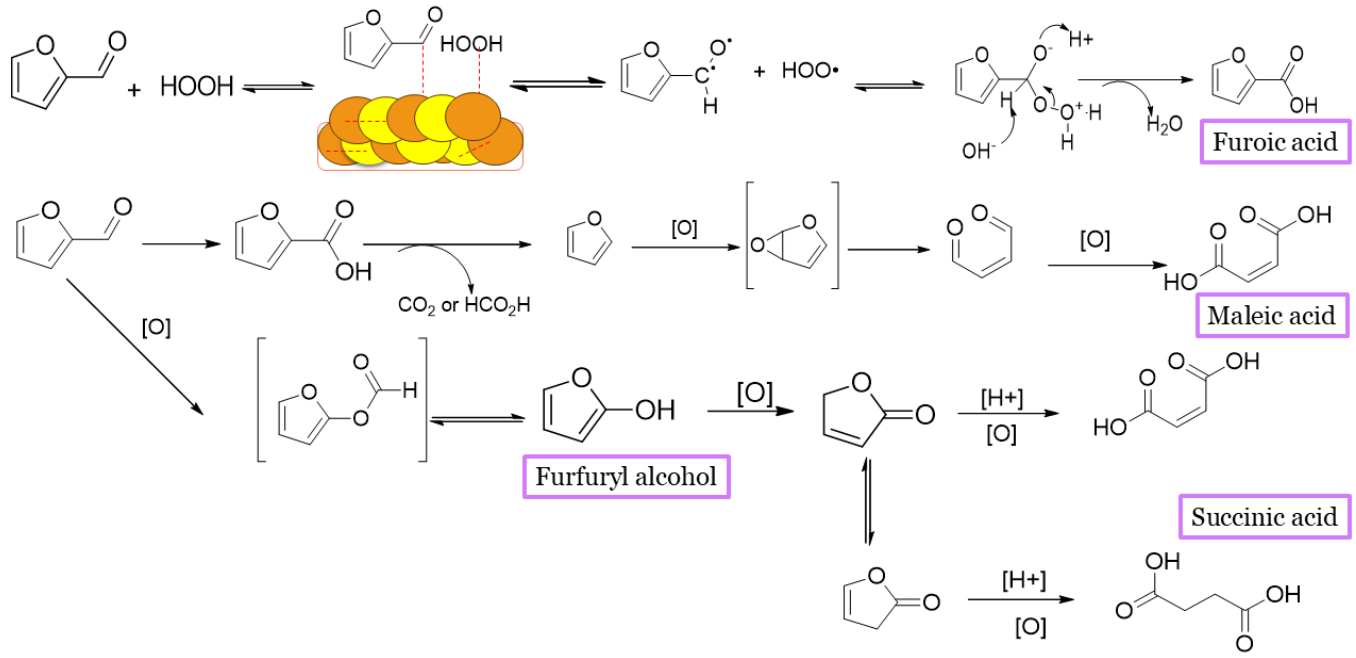

Scheme III-2: The proposed mechanism illustrates the stepwise oxidation of furfural to succinic acid, catalyzed by gold nanoparticles on LDH materials.

IV. Conclusions

This work focuses on the valorization of lignocellulosic biomass as a renewable raw material for producing high value-added chemicals. It aims to develop an eco-friendly and economically viable process for synthesizing succinic acid from biomass-derived furfural using heterogeneous catalysis, instead of petroleum derivatives.

The study develops catalysts based on gold nanoparticles (Au NPs) supported on layered double hydroxides (LDHs) modified with zirconium (Zr). Specifically, MgAl-LDHs were prepared and modified with Zr either during synthesis or post-synthesis. Zr modification during synthesis embeds Zr in the crystallographic structure, while post-synthesis modification embeds Zr in the inter-layer space, serving as pillars. These structural differences influence the catalytic behavior of these

materials.

When combined with Au NPs, the catalysts showed excellent selectivities ≥ 97%, in particular with 0.25% Au/$Zr_{4.5}$-$MgAl_2$-LDH and 0.25% Au/$MgAl_2Zr_{4.5}$-LDH. The best performances were achieved with 0.25% Au/$MgAl_2Zr_{4.5}$-LDH, reaching an 84% conversion and 99% selectivity, which evidence a positive synergy between Zr and Au NPs.

The study paves the way for a sustainable, economically viable process for the production of succinic acid from renewable biomass.

In the other hand, one of the most important results of this study is the development of a catalyst preparation method ensuring the formation of Au particles of sub-nanometre dimensions. In fact, the introduction of Zr during the synthesis of LDH allows us to prepare a support favouring the formation of very small Au nanoparticles.

References

[1] M.J. Hernandez-Moreno, M.A. Ulibarri, J. Rendon and C.J. Serna, Physics and Chemistry of Minerals, 12 (1985) 34.

[2] V. Rives and S. Kannan, Journal of Materials Chemistry, 10 (2000) 489.

[3] I.I. Soykal, H. Sohn and U.S. Ozkan, Acs Catalysis, 2 (2012) 2335.

[4] H.-y. Zeng, Z. Feng, X. Deng and Y.-q. Li, Fuel, 87 (2008) 3071.

[5] H.-Y. Zeng, S. Xu, M.-C. Liao, Z.-Q. Zhang and C. Zhao, Applied Clay Science, 91 (2014) 16.

[6] Z.-q. Zhang, M.-c. Liao, H.-Y. Zeng, S. Xu, X.-j. Liu, J.-z. Du, P.-h. Zhu and Q.-j. Huang, Applied Clay Science, 102 (2014) 246.

[7] A. Di Bitetto, G. Kervern, E. André, P. Durand and C. Carteret, The Journal of Physical Chemistry C, 121 (2017) 6104.

[8] M. del Arco, R. Trujillano and V. Rives, Journal of Materials Chemistry, 8 (1998) 761.

[9] E. Uzunova, D. Klissurski, I. Mitov and P. Stefanov, Chemistry of materials, 5 (1993) 576.

[10] H.C.B. Hansen, C.B. Koch and R.M. Taylor, Journal of Solid State Chemistry, 113 (1994) 46.

[11] K. Rybka, J. Matusik, A. Kuligiewicz, T. Leiviskä and G. Cempura, Applied Surface Science, 538 (2021) 147923.

[12] R.G.L. Gonçalves, P.A. Lopes, J.A. Resende, F.G. Pinto, J. Tronto, M.C. Guerreiro, L.C.A. de Oliveira, W. de Castro Nunes and J.L. Neto, Applied Clay Science, 179 (2019) 105152.

[13] P.D. Marcato, N.V. Parizotto, D.S.T. Martinez, A.J. Paula, I.R. Ferreira, P.S. Melo, N. Durán and O.L. Alves, Journal of the Brazilian Chemical Society, 24 (2013) 266.

[14] L. Gritsch, C. Lovell, W.H. Goldmann and A.R. Boccaccini, Carbohydrate polymers, 179 (2018) 370.

[15] F. Cavani, F. Trifirò and A. Vaccari, Catalysis today, 11 (1991) 173.

[16] B.K. Theng, G. Lagaly, F. Bergaya, B. Theng and G. Lagaly, Handbook of clay science, Elsevier, 2006.

[17] W.T. Reichle, Solid State Ionics, 22 (1986) 135.

[18] S. Miyata, Clays and Clay minerals, 28 (1980) 50.

[19] M.A. Peña and J.L. Fierro, Chemical reviews, 101 (2001) 1981.

[20] D.P. Debecker, E.M. Gaigneaux and G. Busca, Chemistry–A European Journal, 15 (2009) 3920.

[21] D. Tichit, M.N. Bennani, F. Figueras and J.R. Ruiz, Langmuir, 14 (1998) 2086.

[22] M. Yi, Y. Zhang, J. Xu, D. Deng, Z. Mao, X. Meng, X. Shi and B. Zhao, Nanomaterials, 11 (2021) 2162.

[23] A.-L. Johnston, E. Lester, O. Williams and R.L. Gomes, Journal of Environmental Chemical Engineering, 9 (2021) 105197.

[24] J. Huo, X. Min and Y. Wang, Environmental Research, 194 (2021) 110685.

[25] M. Vargas-Zamarripa, A.A. Rivera, U. Sierra, P. Salas, A.H. Serafín-Muñoz and G. Ramírez-García, Chemosphere, 320 (2023) 138081.

[26] F.C. Jentoft, A. Hahn, J. Kröhnert, G. Lorenz, R.E. Jentoft, T. Ressler, U. Wild, R. Schlögl, C. Häßner and K. Köhler, Journal of Catalysis, 224 (2004) 124.

[27] I.O. Iordanov, V.M. Bermudez and C.K. Knox, The Journal of Physical Chemistry C, 122 (2018) 5385.

[28] V.R. Cunha, P.A. Petersen, M.B. Goncalves, H.M. Petrilli, C. Taviot-Gueho, F. Leroux, M.L. Temperini and V.R. Constantino, Chemistry of materials, 24 (2012) 1415.

[29] R.L. Frost, S.J. Palmer and L.M. Grand, Journal of Raman Spectroscopy, 41 (2010) 1797.

[30] L. Pesic, S. Salipurovic, V. Markovic, D. Vucelic, W. Kagunya and W. Jones, Journal of Materials Chemistry, 2 (1992) 1069.

[31] I.J. Dávila, M. Rosset, O.P. Lopez and L.A. Féris, Revista internacional de contaminación ambiental, 36 (2020) 443.

[32] A. Zaghloul, R. Benhiti, A. Soudani, M. Chiban, M. Zerbet and F. Sinan, Mediterranean Journal of Chemistry, 9 (2019) 155.

[33] T.P.F. Teixeira, S. Aquino, S. Pereira and A. Dias, Brazilian journal of chemical engineering, 31 (2014) 19.

[34] J. Thuriot-Roukos, R. Khadraoui, S.b. Paul and R. Wojcieszak, ACS omega, 5 (2020) 14283.

[35] N. Das and R. Das, Applied Clay Science, 42 (2008) 90.

[36] N. Das, J. Konar, M. Mohanta and S. Srivastava, Journal of colloid and interface science, 270 (2004) 1.

[37] N.D. Hutson, S.A. Speakman and E.A. Payzant, Chemistry of materials, 16 (2004) 4135.

[38] S.K. Yun and T.J. Pinnavaia, Chemistry of materials, 7 (1995) 348.

[39] G. Zi, Z. Yan, Y. Wang, Y. Chen, Y. Guo, F. Yuan, W. Gao, Y. Wang and J. Wang, Carbohydrate polymers, 115 (2015) 146.

[40] H. Cao, X. Qiu, B. Luo, Y. Liang, Y. Zhang, R. Tan, M. Zhao and Q. Zhu, Advanced Functional Materials, 14 (2004) 243.

[41] H. Choudhary, S. Nishimura and K. Ebitani, Applied Catalysis A: General, 458 (2013) 55.

[42] M.L. Granados, J. Moreno, A. Alba-Rubio, J. Iglesias, D.M. Alonso and R. Mariscal, Green Chemistry, 22 (2020) 1859.

[43] P. Maneechakr and S. Karnjanakom, Energy conversion and management, 154 (2017) 299.

[44] K. Anjali and S. Nishimura, Journal of Catalysis, 428 (2023) 115182.

[45] S. Fulignati, D. Licursi, N. Di Fidio, C. Antonetti and A.M. Raspolli Galletti, Catalysts, 12 (2022) 1664.

[46] Z.-H. Zhang, Z. Sun and T.-Q. Yuan, Transactions of Tianjin University, 28 (2022)

References:

[1] W.T. Reichle, Solid State Ionics, 22 (1986) 135.

[2] M.A. Aramendía, Y. Avilés, V. Borau, J.M. Luque, J.M. Marinas, J.R. Ruiz and F.J. Urbano, Journal of Materials Chemistry, 9 (1999) 1603.

[3] P. Bera, M. Rajamathi, M. Hegde and P.V. Kamath, Bulletin of Materials Science, 23 (2000) 141.

[4] W. Tongamp, Q. Zhang and F. Saito, Journal of materials science, 42 (2007) 9210.

[5] M. Lakraimi, A. Legrouri, A. Barroug, A. De Roy and J.P. Besse, Journal of Materials Chemistry, 10 (2000) 1007.

[6] C. Barriga, M. Gaitan, I. Pavlovic, M. Ulibarri, M. Hermosĩn and J. Cornejo, Journal of Materials Chemistry, 12 (2002) 1027.

[7] V. Kovalenko and V. Kotok, Восточно-Европейский журнал передовых технологий, (2019) 58.

[8] X. Hu, X. Guo, T. Meng, Q. Guo, J. Cheng, Y. Wang, W. Huang and F.T. Ng, Applied Surface Science, (2024) 160705.

[9] X. Yue, Y. Dong, H. Cao, X. Wei, Q. Zheng, W. Sun and D. Lin, Journal of Colloid and Interface Science, 630 (2023) 973.

[10] R. Rojas, M.Á. Ulibarri, C. Barriga and V. Rives, Applied Clay Science, 49 (2010) 176.

[11] J. Keller, F. Dreisbach, H. Rave, R. Staudt and M. Tomalla, adsorption, 5 (1999) 199.

[12] K.S. Sing, Journal of Porous Materials, 2 (1995) 5.

[13] M.a.A. Aramendía, V. Borau, C. Jiménez, J.M. Marinas, J.R. Ruiz and F.J. Urbano, Journal of solid state chemistry, 168 (2002) 156.

[14] A. Vaccari, Applied Clay Science, 22 (2002) 75.

[15] G.J. Hutchings, Catalysis today, 72 (2002) 11.

[16] M. Haruta, The chemical record, 3 (2003) 75.

[17] M. Chen and D. Goodman, science, 306 (2004) 252.

[18] X.Y. Liu, A. Wang, T. Zhang and C.-Y. Mou, Nano Today, 8 (2013) 403.

[19] J.A. Rodriguez and D.W. Goodman, science, 257 (1992) 897.

[20] M. Haruta, Catalysis today, 36 (1997) 153.

[21] A. Corma and H. Garcia, Chemical Society Reviews, 37 (2008) 2096.

[22] G.C. Bond and D.T. Thompson, Catalysis Reviews, 41 (1999) 319.

[23] J.-F. Sun, Q.-Q. Xu, J.-L. Qi, D. Zhou, H.-Y. Zhu and J.-Z. Yin, ACS sustainable chemistry & engineering, 8 (2020) 14630.

[24] S. Yan and S. Zhang, International journal of hydrogen energy, 37 (2012) 9636.

[25] M. Kabbour and R. Luque, Biomass, biofuels, biochemicals, (2020) 283.

[26] Z.P. Xu and G. Lu, Pure and Applied Chemistry, 78 (2006) 1771.

[27] L. Liu and A. Corma, Chemical reviews, 118 (2018) 4981.

Chapter V. Glucose (photo)oxidation over $Au/NiAl_2Zr_{4.5}$ Catalyst

I. Introduction

This chapter is dedicated to the presentation of the results of work carried out as part of an internship in the laboratory of "Laboratory of Reactivity and Chemistry of Solids (LRCS), UMR CNRS 7314, University of Picardy Jules Verne, Energy Hub, 15 rue Baudelocque, FR-80000 Amiens, France". The objective of this internship was to extend the utisation of Au/LDH catalysts for the transformation and valorisation of glucose as a raw material issued from lignocellulosic biomass.

Indeed, among the various organic transformations of carbohydrates, C1-oxidation is particularly important, producing valuable oxidized derivatives like aldonic acids, salts, esters, and lactones, widely used across industries **[1]**. The shift toward renewable chemicals from carbohydrates, which make up 75% of biomass **[2]**, is driven by concerns over fossil resource depletion and pollution. However, traditional synthesis methods for these derivatives often involve harsh reagents, low selectivity, and difficult product separation **[3, 4]**.

Gold nanoparticles (Au NPs) offer a greener alternative, acting as oxidation catalysts with enhanced selectivity and reduced waste **[5-9]**. When supported on layered double hydroxides (LDHs), which provide a high surface area and strong metal-support interactions, these systems can facilitate photocatalytic reactions under mild conditions. The combination of Au NPs and LDHs leverages the plasmonic properties of gold and the basic sites of LDHs, enabling efficient and eco-friendly carbohydrate transformations.

As the aim of this work was to find a direct application of Au/LDH catalysts in the transformation of glucose under photocatalysis conditions, the $0.5\%Au/NiAl_2Zr_{4.5}$-LDH catalyst which had shown very good catalytic performances was chosen to be tested in the synthesis reaction of sodium D gluconate from glucose in the presence of H_2O_2, NaOH and a light source (**scheme V-1**).

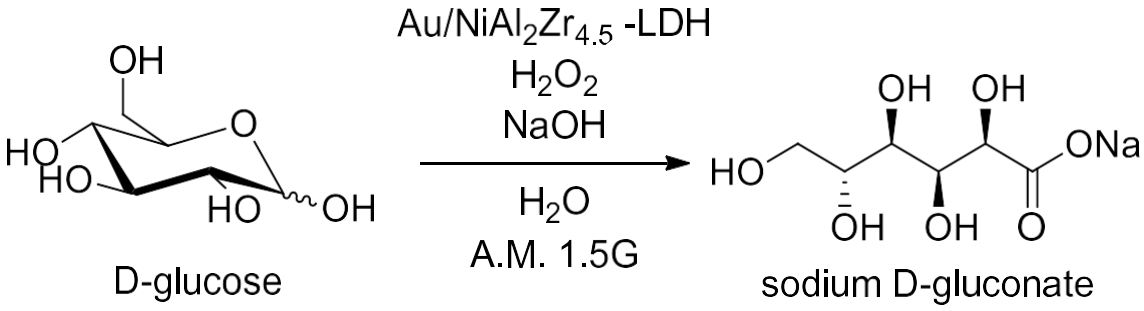

Scheme V-1: The synthesis reaction of sodium D-gluconate from glucose involves the presence of H_2O_2, NaOH, and exposure to a light source.

As the objective of this work was to find a direct application of Au/LDH catalysts in the transformation of glucose under photocatalysis conditions, the $0.5\%Au/NiAl_2Zr$-LDH catalyst which had shown very good catalytic performances was chosen to be tested in the reaction of synthesis of sodium D gluconate from glucose in the presence of H_2O_2, NaOH and a light source (xenon lamp

source paired with an AM 1.5G filter). In a first step the catalyst was characterized by DRUV-visible in order to verify its ability to activate photons. The operating conditions were subsequently developed via a full factorial experimental design method relating to the mass of the catalyst, the amount of H_2O_2, the amount of NaOH and the illumination and reaction time. The glucose concentration and illumination conditions were set according to the work of **[10]**.

Finally, a kinetic monitoring of the reaction with the operating conditions previously developed was carried out with different ways of illuminations.

II. DRUV-visible characterization

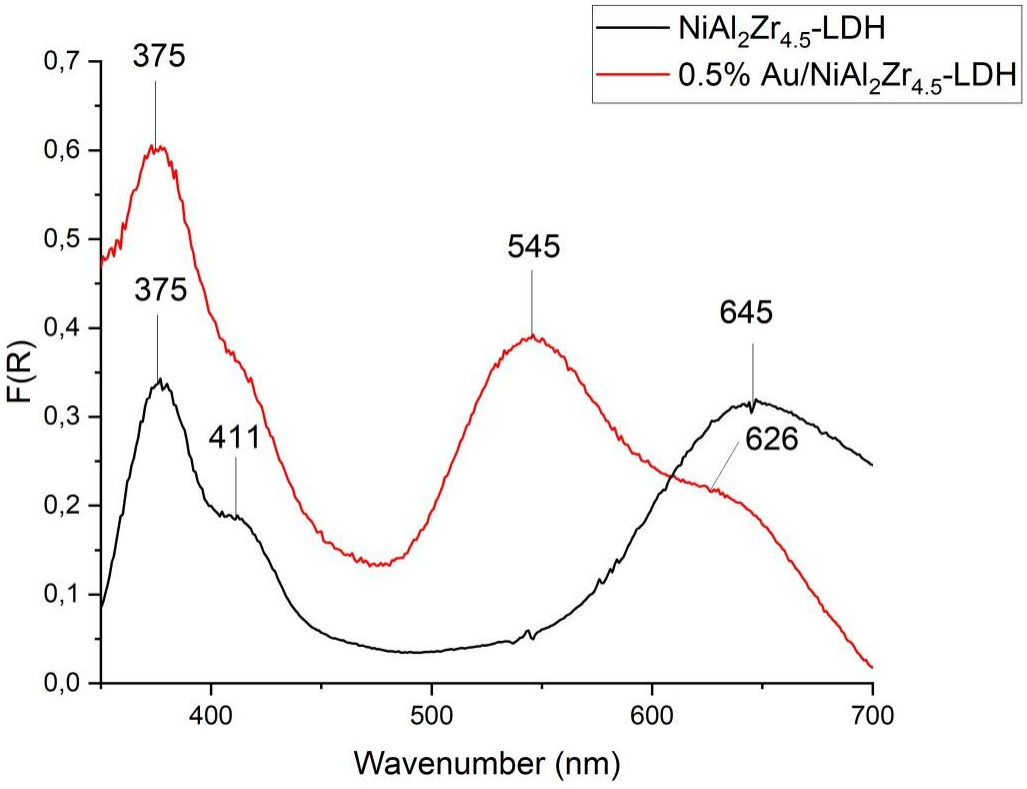

Figure V-1: DRUV-Visible Diffuse Reflectance Spectra of Pristine $NiAl_2Zr_{4.5}$ LDH and Au-Decorated 0.5% $Au/NiAl_2Zr_{4.5}$ LDH Samples Analyzed Using the Kubelka-Munk Function.

The optical properties of the two layered double hydroxide (LDH) samples were systematically analyzed using the Kubelka-Munk function, which was applied to reflectance measurements obtained from dense pellet samples (**Figure V-1**). This method allowed for a precise determination of the samples' absorption characteristics. The pristine LDH powder, which exhibits a green hue, showed two prominent absorption bands at wavelengths of 375 nm and 644 nm. These bands are indicative of electronic transitions occurring within the material, and their presence in the

visible spectrum corresponds well with the observed color of the sample (black curve). The absorption band at 375 nm is likely associated with transitions related to the intrinsic electronic structure of the LDH, while the 644 nm band suggests additional transitions that contribute to the material's visible light absorption.

Upon introducing gold nanoparticles (Au NPs) onto the surface of the LDH, the optical landscape of the material changed significantly. A new absorption band appeared at 545 nm, which is attributed to the localized surface plasmon resonance (LSPR) of the gold nanoparticles. This phenomenon occurs when the conduction electrons on the surface of the Au NPs oscillate in resonance with the incident light, leading to enhanced absorption at specific wavelengths. The emergence of this band highlights the successful incorporation of Au NPs into the LDH matrix and underscores their influence on the material's optical properties.

Interestingly, the presence of the Au NPs did not merely introduce a new optical feature; it also altered the behavior of the existing absorption band at 644 nm. This band, which was initially observed in the pristine LDH, remained in the Au NP-decorated sample but showed signs of interaction with the newly introduced LSPR band (red curve). The persistence and possible modification of the 644 nm band suggest that there may be a charge transfer between the Au NPs and the LDH support. Such an interaction could enhance the electronic coupling between the metal nanoparticles and the LDH, potentially leading to improved catalytic or photocatalytic properties. This charge transfer is a crucial aspect, as it indicates that the introduction of Au NPs does not simply modify the optical absorption of the material but could also impact its electronic structure and reactivity, thereby expanding the potential applications of the composite material in fields such as photocatalysis and optoelectronics.

III. Optimization of reaction conditions by factorial experimental design method

Employing a full factorial design method (FFD), four factors were precisely selected, namely the amount of NaOH, H_2O_2, Au/LDH photo-catalyst and the time, each having two levels (high [+] and low [-]), to develop the factorial plan. **Table V-1** outlines the operating conditions in this study.

Table V-1: Factors and levels evaluated by FFD.

Factors	**Levels**		
	Low (-)	**Center (0)**	**High (+)**
A - Catalyst mass (mg)	2.5	13.75	25
B - H_2O_2 Volume (µL)	200	400	600
C - NaOH Mass (mg)	10	32	55
D - Time (min)	30	60	90

Table V-2: Design matrix for 2^4 (16) full-factorial design and corresponding experimental responses (mglucose= 250 mg, VH_2O = 6 mL, A.M.1.5G illumination).

Trial n°	Catalyst weight (g)	H_2O_2 volume (µL)	NaOH weight (mg)	Reaction time (min)	Conversion yield (%)
1	25	200	10	30	**6**
2	2.5	200	10	30	**0**
3	25	600	10	30	**12**
4	2.5	600	10	30	**0**
5	25	200	55	30	**27**
6	2.5	200	55	30	**18**
7	25	600	55	30	**74**
8	2.5	600	55	30	**24**
9	25	200	10	90	**13**
10	2.5	200	10	90	**0**
11	25	600	10	90	**14**
12	2.5	600	10	90	**0**
13	25	200	55	90	**73**
14	2.5	200	55	90	**0**
15	25	600	55	90	**76**
16	**2.5**	**60**	**55**	**90**	**23**

Design Expert software was used to calculate the average effect and the primary interaction effects of the conversion of glucose into sodium D gluconate. The results of the analysis of variance (ANOVA) are presented in **Table V-2**.

Table V-3: Analysis of variance table [Partial sum of squares - Type III of conversion response].

Source	Sum of Squares	df	Mean Square	F Value	P-valueProb> F	Conclusion
Model	10325.00	7	1475.00	13.74	0.0007	Significant
A-m_{cat}	3306.25	1	3306.25	30.79	0.0005	Significant
B-V_{H2O2}	462.25	1	462.25	4.31	0.0717	Significant
C-m_{NaOH}	4556.25	1	4556.25	42.43	0.0002	Significant
D-Time	90.25	1	90.25	0.84	0.3861	Not significant
AC	1225.00	1	1225.00	11.41	0.0097	Significant
AD	361.00	1	361.00	3.36	0.1041	Not significant
BC	324.00	1	325.00	3.02	0.1206	Not significant
Residual	859.00	8	107.38			
Cor Total	11184.00	15				

The model F-value is 13.74 for the conversion response. It should be noted that "Prob> F" values below 0.05 indicate that the model terms are significant. Conversely, a "P-value" greater than 0.1 suggests the non-significance of the model terms. Notably, the extremely low p-value (< 0.0001) underscores the rarity of the "model F-value" occurring due to experimental noise, with only a 0.01% chance.

The main factors A (m_{cat}) and C (m_{NaOH}) are significant. Values between 0.05 and 0.10, such as AC are considered slightly significant.The conversion response model exhibits high determination values: $R^2 = 0.9232$, Adj-$R^2 = 0.8560$ and pred $R^2 = 0.6928$.

The obtained polynomial equation through multiple regression analysis in coded units provides a means to relate the rate of conversion reaction of glucose to sodium D gluconate to the investigated factors. All main effects and responses have a linear relationship, as demonstrated by the regression equation that was produced from the variance analysis. The predictive models for estimating the conversion of glucose (Conversion (%) can be expressed by the following equation (yet shown in the main article):

Conversion (%) = + 22.50 + 14.38*A + 5.38* B + 16.88*C + 2.38 * D + 8.75*A*C + 4.75*A*D + 4.50 *B* C

Figure V-2 illustrates the effectiveness of the model in explaining the experimental range under investigation by comparing the graphical representation of actual conversion values versus predicted conversion values.

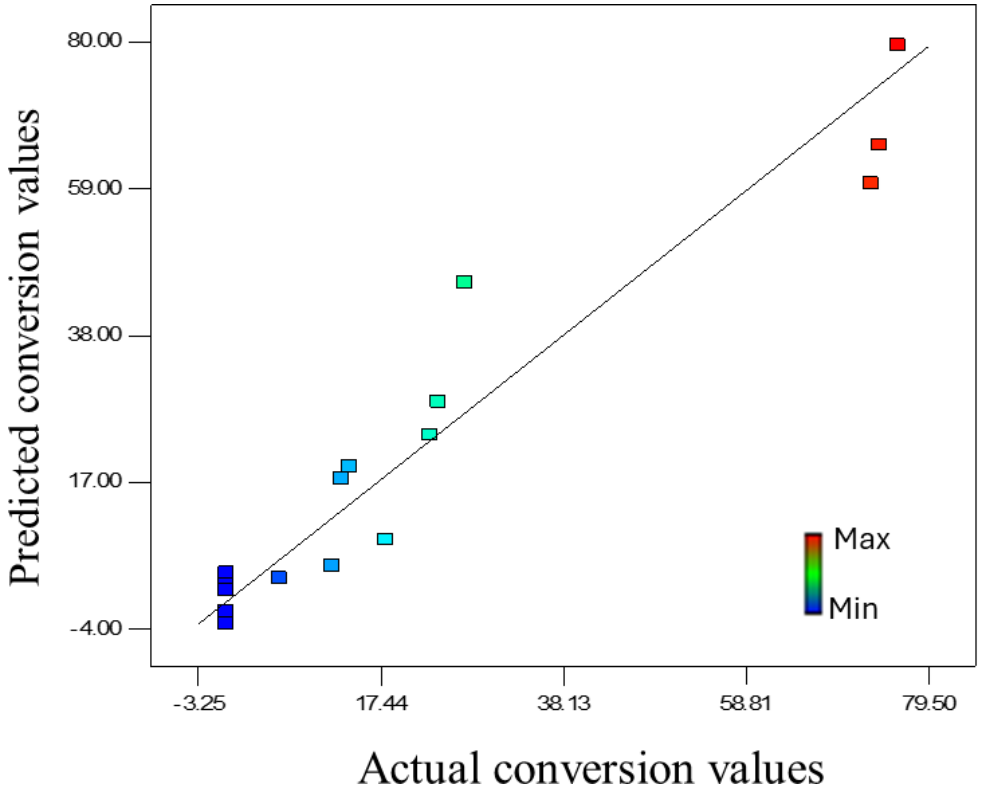

Figure V-2: Plot of actual conversion values vs. predicted conversion values.

The previous results are verified by a Pareto chart (**Figure V-3**), a specialized type of bar graph used to illustrate the relative importance of various effects in a dataset. A **Pareto chart** is based on the Pareto principle, which states that a small number of causes often lead to the majority of the effects. In this chart, effects are displayed in descending order of their impact, with the most significant effects shown first. This visualization helps to quickly identify which factors contribute most significantly to the outcomes being studied.

The chart displays the **t-values** of the effects, which are statistical measures used to determine the significance of each effect within the model. The **t-value** is calculated by dividing the estimated effect by its standard error, and it provides an indication of whether the effect is likely to be statistically significant. A higher absolute t-value suggests that the effect is more significant, meaning it is less likely to have occurred by random chance.

These t-values are compared to reference lines to assess their significance. The **standard t-Value Limit** of 2.306 represents the threshold above which an effect is considered potentially

significant or moderately important. This limit is based on the t-distribution and reflects the level of significance typically used in hypothesis testing.

In addition to this standard threshold, the **Bonferroni limit** is a more stringent threshold set at 4.122. The Bonferroni limit is used to adjust for the increased risk of false positives when multiple statistical tests are conducted simultaneously. It is a correction factor that lowers the significance level to account for the number of comparisons made, thereby reducing the likelihood of incorrectly identifying an effect as significant. Effects that exceed the Bonferroni limit are considered not only significant but also highly important, as they have passed an even stricter test of significance.**[11]**.

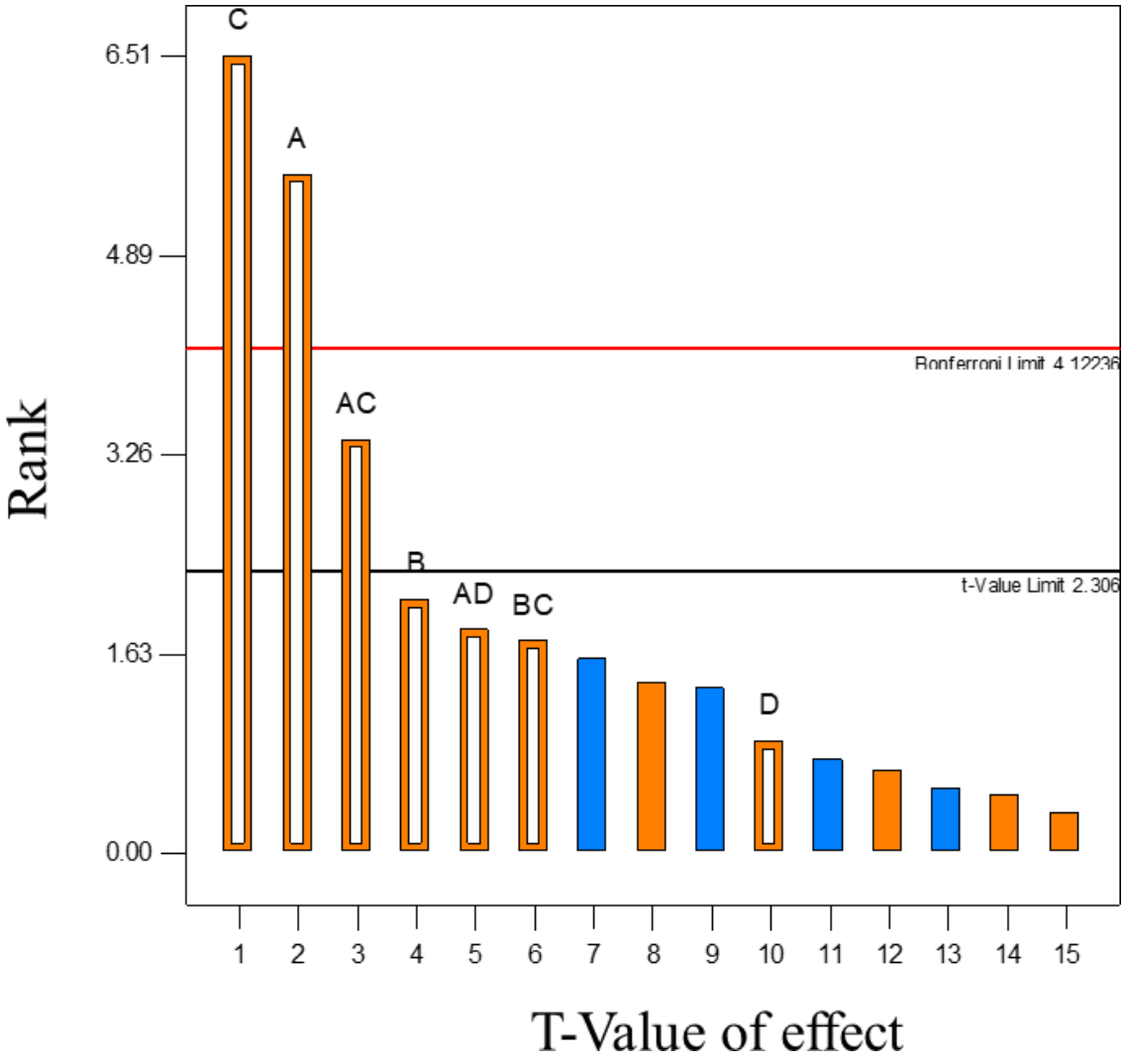

Figure V-3: Pareto chart of effects.

The values of the effects of the variables are represented in "bar" diagrams; the area of each bar is proportional to the value of the effect.

This model equation, as well as Pareto chart (**Figure V-3**) evidenced the importance of the factors A (m_{cat}) and C (m_{NaOH}) on the conversion yield of glucose. The amount of NaOH is the first and the most sensitive variable on the yield of conversion of glucose. This first result is interesting and counterintuitive given the basicity provided by the LDH support. This effect is positive (+16.88) meaning that the increase of the amount of NaOH increases the yield of the glucose conversion. Sodium hydroxide plays a pivotal role as an alkaline agent in the process. It governs the catalytic activity of the gold nanoparticles (Au NPs) and allows maintaining the ideal surface conditions to avoid poisoning of the catalyst in particular when pH get to acidic while promoting the chemisorption of glucose by its hydrated form.[31] This result endorses that contrary to what one could expect, the intrinsic basicity of the LDH material is unfortunately not strong enough to initiate the photocatalytic process.

The quantity of the catalyst is the second most important factor having also a positive effect (+14.09). Lastly, our results underline that the reaction time and H_2O_2 quantity are not influencing factors. The most important interaction worth mentioning is that occurring between weight of NaOH and catalyst (+ 8.75). Examining surface plots as a function of two factors while maintaining constant values of the others, is an effective method to determine the relationship between the reaction condition and the conversion yield as a response. **Figure V-4** gives the three-dimensional and contour plots about the effect of the most significant two-factor interactions (AC: weights of NaOH and catalyst) on the yield of glucose conversion, confirming the positive effect of both factors. Utilizing Expert-Design 7.0.0 software, numerical optimization technique was employed to determine the optimal conditions for glucose conversion as displayed in **table V-4**.

Table V-4: Predicted (Pred.) and experimental (Exp.) results obtained for optimal operating conditions determined using factorial plan.

	m_{cat} (mg)	$V(H_2O_2)$ (µL)	m_{NaOH} (mg)	Time (min)	Conv (%)
Pred.	29.7	519.13	64.92	89.89	100
Exp.	30	520	65	90	87

By experimentally applying the conditions determined by the numerical model, a noticeable gain in conversion yield to 87 % was obtained. This result corroborates well with the predicted conversion yield value determined by the FFD method. Indeed, this latter value is the best result obtained with this catalyst so far, which allows to further confirm the accuracy and validity of the herein proposed predictive model.

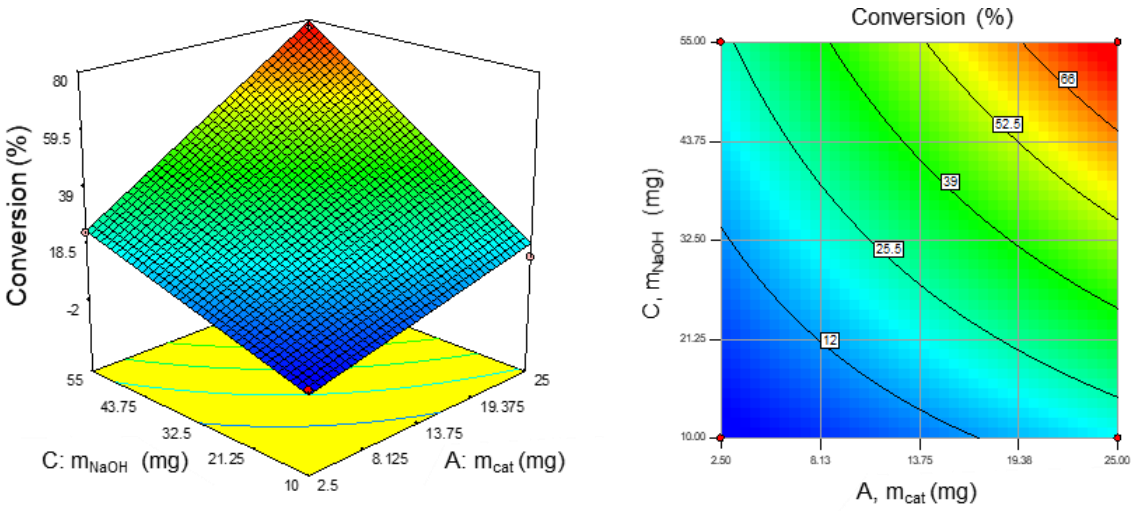

Figure V-4: 3D response surface plot (left), and the corresponding contour plot (right) of significant AC interaction at VH_2O_2= 600µL and time =90 min with conversion yield.

IV. Catalytic tests

Briefly, a catalytic charge of gold (substrate/gold mol ratio: 43 000) was added to an alkaline solution of glucose (5 mol. %) in presence of 1.1 equivalent of hydrogen peroxide as an oxidizing agent and potentially also electron scavenger. After 90 minutes of continuous illumination using standardized A.M. 1.5G light (100 mW/cm^2), the catalyst was filtrated, and the resulting reaction media was freeze-dried and analyzed by NMR to determine both conversion yield and selectivity towards sodium D gluconate.

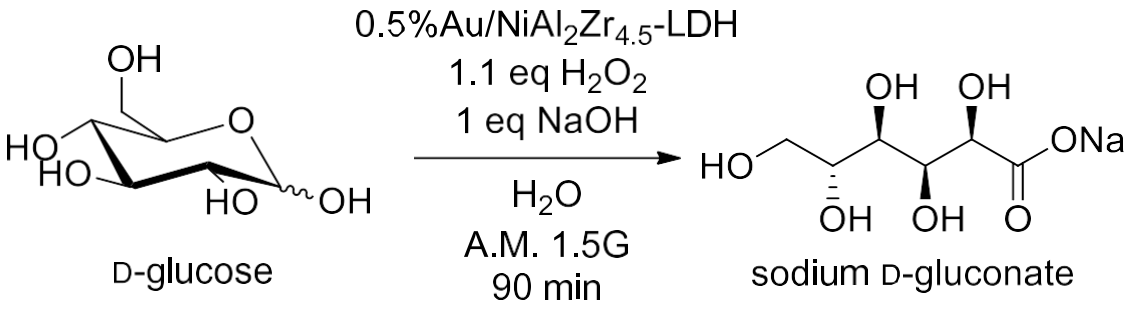

Scheme V-2: Catalytic (photo)oxidation of glucose using 0.5% $Au/NiAl_2Zr_{4.5}$-LDH under standardized conditions.

Using the optimal conditions from the experimental design (**Scheme V-2**) **[10]**, the materials $NiAl_2Zr_{4.5}$-LDH and x% Au / $NiAl_2Zr_{4.5}$-LDH were tested and the results are shown in **Table V-5**.

The table shows the catalytic performance of $NiAl_2Zr_{4.5}$-LDH and $Au/NiAl_2Zr_{4.5}$-LDH catalysts in the (photo)oxidation of glucose. The unmodified $NiAl_2Zr_{4.5}$-LDH leads to degradation without selective hydrogenation. However, the introduction of Au significantly enhances both conversion and selectivity, with optimal performance observed at lower Au loadings. The 0.5% $Au/NiAl_2Zr_{4.5}$-LDH catalyst stands out, achieving the best balance between high conversion and perfect selectivity, while higher Au content seems to diminish the conversion efficiency without greatly affecting selectivity. These findings suggest that moderate Au loading is key to optimizing the catalytic activity of $NiAl_2Zr_{4.5}$-LDH for this reaction.

Based on these results, the study will proceed using the 0.5% $Au/NiAl_2Zr_{4.5}$-LDH catalyst, as it demonstrated the best combination of high conversion and complete selectivity.

Table V-5: Catalytic Performance of $NiAl_2Zr_{4.5}$-LDH and $Au/NiAl_2Zr_{4.5}$-LDH in the Glucose (photo)oxidation.

Materials	Conversion (%)	Selectivity (%)
$NiAl_2Zr_{4.5}$-LDH	Degradation only	
0.25% $Au/NiAl_2Zr_{4.5}$-LDH	13	nd
0.5% $Au/NiAl_2Zr_{4.5}$-LDH	87	100
1% $Au/NiAl_2Zr_{4.5}$-LDH	85	100
2% $Au/NiAl_2Zr_{4.5}$-LDH	63	≥ 95

The experimental conditions for all reactions include: 30 mg of catalyst, 520 µL of H_2O_2, 65 mg of NaOH, and a reaction time of 90 minutes.

As a result, this first attempt yielded only 31% conversion despite an excellent selectivity towards sodium D gluconate thus demonstrating that transferability strongly depends on the type of photocatalyst. Consequently, we used the optimized reactions conditions developed previously by full factorial design method (FFD) reported in **table V-4**.

Moreover, in order to check if a light-induced mechanism is herein involved, the reaction was deliberately conducted in dark (**FigureV-6**, black curve). Compared to darkness, it is clear that in presence of light (**Figure V-6**, red curve), a much faster reaction is observed, reaching a maximum of 77% conversion yield within only 30 minutes, vs 74% conversion yield after 90 minutes in darkness. This first comparative result stresses the contribution of incident light to accelerate the kinetic of glucose oxidation, therefore on the photocatalytic nature of the reaction. To confirm this hypothesis and also rule out any heat-induced activation for this reaction, a similar reaction was conducted at a temperature of 35°C corresponding to the reaction media temperature after 90 minutes of continuous illumination. As showed in **Figure V-6** (blue curve), the kinetic enhancement by temperature remains marginal, thus excluding any thermal effect.

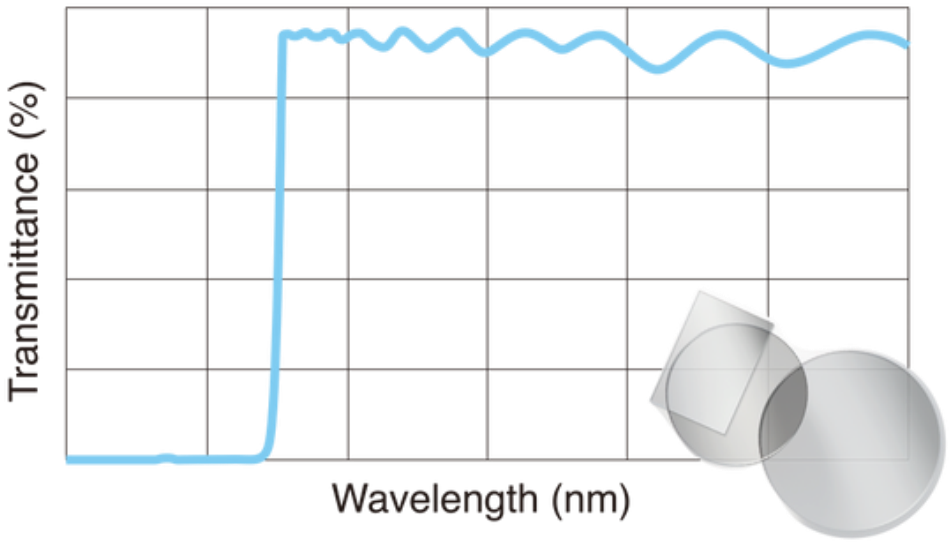

Figure V-5: Optical Transmittance Spectrum of a Transparent Film.

Figure V-5 illustrates the optical behavior of long-pass filters such as the LP 475 nm and LP 780 nm filters. These filters are specifically designed to block shorter wavelengths below their cutoff point, while allowing longer wavelengths to pass with high transmittance. The LP 475 nm filter blocks ultraviolet (UV) and blue light (wavelengths below 475 nm) and transmits green, red, and near-infrared (NIR) light. It is commonly used in fluorescence imaging to isolate signals in the longer wavelength range by removing unwanted UV and blue light. The LP 780 nm filter blocks the visible spectrum (wavelengths below 780 nm) and allows only near-infrared light to pass. It is widely used in spectroscopy, infrared imaging, and optical communication systems that require precise transmission of NIR wavelengths.

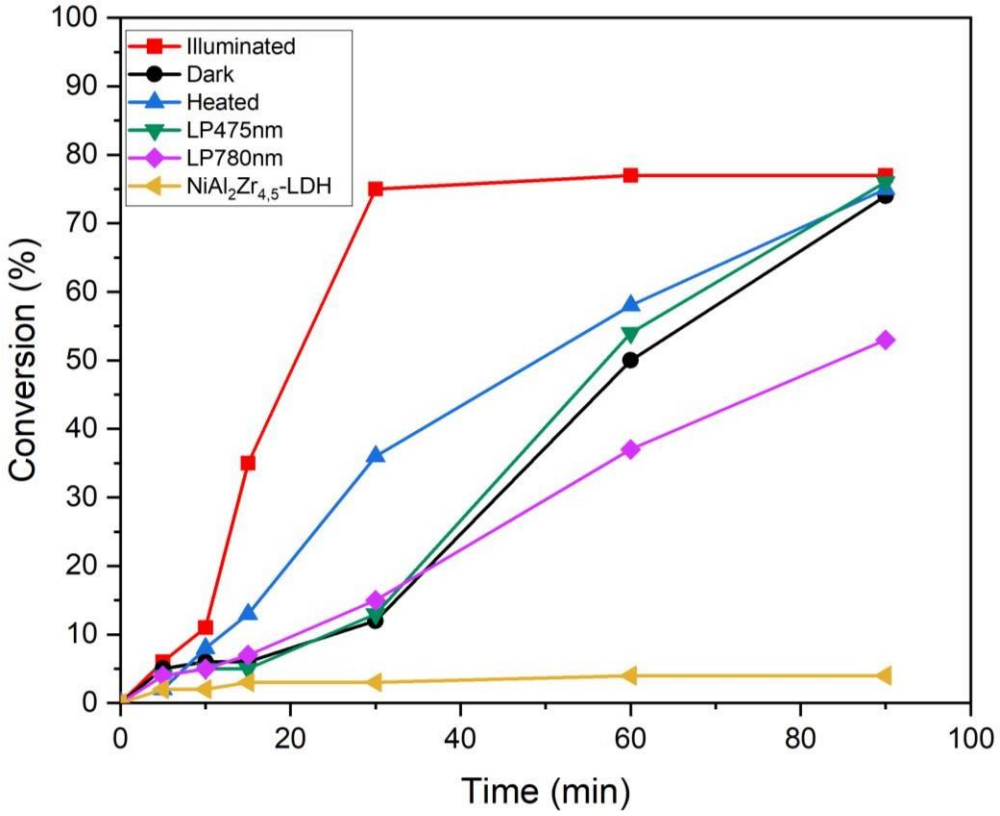

Figure V-6: Kinetic comparison of glucose oxidation under standardized A.M. 1.5G (red), dark (black), or heating at 35°C (blue) conditions. In addition, long-pass filters at 475 nm (LP475, green) and at 780 nm (LP780, purple) were used for incident light.

The involvement of photon-induced free carriers on the glucose oxidation demonstrated, two potential mechanisms can be proposed: (1) a charge transfer reaction from the LDH bandgap excitation into the gold nanoparticles, (2) gold plasmonic induced charge transfer reaction to the LDH. To identify the main activation path, we introduced long-pass filter with two different cutoff wavelengths between the light source and the photocatalytic reactor (475 nm and 780 nm). The selection of these filters is guided by the optical characteristics of the photocatalyst: $NiAl_2Zr_{4.5}$-LDH has maximum absorption at 375 nm and 644 nm whereas the LSPR of gold nanoparticles is located at ca. 550 nm. Thus, the 475 nm filter principally annihilates the high energy photons excitation of the LDH band at 375 nm while leaving the possibility of LSPR excitation. By contrast, the 780 nm long pass filter hampers both gold and LDH excitation.

Interestingly, when using long-pass filters at 780nm (LP780nm) (**Figure V-6**, purple curve), there appears to be no discernible impact of the filtered light on the kinetic of glucose conversion compared to the darkness experiment. This confirms that the near-infrared radiation of the Xe lamp filtered A.M.1.5G condition is not responsible for the photo-induced activation. This is in good agreement with dark temperature test at 35°C. Interestingly, it is observed that when employing the

long-pass filters at 475nm (LP475nm) (**Figure V-6**, green curve), the glucose conversion rate is very similar to that obtained under darkness. This result led us to the conclusion that the photocatalytic activity stems from the high energy photons bandgap excitation in UV and that Au NPs excitation is not responsible for the photon-induced oxidation of glucose. Besides, the necessity of gold deposition on LDH material is undoubtedly highlighted by the experience involving support material alone under light, yielding a 4% conversion rate after 90 minutes (yellow curve).

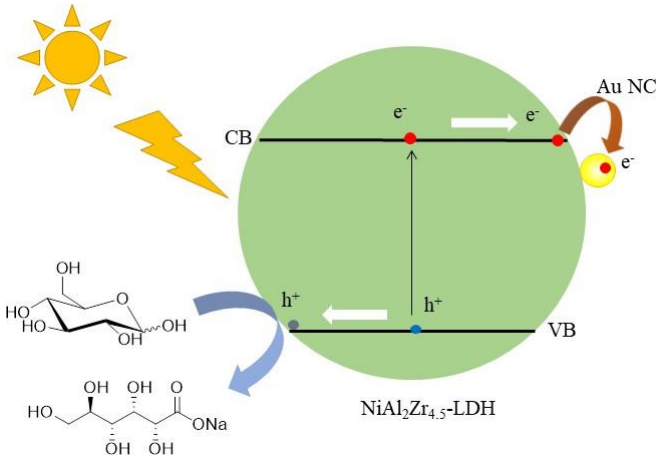

Figure V-7: Proposed mechanism for the selective glucose oxidation using $Au/NiAl_2Zr_{4.5}$-LDH under solar simulated illumination.

V. Conclusion

This work has demonstrated the possibility of using 0.5%$Au/NiAl_2Zr$-LDH in photocatalysis. Indeed, after optimization of the reaction conditions via full factorial design method (FFD) for the synthesis reaction of sodium D gluconate from glucose, a conversion of 87% with a selectivity of 100% were obtained.

The results clearly demonstrate a charge-driven transfer process that originates from the excitation of the layered double hydroxide (LDH) and is directed towards the supported gold nanoparticles. This interaction was evidenced by the emergence of new optical features, particularly the localized surface plasmon resonance (LSPR) band associated with the gold nanoparticles, which suggests a strong electronic coupling between the LDH support and the Au NPs. Understanding this mechanism is crucial as it provides valuable insights for the rational design of new materials. By adjusting the bandgap of the LDH support, it becomes possible to optimize light absorption, thereby enhancing the material's photocatalytic efficiency. This approach could lead to more effective and selective transformations of free carbohydrates, paving the way for the development of more sustainable and efficient catalytic systems in the future.

Annex

NMR spectra

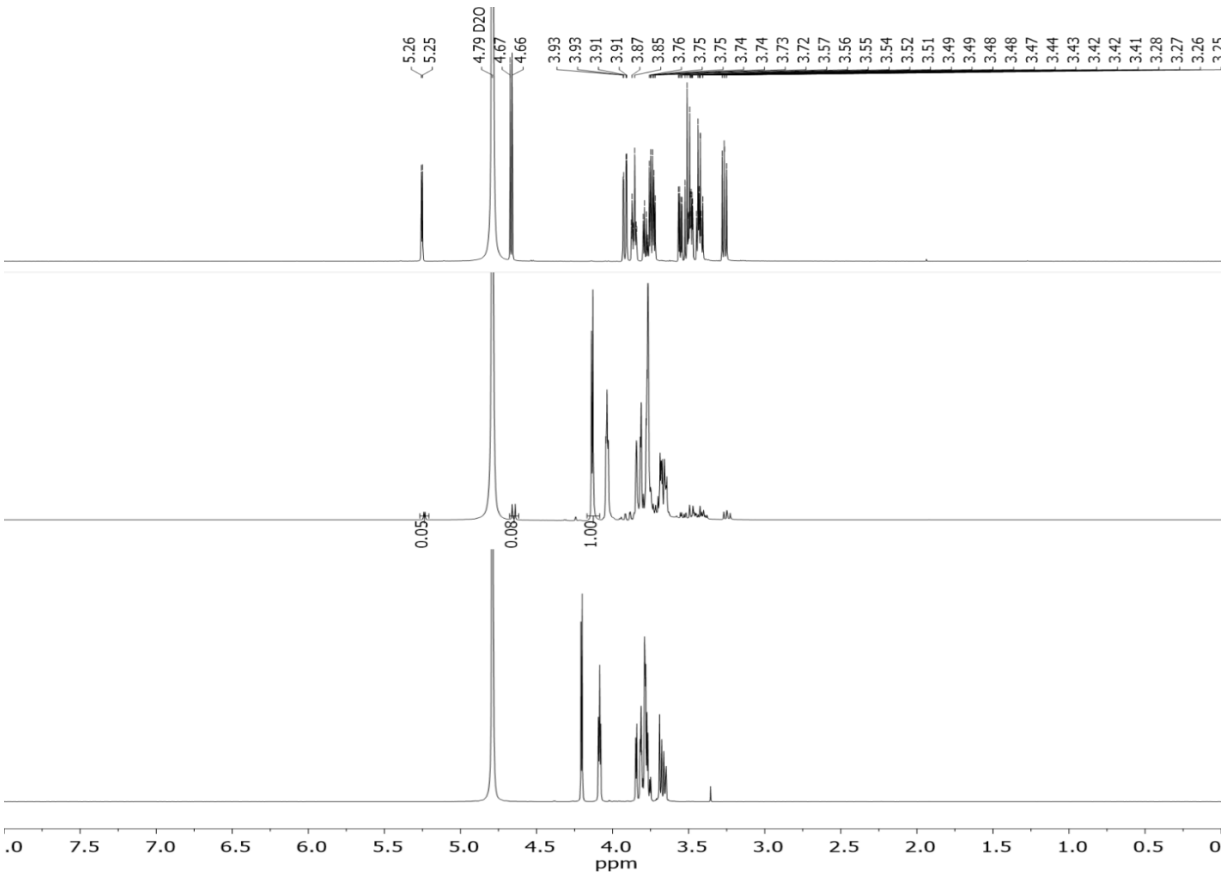

Figure V-8: ^{1}H NMR spectra (in D_2O) obtained for glucose (top), experimental crude obtained using the conditions proposed by the factorial plan (middle, conditions of Table V-4) and commercial gluconic acid (bottom).

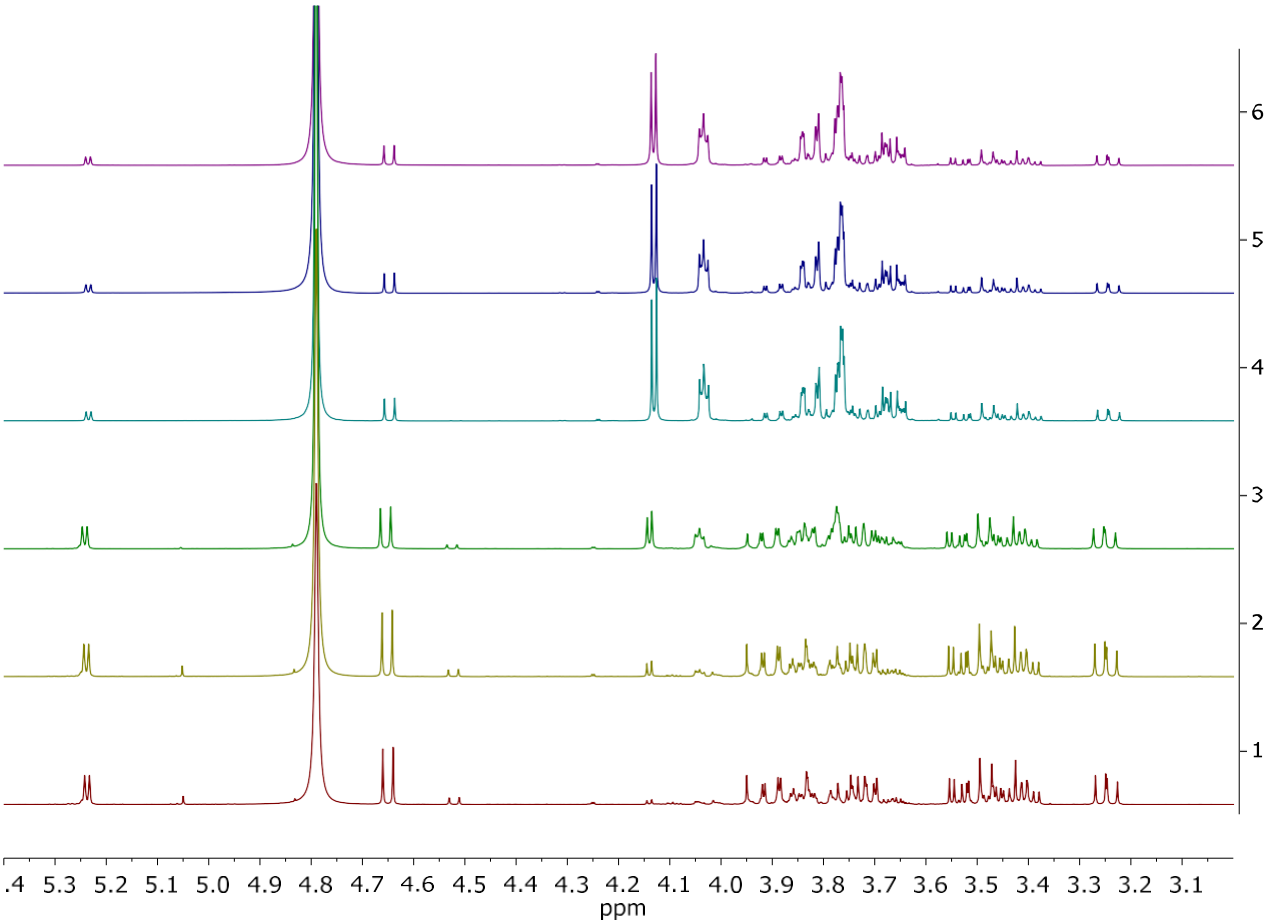

Figure V-9: ^{1}H NMR spectra (in D_2O) of the crude obtained under A.M.1.5G illumination at several times (red-1: 5 min, yellow-2:10 min, green-3: 15 min, cyan-4: 30 min, blue-5: 60 min, purple-6: 90 min). *Cond.: $m_{glucose}$ = 250 mg, m_{cat} = 25 mg, m_{NaOH} = 55 mg, V_{H2O2} = 200 µL, V_{H2O} = 6 mL*

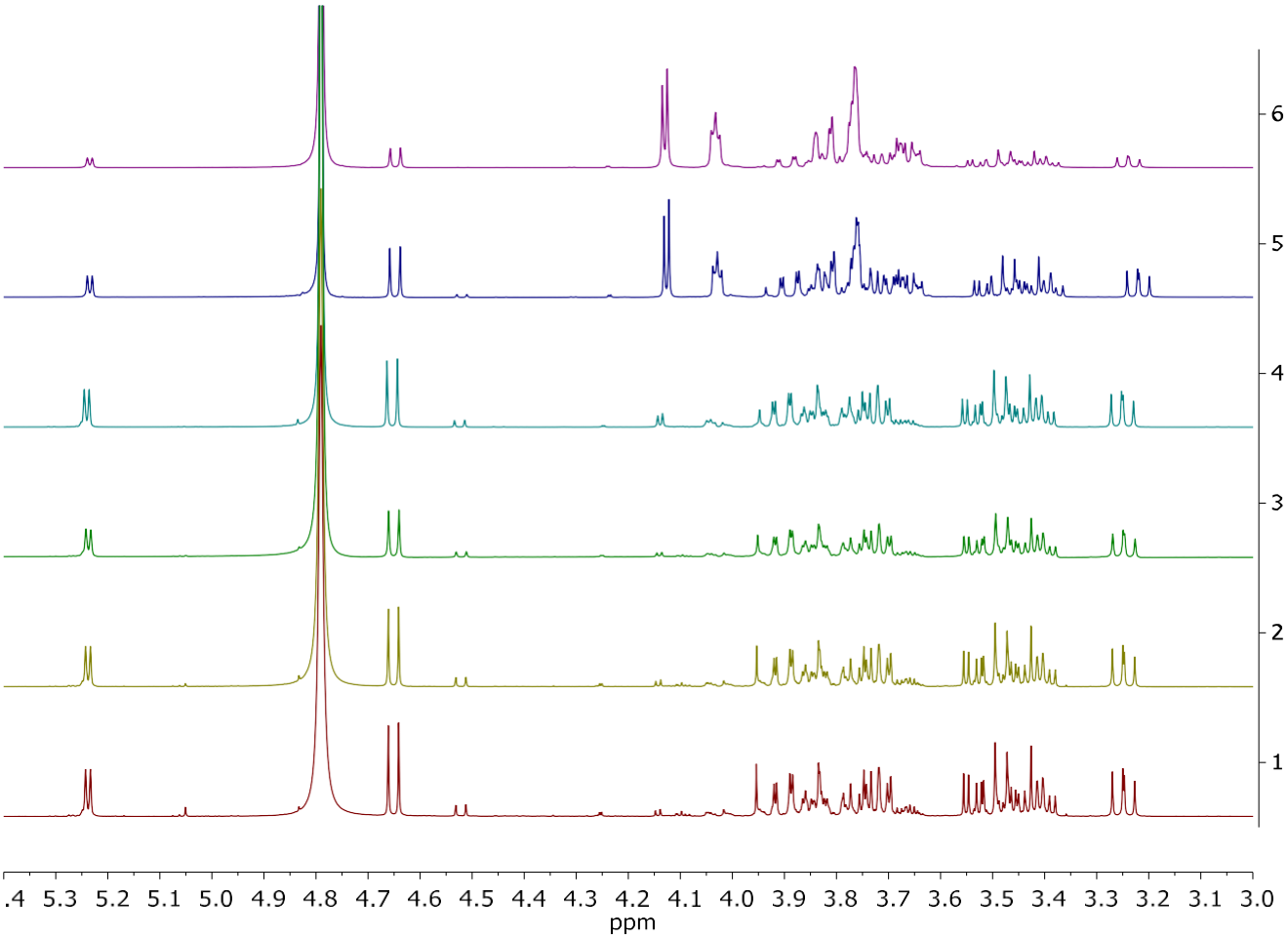

Figure V-10: ^{1}H NMR spectra (in D_2O) of the crude obtained under darkness conditions at several times (red-1: 5 min, yellow-2:10 min, green-3: 15 min, cyan-4: 30 min, blue-5: 60 min, purple-6: 90 min). *Cond.: $m_{glucose}$ = 250 mg, m_{cat} = 25 mg, m_{NaOH} = 55 mg, V_{H2O2} = 200 µL, V_{H2O} = 6 mL*

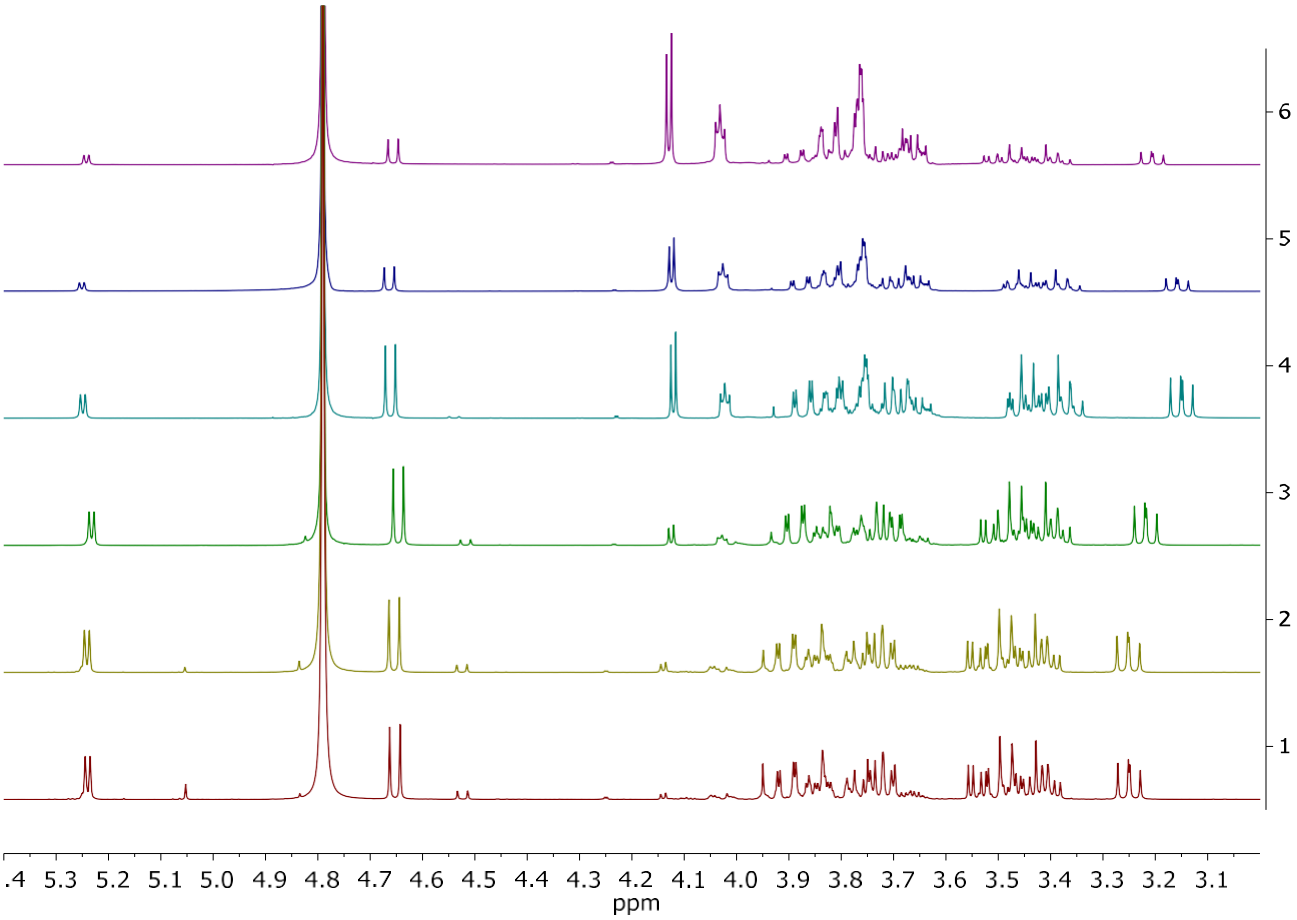

Figure V-11: ^{1}H NMR spectra (in D_2O) of the crude obtained under heating at 35°C at several times (red-1: 5 min, yellow-2:10 min, green-3: 15 min, cyan-4: 30 min, blue-5: 60 min, purple-6: 90 min). *Cond.: $m_{glucose}$ = 250 mg, m_{cat} = 25 mg, m_{NaOH} = 55 mg, V_{H2O2} = 200 µL, V_{H2O} = 6 mL*

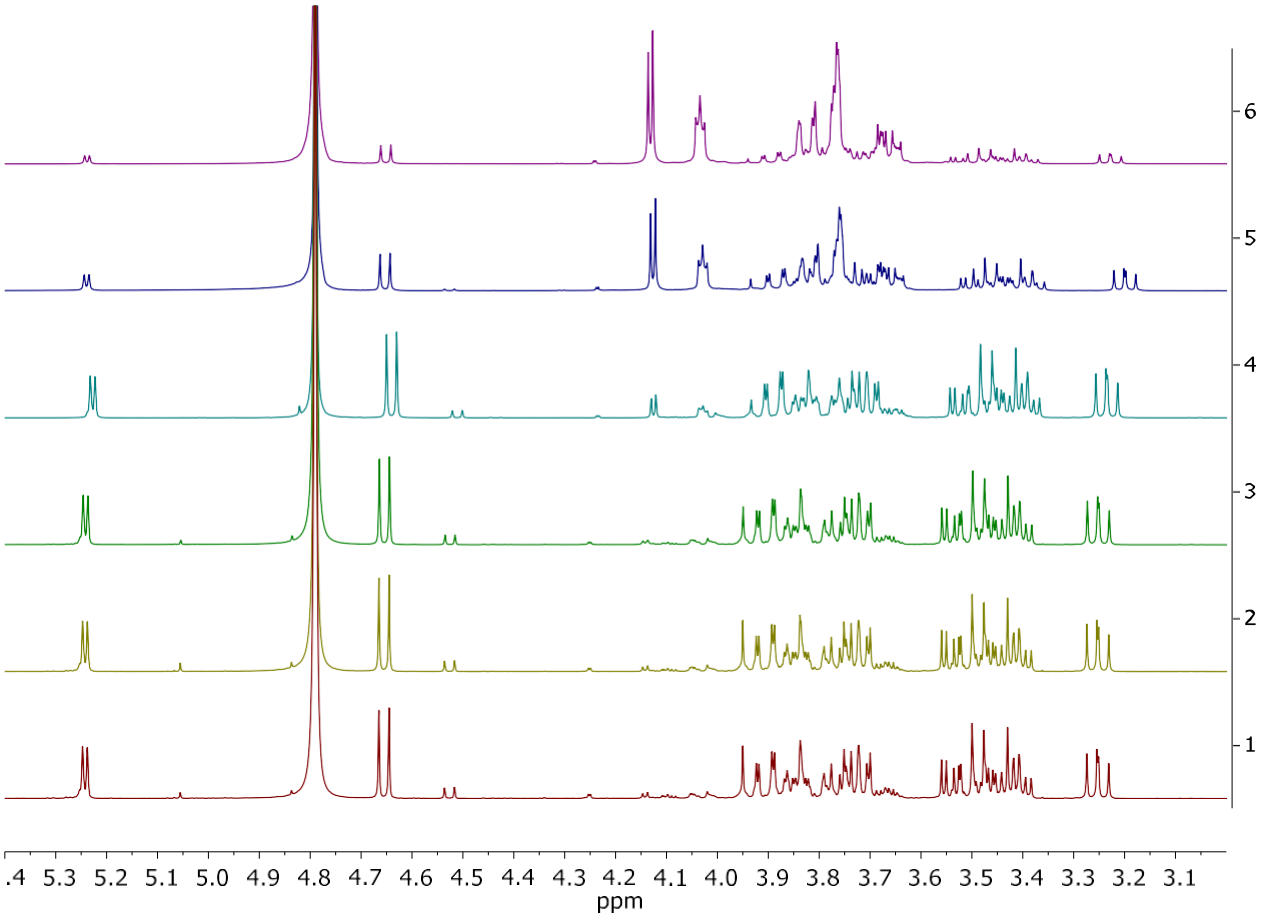

Figure V-12: ^{1}H NMR spectra (in D_2O) of the crude obtained under A.M.1.5G illumination using LP475 nm filter at several times (red-1: 5 min, yellow-2:10 min, green-3: 15 min, cyan-4: 30 min, blue-5: 60 min, purple-6: 90 min). *Cond.: $m_{glucose}$ = 250 mg, m_{cat} = 25 mg, m_{NaOH} = 55 mg, V_{H2O2} = 200 µL, V_{H2O} = 6 mL*

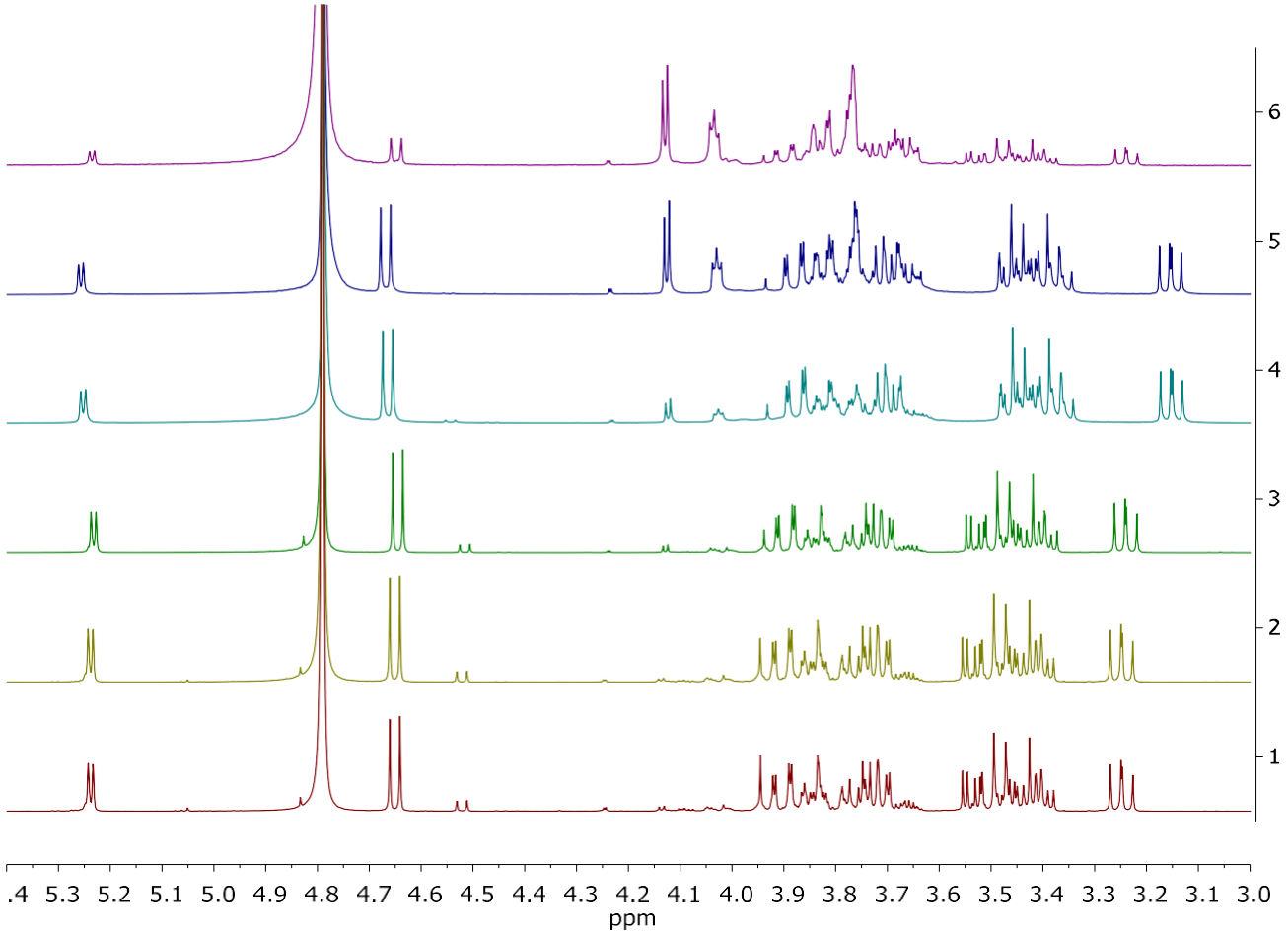

Figure V-13: ^{1}H NMR spectra (in D_2O) of the crude obtained under A.M.1.5G illumination using LP780 nm filter at several times (red-1: 5 min, yellow-2:10 min, green-3: 15 min, cyan-4: 30 min, blue-5: 60 min, purple-6: 90 min). *Cond.: $m_{glucose}$ = 250 mg, m_{cat} = 25 mg, m_{NaOH} = 55 mg, V_{H2O2} = 200 µL, V_{H2O} = 6 mL*

References :

[1] C. Chatterjee, F. Pong and A. Sen, Green Chemistry, 17 (2015) 40.

[2] P. Gallezot, Chemical Society Reviews, 41 (2012) 1538.

[3] H.S. Isbell, Journal of the American Chemical Society, 54 (1932) 1692.

[4] D.H. Hollenberg, R.S. Klein and J.J. Fox, Carbohydrate Research, 67 (1978) 491.

[5] C. Della Pina, E. Falletta, L. Prati and M. Rossi, Chemical Society Reviews, 37 (2008) 2077.

[6] C. Della Pina, E. Falletta and M. Rossi, Chemical Society Reviews, 41 (2012) 350.

[7] M. Omri, G. Pourceau, M. Becuwe and A. Wadouachi, ACS sustainable chemistry & engineering, 4 (2016) 2432.

[8] W. Yan, D. Zhang, Y. Sun, Z. Zhou, Y. Du, Y. Du, Y. Li, M. Liu, Y. Zhang and J. Shen, Chinese Journal of Catalysis, 41 (2020) 1320.

[9] L. Quéhon, F. Sauvage, H. Ahouari, S. Golonu, H. Vezin, A. Wadouachi and G. Pourceau, ACS sustainable chemistry & engineering, 11 (2023) 11041.

[10] M. Omri, F.d.r. Sauvage, Y. Busby, M. Becuwe, G. Pourceau and A. Wadouachi, Acs Catalysis, 8 (2018) 1635.

[11] R.H. Myers, D.C. Montgomery and C.M. Anderson-Cook, Response surface methodology: process and product optimization using designed experiments, John Wiley & Sons, 2016.

General conclusion

This doctoral thesis focuses on the development of innovative catalysts and processes for biomass valorization, addressing the global challenges of renewable energy and sustainable chemical production. The research investigates three specific pathways: furfural oxidation, furfural hydrogenation, and glucose photo-oxidation, each offering potential for transforming biomass into high-value chemicals. To achieve this, the thesis explores the synthesis of heterogeneous catalysts, specifically low-content gold nanoparticles supported on Zr-modified layered double hydroxides (LDHs), tailored for these reactions. The catalysts aim to enhance the efficiency and selectivity of the conversions, contributing to the broader goal of integrating renewable raw materials into industrial processes and reducing carbon footprints. Two series of Zr modified LDHs, MgAlZr and NiAlZr, were synthesized then used as support for gold nanoparticles. The materials thus prepared were characterised and tested, with their catalytic performances evaluated in the context of furfural oxidation in the case of Au/ MgAlZr and furfural hydrogenation and glucose photo-oxidation in the case of Au/ NiAlZr.

I. Furfural oxidation over Au/MgAlZr-LDH catalysts

In this study, Au/MgAlZr-LDH catalysts were prepared and characterised then tested in liquid aqueous phase oxidation with a focus on improving selectivity and yield of the desired products.

Furfural, obtained through the hydrolysis of hemicellulose, is a valuable platform chemical for synthesizing high-value products. The oxidation of furfural is a crucial process in the valorization of biomass-derived raw materials. Indeed, the oxidation of furfural provides pathways to produce important intermediates such as furoic acid and succinic acid, which are used in various sectors, including pharmaceuticals, polymers, and agriculture.

The catalytic performances of various materials in the oxidation of furfural using H_2O_2, aiming to develop eco-friendly and economically viable processes for converting biomass into high-value chemicals, specifically succinic acid.

For this, MgAl-based layered double hydroxides (LDHs) modified with zirconium (Zr) were used as a support for gold (0.25% wgh) nanoparticles deposited using the deposition-precipitation with urea (DPU) method.

The modification of LDHs with zirconium (Zr) and gold (Au) aims to enhance catalytic properties, particularly in terms of selectivity and conversion. Zr is introduced either post-synthesis or during the preparation of LDHs, influencing the crystalline structure and surface properties of the catalysts in different ways.

All materials ether LDHs and Au LDHs were characterised by Infrared (FTIR) and Raman Spectroscopy, X-Ray Diffraction (XRD), Atomic Absorption Spectroscopy and Nitrogen Adsorption-Desorption and Electron Microscopy (SEM, TEM)

FTIR and Raman analyses reveal key information about the chemical bonds present in the materials. The spectra show that the introduction of Zr and Au into the LDHs modifies the vibration modes, indicating specific interactions between these elements and the LDH matrix. For instance, the introduction of Zr tends to intensify bands attributed to the vibrations of Zr-O and Zr-O-M bonds, suggesting significant incorporation of Zr into the LDH structure.

X-ray diffraction analysis was used to confirm the crystalline structure of the synthesized materials. The results show characteristic LDH peaks, with subtle modifications in lattice parameters due to the addition of Zr and Au. Notably, the introduction of Zr may lead to a slight decrease in the c parameter, suggesting that Zr is inserted into the interlayer space of the LDHs.

Atomic absorption spectroscopy (AAS) quantified the gold content in the catalysts, confirming the precision of the DPU deposition method. Nitrogen adsorption-desorption isotherms provided information about the porosity of the materials, with specific surface areas varying depending on the method of Zr and Au introduction. The addition of gold, for example, tends to reduce the specific surface area, likely due to the agglomeration of the LDH layers.

Scanning electron microscopy (SEM) images show typical LDH morphology, with a "rose-like" structure. Transmission electron microscopy (TEM) and HAADF-STEM mode observations reveal a homogeneous distribution of gold on the supports, with gold nanoparticles of varying sizes depending on the preparation conditions. Nano-particle sizes range from 1.2 nm to 8.2 nm.

I.1. Catalytic tests results

The addition of Zr to LDHs modifies the electronic structure and reactivity of the catalytic sites. Zr, as a larger and more electropositive cation than Mg or Al, can create new active sites or alter the properties of existing sites, potentially leading to better activation of the reactants. Additionally, the addition of gold, even in small quantities (0.25%), can introduce surface plasmon resonance effects that might enhance conversion rates.

Reaction conditions, such as temperature, pressure, and pH, were optimized to maximize succinic acid production while minimizing by-products.

The $MgAl_2$-LDH catalyst, without modifications, achieved a furfural conversion of 66% and produced a mix of furoic, succinic, and fumaric acids. However, the incorporation of Zr post-synthesis ($Zr_{4.5}$-$MgAl_2$-LDH) dramatically improved the conversion to 99%, with a selectivity of 45% towards succinic acid. Furthermore, the introduction of Au NPs notably enhanced catalytic efficiency and selectivity. The best results were obtained with 0.25% Au/$MgAl_2Zr_{4.5}$-LDH, which achieved an 84% conversion and 99% selectivity for succinic acid, showcasing a positive synergy between Zr and Au NPs. This research highlights the potential of Zr-modified and Au-decorated LDHs as effective catalysts for biomass valorization, offering a sustainable pathway for succinic acid production from renewable resources.

II. Furfural hydrogenation over Au/NiAlZr-LDH catalysts

Furfural hydrogenation is a crucial step in the synthesis of valuable alcohols and aldehydes, which serve as essential building blocks for numerous industrial applications. The study's primary objective is to investigate efficient catalytic systems and optimize reaction conditions for furfural hydrogenation, with an emphasis on enhancing selectivity towards target products while minimizing the formation of undesired by-products. By elucidating the underlying reaction mechanisms and optimizing catalyst design.

In this study, layered double hydroxides (LDHs) of nickel (Ni) and aluminum (Al) with a Ni/Al ratio of 2 (by weight) were synthesized, followed by modification with zirconium (Zr), maintaining an Al/Zr ratio of 4.5. The Zr was added in situ during the synthesis of the LDH. The resulting NiAl-LDH and NiAlZr-LDH materials were then used as supports for the deposition of gold (Au) nanoparticles, with varying Au contents of 0.25%, 0.5%, 1%, and 2% by weight. Gold was deposited using the Deposition-Precipitation with Urea (DPU) method. The synthesized materials were characterized using various techniques, including X-ray diffraction (XRD), X-ray photoelectron spectroscopy (XPS), Brunauer-Emmett-Teller (BET) surface area analysis, scanning electron microscopy (SEM), and transmission electron microscopy (TEM). The prepared catalysts were subsequently tested for their activity in the hydrogenation of furfural.

Gold loadings in the Au/NiAlZr-LDH materials were measured using atomic absorption spectroscopy (AAS). The experimental Au loadings closely matched the theoretical values, confirming the efficiency of the DPU method for depositing gold onto the NiAlZr-LDH supports.

XRD analysis revealed that the NiAl-LDH exhibits characteristic reflections of hydrotalcite, with a hexagonal crystal system and rhombohedral symmetry. The diffraction pattern of NiAlZr-LDH showed that the lamellar structure of hydrotalcite was preserved, and the addition of Zr improved the crystallinity of the material by reducing structural defects and increasing the size of crystalline domains. The lattice parameter "a," linked to the unit cell size, remained unchanged, indicating that Zr was not substituted for Al or Ni. However, the slight increase in parameter "c" suggested that Zr might occupy vacancies within the crystal lattice, acting as a dopant rather than intercalating as a pillar between layers.

Nitrogen adsorption-desorption isotherms indicated that all materials exhibited a mesoporous structure, with pore sizes ranging between 2 and 50 nm. The BET surface area analysis showed that the incorporation of Zr into the NiAl-LDH increased the specific surface area from 86 m^2/g to 160 m^2/g. The pore volume and diameter also varied with Au loading, indicating complex interactions between the Au nanoparticles and the LDH support.

SEM micrographs of the NiAlZr-LDH revealed that the LDHs consisted of small platelets aggregated into a sand flower morphology. The regularity and asymmetric aggregation of the plates suggested successful co-precipitation of the LDH structure, consistent with the XRD results.

TEM analysis of the Au/NiAlZr-LDH materials revealed that the size of the Au nanoparticles was strongly dependent on the Au content. For low Au loadings (0.25% and 0.5%), larger average particle sizes of 18 nm and 19 nm were observed, respectively. In contrast, higher Au loadings (1% and 2%) resulted in significantly smaller particle sizes of 1.6 nm and 0.9 nm, respectively. Particularly at 2% Au loading, a large proportion of the Au nanoparticles were sub-nanometer in size, confirming the successful deposition of ultra-small Au particles on the Zr-modified NiAl-LDHs. The observed size distribution suggests that higher Au content promotes the formation of smaller, well-dispersed nanoparticles, possibly due to the increased number of nucleation sites and enhanced interactions between Au ions and the Zr-modified support.

II.1. Catalytic Tests results

The prepared catalysts were tested in the hydrogenation of furfural. The reaction predominantly produced two products: furfuryl alcohol (FA) and furfuryl isopropyl ether (iPFE). FA is formed via the hydrogenation of the carbonyl group in furfural, while iPFE results from the condensation of furfural with isopropanol.

Preliminary experiments were conducted using $NiAl_2$-LDH as a reference catalyst to optimize reaction conditions, with parameters such as a furfural volume of 0.5 mL, isopropanol volume of 15 mL, catalyst mass of 0.08 g, temperature of 180°C, hydrogen pressure of 10 bar, and a reaction time of 6 hours. Subsequent catalytic tests revealed that $NiAl_2$-LDH exhibited low activity, achieving only 10% conversion. However, the introduction of Au nanoparticles (NPs) significantly enhanced the catalytic performance, with conversion increasing progressively with higher Au content, reaching 100% with 2% Au loading.

Further investigation with Zr-modified $NiAl_2$-LDH catalysts showed that Zr alone did not improve catalytic performance, but when combined with Au, a substantial increase in conversion was observed. For instance, 0.25% Au/$NiAl_2Zr_{4.5}$-LDH achieved 86% conversion, while 0.5% Au/$NiAl_2Zr_{4.5}$-LDH reached 100%. Notably, the 0.5% Au/$NiAl_2Zr_{4.5}$-LDH catalyst exhibited exceptional selectivity towards iPFE, with a 90% selectivity, highlighting the synergistic effect of Zr in stabilizing Au NPs and enhancing their catalytic efficiency.

Kinetic studies indicated that the hydrogenation reaction follows a second-order rate law, with the reaction rate significantly influenced by Au content. The catalytic mechanism involves the initial hydrogenation of furfural to FA, followed by the condensation of FA with isopropanol to form iPFE, facilitated by the acidic and basic sites of the LDH and Au NPs. These findings demonstrate the potential of Au/Zr-modified LDHs as highly selective and efficient catalysts for the sustainable production of bio-based chemicals from furfural.

The selective formation of these products indicates the catalytic system's ability to steer the reaction towards specific pathways, depending on the catalyst composition and reaction conditions.

III. Glucose photo oxidation

In the realm of organic transformations, C_1-oxidation of carbohydrates holds particular importance due to its capacity to generate highly valuable oxidized derivatives, including aldonic acids, salts, esters, and lactones. These derivatives find widespread use across numerous industries. The ongoing transition from fossil-based chemicals to renewable alternatives derived from carbohydrates, which constitute approximately 75% of biomass, has been largely driven by increasing concerns about the depletion of fossil resources and the environmental impact of pollution. However, traditional synthetic methods for producing these oxidized derivatives typically rely on harsh reagents, exhibit low selectivity, and present challenges in product separation.

In response to these challenges, gold nanoparticles (Au NPs) have emerged as a promising green alternative, offering enhanced selectivity and reduced waste in oxidation reactions. When supported on layered double hydroxides (LDHs), which provide a high surface area and strong metal-support interactions, these catalysts can facilitate photocatalytic reactions under mild conditions. The combination of Au NPs with LDHs leverages the plasmonic properties of gold and the basic sites of LDHs, enabling efficient and environmentally friendly transformations of carbohydrates.

The primary objective of this research was to explore the application of Au/LDH catalysts in the photocatalytic transformation of glucose into sodium D-gluconate. The catalyst selected for this study was a 0.5% Au/$NiAl_2Zr_{4.5}$-LDH, which had previously demonstrated excellent catalytic performance. The synthesis of sodium D-gluconate from glucose was conducted in the presence of H_2O_2, NaOH, and a light source, as illustrated in the provided reaction **Scheme V-2**.

To verify the photon-activating capability of the catalyst, DRUV-visible spectroscopy was employed to characterize the optical properties of the 0.5% Au/$NiAl_2Zr_{4.5}$-LDH catalyst. The DRUV-visible diffuse reflectance spectra revealed that the pristine $NiAl_2Zr_{4.5}$-LDH exhibited absorption bands at 375 nm and 644 nm, corresponding to electronic transitions within the material. Upon the incorporation of Au NPs, a new absorption band emerged at 545 nm, attributed to the localized surface plasmon resonance (LSPR) of the Au NPs. This LSPR band, along with the persistent absorption band at 644 nm, indicated a possible charge transfer between the Au NPs and the LDH support, which could enhance the electronic coupling and potentially improve the photocatalytic properties of the composite material.

To optimize the reaction conditions for the photocatalytic conversion of glucose into sodium D-gluconate, a full factorial experimental design (FFD) method was employed. Four factors (catalyst mass, H_2O_2 volume, NaOH mass, and reaction time) were selected for the factorial plan, each with two levels (high and low). The design matrix for the 2^4 full factorial design and the corresponding experimental responses (conversions) were developed.

The predictive models for estimating glucose conversion were expressed through a polynomial equation derived from the variance analysis. The equation demonstrated a linear relationship between the main effects and responses, allowing for the prediction of conversion rates under various

conditions. The validity of the model was further confirmed by comparing actual values with predicted values.

The optimized reaction conditions, determined by the FFD method, were experimentally applied to the photocatalytic oxidation of glucose into sodium D-gluconate using the 0.5% $Au/NiAl_2Zr_{4.5}$-LDH catalyst. Under the optimized conditions

The 0.5% $Au/NiAl_2Zr_{4.5}$-LDH catalyst demonstrated a significant potential for the photocatalytic oxidation of glucose into sodium D-gluconate under mild conditions. The successful application of the factorial experimental design method for optimizing reaction conditions highlights the effectiveness of this approach in improving conversion yields and selectivity in catalytic processes. This research provides a foundation for further exploration of Au/LDH catalysts in the sustainable transformation of biomass-derived carbohydrates into valuable chemical derivatives.

Publication

Journal of Environmental Chemical Engineering 12 (2024) 113357

Contents lists available at ScienceDirect

Journal of Environmental Chemical Engineering

journal homepage: www.elsevier.com/locate/jece

Zr-doped MgAl-LDH@Au nano-catalysts for selective and efficient oxidation of biomass-derived furfural

Dib Nihel [a,b], Bachir Redouane [a,*], Berrichi Amina [a,d], Blanco Ginesa [b,c], Bedrane Sumeya [a], Calvino José Juan [b,c]

[a] Laboratory of Catalysis and Synthesis in Organic Chemistry (LCSCO), University of Tlemcen, BP 119 Poˆle Imama, Tlemcen 13000, Algeria
[b] Departamento de Ciencia de los Materiales, Ingeniería Metalúrgica y Química Inorga´nica, Facultad de Ciencias, Universidad de Ca´diz, Campus Río San Pedro, Puerto Real, Ca´diz E-11510, Spain
[c] Instituto Universitario de Investigaci´on en Microscopía Electro´nica y Materiales (IMEYMAT), Universidad de Ca´diz,Campus Río San Pedro, Puerto Real, Ca´diz E-11510, Spain
[d] University of Ain Temouchent, BP 284, Ain T´emouchent 46000, Algeria

ARTICLE INFO

Keywords:
Biomass upgrading
Hydrotalcite-derived materials
Gold catalysts
Furfural oxidation
Succinic acid synthesis

ABSTRACT

Lignocellulosic biomass upgrading is a pivotal axis in the transition from an economy based on fossil resources to one reliant on renewable biomass resources. Within this context, low-cost Zr-doped MgAl-LDH@Aunano-catalysts are reported in this study as efficient catalysts to synthesize bio-based succinic acid. A series of Zr-doped MgAl-LDH and Au/Zr-doped MgAl-LDH catalysts have been successfully prepared. All catalysts have a lamellar double hydroxide structure LDH even after enrichment with Zr and addition of Au.Au NPs have small average sizes ranging from 1.2 to 8.5 nm. The materials under study showed exalted catalytic performances in the direct synthesis of succinic acid from bio based furfural via an aqueous phase oxidation reaction with H_2O_2. 84 % of furfural conversion and 99 % selectivity towards succinic acid were achieved.A positive synergy between Zr and Au NPs is highlighted and related to this catalytic performances improvement.

1. Introduction

In a world grappling with the pressing challenges of climate change and the decline of fossil resources, exploring innovative and sustainable solutions to replace current polluting chemical processes with environmentally friendly ones is a priority of many research groups both in academic andapplied industrial researches. Using renewable raw materials instead of fossil sources is one of the most interesting and explored ways to reduce the carbon impact.

In this context, lignocellulosic biomass emerges as a promising resource, offering huge potential to produce high-value chemicals and enablingcircular economy objectives to be achieved.As it happens with fossil sources, lignocellulosic biomass transformation goes through refining steps, commonly known as a bio-refinery, at the end of which platform molecules are produced. These molecules can subsequently be used as in put reactants in manyprocesses.

Furfural is one of the most important platform molecules due to its environmental, economic and valorisation potential [1–3]. Indeed, furfural resulting from the refining of lignocellulosic biomass, is an abundant and renewable reservoir that offers a sustainable substitute for fossil fuels [4,5]. Moreover, the inherent versatility of furfural's molecular structure makes it usable across various industrial sectors, spanning from fine chemicals to biofuels.

Succinic acid,also known traditionally as Amber acid, is a four-carbon dicarboxylic acid. Currently, it is being recognizedas a fundamental C_4 building blockof many important chemicals applied in food, chemical and pharmaceutical industries [6–9]. Additionally, succinic acid plays a pivotal role in the synthesis of biopolymers, polyesters, polyurethanes, plasticizers, and various other fine chemicals, highlighting its versatility across multiple industrial domains [10].

It is nowadays produced industrially from petroleum derivatives (acetylene and formaldehyde).Recently, processes using biomass as raw material and relying on fermentation technologies are emerging.However, these processes, although they open access to integrate a circular economy, have several defects linked to low yields and lack of economic competitiveness.

Against this backdrop, our study was directed towards the production of succinic acid, derived from furfural through a heterogeneous

* Corresponding author.
E-mail address: redouane.bachir@univ-tlemcen.dz (B. Redouane).

https://doi.org/10.1016/j.jece.2024.113357
Received 8 April 2024; Received in revised form 24 May 2024; Accepted 15 June 2024
Available online 16 June 2024

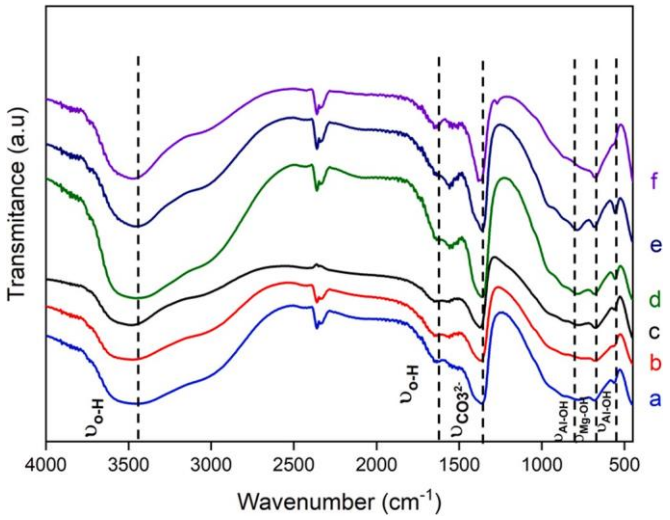

Fig. 1. FT-IR spectra of $MgAl_2$-LDH (a), $MgAl_2Zr_{4.5}$-LDH (b), 0.25 %Au/$MgAl_2Zr_{4.5}$-LDH (c), $Zr_{4.5}$-$MgAl_2$-LDH (d), 0.25 %Au/$Zr_{4.5}$-$MgAl_2$-LDH (e), 0.25 %Au/$MgAl_2$-LDH (f).

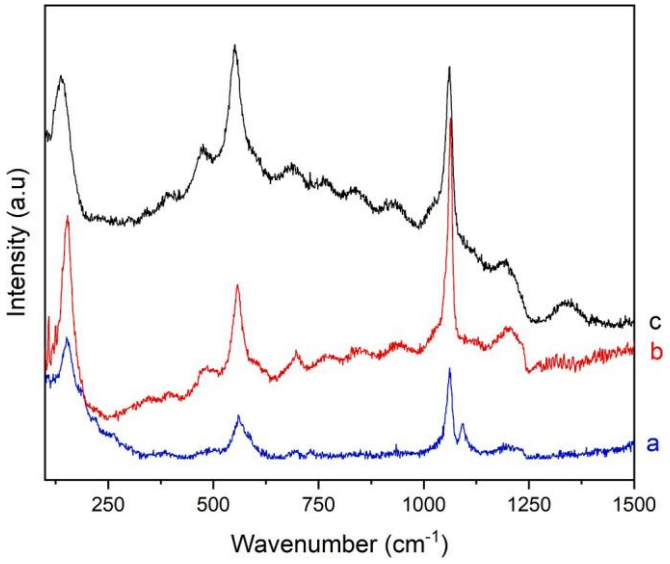

Fig. 2. Raman spectra of $MgAl_2$-LDH (a), $MgAl_2Zr_{4.5}$ -LDH (b), Zr-$MgAl_2$-LDH (c).

catalytic way. We have checked the efficiency of modified layered double hydroxides (LDHs) as catalysts for this transformation, offering notable advantages in terms of selectivity, yield, and sustainability. This catalytic approach holds high potential for converting furfural into a valuable resource, thus facilitating the transition towards a circular and sustainable bioeconomy.

Layered double hydroxides (LDHs)are classified as porous layered ionic solids. They have sheet structures of metal hydroxide cations intercalated by anions. [11,12]. A very common class derives from magnesium hydroxide where the layers are made of octahedral units Mg $(OH)_6$ with split edges. Besides the classic LDH having M^{2+}/M^{3+}cations in the brucite-type layers, there are also other systems that contain M^{+}/M^{3+}, M^{2+}/M^{4+} and $M^{2+}/M^{3+}/M^{4+}$ in the positive layers [13,14]. The general formula of an LDH is $[M^{2+}_{1-x}M^{3+}_{x}(OH)_2]^{x+}[A^{m-}_{x/m}\bullet nH_2O]^{x-}$, where M^{2+} and M^{3+} represent the di and trivalent metal ions, $x = M^{3+}/[M^{2+}+ M^{3+}]$ and A^{m-} are the intercalary anions of charge m [15–17].

The excess positive charge of the layers is usually compensated by simple and exchangeable inorganic anions located between the layers with interlayer water molecules.

Many physical and chemical LDH characteristics can be controlled by varying anions or also by varying the divalent/trivalent metal ions ratios in the sheets. A wide range of materials with various uses can thus be synthesized from LDH [18–21].

This allows for multiple applications of LDHs, especially with regard to heterogeneous catalysic applications by taking advantage of their unique adjustable base and surface properties [22–26]. Indeed, they wereused as flame retardants [27], effective adsorbents [28–31]or models of supramolecular systems [32,33]. LDHs also have tremendous potential in health care; they can be applied as antacids, drug stabilizers and even as transport vehicles in the delivery of drug molecules [34,35].

Moreover, nano-particles (NPs) have attractedgreat attention due to their tiny size leading to a high metal surface area volume ratio which can enhance catalytic activity [20]. Gold nano-particles (Au NPs) have been successfully immobilized on LDH using in-situ reduction strategies [36], homogeneous deposition precipitation [37] and calcination-reconstruction [38].

Recently, more attention has been paid to basic LDH-supported gold nanoparticles for many applications in a wide range of organic reactions [39–42]. Previous studies have shown that these catalysts can be more efficient than Au/oxide catalysts such as Au/TiO_2or Au/Al_2O_3[43–45].

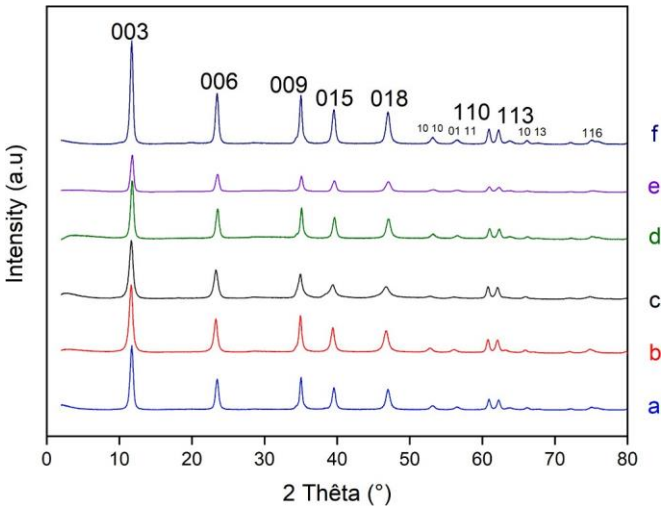

Fig. 3. XRD patterns of $MgAl_2$-LDH (a), $MgAl_2Zr_{4.5}$-LDH (b), $Zr_{4.5}$-$MgAl_2$-LDH (c), 0.25 %Au/$MgAl_2$-LDH (d) 0.25 %Au/$MgAl_2Zr_{4.5}$-LDH(e), 0.25 %Au/$Zr_{4.5}$-$MgAl_2$-LDH (f).

Table 1
Lattice parameters of materials.

Lattice parameters	d (110)	a (Å)	d (003)	c (Å)
$MgAl_2$-LDH	1.52	3.04	7.53	22.60
$MgAl_2Zr_{4.5}$-LDH	1.51	3.02	7.36	22.09
Zr-$MgAl_2$-LDH	1.51	3.03	7.49	22.70
0.25 %Au/$MgAl_2$-LDH	1.52	3.04	7.54	22.62
0.25 %Au/$MgAl_2Zr_{4.5}$-LDH	1.52	3.04	7.59	22.78
0.25 %Au/Zr-$MgAl_2$-LDH	1.42	2.85	7.06	21.18

Table 2
Gold loadings as measured by atomic absorption spectroscopy (AAS).

Catalysts	Theoretical Au content (wt%)	Experimental Au content (wt%)
0.25 %Au/$MgAl_2$-LDH	0.25	0.20
0.25 %Au/$MgAl_2Zr_{4.5}$-LDH	0.25	0.16
0.25 %Au/Zr-$MgAl_2$-LDH	0.25	0.24

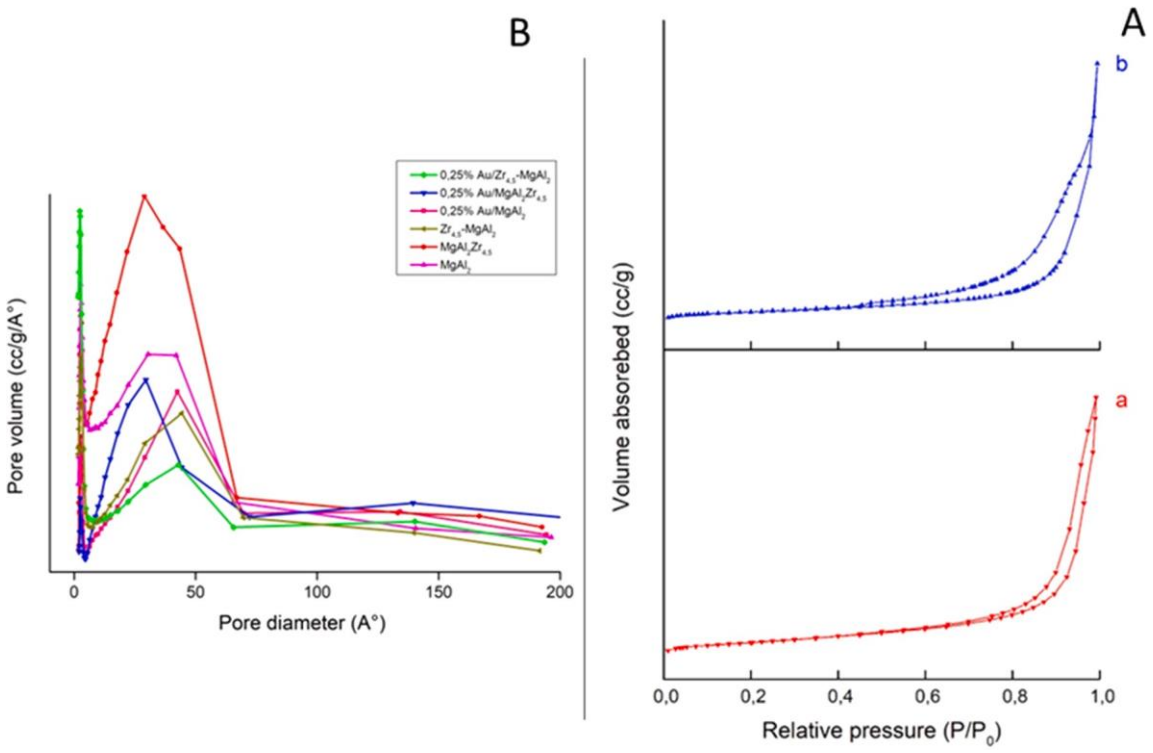

Fig. 4. a: N_2 adsorption–desorption isotherms $MgAl_2Zr_{4.5}$-LDH (a), 0.25 %Au/$MgAl_2Zr_{4.5}$-LDH (b) and Fig. 4**b:**Pore size distribution of different materials.

Table 3
Porous structure characterization of different catalysts.

Catalysts	S_{BET}(m^2/g)	V_p (cm^3/g)[a]	D_p (nm)[a]
$MgAl_2$-LDH	132	0.74	24
$MgAl_2Zr_{4.5}$-LDH	88	0.5	27
Zr-$MgAl_2$-LDH	158	1.05	27
0.25 %Au/$MgAl_2$-LDH	55	0.61	41
0.25 %Au/$MgAl_2Zr_{4.5}$-LDH	59	0.7	43
0.25 %Au/Zr-$MgAl_2$-LDH	96	0.5	24

[a] Pore volume diameters determined from BJH method[3].

Comparative studies showed that layered double hydroxide (LDH) catalysts can surpass Au/oxide catalysts in certain reactions in terms of yield and selectivity. For example, in CO oxidation, Au/TiO_2 catalysts, studied by Haruta et al.[46], exhibit high yields and excellent selectivity at low temperatures, while MgAl-LDH catalysts, analyzed by Zhang et al. [47], are less effective at very low temperatures but show good activity at moderate temperatures with good selectivity and fewer by-products. In furfural hydrogenation, Au/Al_2O_3 catalysts, studied by Teixeira et al. [48], achieved a 60 % yield with an important selectivity for furfuryl alcohol, though by-products are present, whereas LDH/NiFe catalysts, studied by Wang et al. [49], showed a higher yield of 80 % with superior selectivity for furfuryl alcohol. For bioethanol production from lignocellulosic biomass, Au/TiO_2 catalysts, studied by Liu et al. [50]., converted about 65 % of fermentable sugars with high selectivity but significant losses, while ZnCr-LDH catalysts, studied by the same authors [51], achieved a 70 % conversion with very good selectivity and fewer by-products. Thus, while Au/oxide catalysts are effective for certain applications, LDH catalysts offer advantages in terms of stability, cost, and overall performances in various chemical reactions.

Remarkable acid-base properties could be obtained upon modification of LDH structure with tetravalent cations [52–55]. Zr-containing hydrotalcite-derived materials have been proven to be effective catalysts for several reactions [55–57].

In this work, catalysts based on Zr-modified MgAl-LDH and Au NPs were designed, prepared and characterized. Homemade LDHs were modified with Zr in order to control their acid-base properties. Subsequently, a low content of gold (0.25 %wt) Au NPs was deposited on these Zr-modified MgAl-LDH. The catalytic performances of these materials were checked in the oxidation reaction of furfural by H_2O_2 in aqueous phase.

Basically, this reaction may lead to several productsas shown on scheme1.

2. Experimental section

2.1. Materials and catalysts synthesis

2.1.1. Synthesis of $MgAl_2$-LDH

$MgAl_2$-LDH synthesis was inspired by the work reported by G. Berrahou et al. [58]. First, a solution of magnesium nitrates and aluminum salts with a molar ratio of MgAl = 2, wasprepared by dissolving 0.2 mol of $Mg(NO_3)_3.9\ H_2O$ and 0.2 mol of $Al(NO_3)_2.6\ H_2O$ in 100 mL of distilled water (this solution is called MgAl salts).

Subsequently, 100 mL of a solution of Na_2CO_3 (0.05 mol) was placed in a flask at a temperature of 20–22°C. To this solution were added 100 mL of the MgAl salts solution as well as 100 mL of a sodium hydroxide solution (2 M) drop wise and at the same time. This operation is ensured by a flow pump. The final pH of the mixture must have a value of 10 ± 0.05. Finally, the precipitate was recovered by centrifugation and the solid obtained was washed several times with distilled water until complete elimination of the excess nitrates and then finally dried at 80°C over24 hours.

2.1.2. Modification of $MgAl_2$-LDH by Zr

The modification of $MgAl_2$-LDH by Zr was carried out according to two different ways. The first one is by introducing Zr in situ during the preparation of LDH and the second one is by adding Zr to $MgAl_2$-LDH post synthesis.

Materials prepared according to the first way are designated by $MgAl_2Zr_{4.5}$-LDH and those prepared according to the second way are

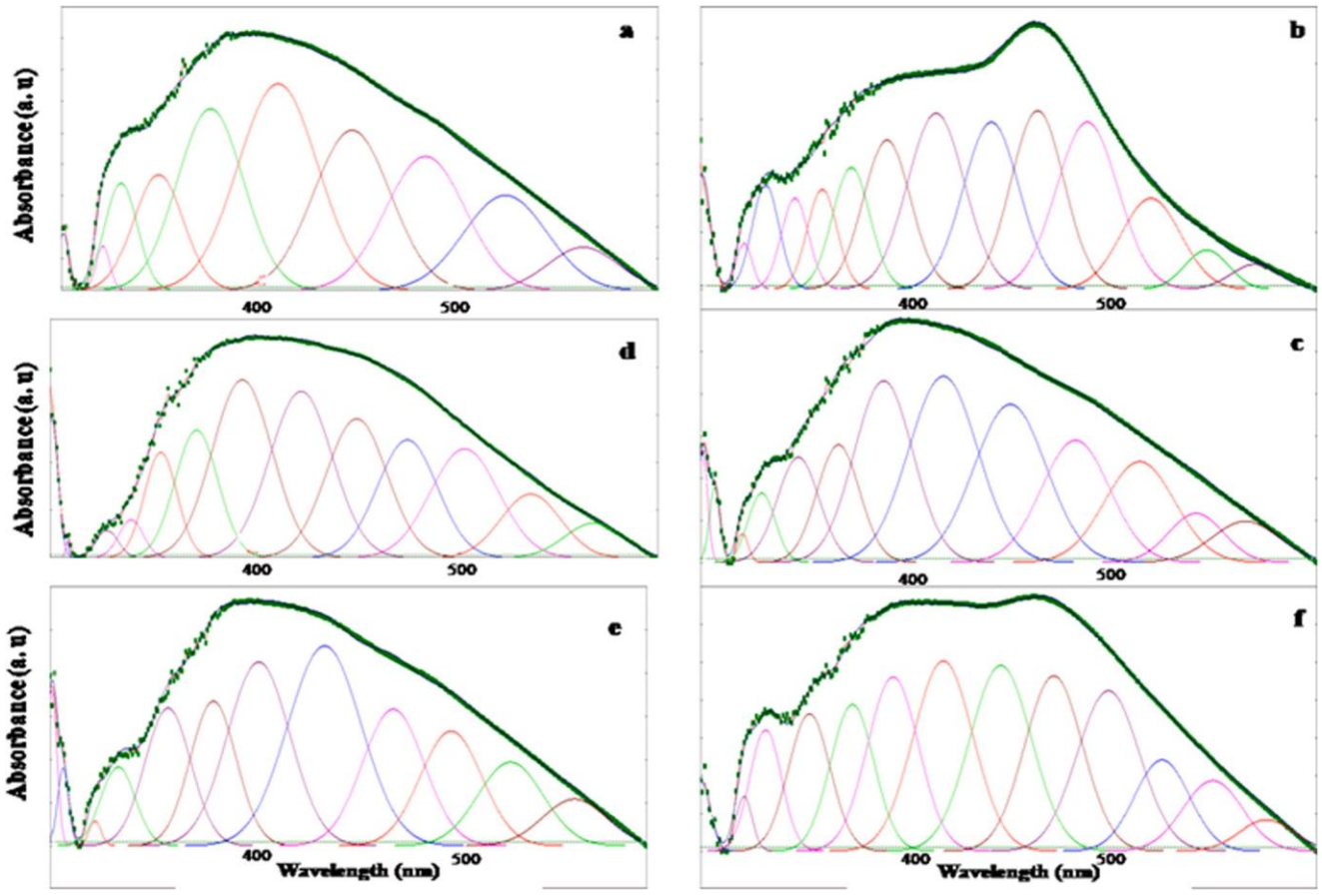

Fig. 5. DRS UV–vis spectra of $MgAl_2$-LDH (a), 0.25 %Au/$MgAl_2$-LDH (b), $MgAl_2Zr_{4.5}$-LDH (c), 0.25 %Au/$MgAl_2Zr_{4.5}$-LDH (d), $Zr_{4.5}$-$MgAl_2$-LDH (e), 0.25 %Au/$Zr_{4.5}MgAl_2$-LDH (f).

Table 4
Peak centers of deconvoluted DRS-UV visible spectra.

	$MgAl_2$-LDH	$MgAl_2Zr_{4.5}$-LDH	Zr-$MgAl_2$-LDH	Au/ $MgAl_2$-LDH	Au/$MgAl_2Zr_{4.5}$-LDH	Au/Zr-$MgAl_2$- LDH
Peak center	202	201	200	200	200	203
	-	212	215	-	211	213
	248	243	250	252	241	246
	283	296	280	289	266	268
	339	342	357	346	341	357
	405	400	409	392	403	405
	475	474	479	454	464	464
	-	-	-	522	520	526
	-	-	-	-	-	-
	549	550	561	-	-	-
	-	-	-	590	575	586
	630	632	643	659	640	655
	710	715	722	722	712	726
	800	800	800	800	797	800

designated by $Zr_{4.5}$-$MgAl_2$-LDH.

2.1.3. Synthesis of $MgAl_2Zr_{4.5}$-LDH

These materials were prepared according to the same procedure described for the synthesis of $MgAl_2$-LDH. The Zr was added to the solution containing the metallic salts of Mg and Al. The salts solution was obtained by dissolving 3.38 g $Mg(NO_3)_3.9\ H_2O$, 2.03 g $Al(NO_3)_2.6\ H_2O$ and 0.28g$ZrO(NO_3)_2.9\ H_2O$ in 100 mL of distilled water.

The solution thus prepared has a ratio of Mg/Al=2 and Al/Zr=4.5.

2.1.4. Synthesis of $Zr_{4.5}$-$MgAl_2$-LDH

Zr was added to $MgAl_2$-LDHby impregnation in excess water.

1 g of$MgAl_2$-LDH was introduced in a beaker with 100 mL of distilled water. A solution of 0,28 g of zirconium precursor $ZrO(NO_3)_2.9\ H_2O$ was added and the mixture was stirred for 24 hours. After filtration, the solid was washed and dried.

2.1.5. Preparation of 0.25 %Au/$MgAl_2Zr_{4.5}$-LDH and 0.25 %Au/$Zr_{4.5}$-$MgAl_2$-LDH

Gold-based monometallic catalyst wasprepared by ure-aprecipitationdeposition method (UPD)as described elsewhere [59,60]. 1 g of the support wasdispersedin 200 mL of distilled water in a double-wallreactor. The temperaturewasthen raised up to 80°C. Once this temperature was reached, 0.5mLof $HAuCl_4$ (10 g/L) solution to was

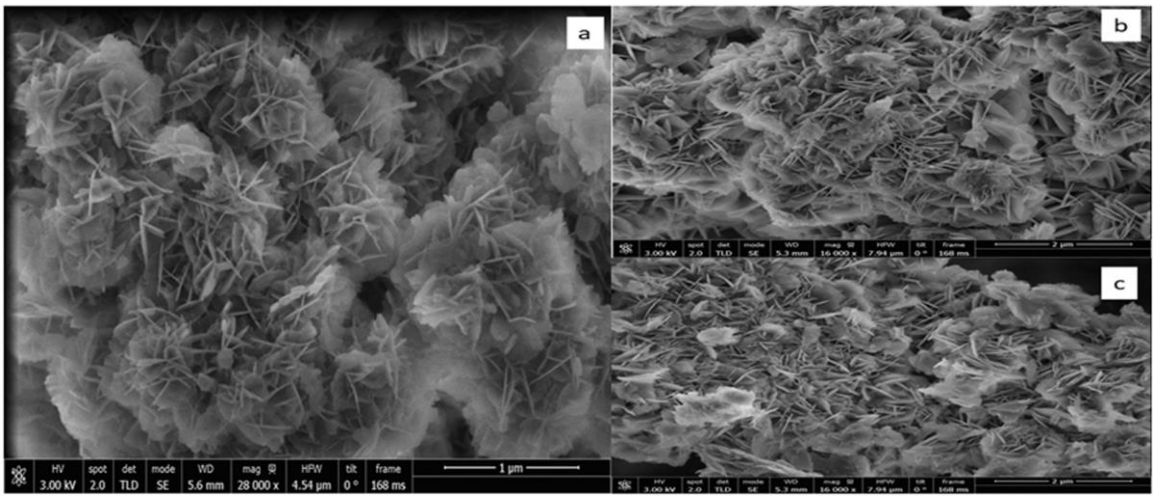

Fig. 6. SEM images of $MgAl_2$-LDH (a), $MgAl_2Zr_{4.5}$-LDH (b) and $Zr_{4.5}$-$MgAl_2$-LDH (c).

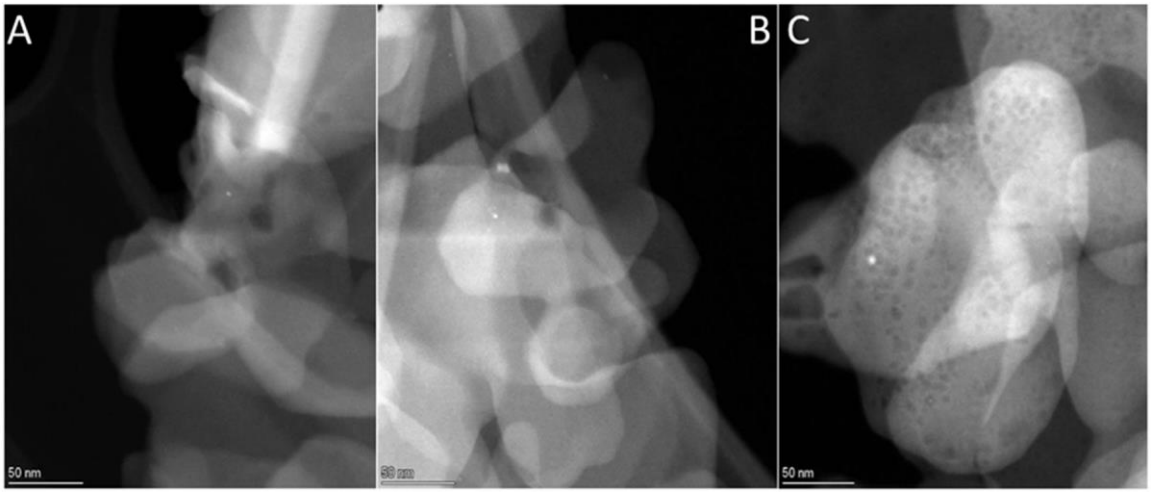

Fig. 7. HAADF-STEM images of 0.25 %Au/$MgAl_2$-LDH (A)0.25 %Au/$MgAl_2Zr_{4.5}$-LDH (B) and 0.25 %Au/$Zr_{4.5}$-$MgAl_2$-LDH.

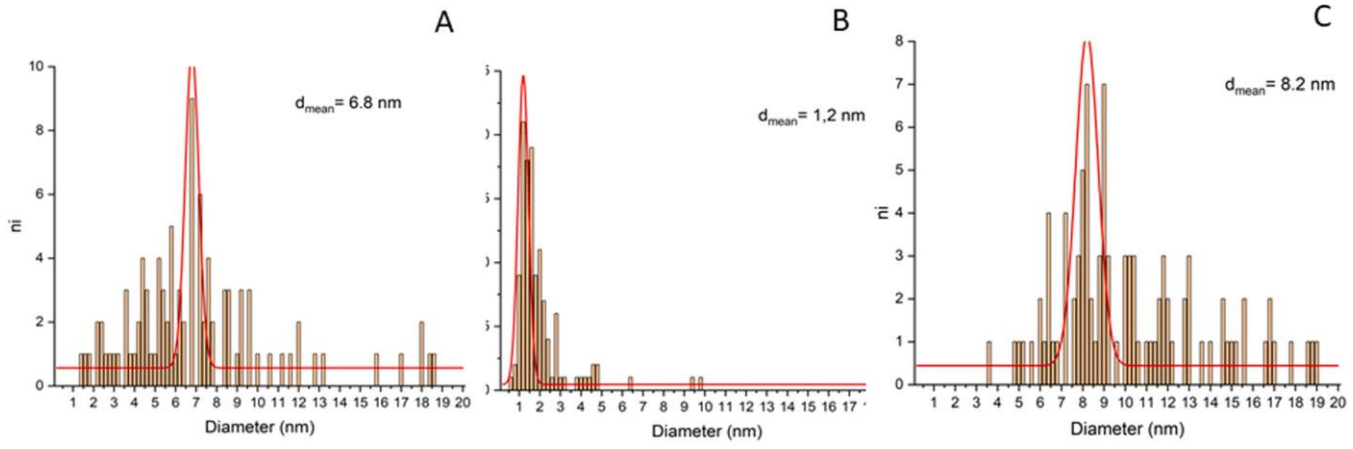

Fig. 8. Gold nanoparticles size distribution for 0.25 %Au/ $MgAl_2$-LDH (A) 0.25 %Au/ $MgAl_2Zr_{4.5}$-LDH (B) and 0.25 %Au/ $Zr_{4.5}$-$MgAl_2$-LDH (C).

added in order to reach a gold loading 0.25 wt%. 0.0012 mol of solid urea were next added and the mixture wasmaintained under vigorous agitation at the stabilized temperature of 80°C for 16 hours. The solid was finally filtered, washed several times with water and then dried at 80°C over 24 hours.

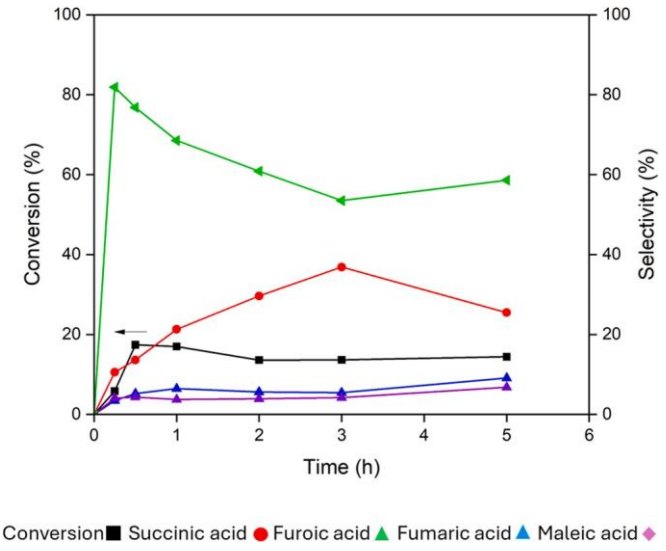

Fig. 9. Blank test: Conversion and product distribution for furfural oxidation without catalyst.

Table 5
Furfural conversion and products selectivity after 5 hoursof reaction.

	Conversion	Selectivity (%)			
	(%)	S.A.	Fu.A.	Fm.A.	M.A.
Blank reaction	14	25	59	9	7
$MgAl_2$-LDH	66	34	33	32	0
$MgAl_2Zr_{4.5}$-LDH	50	39	28	30	2
$Zr_{4.5}$-$MgAl_2$-LDH	99	45	25	6	14
0.25 %Au/$MgAl_2$-LDH	92	69	8	20	2
0.25 %Au/$MgAl_2Zr_{4.5}$-LDH	**84**	**99**	**1**	**0**	**0**
0.25 %Au/$Zr_{4.5}$-$MgAl_2$-LDH	59	97	2	1	0

S.A.: Succinic Acid, Fu.A: Furoic Acid, Fm.A.: Fumaric Acid, M.A.: Maleic Acid.

2.2. Materials characterizations

Atomic absorption spectroscopy (AAS) analysis was performed with a Perkin Elmer Instrument Analyst 300 with flame.FT-IR spectrawerer-ecordedat room temperature using an Agilent Technologies Cary 640 series equipped with ATR accessories in the spectral range from 400 to 4000 cm^{-1}usingKBr background. X-ray powderdiffractograms (XRD) werecollected in the range of 2θ = 10–80° using a Rigaku Miniflex 600 diffractometer with Ni-filtered Cu Kα radiation (λ = 1.541874 Å) using a scanning speed of 2 degrees per minute.Raman scattering data were collected using a Horiba Jobin-Yvon LABRAM HR spectrometer equipped with a Peltier-cooled CCD detector, and excitation source from a helium–neon laser at 633 nm with an accumulation time of 30 s.The specific surface area and pore volumes weredeterminedfrom N_2 adsorption-desorption isothermsat 77 K usingaQuantaChrome Nova 1000 instrument. The surface area wascalculated according to the Brunauer-Emmett-Teller (BET) method and the porosity distribution was determined by Barrett-Joyner-Halenda (BJH) analysis. Prior to physisorption measurements, samples wereoutgassedat 200°C for 2 h under vacuum.Diffusereflectance DRUV–Vis spectroscopy measurements were carried out at room temperature on a Lambda 800 UV–Vis spectrometer in the range of 200–800 nm. This apparatus was equipped with a diffusereflectance accessory set to collect the diffuse reflected light only. $BaSO_4$ was used as standard.Scanning electron microscopy (SEM) images wereobtained in a FEI Nova Nano SEM 450, while transmission electron microscopy (TEM) was carried out with a FEI-TALOS F200X microscope.

2.3. Catalytic tests

The oxidation of furfural wascarried out in a three-necked glass flask.2 mmol of distilled furfuraldehyde and 8 mmol H_2O_2freshly prepared werecharged in the reactor and heated to 80°C which is the reaction temperature. 0.08 g of catalyst was added to the flask. At this time, a vigorous stirring of the reaction mixture was started and considered as the initial time of the reaction (t_0).The reaction products were collected after 5 hours of reaction, diluted with distilled water then filtered before analysis. In order to study the reaction evolution over time, several samples from the reaction mixture were collected at various times, diluted with distilled water then filtered before analysis. The furfural oxidation products were analyzed by HPLC- YL9100 with YL 9120 equipped with UV–visible detector and C18 column (250 mm × 4.6 mm, 5 µm, Fuli instruments). The products were analyzed at the wavelength of 280 nm. The mobile phase was composed with 2 % acetonitrile, 25 % water, 73 % H_2SO_4. The flow rate and column temperature were 1.0 mL min^{-1} and 30°C, respectively.

The conversion of furfural wascalculated using the followingformula:

$$\text{Conversion (\%)} = \left(\frac{\text{Fur}_{\text{int}} - \text{Fur}_{fin}}{\text{Fur}_{\text{int}}}\right) \times 100$$

The selectivity of each product was calculated as follows:

$$\text{Selectivity(\%)} = \left(\frac{n_i}{n_T}\right) \times 100$$

Where Fur_{init} and Fur_{fin} indicate the initial and final mole number of furfural respectively,n_i and $n_T$indicatenumber of moles of product i and total number of moles of all products.

3. Results and discussion

3.1. Catalysts characterization

The FT-IR spectra corresponding to the samples $MgAl_2$-LDH, $MgAl_2Zr_{4.5}$-LDH and 0.25 % Au/$MgAl_2Zr_{4.5}$-LDH are shown in Fig. 1.

All samples showed a broad intense band between 3500 and 3000 cm^{-1} due to the OH stretching mode of the layer's hydroxy groups and of the interlayer's H_2O molecules [61]. Although the position of this band should be dependent on the nature of the cations layer, as its electronegativity will modify the electron density on the O-H bond (M-OH), the extreme broadness of this band, owing to hydrogen bonding, precludes any meaningful discussion [62].The band at 2300–2350 cm^{-1} is attributed to CO_2 (Fig. 1) [63].

The medium intensity absorption band around 1587 $cm^{-1}$is due to the deformation (νHOH bending) mode of H_2O_2 molecules [64,65]. A sharp and intense band appears at 1360 cm^{-1}describing the CO_3^{2-} ion stretching vibration [66]. Bands located at 963, 770 and 687 cm^{-1} are attributed to the ν1, ν2 and ν4 bands of CO_3^{2-}, respectively [67]. Bands observed below 1000 cm^{-1} are generally attributed to the vibration of M–O, M–O–M and O–M–O bonds in the brucite-likelattice[68–74]

Spectra of $Zr_{4.5}$-$MgAl_2$-LDH and $MgAl_2Zr_{4.5}$-LDH, (Fig. 1b and c) have similar profiles as the $MgAl_2$-LDH spectrum. However, bands below 1000 cm^{-1} attributed to M–O, M–O–M and O–M–O bonds are more intense for $Zr_{4.5}$-$MgAl_2$-LDH and $MgAl_2Zr_{4.5}$-LDH. This indicates a greater enrichment of the LDH surface with Zr-O, Zr-O-M species when Zr is introduced post-synthesis of LDH.

The Raman characterization is shown in Fig. 2. There is a band appearing at 1061 cm^{-1} typical of the C–O bond stretching of carbonate ion, which can be altered by H_2O molecules in the interlayer region of LDH. This band increase in the spectra corresponding to samples containing Zr can be attributed to multiple factors [75,76]. Zirconium electronic and structural properties enhance scattering [77]. Its introduction in the LDH alters the molecular environment, affecting crystal structures and bonding configurations, consequently influencing

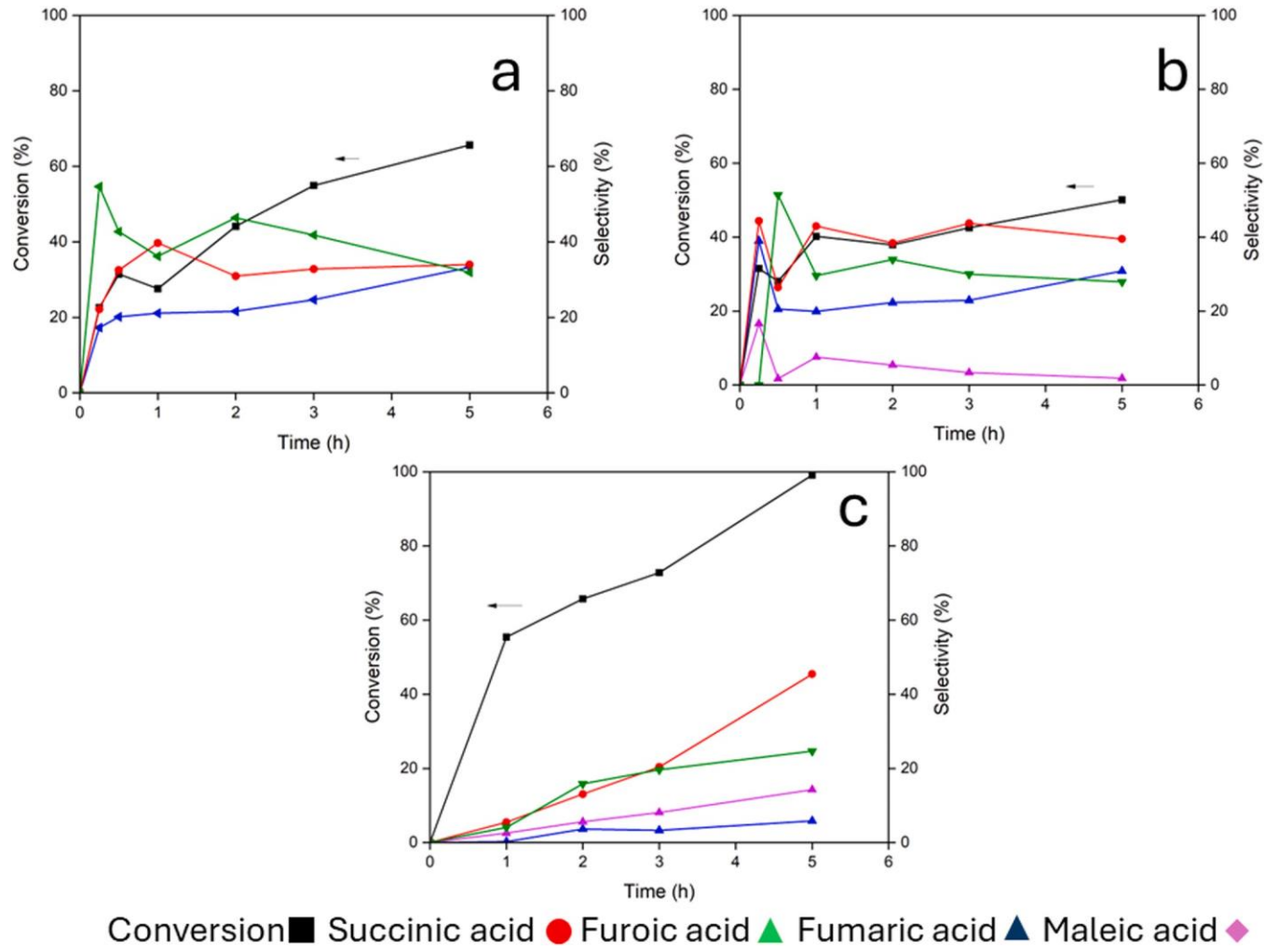

Fig. 10. Conversion and product distribution forfurfural oxidation using $MgAl_2$-LDH (a), $MgAl_2Zr_{4.5}$-LDH (b) and $Zr_{4.5}$-$MgAl_2$-LDH (c).

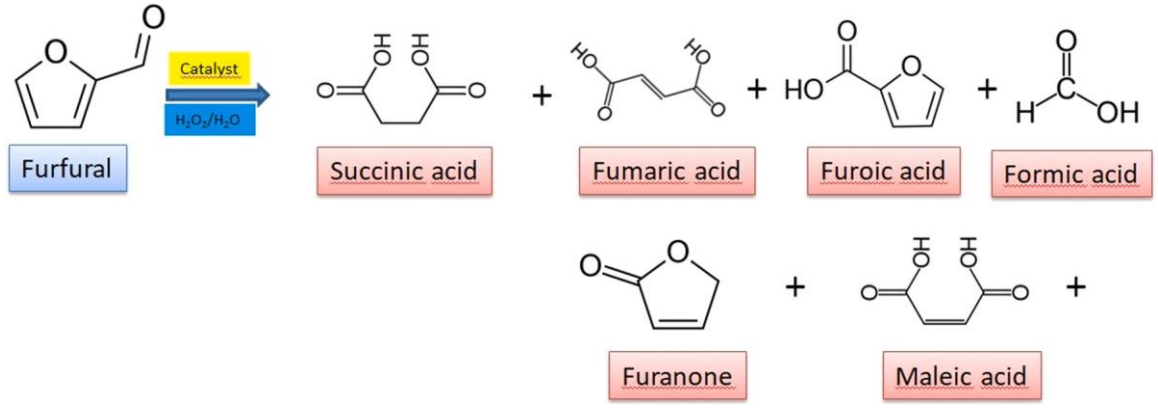

Scheme 1. Distribution of Furfural oxidation reaction products.

scattering cross-sections [30]. Incorporation of Zr cations modifies vibrational modes, leading to shifts in frequencies [78]. Surface plasmon resonance effects induced by Zr may amplify local electromagnetic fields, boosting scattering [79]. Variations in sample preparation methods, including Zr containing compounds, impact signal intensity [80].

The band situated at 555 cm^{-1} can be assigned to lattice vibrations of Mg–O–Al and Mg–O–Mg stretching in brucite-like layers [81,82].

A new band appearing around 700 cm^{-1} is attributed to the presence of carbonate anions in different environments with in the hydrotalcite structure [83].Gold containing samples showed very similar spectra to those of the supports, probably due to the very low gold content (0.25 %).

Fig. 3 showsthe XRD patterns of $MgAl_2$-LDH, $MgAl_2Zr_{4.5}$-LDHand 0.25 % Au/$MgAl_2Zr_{4.5}$-LDH samples. All sampleshavesharp and intense peaks situated at 2Θ = 11.73°, 23.50°, 35.03°, 62.92° and

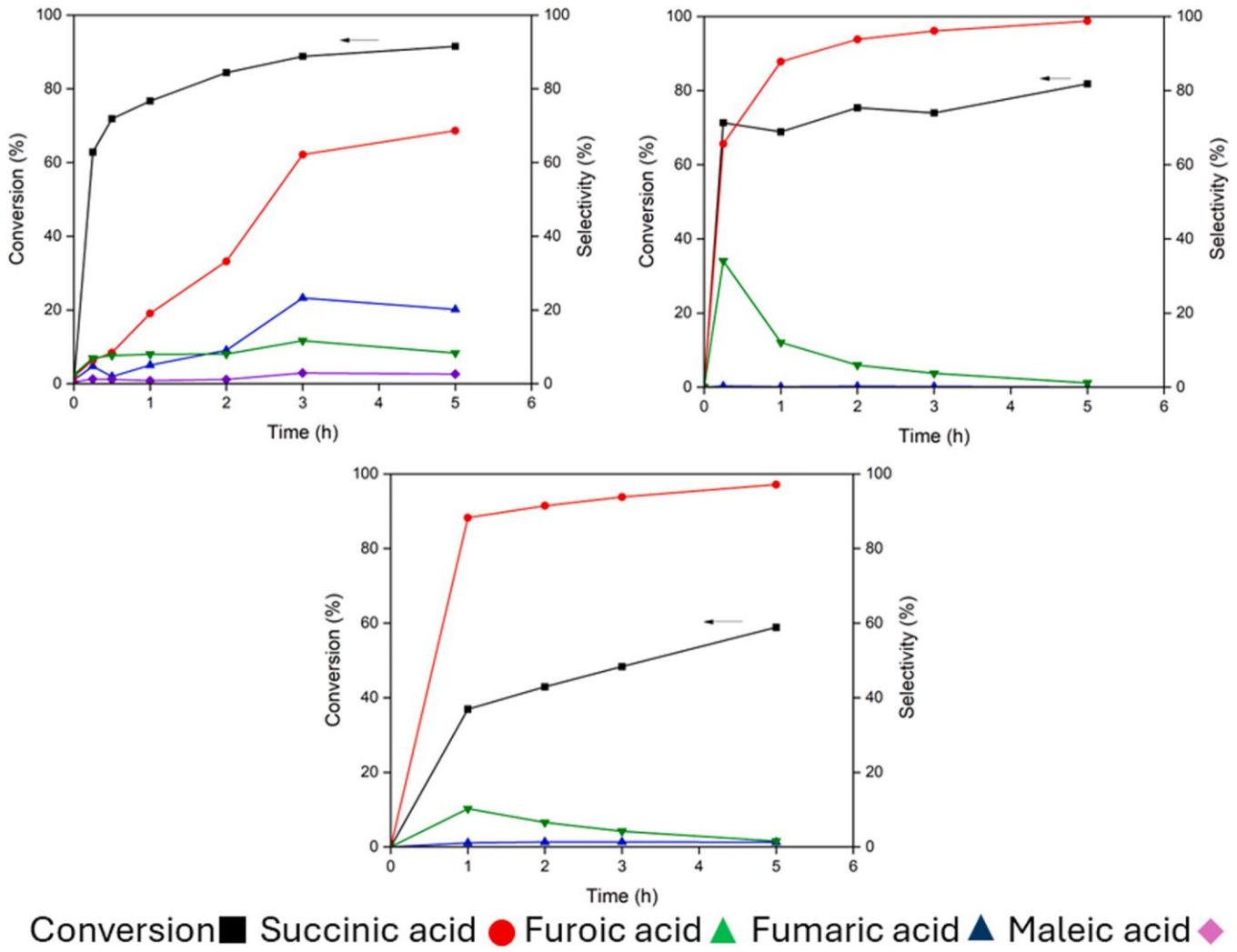

Fig. 11. Conversion and product distribution for furfural oxidation using 0.25 %Au/$MgAl_2$-LDH (a), 0.25 %Au/$MgAl_2Zr_{4.5}$-LDH(b) and 0.25 %Au/$Zr_{4.5}$-$MgAl_2$-LDH (c).

Table 6
Conversion of Furfural to Succinic Acid in the literature.

Catalyst	Furfural conversion (%)	S.A Selectivity (%)	Reference
Amberlyst-15	≥99	74	[9]
Nb_2O_5	≥99	25	
ZSM-5	≥99	17	
ZrO_2	≥99	17	
SO_4/ZrO_2	97	10	
Au/C	98	25	[92]
SO_3H-CD-Carbon	99	80	[93]
Amberlyst-35	99	78	
Cobalt-Porphyrin on CNT-NH_2	60	89	[94]
Amberlyst-15	93	/	[95]
Hydrotalcite-Supported Gold Nanoparticles	100	/	[96]
0.25 %Au/$MgAl_2Zr_{4.5}$-LDH	84	99	Present work

62.27°characteristic of the typical layered double hydroxide structure of MgAl-LDH and corresponding to(003), (006), (009), (110) and (113) planesrespectively. Other broad peaks at2Θ = 11.66°, 23.31°, 34.95°, 60.81° and 62.12° correspond to MgAl-LDH planes (015), (012) and (018)respectively [84]. However, no gold characteristic peaks were observed which is mostly due to the very low gold content (0.25 %) which might be under the technique detection limit [85].

The lattice parameters were calculated as $a = 2 \times d_{(110)}$and $c = 3 \times d_{(003)}$respectively (Table 1). The $d_{(003)}$values correspond to the basal spacing of two consecutive brucite-like hydroxide layers in the hydrotalcites. Therefore, the interlayer free spacing could be calculated by subtracting the brucite sheet thickness (0.480 nm as reported by Das et al. [86]) from the basal spacing $d_{(003)}$. Further analysis of the XRD patterns revealed some differences in the unit cell parameters among the three samples. Addition of Zr to $MgAl_2$-LDH leads to a slight variation of the "c" parameter with both synthesis techniques, while the "a" parameter remains constant. Indeed, the "c" parameter decreases with the one-pot preparation method and slightly increases with the impregnation method. This indicates that Zr was deposited in the LDH interlayer space in the Zr-$MgAl_2$-LDH sample. These results also may be explained by a Zr-induced distortion of the ordered layered structure when compared to MgAl hydrotalcite [63].

The addition of Au to $MgAl_2$-LDH and Zr-modified $MgAl_2$-LDH has no influence on the crystallographic parameters. This suggests that Au was deposited on the surface of these supports. However, it is worth signalling the 0.25 %Au/Zr-$MgAl_2$-LDH catalyst, where both "a" and "c" parameters decrease upon gold addition.These results suggest the presence of a strong interaction between Au, Zr, Mg and Al but they do not necessarily indicate the position of Au deposition since Zr can move

by interaction with Au [9]. It was reported in the literature that the isomorphic replacement of Al^{3+} (ionic radius, 0.053 nm) and/or Mg^{2+} (ionic radius, 0.065 nm) by Zr^{4+} leads to an increase of the "a" parameter since Zr^{4+} (ionic radius, 0.072 nm) are bigger [87]. In our case, there was a decrease of both "a" and "c" parameters, which could be explained by the creation of vacancies in the LDH lattice upon addition of gold. As Au^{3+} (ionic radius, 0,085 nm) are also bigger, the substitution of Al^{3+} and/or Mg^{2+} by $Au^{3+}$is ruled out as it would result in an increase of the lattice parameters.

Gold metal loadings for 0.25 %Au/$MgAl_2$-LDH, 0.25Au/$MgAl_2Zr_{4.5}$-LDH and 0.25 %Au/$Zr_{4.5}$-$MgAl_2$-LDH catalysts were measured by Atomic Absorption Spectroscopy (AAS) in order to check the efficiency of the UDP method to deposit gold on $MgAl_2$-LDH,$MgAl_2Zr_{4.5}$-LDH and Zr-$MgAl_2$-LDH. Results reported in (Table 2) show good agreement between the theoretical and experimental gold loadings.

Fig. 4a shows a N_2 adsorption–desorption isotherm representative of those of all samples. In fact, all isotherms are of type II according to the IUPAC classification, and they all exhibit H3 type hysteresis loops, indicating the presence of mesopores in the form of slits in the samples [88–90].

Fig. 4b shows the pores sizes distributions for all samples, showing strong heterogeneity in sizes, ranging from 2 to 50 nm.

It should be noted that the specific surface of $MgAl_2$-LDH which is 132 m^2/g has substantially increased after addition of Zr by impregnation on $MgAl_2$-LDH whereas it decreases when Zr was introduced during the preparation of the LDH (Table 3). This is in agreement with XRD results which indicate that in the first case Zr can occupy pillar positions between the LDH sheets.

The deposition of Au systematically induces a decrease in the specific surface area; which can be linked to an agglomeration of the LDH sheets during their basic treatment during the UPD method.

Diffuse reflectance DRUV–VIS spectroscopy was used to study the environment of metallic ions in the samples. Fig. 5 shows the deconvoluted spectra of all materials and Table 4 summarizes the peaks centers of all deconvoluted spectra.The six spectra show characteristic bands of $MgAl_2$-LDH. These bands are slightly affected after addition of Zr and Au. In addition, a new band at 211–215 nm appears after addition of Zr. This is assigned to Zr^{4+}species [91]. Finally, the three materials containing Au (0.25 %Au/$MgAl_2$-LDH, 0.25 % Au/$MgAl_2Zr_{4.5}$-LDH and 0.25 %Au/$Zr_{4.5}$-$MgAl_2$-LDH) exhibit bands at 522, 520 and 526 nm that are related to the gold plasmon resonance, characteristic of metallic nanoparticles.These results confirm on one hand, the introduction of Zr in the form of Zr^{4+}, and on the other hand, the deposition of Au^0 NPs.

The scanning electron microscopy (SEM) was performed on the MgAl-LDH and Zr-modified MgAl-LDH samples (Fig. 6). The corresponding SEM images show that the morphologies of LDH strongly depend on the composition of the matrices.

The formation of hydrotalcite by this preparative route has been confirmed by SEM (Fig. 6), where the "sand rose" characteristic morphology of hydrotalcite materials has been observed for all samples.

Fig. 7 shows HAADF-STEM images of $MgAl_2$-LDH (A), $MgAl_2Zr_{4.5}$-LDH (B) and $Zr_{4.5}$-$MgAl_2$-LDH (C) samples. It can be clearly seen that gold nanoparticles are uniformly distributed on the support.

Fig. 8 reports the gold nanoparticles size distribution. It shows that gold nanoparticles average sizes are 6.8, 1.2 and 8.2 nm for $MgAl_2$-LDH, $MgAl_2Zr_{4.5}$-LDH and $Zr_{4.5}$-$MgAl_2$-LDH respectively.

3.2. Catalytic tests

The catalytic performances of all materials in the furfural oxidation by H_2O_2 were tested as described in the Experimental section. A blank test was registered by running the reaction without catalyst (Fig. 9). In this case, conversion reached 14 % after 5 h (Table 5). Furoic acid (59 % selectivity) and succinic acid (25 % selectivity) are the main products. Smaller amounts of fumaric and maleic acids were detected as well (9 and 7 % selectivity, respectively). This first result shows a very low chemical reactivity of furfural in the presence of H_2O_2, due to the oxidizing ability of H_2O_2 and the thermal effect.

In Fig. 10a are reported the reaction results (furfural conversion and products distribution), with $MgAl_2$-LDH as catalyst. It shows a gradual increase of conversion over time, reaching up to 66 % after 5 hours of reaction. Moreover, the selectivity which initially was directed towards furoic acid, change over time and after 5 hours, succinic, furoic and fumaric acids were produced in equivalent quantities while maleic acid was not detected.

These results evidence the catalytic efficiency of $MgAl_2$-LDH improving the conversion from 14 % to 66 %. Moreover, the evolution of selectivity over time shows that the furoic acid is a primary product which is further transformed into succinic and fumaric acids.

3.2.1. Influence of Zr

Fig10b and 10c show the effect of Zr on the activity and selectivity depending on the synthesis method. In one hand, Fig. 10b representing the results of the reaction with $MgAl_2Zr_{4.5}$-LDHas catalyst (one pot synthesis) shows that the introduction of Zr in$MgAl_2$-LDH during LDH synthesis does not bring any improving of the catalytic activity. Instead, the conversion drops from 66 % to 50 %. Moreover, no particular effect on the furoic, succinic and fumaric acids selectivities is shown. (Table 5).

In the other hand,Zr has an extremely beneficial effecton the activity $MgAl_2$-LDHwhen it is added post-sybthesis. In fact, the results reported on Fig. 10c show that with the $Zr_{4.5}$-$MgAl_2$-LDH catalyst, conversion reaches 99 % with a selectivity of 45 % towards succinic acid (Table 5) after 5 hours. This exaltation may be due to a better accessibility of Zr cations to the reaction mixture when Zr is precipitated over the LDH, while Zr cations could be partially buried in the LDH lattice upon the one-pot synthesis.

It is worth mentioning that when using Zr-containing catalysts, a small amount of maleic acid is generated, despite succinic acid being the main product. Maleic acid and succinic acid share a similar structure (Scheme 1), differing only in the presence of a C–C double bond. The incorporation of Zr into layered double hydroxides (LDH) and the consequent production of maleic acid can be attributed to various factors. Firstly, Zr might catalyze secondary reactions such as the dehydration or isomerization of succinic acid into maleic acid. Additionally, the presence of Zr could result in the formation of specific reaction intermediates or by-products, including maleic acid, within the LDH during the reaction process.

3.2.2. Influence of gold nanoparticles

Fig. 11 presents conversions and product distributions of the three catalysts containing gold nano particles: Au/$MgAl_2$-LDH (a), Au/$MgAl_2Zr_{4.5}$-LDH (b), and Au/$Zr_{4.5}$-$MgAl_2$-LDH(c).

In the case of Au/$MgAl_2$-LDH, the results clearly show the promoting effect of gold nanoparticles on activity and selectivity. Indeed, the conversion is very high from the beginning of the reaction and reaches 92 % after 5 hours. In addition, the selectivity towards succinic acid is improved up to 70 %. This beneficial effect of gold nanoparticles is also observed in the case of the Au/$MgAl_2Zr_{4.5}$-LDH catalyst, as evident in Fig. 11b and Table 5, where the conversion exhibits remarkable stability throughout the evolution of the reaction, remaining consistently above 70 % within the initial 15 minutes. In this case as well, the reaction is clearly oriented towards succinic acid with a selectivity close to 70 % right from the beginning and reaches 99 % after 5 hours. Finally, withAu/$Zr_{4.5}$-$MgAl_2$-LDH (Fig. 11 c, Table 5) there is an unexpected decline in conversion when compared to the gold-free LDH (59 vs.99 %). That might be related to the structural modification observed upon XRD characterization, where this sample was the only material with a decrease in the "a" and "c" parameters, result of the creation of structure vacancies in the LDH lattice. This catalyst also containsthe biggest gold particles size (8.2 nm) that may be less active than the smaller ones (1.2 nm in the case of Au/$Zr_{4.5}$-$MgAl_2$-LDH our best catalyst).

Nevertheless, the effect of gold nanoparticles on selectivity is clearly shown. Indeed, within the first hour of reaction, the selectivity towards succinic acid is over 90 % and reaches 97 % at the end of the reaction. The results reported in Table 5 clearly evidence a positive synergy between gold and zirconium, as a significant enhancement of the reaction selectivity towards succinic acid in observed with both Au-based Zr-doped catalysts (Table 5, lines 6 and 7).

A comparative analysis of different catalysts reported in the literature for the conversion of furfural to succinic acid highlights the outstanding performances of the catalyst developed in the present work (Table 6). With a 84 % conversion, 0.25 %Au/$MgAl_2Zr_{4.5}$-LDH is the only catalyst achieving a total selectivity towards succinic acid production. In comparison, the other catalysts with total conversion (≥99 %), such as Amberlyst-15, Amberlyst-35 and SO_3H-CD-Carbon show lower selectivities not exceeding 80 %. From an industrial point of view, total selectivity means an important cost reduction as no separation steps will be required for the reaction products. This suggests a promising advancement in catalyst development, with significant potential to enhance the production of succinic acid from furfural.

4. Conclusions

This work focuses on the valorization of lignocellulosic biomass as a renewable raw material for producing high-value added chemicals. It aims to develop an eco-friendly and economically viable process for synthesizing succinic acid from biomass-derived furfural using heterogeneous catalysis, instead of petroleum derivatives.

The study develops catalysts based on gold nanoparticles (Au NPs) supported on layered double hydroxides (LDHs) modified with zirconium (Zr). Specifically, MgAl-LDHs were prepared and modified with Zr either during synthesis or post-synthesis. Zr modification during synthesis embeds Zr in the crystallographic structure, while post-synthesis modification embeds Zr in the inter-layer space, serving as pillars. These structural differences influence the catalytic behavior of these materials.

When combined with Au NPs, the catalysts showed excellent selectivities ≥ 97 %, in particular with 0.25 % Au/$Zr_{4.5}$-$MgAl_2$-LDH and 0.25 % Au/$MgAl_2Zr_{4.5}$-LDH. The best performances were achieved with 0.25 % Au/$MgAl_2Zr_{4.5}$-LDH, reaching an 84 % conversion and 99 % selectivity, which evidences a positive synergy between Zr and Au NPs.

The study paves the way for a sustainable, economically viable process for the production of succinic acid from renewable biomass.

CRediT authorship contribution statement

Redouane Bachir: Writing – review & editing, Validation, Supervision, Project administration, Conceptualization. **Bedrane Sumeya:** Methodology, Investigation. **Jose´ Juan Jose´ Calvino:** Supervision, Methodology, Conceptualization. **Dib Nihel:** Writing – original draft, Methodology, Investigation. **Berrichi Amina:** Methodology, Investigation. **Ginesa Blanco:** Writing – review & editing, Validation, Supervision, Investigation.

Declaration of Competing Interest

The authors declare that they have no known competing financial interests or personal relationships that could have appeared to influence the work reported in this paper.

Data availability

Data will be made available on request.

Acknowledgements

Authors would like to express their sincere appreciation to the Algerian General Directorate for Scientific Research and Technological Development (DGRSDT), as well as to the University of Cadiz, Spain and the University Aboubekr Belkaid Tlemcen, Algeria for the financial support of this research project.

References

[1] G. Dedes, Valorization of Lignocellulosic Biomass for the Production of Fructose and Furan Monomer Derivatives, (2024).
[2] G.T. Jaya, R. Insyani, J. Park, A.F. Barus, M.G. Sibi, V. Ranaware, D. Verma, J. Kim, One-pot conversion of lignocellulosic biomass to ketones and aromatics over a multifunctional Cu–Ru/ZSM-5 catalyst, Appl. Catal. B Environ. 312 (2022) 121368.
[3] Y.-A. Chen, H. Yang, D. Ouyang, T. Liu, D. Liu, X. Zhao, Construction of electron transfer chains with methylene blue and ferric ions for direct conversion of lignocellulosic biomass to electricity in a wide pH range, Appl. Catal. B Environ. 265 (2020) 118578.
[4] X. Li, P. Jia, T. Wang, Furfural: a promising platform compound for sustainable production of C4 and C5 chemicals, ACS Catal. 6 (2016) 7621–7640.
[5] X. Zhang, S. Xu, Q. Li, G. Zhou, H. Xia, Recent advances in the conversion of furfural into bio-chemicals through chemo-and bio-catalysis, RSC Adv. 11 (2021) 27042–27058.
[6] J.N. Chheda, G.W. Huber, J.A. Dumesic, Liquid-phase catalytic processing of biomass-derived oxygenated hydrocarbons to fuels and chemicals, Angew. Chem. Int. Ed. 46 (2007) 7164–7183.
[7] J.M. Pinazo, M.E. Domine, V. Parvulescu, F. Petru, Sustainability metrics for succinic acid production: a comparison between biomass-based and petrochemical routes, Catal. Today 239 (2015) 17–24.
[8] A. Mazie`re, P. Prinsen, A. García, R. Luque, C. Len, A review of progress in (bio) catalytic routes from/to renewable succinic acid, Biofuels Bioprod. Bioref. 11 (2017) 908–931.
[9] H. Choudhary, S. Nishimura, K. Ebitani, Metal-free oxidative synthesis of succinic acid from biomass-derived furan compounds using a solid acid catalyst with hydrogen peroxide, Appl. Catal. A Gen. 458 (2013) 55–62.
[10] W. Zhu, F. Tao, S. Chen, M. Li, Y. Yang, G. Lv, Efficient oxidative transformation of furfural into succinic acid over acidic metal-free graphene oxide, ACS Sustain. Chem. Eng. 7 (2018) 296–305.
[11] A. Vaccari, Clays and catalysis: a promising future, Appl. Clay Sci. 14 (1999) 161–198.
[12] E.A. Emam, Clays as catalysts in petroleum refining industry, ARPN J. Sci. Technol. 3 (2013) 356–375.
[13] V. Rives, Layered Double Hydroxides: Present and Future, Nova Publishers, 2001.
[14] J. He, M. Wei, B. Li, Y. Kang, D.G. Evans, X. Duan, Preparation of layered double hydroxides, LLayered Double Hydroxides (2006) 89–119.
[15] T. Baskaran, R. Kumaravel, J. Christopher, A. Sakthivel, Silicate anion-stabilized layered magnesium–aluminium hydrotalcite, RSC Adv. 3 (2013) 16392–16398.
[16] P. Neethu, A. Sreenavya, A. Sakthivel, Molybdate stabilized magnesium-iron hydrotalcite materials: potential catalysts for isoeugenol to vanillin and olefin epoxidation, Appl. Catal. A Gen. 623 (2021) 118292.
[17] T. Wang, D. Zhang, K. Fang, W. Zhu, Q. Peng, Z. Xie, Enhanced nitrate removal by physical activation and Mg/Al layered double hydroxide modified biochar derived from wood waste: adsorption characteristics and mechanisms, J. Environ. Chem. Eng. 9 (2021) 105184.
[18] T. Jyothi, T. Raja, K. Sreekumar, M. Talawar, B. Rao, Influence of acid–base properties of mixed oxides derived from hydrotalcite-like precursors in the transfer hydrogenation of propiophenone, J. Mol. Catal. A Chem. 157 (2000) 193–198.
[19] M. Sipiczki, E. Kuzmann, Z. Homonnay, J. Megyeri, I. P´alinko´, P. Sipos, The structure and stability of CaFe layered double hydroxides with various Ca: Fe ratios studied by Mo¨ssbauer spectroscopy, X-ray diffractometry and microscopic analysis, J. Mol. Struct. 1044 (2013) 116–120.
[20] S. Chaturvedi, P.N. Dave, N. Shah, Applications of nano-catalyst in new era, J. Saudi Chem. Soc. 16 (2012) 307–325.
[21] S. Tyagi, A. Kharkwal, M. Kharkwal, R. Sharma, Synthesis and characterization of layered double hydroxides containing optically active transition metal ion, Solid State Sci. 63 (2017) 93–102.
[22] M. Szabados, A.A. A´d´am, P. Traj, S. Mur´ath, K. Ba´an, P. B´elteky, Z. Ko´nya, A´. Kukovecz, P. Sipos, I. Pa´linko´, Mechanochemical and wet chemical syntheses of CaIn-layered double hydroxide and its performance in a transesterification reaction compared to those of other Ca2M (III) hydrocalumites (M: Al, Sc, V, Cr, Fe, Ga) and Mg (II)-, Ni (II)-, Co (II)-or Zn (II)-based hydrotalcites, J. Catal. 391 (2020) 282–297.
[23] A. Devarajan, S. Thiripuranthagan, R. Radhakrishnan, S. Kumaravel, Solvent free transesterification of glycerol into glycerol carbonate over nanostructured CaAl hydrotalcite catalyst, J. Nanosci. Nanotechnol. 18 (2018) 4588–4599.
[24] L.C. Meher, R. Gopinath, S. Naik, A.K. Dalai, Catalytic hydrogenolysis of glycerol to propylene glycol over mixed oxides derived from a hydrotalcite-type precursor, Ind. Eng. Chem. Res. 48 (2009) 1840–1846.
[25] J.M. Rodilla, P.P. Neves, S. Pombal, V. Rives, R. Trujillano, D. Díez, Hydrotalcite catalysis for the synthesis of new chiral building blocks, Nat. Prod. Res. 30 (2016) 834–840.
[26] B. Wiyantoko, P. Kurniawati, T.E. Purbaningtias, I. Fatimah, Synthesis and characterization of hydrotalcite at different Mg/Al molar ratios, Procedia Chem. 17 (2015) 21–26.

[27] S. Wang, J. Huang, F. Chen, Study on Mg-Al hydrotalcites in flame retardant paper preparation, BioResources 7 (2012) 0997–1007.
[28] Y. Yang, Y. Li, Y. Tao, X. Feng, Y. Ma, W. Ji, Y. Sun, Preparation of 3D flower-like double oxide hydrotalcite composite using pollen as a biotemplate and their effective adsorption for quinolone antibiotics, Microchem. J. (2021) 106796.
[29] P. Huang, Z. Liang, Z. Zhao, F. Cui, Synthesis of hydrotalcite-like compounds with drinking water treatment residuals for phosphorus recovery from wastewater, J. Clean. Prod. 301 (2021) 126976.
[30] A.-L. Johnston, E. Lester, O. Williams, R.L. Gomes, Understanding layered double hydroxide properties as sorbent materials for removing organic pollutants from environmental waters, J. Environ. Chem. Eng. 9 (2021) 105197.
[31] R. Wang, F. Chen, L. Gao, X. Ren, W. Guo, Cobalt (II)-intercalated layered double hydroxide as an efficient activator for catalytic oxidation of organic contaminants, J. Environ. Chem. Eng. 10 (2022) 108361.
[32] E. Delgado-Pinar, A.L. Costa, I.S. Gonç alves, M. Pineiro, M. Pillinger, J.Sr Seixas de Melo, Tuning the behavior of a hydrotalcite-supported sulfonated bithiophene from aggregation-caused quenching to efficient monomer luminescence, J. Phys. Chem. C. 125 (2021) 8294–8303.
[33] I. Shlar, E. Poverenov, A nanohybrid layered double hydroxide as an effective carrier for delivery and application of the phytohormone indole acetic acid, Colloids Surf. B Biointerfaces 207 (2021) 112032.
[34] A.S. Burange, C.S. Gopinath, Catalytic applications of hydrotalcite and related materials in multi-component reactions: concepts, challenges and future scope, Sustain. Chem. Pharm. 22 (2021) 100458.
[35] K. Simeonidis, E. Kaprara, P. Rivera-Gil, R. Xu, F.J. Teran, E. Kokkinos, A. Mitropoulos, N. Maniotis, L. Balcells, Hydrotalcite-embedded magnetite nanoparticles for hyperthermia-triggered chemotherapy, Nanomaterials 11 (2021) 1796.
[36] D. Varade, K. Haraguchi, Efficient approach for preparing gold nanoparticles in layered double hydroxide: synthesis, structure, and properties, J. Mater. Chem. 22 (2012) 17649–17655.
[37] Z. Ma, S. Dai, Design of novel structured gold nanocatalysts, ACS Catal. 1 (2011) 805–818.
[38] G. Carja, M. Birsanu, K. Okada, H. Garcia, Composite plasmonic gold/layered double hydroxides and derived mixed oxides as novel photocatalysts for hydrogen generation under solar irradiation, J. Mater. Chem. A 1 (2013) 9092–9098.
[39] T. Mitsudome, A. Noujima, Y. Mikami, T. Mizugaki, K. Jitsukawa, K. Kaneda, Supported gold and silver nanoparticles for catalytic deoxygenation of epoxides into alkenes, Angew. Chem. Int. Ed. 49 (2010) 5545–5548.
[40] T. Mitsudome, Y. Mikami, M. Matoba, T. Mizugaki, K. Jitsukawa, K. Kaneda, Design of a silver–cerium dioxide core–shell nanocomposite catalyst for chemoselective reduction reactions, Angew. Chem. Int. Ed. 51 (2012) 136–139.
[41] J. Wang, X. Lang, B. Zhaorigetu, M. Jia, J. Wang, X. Guo, J. Zhao, Aerobic oxidation of alcohols on Au nanocatalyst: insight to the roles of the Ni–Al layered double hydroxides support, ChemCatChem 6 (2014) 1737–1747.
[42] A. Smata, C. Yoshimura, One-step synthesis of magnetic–layered double hydroxide and its application for oxytetracycline removal from water, J. Environ. Chem. Eng. 10 (2022) 107819.
[43] P. Liu, Y. Guan, R.A. van Santen, C. Li, E.J. Hensen, Aerobic oxidation of alcohols over hydrotalcite-supported gold nanoparticles: the promotional effect of transition metal cations, Chem. Commun. 47 (2011) 11540–11542.
[44] F. Zhang, X. Zhao, C. Feng, B. Li, T. Chen, W. Lu, X. Lei, S. Xu, Crystal-face-selective supporting of gold nanoparticles on layered double hydroxide as efficient catalyst for epoxidation of styrene, ACS Catal. 1 (2011) 232–237.
[45] A. Noujima, T. Mitsudome, T. Mizugaki, K. Jitsukawa, K. Kaneda, Selective deoxygenation of epoxides to alkenes with molecular hydrogen using a hydrotalcite-supported gold catalyst: a concerted effect between gold nanoparticles and basic sites on a support, Angew. Chem. Int. Ed. 50 (2011) 2986–2989.
[46] G.J. Hutchings, Catalysis using gold containing materials, J. Catal. (2024) 115392.
[47] J. Zhang, M. Gao, R. Wang, X. Li, J. Wang, S. Li, K. Cao, J. Li, Y. Wang, Z. Zheng, Bifunctional role of oxygen vacancy in LDH supported Au nanoparticles catalyst for selective photocatalytic hydrogenation of cinnamaldehyde, Fuel 365 (2024) 131235.
[48] T.A. Silva, E. Teixeira-Neto, N. Lo´pez, L.M. Rossi, Volcano-like behavior of Au-Pd core-shell nanoparticles in the selective oxidation of alcohols, Sci. Rep. 4 (2014) 5766.
[49] G. Scott, E. Eley, R. Jones, K. Lim, R. Massey, H. Potter, V. Richards, M. White, V. Adams, B. Johnson, Cutting-edge research for a greener sustainable future www.rsc. org/greenchem, Green. Chem. 16 (2014) 1653–1671.
[50] R. Chong, J. Li, Y. Ma, B. Zhang, H. Han, C. Li, Selective conversion of aqueous glucose to value-added sugar aldose on TiO2-based photocatalysts, J. Catal. 314 (2014) 101–108.
[51] Q. Liu, J. Ma, K. Wang, T. Feng, M. Peng, Z. Yao, C. Fan, S. Komarneni, BiOCl and TiO2 deposited on exfoliated ZnCr-LDH to enhance visible-light photocatalytic decolorization of Rhodamine B, Ceram. Int. 43 (2017) 5751–5758.
[52] D. Wang, X. Zhang, J. Ma, H. Yu, J. Shen, W. Wei, La-modified mesoporous Mg–Al mixed oxides: effective and stable base catalysts for the synthesis of dimethyl carbonate from methyl carbamate and methanol, Catal. Sci. Technol. 6 (2016) 1530–1545.
[53] H. Li, X. Jiao, L. Li, N. Zhao, F. Xiao, W. Wei, Y. Sun, B. Zhang, Synthesis of glycerol carbonate by direct carbonylation of glycerol with CO 2 over solid catalysts derived from Zn/Al/La and Zn/Al/La/M (M= Li, Mg and Zr) hydrotalcites, Catal. Sci. Technol. 5 (2015) 989–1005.
[54] P. Liu, M. Derchi, E.J. Hensen, Promotional effect of transition metal doping on the basicity and activity of calcined hydrotalcite catalysts for glycerol carbonate synthesis, Appl. Catal. B Environ. 144 (2014) 135–143.
[55] P. Gao, F. Li, H. Zhan, N. Zhao, F. Xiao, W. Wei, L. Zhong, H. Wang, Y. Sun, Influence of Zr on the performance of Cu/Zn/Al/Zr catalysts via hydrotalcite-like precursors for CO2 hydrogenation to methanol, J. Catal. 298 (2013) 51–60.
[56] J. Nowicki, J. Lach, M. Organek, E. Sabura, Transesterification of rapeseed oil to biodiesel over Zr-dopped MgAl hydrotalcites, Appl. Catal. A Gen. 524 (2016) 17–24.
[57] Y. Wang, G. Ding, X. Yang, H. Zheng, Y. Zhu, Y. Li, Selectively convert fructose to furfural or hydroxymethylfurfural on Beta zeolite: the manipulation of solvent effects, Appl. Catal. B Environ. 235 (2018) 150–157.
[58] G. Berrahou-Harchaoui, R. Bachir, S. Bedrane, J.J. Calvino, J.C. Hernandez Garrido, Oxidation of furfural to bio-based molecules with hydrogen peroxide via modified layered double hydroxides: the effect of gold nanoparticles on the selectivity, J. Porous Mater. 30 (2023) 55–64.
[59] N. Ameur, S. Bedrane, R. Bachir, A. Choukchou-Braham, Influence of nanoparticles oxidation state in gold based catalysts on the product selectivity in liquid phase oxidation of cyclohexene, J. Mol. Catal. A Chem. 374 (2013) 1–6.
[60] N. Ameur, A. Berrichi, S. Bedrane, R. Bachir, Preparation and characterization of Au/Al2O3 and Au-Fe/Al2O3 materials, active and selective catalysts in oxidation of cyclohexene, in: Advanced Materials Research, Trans Tech Publ, 2014, pp. 48–52.
[61] M.J. Hernandez-Moreno, M.A. Ulibarri, J. Rendon, C.J. Serna, IR characteristics of hydrotalcite-like compounds, Phys. Chem. Miner. 12 (1985) 34–38.
[62] V. Rives, S. Kannan, Layered double hydroxides with the hydrotalcite-type structure containing Cu2+, Ni2+ and Al3, J. Mater. Chem. 10 (2000) 489–495.
[63] I.I. Soykal, H. Sohn, U.S. Ozkan, Effect of support particle size in steam reforming of ethanol over Co/CeO2 catalysts, ACS Catal. 2 (2012) 2335–2348.
[64] H.-y Zeng, Z. Feng, X. Deng, Y.-q Li, Activation of Mg–Al hydrotalcite catalysts for transesterification of rape oil, Fuel 87 (2008) 3071–3076.
[65] H.-Y. Zeng, S. Xu, M.-C. Liao, Z.-Q. Zhang, C. Zhao, Activation of reconstructed Mg/Al hydrotalcites in the transesterification of microalgae oil, Appl. Clay Sci. 91 (2014) 16–24.
[66] Z.-q Zhang, M.-c Liao, H.-Y. Zeng, S. Xu, X.-j Liu, J.-z Du, P.-h Zhu, Q.-j Huang, Temperature effect on chromium (VI) removal by Mg/Al mixed metal oxides as adsorbents, Appl. Clay Sci. 102 (2014) 246–253.
[67] A. Di Bitetto, G. Kervern, E. Andr´e, P. Durand, C. Carteret, Carbonate–hydrogenocarbonate coexistence and dynamics in layered double hydroxides, J. Phys. Chem. C. 121 (2017) 6104–6112.
[68] M. del Arco, R. Trujillano, V. Rives, Cobalt–iron hydroxycarbonates and their evolution to mixed oxides with spinel structure, J. Mater. Chem. 8 (1998) 761–767.
[69] E. Uzunova, D. Klissurski, I. Mitov, P. Stefanov, Cobalt-iron hydroxide carbonate as a precursor for the synthesis of high-dispersity spinel mixed oxides, Chem. Mater. 5 (1993) 576–582.
[70] H.C.B. Hansen, C.B. Koch, R.M. Taylor, Synthesis and characterization of cobalt (II)-iron (III) hydroxide carbonate, a layered double hydroxide belonging to the pyroaurite group, J. Solid State Chem. 113 (1994) 46–53.
[71] K. Rybka, J. Matusik, A. Kuligiewicz, T. Leivisk¨a, G. Cempura, Surface chemistry and structure evaluation of Mg/Al and Mg/Fe LDH derived from magnesite and dolomite in comparison to LDH obtained from chemicals, Appl. Surf. Sci. 538 (2021) 147923.
[72] R.G.L. Gonçalves, P.A. Lopes, J.A. Resende, F.G. Pinto, J. Tronto, M.C. Guerreiro, L. C.A. de Oliveira, W. de Castro Nunes, J.L. Neto, Performance of magnetite/layered double hydroxide composite for dye removal via adsorption, Fenton and photo-Fenton processes, Appl. Clay Sci. 179 (2019) 105152.
[73] P.D. Marcato, N.V. Parizotto, D.S.T. Martinez, A.J. Paula, I.R. Ferreira, P.S. Melo, N. Dur´an, O.L. Alves, New hybrid material based on layered double hydroxides and biogenic silver nanoparticles: antimicrobial activity and cytotoxic effect, J. Braz. Chem. Soc. 24 (2013) 266–272.
[74] L. Gritsch, C. Lovell, W.H. Goldmann, A.R. Boccaccini, Fabrication and characterization of copper (II)-chitosan complexes as antibiotic-free antibacterial biomaterial, Carbohydr. Polym. 179 (2018) 370–378.
[75] D.P. Debecker, E.M. Gaigneaux, G. Busca, Exploring, tuning, and exploiting the basicity of hydrotalcites for applications in heterogeneous catalysis, Chem. –A Eur. J. 15 (2009) 3920–3935.
[76] D. Tichit, M.N. Bennani, F. Figueras, J.R. Ruiz, Decomposition processes and characterization of the surface basicity of Cl-and CO32-hydrotalcites, Langmuir 14 (1998) 2086–2091.
[77] M. Yi, Y. Zhang, J. Xu, D. Deng, Z. Mao, X. Meng, X. Shi, B. Zhao, Surface-enhanced Raman scattering activity of ZrO2 nanoparticles: effect of tetragonal and monoclinic phases, Nanomaterials 11 (2021) 2162.
[78] J. Huo, X. Min, Y. Wang, Zirconium-modified natural clays for phosphate removal: effect of clay minerals, Environ. Res. 194 (2021) 110685.
[79] M. Vargas-Zamarripa, A.A. Rivera, U. Sierra, P. Salas, A.H. Serafín-Mun˜oz, G. Ramírez-García, Improved charge-transfer resonance in graphene oxide/ZrO2 substrates for plasmonic-free SERS determination of methyl parathion, Chemosphere 320 (2023) 138081.
[80] F.C. Jentoft, A. Hahn, J. Kro¨hnert, G. Lorenz, R.E. Jentoft, T. Ressler, U. Wild, R. Schlo¨gl, C. H¨aßner, K. Ko¨hler, Incorporation of manganese and iron into the zirconia lattice in promoted sulfated zirconia catalysts, J. Catal. 224 (2004) 124–137.
[81] I.O. Iordanov, V.M. Bermudez, C.K. Knox, Computational modeling of the structure and properties of Zr (OH) 4, J. Phys. Chem. C. 122 (2018) 5385–5400.
[82] V.R. Cunha, P.A. Petersen, M.B. Goncalves, H.M. Petrilli, C. Taviot-Gueho, F. Leroux, M.L. Temperini, V.R. Constantino, Structural, spectroscopic (NMR, IR, and Raman), and DFT investigation of the self-assembled nanostructure of pravastatin-LDH (layered double hydroxides) systems, Chem. Mater. 24 (2012) 1415–1425.

[83] R.L. Frost, S.J. Palmer, L.M. Grand, Synthesis and Raman spectroscopy of indium-based hydrotalcites of formula Mg6In2 (CO3)(OH) 16· 4H2O, J. Raman Spectrosc. 41 (2010) 1797–1802.
[84] F. Cavani, F. Trifiro, A. Vaccari, Hydrotalcite-type anionic clays: preparation, properties and applications, Catal. Today 11 (1991) 173–301.
[85] J. Thuriot-Roukos, R. Khadraoui, Sb Paul, R. Wojcieszak, Raman spectroscopy applied to monitor furfural liquid-phase oxidation catalyzed by supported gold nanoparticles, ACS Omega 5 (2020) 14283–14290.
[86] N. Das, R. Das, Insertion of chromium (III) ascorbate complex into layered double hydroxide through reduction of intercalated chromate by ascorbic acid, Appl. Clay Sci. 42 (2008) 90–94.
[87] N. Das, J. Konar, M. Mohanta, S. Srivastava, Adsorption of Cr (VI) and Se (IV) from their aqueous solutions onto Zr4+-substituted ZnAl/MgAl-layered double hydroxides: effect of Zr4+ substitution in the layer, J. Colloid Interface Sci. 270 (2004) 1–8.
[88] N.D. Hutson, S.A. Speakman, E.A. Payzant, Structural effects on the high temperature adsorption of CO2 on a synthetic hydrotalcite, Chem. Mater. 16 (2004) 4135–4143.
[89] S.K. Yun, T.J. Pinnavaia, Water content and particle texture of synthetic hydrotalcite-like layered double hydroxides, Chem. Mater. 7 (1995) 348–354.
[90] G. Zi, Z. Yan, Y. Wang, Y. Chen, Y. Guo, F. Yuan, W. Gao, Y. Wang, J. Wang, Catalytic hydrothermal conversion of carboxymethyl cellulose to value-added chemicals over metal–organic framework MIL-53 (Al), Carbohydr. Polym. 115 (2015) 146–151.
[91] H. Cao, X. Qiu, B. Luo, Y. Liang, Y. Zhang, R. Tan, M. Zhao, Q. Zhu, Synthesis and room-temperature ultraviolet photoluminescence properties of zirconia nanowires, Adv. Funct. Mater. 14 (2004) 243–246.
[92] M.L. Granados, J. Moreno, A. Alba-Rubio, J. Iglesias, D.M. Alonso, R. Mariscal, Catalytic transfer hydrogenation of maleic acid with stoichiometric amounts of formic acid in aqueous phase: paving the way for more sustainable succinic acid production, Green. Chem. 22 (2020) 1859–1872.
[93] P. Maneechakr, S. Karnjanakom, Catalytic transformation of furfural into bio-based succinic acid via ultrasonic oxidation using β-cyclodextrin-SO3H carbon catalyst: a liquid biofuel candidate, Energy Convers. Manag. 154 (2017) 299–310.
[94] K. Anjali, S. Nishimura, Efficient conversion of furfural to succinic acid using cobalt-porphyrin based catalysts and molecular oxygen, J. Catal. 428 (2023) 115182.
[95] S. Fulignati, D. Licursi, N. Di Fidio, C. Antonetti, A.M.Raspolli Galletti, Novel challenges on the catalytic synthesis of 5-hydroxymethylfurfural (HMF) from real feedstocks, Catalysts 12 (2022) 1664.
[96] Z.-H. Zhang, Z. Sun, T.-Q. Yuan, Recent advances in the catalytic upgrading of biomass platform chemicals via hydrotalcite-derived metal catalysts, Trans. Tianjin Univ. 28 (2022) 89–111.

molecules

MDPI

Article

Exploring the Photocatalytic Efficiency of Gold Nanoparticles Deposited on Ni-Al-Zr-Layered Double Hydroxides for Selective Glucose Oxidation

Nihel Dib [1,2,3], Frédéric Sauvage [4], Lucie Quéhon [4], Khadidja Khaldi [5], Sumeya Bedrane [1], José Juan Calvino [2,3], Redouane Bachir [1], Ginesa Blanco [2,3] and Gwladys Pourceau [4,6,*]

1 Laboratory of Catalysis and Synthesis in Organic Chemistry (LCSCO), University of Tlemcen, BP 119, Tlemcen 13000, Algeria
2 Departamento de Ciencia de los Materiales, Ingeniería Metalúrgica y Química Inorgánica, Facultad de Ciencias, Universidad de Cádiz, Campus Río San Pedro, E-11510 Puerto Real, Cádiz, Spain
3 Instituto Universitario de Investigación en Microscopía Electrónica y Materiales (IMEYMAT), Universidad de Cádiz, Campus Río San Pedro, E-11510 Puerto Real, Cádiz, Spain
4 Laboratoire de Réactivité et Chimie des Solides (LRCS), UMR CNRS 7314, Université de Picardie Jules Verne, Hub de L'énergie, 15 rue Baudelocque, FR-80000 Amiens, France
5 Centre de Recherche Scientifique et Technique en Analyses Physico-Chimiques CRAPC, BP 384, Tipaza 42004, Algeria
6 Laboratoire de Glycochimie et des Agroressources d'Amiens (LG2A) UR 7378, Université de Picardie Jules Verne, FR-80000 Amiens, France
* Correspondence: gwladys.pourceau@u-picardie.fr

Abstract: Confronting escalating challenges in energy security and environmental sustainability has intensified interest in renewable sources for fuels and chemicals. Among the most promising alternatives, sugars derived from biomass are emerging as a cornerstone in advancing an environmentally sustainable economy. Within this framework, the development of sunlight-driven carbohydrate oxidation is of significant interest, as it enables the production of a broad spectrum of high-value, bio-sourced chemicals through eco-friendly processes. Gold nanoparticles (Au NPs) immobilized on inorganic supports have demonstrated considerable potential in this area, although the methodology still requires further exploration. In this study, we explored the selective oxidation of glucose into the corresponding gluconic acid salt in presence of a novel Au/Ni-Al-Zr-layered double hydroxide (LDH) photocatalyst under standardized A.M. 1.5 G light illumination. To optimize the photocatalytic conditions, an experimental plan is herein proposed, highlighting the critical influences of both catalyst loading and pH. In optimal conditions, the Au catalyst demonstrated a high efficiency, achieving 87% glucose conversion and 100% selectivity towards gluconic acid in only 90 min. By means of long-pass filters to select the incident light energy to the photocatalytic reactor, we evidenced that the charge transfer processes were occurring from the Ni-Al-Zr LDH support to the gold nanoparticles, thus opening new directions towards further photocatalyst modifications. This work underlines the potential of Au/LDH materials for sunlight-driven photocatalysis and provides a pathway for the sustainable production of high-value chemicals from renewable biomass sources.

Keywords: photocatalysis; layered double hydroxides; gold nanoparticles; glucose oxidation

Academic Editor: Chen Chen

Received: 29 November 2024
Revised: 20 December 2024
Accepted: 23 December 2024
Published: 24 December 2024

Citation: Dib, N.; Sauvage, F.; Quéhon, L.; Khaldi, K.; Bedrane, S.; Calvino, J.J.; Bachir, R.; Blanco, G.; Pourceau, G. Exploring the Photocatalytic Efficiency of Gold Nanoparticles Deposited on Ni-Al-Zr-Layered Double Hydroxides for Selective Glucose Oxidation. *Molecules* **2025**, *30*, 13. https://doi.org/10.3390/molecules30010013

1. Introduction

The increasing issues related to the depletion of fossil resources and the pollution generated by their use have sparked great enthusiasm for the production of renewable chemicals,

especially those coming from carbohydrates, which account for 75% of biomass [1]. Among the different organic transformations carbohydrates can undergo, C1-oxidation is of particular interest since it leads to oxidized derivatives, such as aldonic acids, salts, esters, or lactones, which are widely used in the chemical, pharmaceutical, food, and cosmetic industries [2]. However, the traditional methods used for the synthesis of oxidized derivatives typically exhibit several inherent limitations [3,4]. These include potential environmental and human toxicity due to the use of harsh reagents; limited reaction selectivity, leading to the formation of undesired by-products; and challenges associated with the efficient separation of the desired products from the reaction mixture. However, the synthesis of bio-based molecules derived from sugars as potential alternatives to petrochemical compounds is meaningful only if it is carried out using sustainable processes.

In this context, photocatalytic transformation is regarded as one of the most promising sustainable and environmentally friendly procedures, especially when realized under realistic conditions [5]. As a clean, a renewable, and an abundant source of energy, the direct utilization of sunlight is of great interest in limiting the constant rise in fossil fuels demand. The concept of harnessing solar energy for organic transformations, inspired by natural photosynthesis, dates back over a century to Ciamician's visionary work, "*The Photochemistry of the Future*", which proposed replacing fossil fuels with sunlight for chemical production [6]. The paramount challenge for chemists is to develop an efficient method for the artificial conversion of solar energy using either biochemical, organic, or inorganic materials. In the latter case, although considerable efforts have been devoted to the design of semiconducting (SC) materials capable of achieving high photocatalytic efficiency and selective charge transfer processes under visible light exposure, rather than relying on the lower photon flux of UV light, the most promising photocatalyst materials developed to date suffer from low oxidative selectivity and limited spectral absorption in the UV region due to their excessively large bandgap. This is the case in the benchmark anatase TiO_2 semiconductor, as its bandgap of 3.20 eV restricts light absorption and conversion to wavelengths of below 410 nm, thus accounting for, at best, only 5% of total solar irradiance. This is notably the first and most widely used material for the photocatalytic transformation of glucose [7–12]. In these studies, the authors reported that the photocatalytic oxidation of glucose led to mixtures of aldoses such as arabinose, erythrose, and glyceraldehyde and oxidized sugars such as arabinonic, gluconic, and glucaric acids. Besides lacking selectivity, these reactions are often carried out under UV light or illumination conditions that are unrealistic with respect to real outdoor applications (high light power). However, the ultimate goal for photocatalysis is the development of a catalytic system that can ultimately work within a solar biorefinery concept using sunlight as its energy source. To this end, it is paramount to develop photocatalytic systems that are able to drive photo-chemical reactions by using visible light. For this, it is fundamental that we develop photocatalytic systems that are active under visible light, with materials such as modified C_3N_4 [13], $Zn_{1-x}Cd_xS$ [14], or metal-doped TiO_2 [15], which have been successfully developed for this purpose.

In particular, the use of gold nanoparticles (Au NP) as oxidation catalysts has been well-known for over 20 years, since the first paper by Biella [16], to enhance the eco-efficiency of carbohydrate transformation while simultaneously increasing selectivity for the desired product and reducing both time and waste [17–19]. Moreover, these oxidizing properties have also been leveraged for the detection of reductive organic molecules such as tramadol and hydrazine [20,21] or Cd^{2+} cations [22]. Thanks to their localized surface plasmon resonance (LSPR), and if deposited on a suitable semi-conducting material, Au NPs can also exhibit interesting photocatalytic properties, even under realistic incident light illumination conditions [23–28]. Nevertheless, in all our investigations concerning

the gold-catalyzed photo-oxidation of sugars, as well as in a majority of the studies reported in the literature, maintaining alkaline conditions has proven essential to avert catalyst deactivation.

Otherwise, two-dimensional inorganic layered double hydroxides (LDHs), also known as anionic clays, have attracted immense interest as fascinating supports for heterogeneous catalysis [29–31]. These materials are made of the periodic stacking of positively charged di- and tri-valent metal hydroxides octahedral layers (brucite-like sheets) and negatively charged interlayer spaces where anions and water are located. Their high specific surface area and abundant hydroxyl groups facilitate the efficient anchoring of metal particles and strong metal–support interactions. Moreover, depending on the nature of the metal centers involved in an LDH, the latter can exhibit visible light absorption and, thus, improved light harvesting as photocatalysts with the potential for electronic coupling [32–36]. In particular, Z-scheme heterojunctions involving LDH-based materials have demonstrated remarkable photocatalytic performances, and they are employed in a wide range of photocatalytic reactions such as CO_2 reduction, water splitting, and pollutant degradation, as very recently well-reviewed by Ding et al. [37]. Through the synergistic combination of gold metal nanoparticles and two-dimensional layered double hydroxides, we hoped to take benefits of the plasmonic behavior of gold nanocatalysts, on the one hand, and of the numerous basic sites derived from hydroxyl networks and of the potential intrinsic photocatalytic activities of the LDH, on the other hand, thus allowing us to carry photocatalytic reactions in a base-free condition [38–40].

In this study, we investigated the efficiency of a novel Au/Ni-Al-Zr LDH photocatalyst for the selective oxidation of glucose, used as a model substrate, into corresponding gluconic acid under standardized A.M. 1.5 G light illumination. To optimize the photocatalytic conditions, an experimental design was implemented. Moreover, the reaction was conducted using long-pass filters to elucidate the reaction mechanism, thereby offering valuable insights and guiding future developments in photocatalyst modification.

2. Results and Discussion

2.1. Material Synthesis and Characterization

Among the various existing LDHs, Ni-Al-Zr LDH was selected in this study and prepared by the alkaline co-precipitation of $Ni(NO_3)_2{\cdot}6H_2O$, $Al(NO_3)_2{\cdot}6H_2O$, and $Zr(NO_3)_2{\cdot}9H_2O$ salts, as previously reported [41,42]. After filtration and drying, the Au NPs were deposited on the LDH material using deposition-precipitation with a urea method [43], and the resulting Au/LDH material was fully characterized by means of X-ray diffraction (XRD), transmission electronic microscopy (TEM), UV-visible spectrometry (Figure 1), N_2 adsorption-desorption (BET analysis, Figure S1), FT-IR spectroscopy (Figure S2), diffuse reflectance measurements represented with Kubelka–Munk function (Figure S3), thermogravimetric analysis (TGA, Figure S4), and inductively coupled plasma atomic emission spectroscopy (ICP-AES) (Table S1). The latter confirmed that the Au/Ni-Al-Zr LDH photocatalyst contained 0.49 wt.% of gold. The X-ray diffractogram (Figure 1a) shows the distinctive diffraction peaks of the layered double hydroxides based on the pristine Ni-Al-Zr LDH material, in accordance with Ni-Al-based LDH materials ([44], ICDD PDF 22-0452). Changes in the lattice parameters (Table S2) indicated a modification in the crystalline lattice of the LDH material due to the possible incorporation of gold between the inorganic layers. In the TEM micrograph showing the Au/Ni-Al-Zr LDH material (Figure 1b), we can distinctly observe the lamellar structure of the LDH, which translated into particles having a nanoscopic, urchin-like morphology. The gold nanoparticles were also visible on the dark field image, appearing as white particles that were relatively heterogeneous in size, with a wide distribution of between 6 and 20 nm. The UV-visible measurements on a

dense pellet were used to determine the optical characteristics of the two LDH samples (Figure 1c).

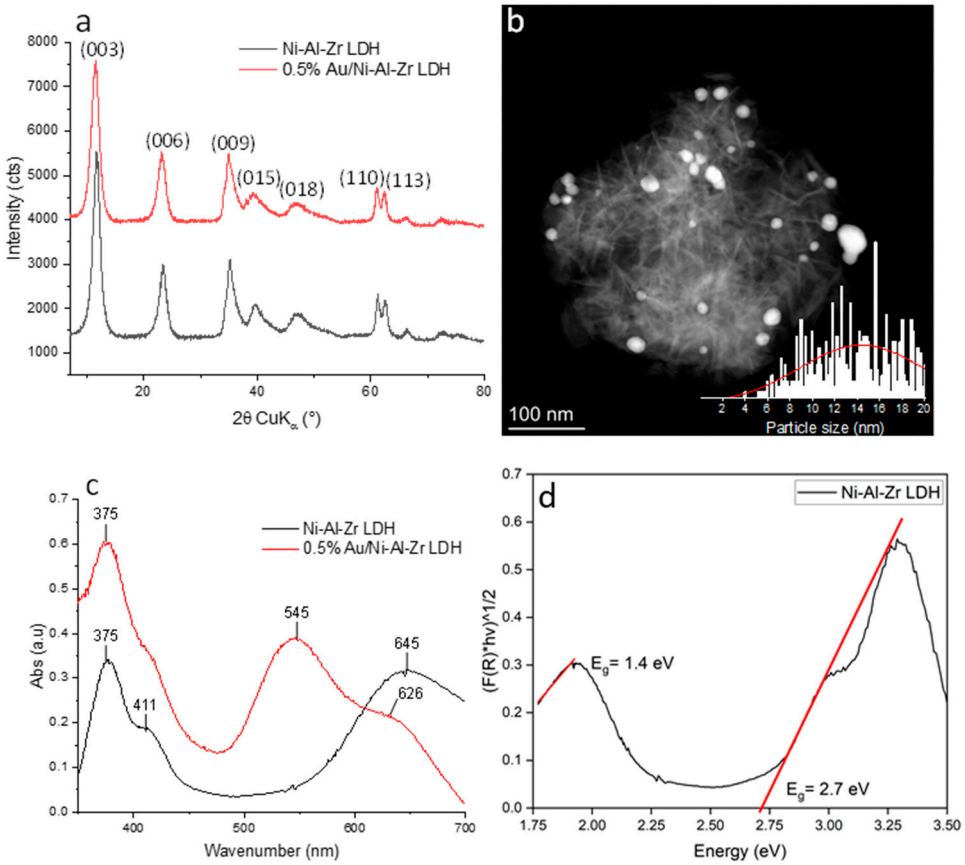

Figure 1. (**a**) Comparative X-ray diffractograms of the Ni-Al-Zr LDH (in black) and 0.5% Au/Ni-Al-Zr LDH (in red). (**b**) TEM micrograph in dark field of the 0.5% Au/Ni-Al-Zr LDH and the gold particle size distribution. (**c**) Comparison of the absorbance spectra of the Ni-Al-Zr LDH (in black) and the 0.5% Au/Ni-Al-Zr LDH (in red) (diffuse reflectance measured with an integration sphere). (**d**) Kubelka–Munk plot of the Ni-Al-Zr pristine material, assuming indirect allowed transition.

Furthermore, the optical properties of the two layered double hydroxide (LDH) samples were systematically analyzed using the Kubelka–Munk function, which was applied to the reflectance measurements obtained from dense pellet samples (Figure 1c). This method allowed for the precise determination of the samples' absorption characteristics. The pristine LDH powder (black curve), which exhibited a green hue, showed two prominent absorption bands at wavelengths of 375 nm and 644 nm. These bands were indicative of the electronic transitions occurring within the material, and their presence in the visible spectrum corresponded well with the observed color of the sample. Upon introducing the gold nanoparticles (Au NPs) onto the surface of the LDH, the optical fingerprint of the material changed significantly (red curve). A new broad absorption band appeared at 545 nm, which was attributed to the localized surface plasmon resonance (LSPR) of the gold nanoparticles [45]. This phenomenon occurs when the conduction electrons on the surface of Au NPs oscillate in resonance with the incident light, leading to enhanced light absorption at specific wavelengths. The emergence of this band highlighted the successful incorporation of the Au NPs into the LDH matrix, and it also highlighted their influence on the material's optical properties. Interestingly, the presence of the Au NPs did not merely introduce a new optical feature; rather, it also altered the behavior of the existing absorption band at 644 nm. This band, which was initially observed in the pristine LDH, remained in the Au NP-decorated sample but showed signs of an interaction with the

newly introduced LSPR band (red curve). The persistence and possible modification of the 644 nm band suggested that there may have been a charge transfer between the Au NPs and the LDH support. Such an interaction could enhance the electronic coupling between metal nanoparticles and the LDH, potentially leading to improved catalytic or photocatalytic properties. This charge transfer is a crucial aspect, as it indicates that the introduction of Au NPs does not simply modify the optical absorption of the material but could also impact its electronic structure and reactivity, thereby expanding the potential applications of composite materials in fields such as photocatalysis and optoelectronics. These spectroscopic measurements also allowed us to determine the optical bandgap of the pristine material using the Kubelka–Munk function (Figure 1d). For the pristine Ni-Al-Zr LDH, two large optical transitions were identified due to the partially filled d-orbitals of the Ni (d-d transition), with a bandgap at ca. 1.4 eV and charge transfer transitions from the ligand to the metal with a bandgap of ca. 2.7 eV [46]. Upon modification with the gold nanoparticles (Au/Ni-Al-Zr LDH), the emergence of the band at 2.27 eV (545 nm), attributed to surface plasmons, skewed the measurement of the bandgap; however, it appeared to be quite similar to that measured on the pristine material (Figure S3). Additionally, the TGA, BET, and FT-IR analyses (ESI) were in accordance with what is generally observed for these kinds of materials [43]. In particular, as expected, the specific BET surface area, measured by nitrogen physisorption, slightly decreased after modification with 0.5% of gold, from 160 m^2/g for the Ni-Al-Zr structure to 150 m^2/g for the 0.5% Au/Ni-Al-Zr-LDH material.

2.2. Catalyst Efficiency

2.2.1. Model Reaction

The ability of the Au/LDH material to onset the oxidation reaction of glucose into sodium gluconate (used as the model reaction) was explored by using the photocatalytic conditions previously optimized (Figure 2) [24]. Briefly, a catalytic charge of gold (substrate/gold mol ratio: 43,000) was added to an alkaline solution of glucose (5 mol. %) in the presence of 1.1 equivalent of hydrogen peroxide as an oxidizing agent and potentially also as an electron scavenger. After 90 min of continuous illumination using standardized A.M. 1.5 G light (100 mW/cm^2), the catalyst was filtrated, and the resulting reaction medium was freeze-dried and analyzed by NMR to determine both the conversion yield and selectivity towards sodium gluconate. As a result, this first attempt yielded only a 31% conversion despite an excellent selectivity towards sodium gluconate, thus demonstrating that transferability strongly depended on the type of photocatalyst. Consequently, we implemented an experimental plan to identify the optimal reaction conditions and estimate the effects of the main influencing parameters and interactions between them.

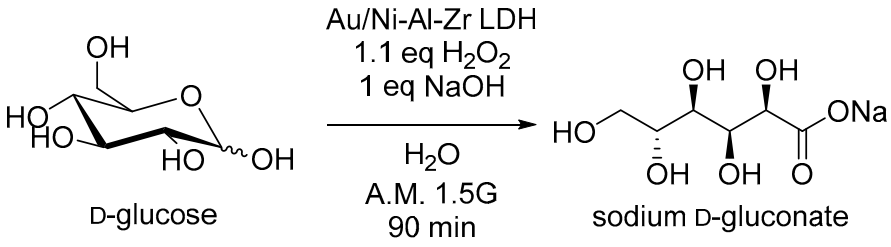

Figure 2. Catalytic oxidation of glucose using the 0.5% Au/Ni-Al-Zr LDH under standardized conditions.

2.2.2. Factorial Experiments

Employing a full factorial design method (FFD), four factors were precisely selected, namely, the amounts of the NaOH, H_2O_2, and Au/LDH photocatalyst and the time, each having two levels (high [+] and low [−]), to develop the factorial plan. Table 1 outlines the operating conditions in this study.

Table 1. Factors and levels studied.

Factors	Level		
	Low (−)	Center (0)	High (+)
A—Catalyst mass (mg)	2.5	13.75	25
B—H_2O_2 volume (µL)	200	400	600
C—NaOH mass (mg)	10	32	55
D—Time (min)	30	60	90

A total of 16 (2^4) factorial trials were conducted (Table S3), and the conversion of glucose into gluconic acid salt was evaluated using NMR spectroscopy (Figures S7–S12). Design Expert 7.0.0 software was used to calculate the average effect and the primary interaction effects of each parameter, and the variance was analyzed using ANOVA (Table S4). All of the main effects and responses had linear relationships, as demonstrated by the linear regression equation determined from the variance analysis. The predictive model for estimating the glucose conversion yield (conversion (%)) can be expressed by the following equation:

$$\text{conversion (\%)} = +22.50 + 14.38 \times A + 5.38 \times B + 16.88 \times C + 2.38 \times D + 8.75 \times A \times C + 4.75 \times A \times D + 4.50 \times B \times C$$

This model equation, as well as a Pareto chart (Figure S6), evidenced the importance of the factors A (m_{cat}) and C (m_{NaOH}) on the conversion yield of glucose. The amount of NaOH was the first and the most sensitive variable affecting the yield of conversion of glucose. This first result was interesting and counterintuitive given the basicity provided by the LDH support. This effect was positive (+16.88), meaning that the increase in the amount of NaOH increased the yield of the glucose conversion. Sodium hydroxide played a pivotal role as an alkaline agent in the process. It governed the catalytic activity of the gold nanoparticles (Au NPs) and allowed for maintaining the ideal surface conditions to avoid poisoning the catalyst, in particular, when the pH was acidic, while promoting the chemisorption of glucose by its hydrated form [47]. This result endorsed that, contrary to what one could expect, the intrinsic basicity of the LDH material was, unfortunately, not strong enough to initiate the photocatalytic process.

The quantity of the catalyst was the second most important factor, having also a positive effect (+14.09). Lastly, our results underlined that the reaction time and H_2O_2 quantity were not influencing factors. The most important interaction worth mentioning was that occurring between the weight of the NaOH and the catalyst (+8.75). Examining surface plots as a function of two factors while maintaining constant values of others is an effective method for determining the relationship between a reaction condition and a conversion yield as a response. Figure 3 provides three-dimensional and contour plots regarding the effect of the most significant two-factor interactions (AC, weights of the NaOH and catalyst) on the yield of glucose conversion, confirming the positive effect of both factors.

Utilizing Expert Design 7.0.0 software, a numerical optimization technique was employed to determine the optimal conditions for glucose conversion, as displayed in Table 2.

Table 2. Predicted (Pred.) and experimental (Exp.) results obtained for the optimal operating conditions determined using a factorial plan.

	m_{cat} (mg)	$V(H_2O_2)$ (µL)	m_{NaOH} (mg)	Time (min)	Conv. (%)
Pred.	29.7	519.13	64.92	89.89	100
Exp.	30	520	65	90	87

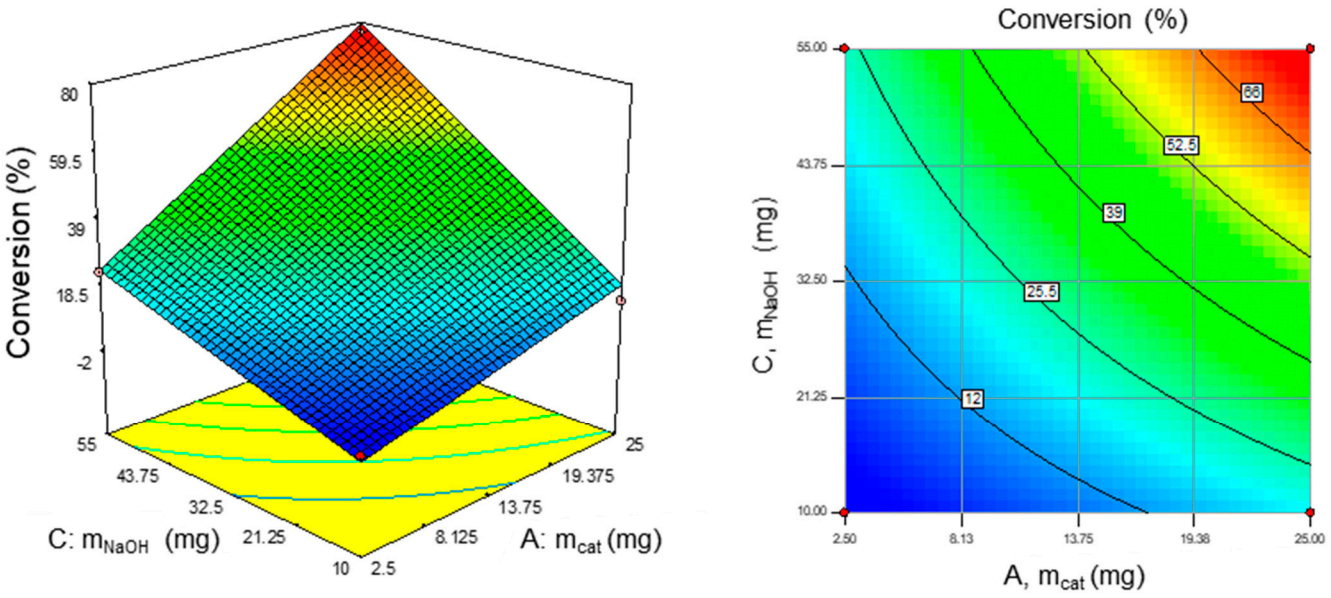

Figure 3. Three-dimensional response surface plot (**left**) and corresponding contour plot (**right**) of the significant AC interaction at VH_2O_2 = 600 µL and time = 90 min with the conversion yield.

By experimentally applying the conditions determined by the numerical model, a noticeable gain in conversion yield to 87% was obtained. This result corroborated well with the predicted conversion yield value determined by the FFD method. Indeed, this latter value was the best result obtained with this catalyst, which allowed us to further confirm the accuracy and validity of the herein-proposed predictive model. Moreover, in comparison with the recently published results summarized in Table 3, this material demonstrated a remarkable performance, achieving one of the highest-reported glucose conversion rates and exceptional selectivity toward gluconic acid salt within just 1.5 h at room temperature. Nevertheless, it did not surpass the results we previously achieved with an Au/CeO_2 material, which enabled quantitative and selective glucose conversion in only 10 min under standardized illumination [24].

Table 3. Photocatalytic performance of various catalysts for glucose conversion under visible-light irradiation.

Catalyst	Illumination	Conditions	Glucose Conversion	Selectivity	Ref.
4.7Mg–CN/CS	500 W Xe short arc lamp with a cut-off filter of λ > 380 nm	50 °C/2 h	97%	71% lactic acid	[13]
$Zn_{0.6}Cd_{0.4}S$	300 W Xenon lamp	25 °C	~90%	~87% lactic acid	[14]
0.2%Pt/TiO_2	300 W Xenon lamp	15 °C/4 h	35.9%	78.6% arabinose and 21.0% erythrose	[11]
0.2%Rh/TiO_2	300 W Xenon lamp	15 °C/4 h	47.0%	74.7% arabinose and 20.6% erythrose	[11]
0.2%Ni/TiO_2	300 W Xenon lamp	15 °C/4 h	27.7%	85.9% arabinose and 7.5% erythrose	[11]
TiO_2	300 W Xenon lamp	15 °C/4 h	42%	7% gluconic acid and 93% C_2–C_5 compounds	[11]
Au/CeO_2	Simulated sunlight (A.M. 1.5 G)	25 °C/10 min	>99%	>95% sodium gluconate	[24]
0.5% Au/Ni-Al-Zr LDH	Simulated sunlight (A.M. 1.5 G)	25 °C/1.5 h	87%	>95% sodium gluconate	This work

2.3. Photocatalytic Behavior and Possible Mechanism

Simultaneously to the factorial experiments, we observed a noticeable variation when standardized illumination or dark conditions were used at room temperature. To decipher if a light-induced mechanism was herein involved, the reaction was deliberately conducted in the dark (Figure 4, black curve). Compared to the darkness, it was clear that in the presence of light (Figure 4, red curve), a much faster reaction was observed, reaching a maximum of 77% conversion yield within only 30 min vs. 74% conversion yield after 90 min in darkness. This first comparative result stressed the contribution of incident light in accelerating the kinetics of glucose oxidation, and therefore, it emphasized the photocatalytic nature of the reaction. Nevertheless, after 90 min of continuous illumination, the reaction medium temperature reached 35 °C. To confirm the photocatalytic hypothesis and also to rule out any heat-induced activation for this reaction, a similar reaction was conducted in the dark at a temperature of 35 °C. As shown in Figure 4 (blue curve), the kinetic enhancement by temperature remained marginal, thus excluding any thermal effect.

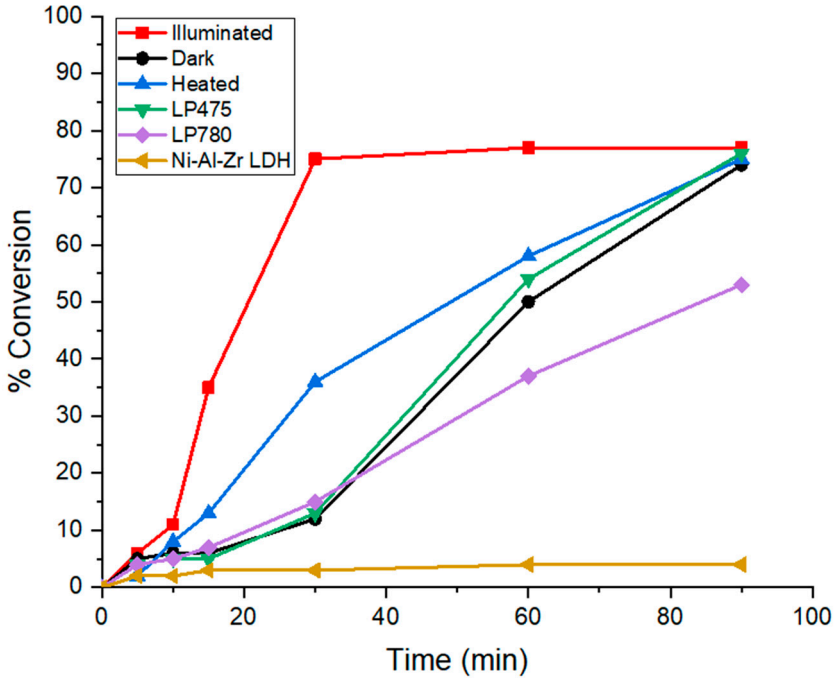

Figure 4. Kinetic comparison of glucose oxidation under standardized A.M. 1.5 G illumination (red), dark conditions (black), or heating to 35 °C (blue). In addition, long-pass filters at 475 nm (green) and 780 nm (purple) were used for incident light spectrum selection. As indicated in yellow, a reaction was performed using the LDH alone.

The involvement of photon-induced free carriers in glucose oxidation demonstrated that the following two potential mechanisms could be proposed: (1) a charge transfer reaction from the LDH bandgap excitation into the gold nanoparticles, and (2) a gold plasmonic-induced charge transfer reaction to the LDH.

To identify the main activation path, we introduced long-pass filters with two different cutoff wavelengths between the light source and the photocatalytic reactor (475 nm and 780 nm). The selection of these filters was guided by the optical characteristics of the photocatalyst, i.e., Ni-Al-Zr LDH has maximum absorptions at 375 nm and 644 nm, whereas the LSPR of gold nanoparticles is located at ca. 550 nm. Thus, the 475 nm filter principally annihilated the high energy photons excitation of the LDH band at 375 nm while leaving the possibility of LSPR excitation. In contrast, the 780 nm long-pass filter hampered both the gold and LDH excitation. Interestingly, when utilizing an LP780 nm filter (Figure 4,

purple curve), there appeared to be no discernible impact of the filtered light on the kinetics of the glucose conversion compared to the darkness experiment. A slight slowing down, particularly at longer times such as 90 min, was even observed, likely due to fluctuations related to the ambient temperature and/or the larger standard deviations. This confirmed that the near-infrared radiation of the Xe-lamp-filtered A.M. 1.5 G condition was not responsible for the photo-induced activation. This was in good agreement with the dark temperature test at 35 °C. Interestingly, it was observed that when employing the LP475 nm filter (Figure 4, green curve), the glucose conversion rate was very similar to that obtained in darkness. This result led us to the conclusion that the photocatalytic activity stemmed from the high-energy photon bandgap excitation in UV and that the Au NPs excitation was not responsible for the photon-induced oxidation of the glucose. Further, the necessity of the gold deposition on the LDH material was undoubtedly highlighted by the experience involving the support material alone under light, yielding a 4% conversion rate after 90 min (yellow curve).

In conclusion, a charge-driven transfer process starting from the excitation of the LDH to the supported gold nanoparticles was evidenced by this bundle of results (Figure 5). As evidenced by the reaction made without H_2O_2, which resulted in no reaction, the latter served as an electron scavenger after the injection of electrons from the conduction band of the LDH into the gold. This electron-scavenging process enhanced the charge separation lifetime, consistent with previous observations in the literature [24,47–49], thereby preventing the undesired rapid radiative recombination processes. This electron transfer resulted in the formation of ·OH oxidant radicals and HO^- anions, which also prevented the poisoning of the gold catalyst by the as obtained gluconic acid. This mechanism knowledge will help to design new materials with tunable bandgaps of the support, allowing for better harvesting of the light and, thus, a better efficiency for the selective transformation of free carbohydrates.

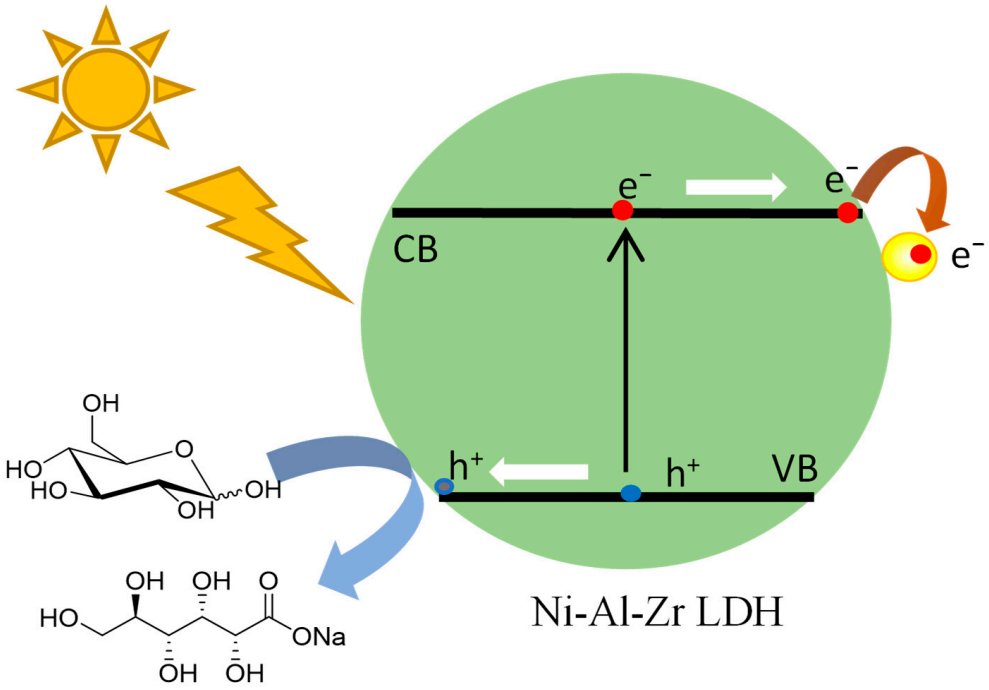

Figure 5. Proposed mechanism for the selective glucose oxidation using Au/Ni-Al-Zr LDH under solar-simulated illumination.

3. Materials and Methods

3.1. General

The solvents and chemical reagents, such as the nickel nitrate ($Ni(NO_3)_2 \cdot 6H_2O$), aluminum nitrate ($Al(NO_3)_2 \cdot 6H_2O$), zirconium nitrate ($Zr(NO_3)_2 \cdot 9H_2O$), sodium carbonate, tetrachloroauric acid ($HAuCl_4 \cdot 3H_2O$), sodium hydroxide, urea, and glucose, were purchased from Merck-Sigma-Aldrich (St Quentin Fallavier, France) or Thermofischer Scientific (Illkirch, France), and used as received.

3.2. Synthesis of the Ni-Al-Zr LDH

The Ni-Al-Zr LDH was prepared by a co-precipitation method, as previously reported [41,42]. A solution containing the $Ni(NO_3)_2 \cdot 6H_2O$, $Al(NO_3)_2 \cdot 6H_2O$, and $Zr(NO_3)_2 \cdot 9H_2O$ in 100 mL of distilled water was slowly dropped under magnetic stirring into a 0.5 M Na_2CO_3 aqueous solution at a rate of 0.1 mL/min. The pH was raised to 10 by adding 2 M NaOH. The precipitate was separated by centrifugation and washed several times with distilled water until the excess nitrates and carbonates were completely removed. The samples were then dried in an oven at 80 °C for 24 h and, finally, ground into fine powders.

3.3. Preparation of the Au/Ni-Al-Zr LDH

The 0.5% Au/Ni-Al-Zr LDH catalyst was prepared by deposition precipitation with urea, as described elsewhere [43]. The Ni-Al-Zr LDH support, prepared by co-precipitation, was dispersed in 200 mL of distilled water under agitation until the temperature reached 80 °C. Subsequently, 0.5 wt. % of gold from $HAuCl_4 \cdot 3H_2O$ (at a concentration of 10 g/L) and urea were added to the mixture, and the mixture was stirred for 16 h.

3.4. Catalytic Test

In the optimized procedure, 1.38 mmol of sugar and 55 mg of NaOH (1 equivalent) were dissolved in 6 mL of water within a glass tube. Subsequently, 25 mg of catalyst, consisting of $Au/NiAl_2Zr_{4.5}$ LDH (0.5 wt. %) and 200 µL of 30% aq. H_2O_2, were added to the solution, and then the reaction mixture was stirred at room temperature under standardized illumination (A.M. 1.5 G) for 90 min. After the reaction, the catalyst was separated by filtration through a nylon membrane (0.25 µm). The resulting filtrate was freeze-dried, and the crude product was characterized by ^1H NMR in D_2O. The area of the H_2 peak of the synthesized gluconate (δ = 4.14 ppm, d, J = 3.7 Hz) was compared to the area of the H1 peaks of the residual glucose (H1α: δ = 5.24 ppm, d, J = 3.7 Hz and H1β: δ = 4.65 ppm, d, J = 7.9 Hz) to calculate a conversion rate according to the following formula:

$$\%\,\text{Conv.} = \frac{\text{A(H2gluconate)}}{\text{A(H1}\alpha\text{glucose)} + \text{A(H1}\beta\text{glucose)} + \text{A(H2gluconate)}} \times 100$$

4. Conclusions

In conclusion, this study highlights the important role of the charge transfer induced by the excitation of the matrix of layered double hydroxides (LDHs) to support gold nanoparticles. This process constitutes a fundamental mechanism for enhancing the photocatalytic properties of the studied materials. The successful integration of gold nanoparticles within the Ni-Al-Zr LDH matrix not only preserved the base crystalline structure but also facilitated efficient electron transfer, which is essential for the activation and selective conversion of free carbohydrates.

To further elucidate this understanding, a factorial design with four parameters was employed, enabling the optimization of the reaction conditions and the systematic ex-

ploration of the influence of each factor on overall process efficiency. This experimental design was instrumental in identifying the optimal conditions, minimizing the number of trials required while maximizing the information obtained on the parameter interactions. Through this methodical approach, specific parameter ranges where photocatalytic yield was maximized, particularly in terms of the adjusted bandgap of the LDH, could be targeted.

The insights gained into this charge transfer mechanism open promising avenues for the design of new materials with finely tunable optoelectronic properties. By manipulating the bandgaps of LDH supports, it becomes feasible to optimize solar light absorption, thereby expanding the usable light spectrum for photocatalytic reactions. This enhanced light capture translates into substantial improvements in the efficiency of selective chemical transformations, particularly in the conversion of free carbohydrates, a major area of interest in green chemistry and renewable energy.

In summary, this study not only demonstrates enhanced photocatalytic capabilities of Au/LDH composites but also provides a robust methodology for the rational design of advanced materials. These advancements could have significant implications in the development of more sustainable chemical processes, fully leveraging solar light for industrial and environmental applications.

Supplementary Materials: The following supporting information can be downloaded at: https://www.mdpi.com/article/10.3390/molecules30010013/s1, instrument specifications, material characterization (BET analysis, FT-IR spectroscopy, ICP-AES, TGA, and XRD), factorial experiments, and the ^{1}H NMR spectra of the crudes.

Author Contributions: G.P. and F.S. conceived and designed the catalytic and photocatalytic experiments; S.B., J.J.C., R.B. and G.B. supervised the synthesis and characterization of the materials; K.K. conceived the full factorial experiments; and N.D., L.Q. and K.K. performed the experiments. All authors analyzed the data, though N.D. and G.P. were the primary authors of the manuscript. All authors proofread the manuscript. All authors have read and agreed to the published version of the manuscript.

Funding: This work was supported by EDUCA and the doctoral school of the University of Cadiz (Escuela Doctorale de la Universidad de Cádiz) through the grant from N.D.'s internship.

Institutional Review Board Statement: Not applicable.

Informed Consent Statement: Not applicable.

Data Availability Statement: The original contributions presented in the study are included in the article and the Supplementary Materials. Further inquiries can be directed to the corresponding author.

Conflicts of Interest: The authors declare no conflicts of interest.

References

1. Gallezot, P. Conversion of biomass to selected chemical products. *Chem. Soc. Rev.* **2012**, *41*, 1538–1558. [CrossRef] [PubMed]
2. Chatterjee, C.; Pong, F.; Sen, A. Chemical conversion pathways for carbohydrates. *Green Chem.* **2015**, *17*, 40–71. [CrossRef]
3. Isbell, H.S. Oxidation of the alpha and beta forms of the sugars. *J. Am. Chem. Soc.* **1932**, *54*, 1692–1693. [CrossRef]
4. Hollenberg, D.H.; Klein, R.S.; Fox, J.J. Pyridinium chlorochromate for the oxidation of carbohydrates. *Carbohydr. Res.* **1978**, *67*, 491–494. [CrossRef]
5. Balzani, V.; Credi, A.; Venturi, M. Photochemical Conversion of Solar Energy. *ChemSusChem* **2008**, *1*, 26–58. [CrossRef]
6. Ciamician, G. The Photochemistry of The Future. *Science* **1912**, *36*, 385–394. [CrossRef]
7. Colmenares, J.C.; Magdziarz, A.; Bielejewska, A. High-value chemicals obtained from selective photo-oxidation of glucose in the presence of nanostructured titanium photocatalysts. *Bioresour. Technol.* **2011**, *102*, 11254–11257. [CrossRef]
8. Colmenares, J.C.; Magdziarz, A. Room temperature versatile conversion of biomass-derived compounds by means of supported TiO_2 photocatalysts. *J. Mol. Catal. A Chem.* **2013**, *366*, 156–162. [CrossRef]

9. Da Vià, L.; Recchi, C.; Gonzalez-Yanez, E.O.; Davies, T.E.; Lopez-Sanchez, J.A. Visible light selective photocatalytic conversion of glucose by TiO_2. *Appl. Catal. B Environ.* **2017**, *202*, 281–288. [CrossRef]
10. Bellardita, M.; García-López, E.I.; Marcì, G.; Megna, B.; Pomilla, F.R.; Palmisano, L. Photocatalytic conversion of glucose in aqueous suspensions of heteropolyacid–TiO_2 composites. *RSC Adv.* **2015**, *5*, 59037–59047. [CrossRef]
11. Chong, R.; Li, J.; Ma, Y.; Zhang, B.; Han, H.; Li, C. Selective conversion of aqueous glucose to value-added sugar aldose on TiO_2-based photocatalysts. *J. Catal.* **2014**, *314*, 101–108. [CrossRef]
12. Jin, B.; Yao, G.; Wang, X.; Ding, K.; Jin, F. Photocatalytic oxidation of glucose into formate on nano TiO_2 catalyst. *ACS Sustain. Chem. Eng.* **2017**, *5*, 6377–6381. [CrossRef]
13. Srikhaow, A.; Chuaicham, C.; Trakulmututa, J.; Shu, K.; Sasaki, K. Mg-modified graphitic carbon nitride/converter slag composites as an efficient photocatalyst for sugar conversion. *Sustain. Energy Fuels* **2024**, *8*, 3065–3076. [CrossRef]
14. Zhao, H.; Li, C.-F.; Yong, X.; Kumar, P.; Palma, B.; Hu, Z.-Y.; Van Tendeloo, G.; Siahrostami, S.; Larter, S.; Zheng, D. Coproduction of hydrogen and lactic acid from glucose photocatalysis on band-engineered $Zn_{1-x}Cd_xS$ homojunction. *Iscience* **2021**, *24*, 102109. [CrossRef]
15. Zhou, B.; Song, J.; Wu, T.; Liu, H.; Xie, C.; Yang, G.; Han, B. Simultaneous and selective transformation of glucose to arabinose and nitrosobenzene to azoxybenzene driven by visible-light. *Green Chem.* **2016**, *18*, 3852–3857. [CrossRef]
16. Biella, S.; Prati, L.; Rossi, M. Selective oxidation of D-glucose on gold catalyst. *J. Catal.* **2002**, *206*, 242–247. [CrossRef]
17. Della Pina, C.; Falletta, E.; Prati, L.; Rossi, M. Selective oxidation using gold. *Chem. Soc. Rev.* **2008**, *37*, 2077–2095. [CrossRef]
18. Della Pina, C.; Falletta, E.; Rossi, M. Update on selective oxidation using gold. *Chem. Soc. Rev.* **2012**, *41*, 350–369. [CrossRef]
19. Yan, W.; Zhang, D.; Sun, Y.; Zhou, Z.; Du, Y.; Du, Y.; Li, Y.; Liu, M.; Zhang, Y.; Shen, J.; et al. Structural sensitivity of heterogeneouscatalysts for sustainable chemical synthesis of gluconic acid from glucose. *Chin. J. Catal.* **2020**, *41*, 1320–1336. [CrossRef]
20. Atta, N.F.; Ahmed, R.A.; Amin, H.M.; Galal, A. Monodispersed gold nanoparticles decorated carbon nanotubes as an enhanced sensing platform for nanomolar detection of tramadol. *Electroanalysis* **2012**, *24*, 2135–2146. [CrossRef]
21. Amin, H.M.; El-Kady, M.F.; Atta, N.F.; Galal, A. Gold nanoparticles decorated graphene as a high performance sensor for determination of trace hydrazine levels in water. *Electroanalysis* **2018**, *30*, 1757–1766. [CrossRef]
22. Shah, A.; Akhtar, S.; Mahmood, F.; Urooj, S.; Siddique, A.B.; Irfan, M.I.; Abbas, A. Fagonia arabica extract-stabilized gold nanoparticles as a highly selective colorimetric nanoprobe for Cd^{2+} detection and as a potential photocatalytic and antibacterial agent. *Surf. Interfaces* **2024**, *51*, 104556. [CrossRef]
23. Wang, C.; Astruc, D. Nanogold plasmonic photocatalysis for organic synthesis and clean energy conversion. *Chem. Soc. Rev.* **2014**, *43*, 7188–7216. [CrossRef] [PubMed]
24. Omri, M.; Sauvage, F.; Becuwe, M.; Pourceau, G.; Wadouachi, A.; Busby, Y. Gold catalysis and photoactivation: A fast and selective procedure for the oxidation of free sugars. *ACS Catal.* **2018**, *8*, 1635–1639. [CrossRef]
25. Omri, M.; Sauvage, F.; Golonu, S.; Wadouachi, A.; Pourceau, G. Photocatalyzed transformation of free carbohydrates. *Catalysts* **2018**, *8*, 672. [CrossRef]
26. Gellé, A.; Jin, T.; de la Garza, L.; Besteiro, L.V.; Moores, A. Applications of plasmon-enhanced nanocatalysis to organic transformations et al. *Chem. Rev.* **2020**, *120*, 986–1042. [CrossRef]
27. Golonu, S.; Pourceau, G.; Quehon, L.; Wadouachi, A.; Sauvage, F. Insight on the contribution of plasmons to gold-catalyzed solar driven selective oxidation of glucose under oxygen. *Solar RRL* **2020**, *4*, 2000084. [CrossRef]
28. Kumar, A.; Choudhary, P.; Kumar, A.; Camargo, P.H.C.; Krishnan, V. Recent advances in plasmonic photocatalysis based on TiO_2 and noble metal nanoparticles for energy conversion, environmental remediation, and organic synthesis. *Small* **2022**, *18*, 2101638. [CrossRef]
29. Kwok, W.L.; Crivoi, D.-G.; Chen, C.; Buffet, J.-C.; O'Hare, D. Silica@layered double hydroxide core–shell hybrid materials. *Dalton Trans.* **2018**, *47*, 143–149. [CrossRef]
30. Mantovani, K.M.; Westrup, K.C.M.; da Silva Junior, R.M.; Jaerger, S.; Wypych, F.; Nakagaki, S. Oxidation catalyst obtained by the immobilization of layered double hydroxide/Mn (III) porphyrin on monodispersed silica spheres. *Dalton Trans.* **2018**, *47*, 3068–3073. [CrossRef]
31. Fan, K.; Xu, P.; Li, Z.; Shao, M.; Duan, X. Layered double hydroxides: Next promising materials for energy storage and conversion. *Next Mater.* **2023**, *1*, 100040. [CrossRef]
32. Xu, S.-M.; Pan, T.; Dou, Y.-B.; Yan, H.; Zang, S.-T.; Ning, F.-Y.; Shi, W.-Y.; Wei, M. Theoretical and experimental study on MIIMIII-layered double hydroxides as efficient photocatalysts toward oxygen evolution from water. *J. Phys. Chem. C* **2015**, *119*, 18823–18834. [CrossRef]
33. Iguchi, S.; Kikkawa, S.; Teramura, K.; Hosokawa, S.; Tanaka, T. Investigation of the electrochemical and photoelectrochemical properties of Ni–Al LDH photocatalysts. *Phys. Chem. Chem. Phys.* **2016**, *18*, 13811–13819. [CrossRef] [PubMed]
34. Zhao, Y.; Waterhouse, G.I.; Chen, G.; Xiong, X.; Wu, L.-Z.; Tung, C.-H.; Zhang, T. Two-dimensional-related catalytic materials for solar-driven conversion of COx into valuable chemical feedstocks. *Chem. Soc. Rev.* **2019**, *48*, 1972–2010. [CrossRef]

35. Ding, G.; Liu, Z.; Wang, Q.; Li, Y.; Liu, W.; Liu, Y. Ag-modified α-Fe_2O_3 spherical particles interspersed on hierarchical flower-like NiAl-LDH microspheres with Z-scheme for significantly enhanced CO_2 photoreduction into CO. *J. Colloid Interf. Sci.* **2023**, *629*, 193–205. [CrossRef]
36. Ding, G.; Li, C.; Ni, Y.; Chen, L.; Shuai, L.; Liao, G. Layered double hydroxides and their composites as high-performance photocatalysts for CO_2 reduction. *EES Catal.* **2023**, *1*, 369–391. [CrossRef]
37. Ding, G.; Wang, Z.; Zhang, J.; Wang, P.; Chen, L.; Liao, G. Layered double hydroxides-based Z-scheme heterojunction for photocatalysis. *EcoEnergy* **2024**, *2*, 22–44. [CrossRef]
38. Gilea, D.; Ciocarlan, R.G.; Seftel, E.M.; Cool, P.; Carja, G. Engineering Heterostructures of Layered Double Hydroxides and Metal Nanoparticles for Plasmon-Enhanced Catalysis. *Catalysts* **2022**, *12*, 1210. [CrossRef]
39. Tomar, R.; Sharma, J.; Nishimura, S.; Ebitani, K. Aqueous oxidation of sugars into sugar acids using hydrotalcite-supported gold nanoparticle catalyst under atmospheric molecular oxygen. *Chem. Lett.* **2016**, *45*, 843–845. [CrossRef]
40. Zhuge, Y.; Fan, G.; Lin, Y.; Yang, L.; Li, F. A hybrid composite of hydroxyapatite and Ca–Al layered double hydroxide supported Au nanoparticles for highly efficient base-free aerobic oxidation of glucose. *Dalton Trans.* **2019**, *48*, 9161–9172. [CrossRef]
41. Arias, S.; Sousa, L.V.; Barbosa, C.B.; Silva, A.O.S.; Fréty, R.; Pacheco, J.G.A. Preparation of NiAlZr-terephthalate LDHs with high Al and Zr content and their mixed oxides for cyclohexane dehydrogenation. *Appl. Clay Sci.* **2018**, *166*, 137–145. [CrossRef]
42. Dib, N.; Bachir, R.; Berrichi, A.; Blanco, G.; Bedrane, S.; Calvino, J.J. Zr-doped MgAl-LDH@Au nano-catalysts for selective and efficient oxidation of biomass-derived furfural. *J. Environ. Chem. Eng.* **2024**, *12*, 113357.
43. Berrichi, A.; Bachir, R.; Benabdallah, M.; Choukchou-Braham, N. Supported nano gold catalyzed three-component coupling reactions of amines, dichloromethane and terminal alkynes (AHA). *Tetrahedron Lett.* **2015**, *56*, 1302–1306. [CrossRef]
44. Zhang, L.-Y.; Han, Y.-L.; Liu, M.; Deng, S.-L. Ni–Al layered double hydroxide-coupled layered mesoporous titanium dioxide (Ni–Al LDH/LM-TiO_2) composites with integrated adsorption-photocatalysis performance. *RSC Adv.* **2023**, *13*, 16797–16814. [CrossRef]
45. Khan, A.W.; Lali, N.S.; Sabei, F.Y.; Irfan, M.I.; Naeem-Ul-Hassan, M.; Sher, M.; Safhi, A.Y.; Alsalhi, A.; Albariqi, A.H.; Kamli, F.; et al. Sunlight-assisted green synthesis of gold nanocubes using horsetail leaf extract: A highly selective colorimetric sensor for Pb^{2+}, photocatalytic and antimicrobial agent. *J. Environ. Chem. Eng.* **2024**, *12*, 112576. [CrossRef]
46. Gomes Silva, C.; Bouizi, Y.; Fornés, V.; Garcia, H. Layered Double Hydroxides as Highly Efficient Photocatalysts for Visible Light Oxygen Generation from Water. *J. Am. Chem. Soc.* **2009**, *131*, 13833–13839. [CrossRef]
47. Comotti, M.; Della Pina, C.; Falletta, E.; Rossi, M. Aerobic oxidation of glucose with gold catalyst: Hydrogen peroxide as intermediate and reagent. *Adv. Synth. Catal.* **2006**, *348*, 313–316. [CrossRef]
48. Castillo, N.C.; Ding, L.; Heel, A.; Graule, T.; Pulgarin, C.J. On the photocatalytic degradation of phenol and dichloroacetate by $BiVO_4$: The need of a sacrificial electron acceptor. *J. Photochem. Photobiol. A* **2010**, *216*, 221–227.
49. Tseng, D.-H.; Juang, L.-C.; Huang, H.-H. Effect of Oxygen and Hydrogen Peroxide on the Photocatalytic Degradation of Monochlorobenzene in TiO_2 Aqueous Suspension. *Int. J. Photoenergy* **2012**, *2012*, 328526. [CrossRef]